



Norwegian University of  
Science and Technology

# Distributed Sacrificial Anode (DSA) - Properties in Mud and at Elevated Temperatures in Seawater

**Audun Ryen**

Subsea Technology

Submission date: June 2017

Supervisor: Roy Johnsen, MTP

Norwegian University of Science and Technology  
Department of Mechanical and Industrial Engineering





---

## Preface

The master thesis is part of the 2-years Master's Degree Programme, Subsea Technology. The Subsea Technology programme is part of Department of Mechanical and Industrial Engineering (MTP) at the Norwegian University of Science and Technology.

This master thesis was written at the Department of Mechanical and Industrial Engineering, Perleporten, Trondheim, in the course, TMM4960 - Engineering Design and Materials, Master's Thesis. The thesis was written during the spring of 2017.

I would like to thank Mr. Nils Inge Nilsen for practical help and guidance in the laboratory at Perleporten, MTP.

I would like to thank Mr. Cristian Torres for excellent help and guidance in the laboratories at Perleporten, MTP.

From the industry I would like to thank Mr. Mariano Ianuzzi, G E Oil and Gas, for valuable discussions and inputs.

I would especially like to thank my supervisor Professor Roy Johnsen, at the Department of Mechanical and Industrial Engineering, for his excellent guidance and assistance throughout the project. His commitment to the subject is highly appreciated.

Trondheim, June 24, 2017

A handwritten signature in blue ink that reads "Audun Ryen". The signature is written in a cursive style and is underlined.

Audun Ryen

---

---

## Abstract

Cost savings with regards to optimizing the Cathodic Protection (CP) design has over the last 50 years not been considered as a major opportunity so far. Sacrificial anodes combined with organic coatings is the main corrosion protection strategy per now for subsea applications. Much experience from this method has been gained, but some limitations exist. The total anode mass can be significant, depending on the size, complexity, environmental conditions and design life of the subsea system. The total anode mass adds weight to the submerged structure. This can cause constraints on installation vessels and cranes, causing increased installation costs. Decreasing the weight on CP system can reduce costs by using less costly installation vessels, and could also favor safer installation campaigns due to less complex lift operations.

A fairly new concept was tested in this study. The concept is named Distributed Sacrificial Anode (DSA) and consists of distributing sacrificial anodes from an anode alloy (Al-Zn-In) onto Carbon Steel (CS) plates. This was in this study achieved by electric arc spraying, a thermal spraying process. The idea behind this solution is to reduce the total "anode mass" required, since the coating itself may provide sufficient CP to CS during lifetime.

The electrochemical properties of DSA at elevated temperatures in natural SW was examined in this study. The experiments were performed in rebuilt glass beakers containing natural SW. SW was replaced with fresh SW at certain intervals to prevent the samples from being exposed to the same electrolyte throughout exposure. Identical tests, including freely exposed and galvanically coupled (with CS) DSA, Thermally Sprayed Aluminum (TSA) (99.5% Al) and Anode (Al-Zn-In) samples, were performed at three temperatures; 22, 50 and 80 °C, respectively. The electrochemical properties of DSA at exposure in saline mud was also examined in this study. The experiment was performed in a container with mud taken from the shoreline outside Statoil Rotvoll, Trondheim. DSA and TSA samples were freely exposed, galvanically coupled with CS and polarized to -1.1 V Ag/AgCl in mud.

The anodic abilities of coatings were investigated and compared. The effect of temperature in SW and exposure in mud on the electrochemical properties was one of the main focus areas, and it was attempted to quantify the effect of temperature on total degradation of the coatings.

This thesis discovered that the electrochemical properties of DSA are similar to those of a sacrificial anode. The results showed that DSA worked better as a CP system, providing increased level of protection to CS at all temperatures compared to TSA. This is overall because DSA contains elements of Zinc and Indium, that activate the Aluminum substrate. Freely exposed DSA and TSA samples suffer initially from high corrosion rates at elevated temperatures, but they decrease rapidly during exposure. No significant difference in corrosion rates as a function of temperature was found after 2 months of exposure, the corrosion rates were in fact slightly lower with increased temperature. It was found that TSA and DSA embedded in mud exhibit low corrosion rates throughout exposure. DSA had active anodic abilities which ensured increased level of protection of CS in mud compared to TSA. It was found that DSA requires slightly less current density compared to TSA when cathodically polarized to -1100 mV Ag/AgCl in mud.

The results obtained in this thesis showed that crevice corrosion is an increasing threat at elevated temperatures in SW both for coupled TSA and DSA samples. Coupled DSA samples at all temperatures in SW appear to suffer from cohesive failure. Quantifying the effect of temperature on total degradation of DSA and TSA samples can not be done solely based on the findings in this report.

---

---

## Sammendrag

Gjennom de siste 50 årene, etter at katodisk beskyttelse ble tatt i bruk, har det ikke blitt vurdert kostnadsbesparelser man kan oppnå med hensyn til optimalisering av designet. Offeranoder kombinert med organiske belegg er den viktigste korrosjonsbeskyttelsesstrategien per dags dato for subsea applikasjoner. Mye erfaring med denne metoden har blitt oppnådd, men noen begrensninger eksisterer. Total anodemasse kan være betydelig, avhengig av størrelsen, kompleksiteten, miljøforholdene og designlevetiden til undervannssystemet. Den totale anodemassen øker vekten på den nedsenkede strukturen. Dette kan føre til begrensninger på installasjonsfartøy og kraner, noe som medfører økte installasjonskostnader. Å redusere vekten på CP-systemet kan redusere kostnadene ved at man kan bruke mindre kostbare installasjonsfartøy, og kan også gi sikrere installasjonskampanjer på grunn av mindre komplekse løfteoperasjoner.

Et ganske nytt konsept ble testet i denne studien. Det kalles Distributed Sacrificial Anode (DSA) og består av å distribuere offeranoder fra en anodelegering (Al-Zn-In) på karbonstål (CS)-plater. Dette ble i denne studien oppnådd ved elektrisk lysbuesprøyting, en termisk sprøyteprosess. Tanken bak denne løsningen er å redusere den totale "anodemassen" som kreves, siden belegget selv kan gi tilstrekkelig CP til CS gjennom levetiden.

De elektrokjemiske egenskapene til DSA ved forhøyede temperaturer i naturlig sjøvann (SW) ble undersøkt i denne studien. Forsøkene ble utført i ombyggede glassbeholdere som inneholdt naturlig SW. SW ble erstattet med ferskt SW med visse intervaller for å hindre at prøvene ble eksponert for samme elektrolytt gjennom hele eksponeringen. Identiske tester, inkludert fritt eksponerte og galvanisk koplede (med CS) DSA, termisk sprøytet aluminium (TSA) (99,5 % Al) og Anode (Al-Zn-In) prøver ble utført ved tre temperaturer, henholdsvis 22, 50 og 80 °C. De elektrokjemiske egenskapene til DSA ved eksponering i saltvannsslam/gjørme ble også undersøkt i denne studien. Forsøket ble utført i en beholder med gjørme tatt fra fjæra utenfor Statoil Rotvoll, Trondheim. DSA- og TSA-prøver ble fritt eksponert, galvanisk koplet med CS og polarisert til -1,1 V Ag / AgCl i gjørme.

De anodiske evnene til beleggene ble undersøkt og sammenlignet. Effekten av temperatur i SW og eksponering i gjørme på elektrokjemiske egenskaper var et av hovedfokusområdene, og det ble forsøkt å kvantifisere effekten av temperatur på total nedbrytning av beleggene.

Denne oppgaven viser at de elektrokjemiske egenskapene til DSA ligner de som en offeranode har. Resultatene viser at DSA fungerer bedre som et CP-system, noe som gir økt nivå på beskyttelse av CS ved alle temperaturer sammenlignet med TSA. Dette er på grunn av at DSA inneholder elementer av sink og indium som aktiverer aluminiumsubstratet. Fritt eksponerte DSA- og TSA-prøver lider i utgangspunktet av høye korrosjonshastigheter ved høye temperaturer, men de avtar raskt under eksponering. Det ble ikke funnet noen signifikant forskjell i korrosjonshastighet som en funksjon av temperatur etter 2 måneders eksponering, korrosjonshastighetene var faktisk litt lavere ved økt temperatur. Det ble funnet at fritt eksponert TSA og DSA i gjørme har lave korrosjonshastigheter. DSA har aktive anodiske evner som sørget for økt beskyttelsesnivå for CS i gjørme sammenlignet med TSA. Det ble funnet at DSA krever noe mindre strømtetthet sammenlignet med TSA når katodisk polarisert til -1100 mV Ag / AgCl i gjørme.

Resultatene oppnådd i denne oppgaven viser at spaltkorrosjon er en økende trussel ved forhøyede temperaturer i SW både for koblede TSA- og DSA-prøver. Koblede DSA-prøver ser, ved alle temperaturer i SW, ut til å lide av kohesive feil i belegget. Kvantifisering av effekten av temperatur på total nedbrytning av DSA og TSA prøver kan ikke gjøres utelukkende basert på funnene i denne rapporten.

---

---

# Table Of Contents

Preface . . . . .	i
Abstract . . . . .	iii
Sammendrag . . . . .	v
Abbreviations . . . . .	xi
List of Figures . . . . .	xiii
List of Tables . . . . .	xvii
<b>1 Introduction</b>	<b>1</b>
1.1 Background . . . . .	1
1.2 Objectives . . . . .	2
<b>2 General Theory</b>	<b>3</b>
2.1 Thermally Sprayed Coatings . . . . .	3
2.1.1 Application methods . . . . .	3
2.1.2 General Coating Properties . . . . .	4
2.1.3 Pre-treatment of substrate surface . . . . .	5
2.1.4 Corrosion Protection . . . . .	6
2.1.5 Thermally Sprayed Aluminum . . . . .	7
2.2 Corrosion of Aluminum . . . . .	8
2.2.1 Effect of temperature . . . . .	10
2.2.2 Pitting Corrosion . . . . .	11
2.2.3 Crevice Corrosion . . . . .	11
2.3 Corrosion of TSA . . . . .	12
2.4 Measurement methods for corrosion testing . . . . .	13
2.5 Cathodic Protection . . . . .	14
2.5.1 CP by Sacrificial Anodes . . . . .	16
2.5.2 Cathodic Protection of steel . . . . .	16
2.5.3 Cathodic Protection of Aluminum . . . . .	17
2.5.4 Cathodic Protection of TSA . . . . .	18
<b>3 Literature Review</b>	<b>21</b>
<b>4 Experimental Work</b>	<b>25</b>
4.1 Exposure at elevated temperatures . . . . .	25
4.1.1 Materials included in the experiment . . . . .	25
4.1.2 Experiment setup . . . . .	27
4.1.3 Test sample setup . . . . .	30
4.1.4 Experimental Conditions . . . . .	31
4.1.5 Linear Polarization Resistance Measurements . . . . .	32
4.1.6 Polarization Curves . . . . .	32
4.1.7 Visual Observations and cleaning with Nitric Acid . . . . .	33
4.1.8 Optical Microscopy . . . . .	34

4.1.9	Surface and Cross Section Analysis . . . . .	34
4.2	Exposure in Mud . . . . .	35
4.2.1	Materials included in the experiment . . . . .	35
4.2.2	Experiment setup . . . . .	35
4.2.3	Test sample setup . . . . .	37
4.2.4	Experimental Conditions . . . . .	38
4.2.5	Linear Polarization Resistance Measurements . . . . .	39
4.2.6	Polarization Curves . . . . .	39
4.2.7	Visual Observations and cleaning with Nitric Acid . . . . .	39
4.2.8	Surface and Cross Section Analysis . . . . .	39
<b>5</b>	<b>Electrochemical Results - Exposure at Elevated Temperatures</b>	<b>41</b>
5.1	pH measurements and Replacement of Seawater . . . . .	41
5.2	Open Circuit Potentials . . . . .	43
5.2.1	The effect of pH . . . . .	45
5.3	Galvanic Coupled Potentials . . . . .	45
5.3.1	The effect of pH and replacement of seawater . . . . .	46
5.4	Galvanic Currents . . . . .	47
5.4.1	The effect of pH and replacement of seawater . . . . .	48
5.5	Linear Polarization Resistance measurements . . . . .	49
5.6	Polarization Curves . . . . .	50
5.6.1	DSA, Anodic Polarization Curves at day 1 . . . . .	51
5.6.2	DSA, Freely Exposed samples at day 63 . . . . .	52
5.6.3	TSA, Freely Exposed samples at day 63 . . . . .	53
5.6.4	Anode, Freely Exposed samples at day 63 . . . . .	54
5.6.5	22°C, Freely Exposed samples at day 63 . . . . .	55
5.6.6	50°C, Freely Exposed samples at day 63 . . . . .	56
5.6.7	80°C, Freely Exposed samples at day 63 . . . . .	57
5.6.8	Summary - Polarization Curves . . . . .	57
5.7	Corrosion Rates . . . . .	57
5.8	Summary - Electrochemical Results . . . . .	58
<b>6</b>	<b>Electrochemical Results - Exposure in Mud</b>	<b>61</b>
6.1	Open Circuit Potentials . . . . .	62
6.2	Galvanic Coupled Potentials and Currents . . . . .	63
6.3	Current Densities of Polarized Samples . . . . .	66
6.4	Linear Polarization Resistance measurements . . . . .	68
6.5	Polarization Curves . . . . .	69
6.5.1	Summary - Polarization Curves . . . . .	70
6.6	Corrosion Rates . . . . .	71
6.7	Summary - Electrochemical Results . . . . .	72
<b>7</b>	<b>Coating Examination - Exposure at elevated temperatures</b>	<b>73</b>
7.1	Visual Examination . . . . .	73
7.1.1	Prior Exposure . . . . .	73
7.1.2	Post Exposure . . . . .	74
7.2	Optical Microscopy . . . . .	77
7.3	EDS of Cross Sections . . . . .	79
7.3.1	Sources for Inaccuracy . . . . .	79
7.3.2	Prior Exposure . . . . .	80
7.4	Post Exposure . . . . .	82



7.4.1	Samples exposed at 22°C . . . . .	82
7.5	Samples exposed at 50 and 80°C . . . . .	84
7.6	Thickness evaluation in SEM . . . . .	84
<b>8</b>	<b>Surface Examination - Mud Exposure</b>	<b>87</b>
8.1	Visual Examination . . . . .	87
8.1.1	Prior Exposure . . . . .	87
8.1.2	Post Exposure . . . . .	88
8.2	EDS of Cross Sections . . . . .	89
8.2.1	Prior Exposure . . . . .	89
8.2.2	Post Exposure . . . . .	90
8.3	Thickness evaluation in SEM . . . . .	90
<b>9</b>	<b>Discussion - Elevated Temperatures in SW</b>	<b>91</b>
9.1	Effect of pH . . . . .	91
9.2	Electrochemical Properties after 63 days . . . . .	94
9.3	Open Circuit Potential . . . . .	94
9.4	Galvanic Coupled Samples . . . . .	96
9.4.1	Galvanic Currents and Potentials . . . . .	97
9.5	LPR measurements . . . . .	99
9.6	Corrosion Rates . . . . .	99
9.7	Thickness Evaluation . . . . .	100
<b>10</b>	<b>Discussion - Exposure in Mud</b>	<b>101</b>
10.1	Open Circuit Potentials . . . . .	101
10.2	Galvanically Coupled Samples . . . . .	102
10.3	Polarized Samples . . . . .	103
10.4	Polarization Curves . . . . .	103
10.5	Corrosion Rates . . . . .	104
10.6	Thickness evaluation . . . . .	105
<b>11</b>	<b>Conclusions</b>	<b>107</b>
<b>12</b>	<b>Suggestions for further work</b>	<b>109</b>
	<b>Bibliography</b>	<b>110</b>
<b>A</b>	<b>Appendix</b>	<b>115</b>
A.1	Arrangement of Test Samples and Measurements Performed on samples at elevated temperatures in SW . . . . .	115
A.2	Corrosion Rate Calculation . . . . .	116
A.3	Technical data of Al-In-Zn alloy used for Anode sample and for the recasting to DSA. . . . .	116
<b>B</b>	<b>Appendix</b>	<b>119</b>
B.1	Polarization Curves on freely exposed samples at 22°C with graphical solution. . . . .	119
B.2	Polarization Curves on freely exposed samples at 50°C with graphical solution. . . . .	120
B.3	Polarization Curves on freely exposed samples at 80°C with graphical solution. . . . .	121
B.4	Polarization Curves on freely exposed samples in mud with graphical solution. . . . .	122

---

<b>C Appendix</b>	<b>123</b>
C.1 Cross Section Measurements and EDS of freely exposed DSA sample at 22° C . . . . .	123
C.2 Cross Section Measurements and EDS of freely exposed TSA sample at 22° C . . . . .	124
C.3 Cross Section Measurements and EDS of freely exposed DSA sample at 50° C . . . . .	125
C.4 Cross Section Measurements and EDS of freely exposed TSA sample at 50° C . . . . .	126
C.5 Cross Section Measurements and EDS of coupled DSA sample at 50° C . . . . .	127
C.6 Cross Section Measurements and EDS of coupled TSA sample at 50° C . . . . .	128
C.7 Cross Section Measurements and EDS of freely exposed DSA sample at 80° C . . . . .	129
C.8 Cross Section Measurements and EDS of freely exposed TSA sample at 80° C . . . . .	130
C.9 Cross Section Measurements and EDS on coupled DSA sample at 80° C . . . . .	131
C.10 Cross Section Measurements and EDS on coupled TSA sample at 80° C . . . . .	132
<b>D Appendix</b>	<b>133</b>
D.1 Cross Section Measurements and EDS of new DSA sample for exposure in Mud . . . . .	133
D.2 Cross Section Measurements and EDS of new TSA sample for exposure in Mud . . . . .	134
D.3 Cross Section Measurements and EDS of coupled DSA sample embedded in Mud . . . . .	135
D.4 Cross Section Measurements and EDS of coupled TSA sample embedded in Mud . . . . .	136
D.5 Cross Section Measurements and EDS of polarized DSA sample embedded in Mud . . . . .	137
D.6 Cross Section Measurements and EDS of polarized TSA sample embedded in Mud . . . . .	138
D.7 Cross Section Measurements and EDS of freely exposed DSA sample embedded in Mud . . . . .	139
D.8 Cross Section Measurements and EDS of freely exposed TSA sample embedded in Mud	140
<b>E Appendix</b>	<b>141</b>
E.1 Risk Assessment . . . . .	141

---

## Abbreviations

**Ag/AgCl** = Silver, silver chloride

**$b_a$**  = Anodic Tafel Constant

**$b_c$**  = Cathodic Tafel Constant

**CE** = Counter Electrode

**CP** = Cathodic Protection

**CS** = Carbon Steel

**DSA** = Distributed Sacrificial Anode

**$E_{corr}$**  = Corrosion Potential

**$E_p$**  = Protection Criteria

**EDS** = Energy-Dispersive X-ray Spectroscopy

**F** = Faradays Constant

**$i_{corr}$**  = Corrosion Current Density

**LPR** = Linear Polarization Resistance

**MTP** = Department of Mechanical and Industrial Engineering

**NTNU** = Norwegian University of Science and Technology

**OCP** = Open Circuit Potential

**OM** = Optical Microscopy

**POL** = Polarization Curves

**RE** = Reference Electrode

**$R_p$**  = Polarization Resistance

**S.G.** = Stern Geary's Equation

**SCE** = Saturated Calomel Electrode

**SEM** = Scanning Electron Microscopy

**SW** = Seawater

**TSA** = Thermally Sprayed Aluminum

**TSC** = Thermally Sprayed Coatings

**TSZ** = Thermally Sprayed Zinc

**WE** = Working Electrode



---

# List of Figures

2.1	A thermal spray source accelerating molten particles on a substrate creating a TSC [1].	4
2.2	Build up of a thermally sprayed coating on a rough substrate, and parameters affecting the properties of the coating [2]. . . . .	5
2.3	Stresses within a coating on a rough vs. a smooth substrate [3]. . . . .	6
2.4	A cathodic coating (top) vs. a cathodic coating (bottom). Adapted from Fauchais [3].	7
2.5	The <u>left</u> illustration is a Pourbaix diagram for pure aluminum in SW, while the <u>right</u> illustration is an experimental Pourbaix diagram for aluminum alloy 5086 in a chloride solution [4]. . . . .	9
2.6	The corrosion rate as a function of pH [5]. . . . .	9
2.7	Effect of temperature on the passivity of aluminum in water, illustrated in a Pourbaix diagram [6]. . . . .	10
2.8	Polarization Curves for Aluminum alloys in SW at 23 and 60°C [7]. . . . .	11
2.9	The open circuit potential of flame sprayed aluminum during exposure in SW [5]. . .	12
2.10	A general galvanic series of metal and alloys in seawater [8]. . . . .	15
2.11	Schematic description of mechanism from CP of aluminum alloys in SW : (a) development of alkaline diffusion layer; (b) crevicing of matrix compound around the particle and selective dissolution of the particle; (c) repassivation of the surface after detachment or undermining of particle. Adapted from [5]. . . . .	18
4.1	Front side of test samples - <u>Left</u> : DSA sample, <u>2nd Left</u> : TSA sample, <u>2nd Right</u> : Anode sample, <u>Right</u> : CS-cube. . . . .	26
4.2	Application of blue silicon gel onto a thermally sprayed sample, creating an extra barrier against leakage. . . . .	27
4.3	CS-cubes attached to M3-rods with shrinkable tubing. . . . .	28
4.4	The 80°C experiment with general description of parts. . . . .	29
4.5	The 22°C experiment and additional description of parts. . . . .	29
4.6	A simple schematic description of the setup of samples on each container. . . . .	30
4.7	A simple schematic description of the setup when performing LPR measurements. . .	33
4.8	Test samples to be embedded in mud - <u>Top</u> : CS samples, <u>Middle</u> : TSA samples, <u>Bottom</u> : DSA samples. . . . .	35
4.9	Exposed side of coated test samples to be embedded in mud - <u>Left</u> : CS samples, <u>Middle</u> : TSA samples, <u>Right</u> : DSA samples. . . . .	36
4.10	Coated side of test samples to be embedded in mud - <u>Left</u> : CS samples, <u>Middle</u> : TSA samples, <u>Right</u> : DSA samples. . . . .	36
4.11	<u>Left</u> : Mud collected at the shoreline outside Statoil Rotvoll, <u>Right</u> : Amount of mud collected in container. . . . .	36
4.12	<u>Left</u> : Picture of samples to-be-embedded in mud, <u>Right</u> : Picture of samples from the opposite direction. . . . .	37
4.13	A general overview of the experiment in mud and description of parts. . . . .	38

5.1	pH measurements of containers throughout exposure period. The arrows show when SW was replaced in the containers (Black = All containers, Red = 80°C container). . . . .	42
5.2	OCP of freely exposed DSA and TSA samples at all temperatures throughout exposure period. The arrows show when SW was replaced in the containers (Black = All containers, Red = 80°C container). . . . .	43
5.3	OCP of freely exposed Anode samples at all temperatures throughout exposure period. The arrows show when SW was replaced in the containers (Black = All containers, Red = 80°C container). . . . .	44
5.4	OCP of DSA and TSA samples at 80°C and pH measurements of the 80°C container throughout the exposure period. The arrows show when SW was replaced in the containers (Black = All containers, Red = 80°C container). . . . .	45
5.5	Galvanic couple potentials of DSA and TSA sample at all temperatures throughout the exposure period. The arrows show when SW was replaced in the containers (Black = All containers, Red = 80°C container). . . . .	46
5.6	Galvanic Currents of Coupled DSA, TSA and Anode samples at all temperatures throughout the exposure period. The arrows show when SW was replaced in the containers (Black = All containers, Red = 80°C container). . . . .	47
5.7	LPR measurement of the 50 and 80°C DSA samples at day 43 showing fluctuating behavior. . . . .	49
5.8	The results from LPR measurements of DSA samples at all temperatures, plotted as $1/R_p$ . . . . .	50
5.9	Anodic Polarization Curves recorded on DSA samples after one day of exposure. . . . .	51
5.10	Recorded Polarization Curves on freely exposed DSA samples after 63 days. . . . .	52
5.11	Recorded Polarization Curves on freely exposed TSA samples after 63 days. . . . .	53
5.12	Recorded Polarization Curves on freely exposed Anode samples after 63 days. . . . .	54
5.13	Recorded Polarization Curves on freely exposed samples at 22°C, after 63 days of exposure. . . . .	55
5.14	Recorded Polarization Curves on freely exposed samples at 50°C, after 63 days of exposure. . . . .	56
5.15	Recorded Polarization Curves on freely exposed samples at 80°C, after 63 days of exposure. . . . .	57
5.16	Corrosion rates from LPR on freely exposed DSA samples which were polarized at day 1. The three single points (day 63) are calculated from graphical solution of Polarization Curves. . . . .	58
6.1	OCP of the freely exposed samples embedded in mud. . . . .	62
6.2	Galvanic current density and couple potential of a DSA:CS coupling embedded in mud. . . . .	63
6.3	Galvanic current density and couple potential of a TSA:CS coupling embedded in mud. . . . .	64
6.4	Galvanic current densities for the coupled DSA and TSA coating embedded in mud. . . . .	65
6.5	Galvanic couple potentials for the DSA and TSA coating embedded in mud. . . . .	66
6.6	Current densities and applied potential of the potentiostatically polarized samples embedded in mud. . . . .	67
6.7	The results from LPR measurements in mud, plotted as $1/R_p$ . . . . .	68
6.8	Recorded Polarization Curves on freely exposed samples in mud at day 61. . . . .	70
6.9	Corrosion rates from LPR on freely exposed DSA and TSA samples in mud. The two single points (day 61) are calculated from graphical solution of Polarization Curves. . . . .	71
7.1	Initial surface conditions of test samples - <u>Left</u> : DSA sample, <u>2nd Left</u> : TSA sample, <u>2nd Right</u> : Anode sample, <u>Right</u> : CS-cube. . . . .	73
7.2	Cross section of new DSA and TSA sample. . . . .	74

7.3	Corrosion products in the protruding part of 80°C container, where the coupled DSA sample was attached. . . . .	74
7.4	<u>Left:</u> Samples at 22°C, immediately after exposure. <u>Right:</u> After cleaning with Nitric Acid. . . . .	75
7.5	<u>Left:</u> Samples at 50°C, immediately after exposure. <u>Right:</u> After cleaning with Nitric Acid. . . . .	75
7.6	<u>Left:</u> Samples at 80°C, immediately after exposure. <u>Right:</u> After cleaning with Nitric Acid. . . . .	76
7.7	Cross sections of selected coupled samples at 22°C, 50°C and 80°C showing cohesive failure and crevice corrosion. . . . .	76
7.8	Galvanic Coupled CS cubes at all temperatures. . . . .	77
7.9	<u>Left:</u> 3D figure of a new DSA sample, showing the contour of the surface of coating. <u>Right:</u> 2D figure of a new DSA sample, showing the location for the line scan. . . . .	78
7.10	Surface topography of a new DSA from a line scan. . . . .	78
7.11	3D figure and 2D image of a new TSA sample. The black lines are showing the locations for a line scan. . . . .	79
7.12	Surface topography of a new TSA from a line scan. . . . .	79
7.13	Specter from EDS of Spot 1 of unexposed DSA sample. . . . .	80
7.14	Chemical composition from EDS of Spot 1 of unexposed DSA sample. . . . .	80
7.15	<u>Left:</u> Cross section measurements of unexposed DSA sample, <u>Right:</u> Areas/Spots for EDS. . . . .	81
7.16	<u>Left:</u> Cross section measurements of unexposed TSA sample, <u>Right:</u> Areas/Spots for EDS. . . . .	81
7.17	<u>Left:</u> Cross section measurements of galvanic coupled DSA sample. <u>Right:</u> Areas/Spots for EDS. . . . .	82
7.18	<u>Left:</u> Cross section measurements of galvanic coupled TSA sample at 22°C with significant degradation beneath rubber gasket. <u>Right:</u> Areas/Spots for EDS. . . . .	83
8.1	Test samples prior exposure in mud - <u>Top:</u> CS samples, <u>Middle:</u> TSA samples, <u>Bottom:</u> DSA samples. . . . .	87
8.2	Cross sections of new DSA and TSA sample - <u>Left:</u> DSA sample, <u>Right:</u> TSA sample. . . . .	88
8.3	Samples embedded in mud after rinsing and brushing. . . . .	89
8.4	Samples embedded in mud after cleaning in Nitric Acid. . . . .	89
9.1	Suggestion for OCP development of samples at 80°C assumed applicable for real exposure conditions in natural SW. . . . .	92
10.1	Coupling scenario of samples embedded in mud from Polarization Curves obtained after 61 days. . . . .	104
A.1	Technical data Al-In-Zn alloy used for Anode sample and for the recasting to DSA [9].	117
B.1	Polarization Curves on freely exposed samples at 22°C with graphical solution. Day 63.	119
B.2	Polarization Curves on freely exposed samples at 50°C with graphical solution. Day 63.	120
B.3	Polarization Curves on freely exposed samples at 80°C with graphical solution. Day 63.	121
B.4	Polarization Curves on freely exposed samples in mud with graphical solution. Day 61.	122
C.1	<u>Left:</u> Cross section measurements of freely exposed DSA sample at 22°C. <u>Right:</u> Areas/Spots for EDS. . . . .	123
C.2	<u>Left:</u> Cross section measurements of freely exposed TSA sample at 22°C. <u>Right:</u> Areas/Spots for EDS. . . . .	124

---

C.3	<u>Left</u> : Cross section measurements of freely exposed DSA sample at 50°C. <u>Right</u> : Areas/Spots for EDS. . . . .	125
C.4	<u>Left</u> : Cross section measurements of freely exposed TSA sample at 50°C. <u>Right</u> : Areas/Spots for EDS. . . . .	126
C.5	<u>Left</u> : Cross section measurements of coupled DSA sample at 50°C. <u>Right</u> : Areas/Spots for EDS. . . . .	127
C.6	<u>Left</u> : Cross section measurements of coupled TSA sample at 50°C. <u>Right</u> : Areas/Spots for EDS. . . . .	128
C.7	<u>Left</u> : Cross section measurements of freely exposed DSA sample at 80°C. <u>Right</u> : Areas/Spots for EDS. . . . .	129
C.8	<u>Left</u> : Cross section measurements of freely exposed TSA sample at 80°C. <u>Right</u> : Areas/Spots for EDS. . . . .	130
C.9	<u>Left</u> : Cross section measurements on coupled DSA sample at 80°C. <u>Right</u> : Areas/Spots for EDS. . . . .	131
C.10	<u>Left</u> : Cross section measurements on coupled TSA sample at 80°C. <u>Right</u> : Areas/Spots for EDS. . . . .	132
D.1	<u>Left</u> : Cross section measurements of New DSA sample for exposure in Mud. <u>Right</u> : Areas/Spots for EDS. . . . .	133
D.2	<u>Left</u> : Cross section measurements of New TSA sample for exposure in Mud. <u>Right</u> : Areas/Spots for EDS. . . . .	134
D.3	<u>Left</u> : Cross section measurements of coupled DSA embedded in Mud. <u>Right</u> : Areas/Spots for EDS. . . . .	135
D.4	<u>Left</u> : Cross section measurements of coupled TSA sample embedded in Mud. <u>Right</u> : Areas/Spots for EDS. . . . .	136
D.5	<u>Left</u> : Cross section measurements of polarized DSA sample embedded in Mud. <u>Right</u> : Areas/Spots for EDS. . . . .	137
D.6	<u>Left</u> : Cross section measurements of polarized TSA sample embedded in Mud. <u>Right</u> : Areas/Spots for EDS. . . . .	138
D.7	<u>Left</u> : Cross section measurements of freely exposed DSA sample embedded in Mud. <u>Right</u> : Areas/Spots for EDS. . . . .	139
D.8	<u>Left</u> : Cross section measurements of freely exposed TSA sample embedded in Mud. <u>Right</u> : Areas/Spots for EDS. . . . .	140



---

# List of Tables

2.1	OCP of TSA at elevated temperatures. Adapted from Fischer et al. [10]. . . . .	13
2.2	Recommended design data for Aluminum and Zinc based sacrificial anodes [11]. . .	16
2.3	Recommended initial and final design current densities ( $A/m^2$ ) for seawater exposed bare metal surfaces, as a function of depth and "climatic region" based on surface water temperature [11]. . . . .	17
4.1	Temperatures in the containers vs. the temperature of the exposed surfaces of the samples. . . . .	32
5.1	Exact times when replacement of natural seawater was performed. . . . .	42
5.2	OCP development during the exposure period for all samples at all temperatures. . .	44
5.3	Galvanic Couple Potential development during the exposure period for samples at all temperatures. . . . .	46
5.4	Galvanic Current densities on coupled DSA, TSA and Anode samples during the exposure period at all temperatures. . . . .	48
5.5	$R_p$ values for both cathodic and anodic direction and computed average value. . . .	50
5.6	Summary of electrochemical properties of freely exposed and coupled samples after 63 days. . . . .	59
6.1	$R_p$ values for both cathodic and anodic direction on freely exposed samples in mud, and avg. value. . . . .	69
6.2	Data and abilities obtained from the Polarization Curves at day 61. . . . .	70
6.3	Summary of electrochemical properties of samples embedded in Mud after 62 days. . . .	72
7.1	Results from EDS of selected points and areas on unexposed DSA sample. . . . .	81
7.2	Results from EDS of selected points on unexposed TSA sample. . . . .	82
7.3	Results from EDS of selected points and areas on galvanic coupled DSA sample. . . .	82
7.4	Results from EDS of selected points and areas on galvanic coupled TSA sample at 22°C. . .	83
7.5	Cross section thickness results for exposed DSA samples at 22, 50 and 80°C. . . . .	84
7.6	Cross section thickness results for exposed TSA samples at 22, 50 and 80°C. . . . .	85
8.1	Cross section thickness results for DSA and TSA samples embedded in mud. . . . .	90
9.1	A summary of electrochemical properties of freely exposed and coupled samples after 63 days with a suggestion for OCPs for $pH \approx 8.0$ for the 80°C container. . . . .	93
9.2	Galvanic Couple Potentials and Galvanic Current Densities after 65 days of exposure, vs results from Polarization Curves obtained after 63 days of exposure. . . . .	98
10.1	Summary of electrochemical properties of samples embedded in Mud after 62 days. . . . .	101
A.1	The test samples, sorted in accordance to testing temperature. . . . .	115
A.2	Physical data used for calculation of corrosion rates. . . . .	116

---

C.1	Results from EDS of selected points and areas on freely exposed DSA sample at 22°C.	123
C.2	Results from EDS of selected points and areas on freely exposed TSA sample at 22°C.	124
C.3	Results from EDS of selected points and areas on freely exposed DSA sample at 50°C.	125
C.4	Results from EDS of selected points and areas on freely exposed TSA sample at 50°C.	126
C.5	Results from EDS of selected points and areas on coupled DSA sample at 50°C. . . .	127
C.6	Results from EDS of selected points and areas on coupled TSA sample at 50°C. . . .	128
C.7	Results from EDS of selected points and areas of freely exposed DSA sample at 80°C.	129
C.8	Results from EDS of selected points and areas of freely exposed TSA sample at 80°C.	130
C.9	Results from EDS of selected points and areas on coupled DSA sample at 80°C. . . .	131
C.10	Results from EDS of selected points and areas on coupled TSA sample at 80°C. . . .	132
D.1	Results from EDS of selected points and areas on new DSA sample for exposure in Mud. . . . .	133
D.2	Results from EDS of selected points and areas on new TSA sample for exposure in Mud.	134
D.3	Results from EDS of selected points and areas of coupled DSA sample embedded in Mud. . . . .	135
D.4	Results from EDS of selected points and areas of coupled TSA sample embedded in Mud. . . . .	136
D.5	Results from EDS of selected points and areas of polarized DSA sample embedded in Mud. . . . .	137
D.6	Results from EDS of selected points and areas of polarized TSA sample embedded in Mud. . . . .	138
D.7	Results from EDS of selected points and areas of freely exposed DSA sample embed- ded in Mud. . . . .	139
D.8	Results from EDS of selected points and areas of freely exposed TSA sample embed- ded in Mud. . . . .	140

---

# Chapter 1

## Introduction

### 1.1 Background

Cost savings with regards to optimizing the Cathodic Protection (CP) design has over the last 50 years not been considered as a major opportunity so far. Sacrificial anodes combined with organic coatings is the main corrosion protection strategy per now for subsea applications. Much experience from this method has been gained, but some limitations exist. The total anode mass can be significant, depending on the size, complexity, environmental conditions and design life of the subsea system. The total anode mass adds weight to the submerged structure. This can cause constraints on installation vessels and cranes, causing increased installation costs. Decreasing the weight on CP system can reduce costs by using less costly installation vessels, and could also favor safer installation campaigns due to less complex lift operations.

An alternative to sacrificial anodes with organic coatings is Thermally Sprayed Aluminum (TSA) with CP. TSA with CP has occasionally been used on projects for long exposure, i.e. 40 – 50 years, to reduce current demand from the CP systems, hence expanding the anode life. TSA is more robust compared to organic coatings, and even though it is bare exposed compared to steel with organic coatings, it has been shown that TSA will drain less current from sacrificial anodes during the total design life. Organic coatings will, on the other hand, get deteriorated during long-time exposure, eventually exposing bare carbon steel (CS), which will increase the current demand from sacrificial anodes. Some limitations exist when it comes to use of TSA without CP. TSA has anodic limitations in terms of providing protection currents to bare CS during exposure, because it quickly develops a protective oxide layer on the surface. The protective oxide layer causes very low corrosion rates of TSA, but limits TSA to serve adequate protection to damages in the coating that exposes large areas of bare steel. This means that TSA itself should not be used for long time exposure without CP.

GE Oil and Gas has proposed a radical new approach to CP design. This concept consists of distributing sacrificial anodes from an anode alloy (Al-Zn-In) onto the to-be-submerged structure. This can be achieved by e.g. thermal spraying. The idea behind this solution is to reduce the total “anode mass” required, since the coating itself may provide sufficient CP during lifetime. The concept is named Distributed Sacrificial Anode (DSA). DSA can be used in combination with smaller weight of sacrificial anodes for increased level of corrosion protection. It is assumed that DSA will require limited current, since the coating will have a chemical composition close to those of sacrificial anodes. The electrochemical properties of the DSA coating in seawater at 10 and 40°C has been documented in an earlier M.Sc. project [12].

One main question that has been raised is possible coating degradation of thermally sprayed coatings, including DSA and TSA at temperatures above 60 to 80°C. Empirical data on this concern exists for TSA, but is limited. The electrochemical properties for DSA at elevated temperatures above 60 to 80°C has not been documented yet.

Another challenge is related to the behavior of DSA and TSA on foundations when submerged in saline mud. The electrochemical properties of DSA embedded in mud has not been documented yet.

## 1.2 Objectives

The main objectives for this thesis are:

1. Document the electrochemical properties of the DSA coatings at 22°C, 50°C and 80°C, when freely exposed in natural seawater and connected to bare carbon steel.
2. Quantify the effect of temperature on total degradation of DSA and TSA as a function of temperature.
3. Compare the properties for DSA with those of TSA (99,5 % Al) and a conventional Al-Zn-In anode.

The main objectives for this thesis with regards to mud exposure is to:

1. Document the electrochemical properties of the DSA and TSA coatings when i) polarized to -1.1 V Ag/AgCl, ii) Coupled to CS without connection to an anode, iii) Freely exposed.

---

# Chapter 2

## General Theory

### 2.1 Thermally Sprayed Coatings

Thermally sprayed coatings (TSC) are applied to substrate material in order to modify the characteristics of the material or protect it from degradation. The usage for the component decides what type of coating that is selected and also the application method for the thermally sprayed coating. Typical application methods for components with thermally sprayed components can be resistance against wear, heat or corrosion [13].

TSC can be applied to a wide range of materials. The ability to apply coatings with limited heat input to the substrate is a great advantage of thermal sprayed coatings. Repairs can be performed without changing the parts properties or dimensions.

A disadvantage for TSC is that they only can spray what the torch or gun can "see" [1]. This restricts spraying of complex geometries.

#### 2.1.1 Application methods

The application methods involves heating of metallic or nonmetallic materials to a molten or semimolten state by a selected power source. Typical power sources are flame spray, electric arc spray, and plasma arc spray. They can be operated by a person holding the "spraying gun", or they can be controlled by a machine/robot. The coating material to be applied is normally in the form of powder, wires or rods . The feedstocks (form of the material) are molted or semimolted by the power source and accelerated towards the substrate material by high pressure gases. The droplets of melted material hits the surface of the substrate and cools rapidly. The operator of the power source controls the movement of the spraying gun, making sure the coating gets evenly distributed on the surface [1].

Continuously spraying will eventually cause an increase of thickness of the coating. Figure 2.1 [1] shows an illustration of a typical thermal spraying process. The thermal spray source together with high pressure gases melts the powder of the coating material and accelerates it towards the substrate in a spray pattern. The thickness is subsequently increased.

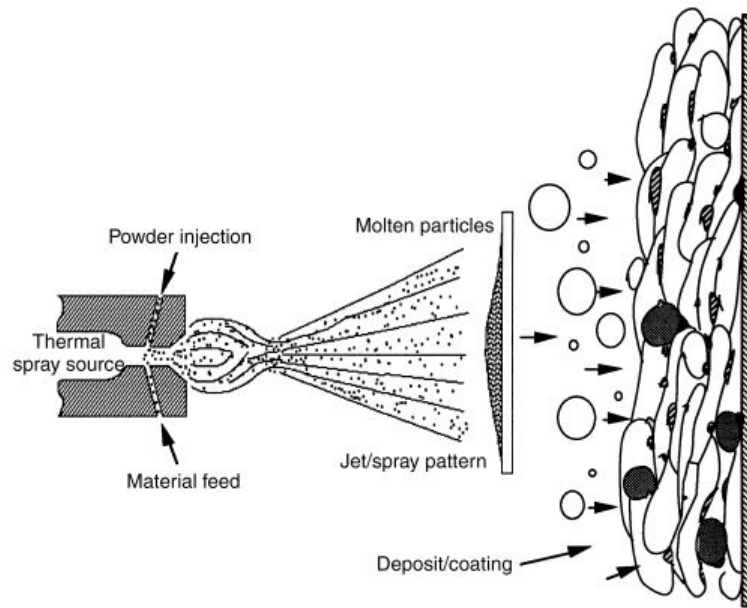


Figure 2.1: A thermal spray source accelerating molten particles on a substrate creating a TSC [1].

### 2.1.2 General Coating Properties

Important parameters that decide the quality of the thermally sprayed coating are adhesion, unmelted particles, oxides and porosity.

Adhesion of a coating is achieved by three fundamental mechanisms: Mechanical, chemical-metallurgical and physical forces [2]. The mechanical mechanism is created by rapid cooling and mechanical anchoring to the rough surface upon impact. Chemical- metallurgical bonding is created by the heat which is transferred from the thermal sprayed droplets to the substrate. This creates micro-welds, localized melting and atomic diffusion between the thermally sprayed coating and substrate. The physical forces that are achieved are considered to be of less importance. They are characterized as weak Van-der-Waals forces. They supply to interatomic attraction within the material. [2] An important step in the process that facilitates adhesion is pre-treatment of the surface. This is described in more detail in Section 2.1.3.

Unmelted particles can be present within a coating due to irregular particle size distribution of the particles or uneven shapes. This causes the particles to receive insufficient heat in order to melt. Another problem that can cause unmelted particles are too high powder injection rate. This can cause irregularities within the coating, promoting voids in the coating, hence increasing the porosity of the coating.

Oxides are caused by particles that are heated in combination with oxygen. Oxides increases the hardness of the coating. For electric arc thermal spraying process, oxides protects against corrosion, particularly in marine environments. A distribution of oxides within a margin from (2.5 to 3.0 mass %) within the coating is considered not unfavorable for the coatings adhesion. [2]

Porosity is the ratio between total volume of voids (space) within the coating vs. the total volume of the coating. High porosity is undesirable in coating for corrosion protection, since this shortens the physical barrier between the environment and the substrate.

A sealer is typically used on top of the TSC surface to "seal off" the porosity. The sealer shall be low viscous and easily penetrate and fill the voids of the coating without necessarily increasing the thickness of the coating. The sealer should be applied on top of the TSC as soon as possible after thermally spraying to avoid that contaminants fill up the pores and reduces the effect of the sealer. Common sealers that are used are vinyl and silicone based. [5]

Figure 2.2 shows a schematic description of particles upon impact, causing oxides and pores within a TSC.

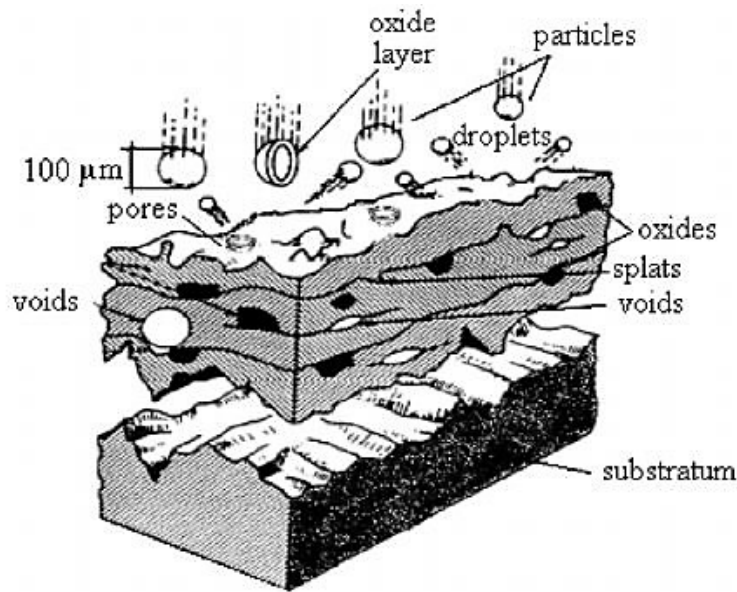


Figure 2.2: Build up of a thermally sprayed coating on a rough substrate, and parameters affecting the properties of the coating [2].

### 2.1.3 Pre-treatment of substrate surface

As mentioned in the previous section, pre-treatment of the substrate is of great importance before thermal spraying begins. The pre-treatment is of great significance when it comes to how well the coating “sticks” to the substrate surface. This is achieved by making sure that the surface is free from contaminations such as oil, grease, paint, rust, scale and moisture [1]. Contaminations which remain on the substrate surface may cause the coating to adhere to these, instead of the substrate. This will result in impaired adhesion between the TSC and the substrate. An irregular surface of the substrate is also important. This will increase the interfacial area between the TSC and substrate, facilitating greater adhesion between the two. This increases the resistance against adhesion failure from residual stresses that are induced from cooling of TSC after the application process. An irregular surface can be created by roughening of the substrate.

Proper pretreatment usually consists of three steps: Cleaning, Roughening and Adsorbates and condensates elimination [3].

Cleaning involves removing contaminants with solvents. Solvents that are commonly used are Methyl Ethyl Ketone (MEK), Acetone or aqueous washer solutions containing acetic acid. The method is quick and efficient, and manual cleaning is normally all that is necessary in order to remove contaminants.

Roughening is performed after the cleaning and typically involves grit blasting the surface with dry abrasive particles. The particles will upon impact scrape off metal from the surface and make the surface irregular and rough.

Adsorbates and condensates elimination are lastly performed by preheating. This drives potentially hidden moisture out from the substrate. It makes the surface dry and warm. The warm surface contribute to a pre-expanded surface, so that the surface after application of the coating shrinks together with the coating during cooling. This will reduce residual stresses within the coating. [1]

It is important that the thermally spraying process starts as quickly as possible after the surface has been pre-treated. The longer time the pre-treated substrate is exposed to air prior to spraying,

increases the risk for new contaminations and heat loss.

Figure 2.3 [3] shows a coating applied onto a rough surface vs a smooth surface. The rough surface will absorb residual stresses in a more efficient manner, resisting adhesion failure between the substrate and coating. The smooth surface will have reduced interfacial area and limited ability to absorb stresses, hence increasing the chance of adhesion failure.

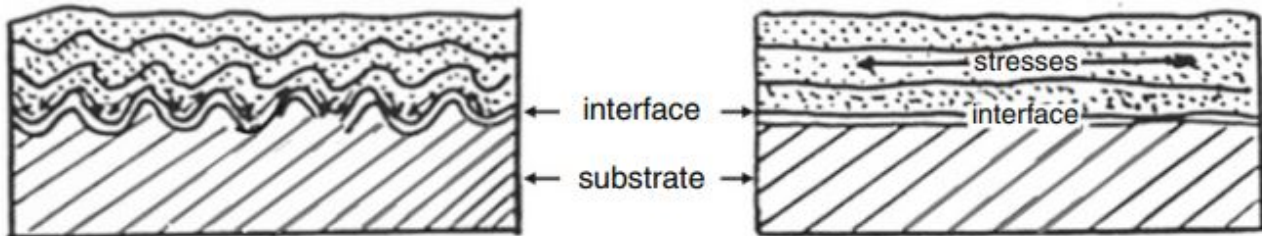


Figure 2.3: Stresses within a coating on a rough vs. a smooth substrate [3].

### 2.1.4 Corrosion Protection

Thermally sprayed coatings has proven to be a good alternative to organic coatings with sacrificial anodes due to its robustness [14]. It has been shown that they have a long service life, with little maintenance needs. Even though they have initial higher costs, the overall lifetime costs can be lower compared with organic coatings. Reduced costs with regards to repairs, replacement, handling and increased lifetime are some of the reasons why they are preferred to organic paint.[14]

TSC is often used for corrosion protection in marine environments [15, 14], and is normally divided into three main groups based on the properties of the coatings: **Anodic coatings**, **cathodic coatings** and **neutral coatings** [13]. Common for all groups are their barrier mechanism. All three groups act as physical barrier, separating the corrosive environment from the substrate surface

**Anodic coatings** are metals which are less noble compared with the substrate material and will perform cathodic protection of the substrate if the coating experience damage in marine environments. Materials such as Zinc, Aluminum or Magnesium or its alloys are all materials that provides protection to steel in offshore structures. [13]

**Cathodic coatings** are metals which are more noble compared with the substrate material and will therefore not perform cathodic protection of the substrate, if the coating is damaged. The substrate material will act as an anode and protect the coating if the substrate is exposed to the corrosive environment. An unfavorable area ratio between the cathodic and anodic area will cause high current densities of the anode area, leading to rapid corrosion. The cathodic coating itself, will ensure good corrosion protection in surrounding environments if it provides a complete barrier from the substrate to the corrosive environment. The density requirements of the coating is high in order to limit porosity and permeability. It is recommended to apply a sealer on cathodic coatings in order to seal off possible voids. [13]

Figure 2.4 [3] shows a simple illustration between an anodic and a cathodic coating. The **upper** figure shows a cathodic coating (Ni-coating) with a damage resulting in corrosion of the less noble steel substrate. The **lower** figure shows an anodic coating corroding (Al or Zn coating) providing cathodic protection to the more noble steel substrate.

**Neutral coatings** are neutral compared with the substrate material. The coating will neither accelerate or decrease the corrosion rate of the substrate if the coating is damaged. It is however important that the coating is dense and non-permeable in order to provide corrosion protection. Exposed substrate material can cause coating separation from the substrate. Examples of materials that are used to form neutral thermal sprayed coatings are Chromium oxide ceramics or Alumina. [13]



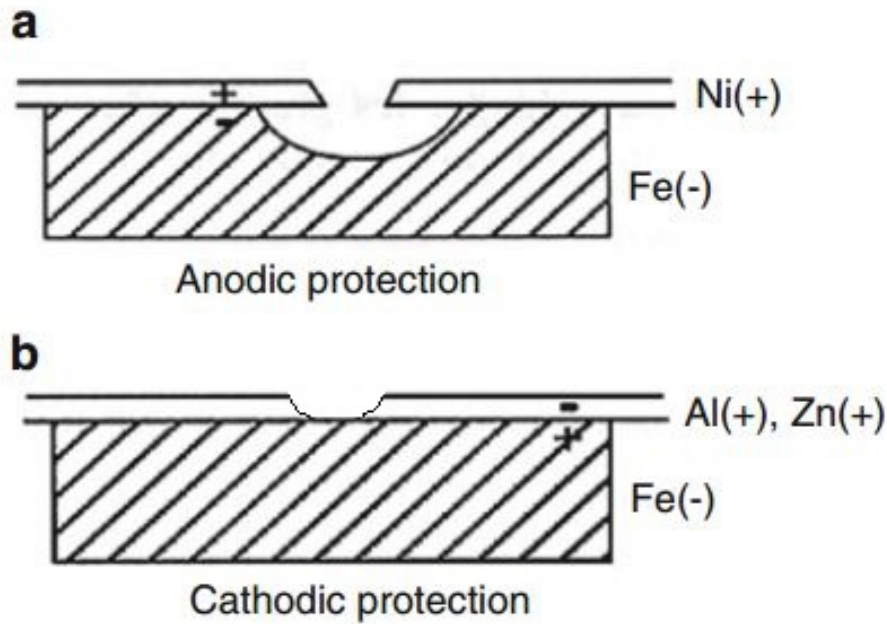


Figure 2.4: A cathodic coating (top) vs. a cathodic coating (bottom). Adapted from Fauchais [3].

### 2.1.5 Thermally Sprayed Aluminum

TSA is used in marine environments due to low corrosion rates. The primary function for the coating is to act as a physical barrier between the substrate and corrosive environment. If required it will, to some extent, function as an anodic coating as described in Section 2.1.4.

TSA is selected over organic coatings due to higher adhesion and being more robust in marine areas such as the marine atmosphere, splash zone and immersion zones. [16, 14]

TSA is a TSC where the coating material is aluminum or aluminum alloys. Common materials that are used for application in seawater (SW) are technically pure aluminum (99,5 % Al) or the alloy AlMg5 (5 % Mg and 95 % Al). It is assumed that AlMg5 creates a sprayed coating with properties close to the 5000-series of solid aluminum. The 5000 series has a magnesium content in the range 2-5%, and has got a reputation of being "seawater resistant". [5]

Important parameters that affects the quality of TSA are adhesion, oxides and porosity as explained in Section 2.1.2. High adhesion is obtained by pretreatment of substrate surface which includes cleaning, roughening and removal of possible condensates as described in Section 2.1.3. Standard NORSOK M-501 – Surface preparation and protective coatings [17] describes requirements for the surface preparation, coating system and thickness for a TSA coating for use in the Norwegian oil and gas industry. TSA is numbered as coating system number 2 in this standard. In addition to the TSA should an adequate sealer be applied to surface. The sealer is not as critical for aluminum coatings compared with zinc coatings. This is because the pores are becoming more naturally sealed on aluminum coatings by formation of hydrated oxide films that block the pores [5]. Typical sealers that have been selected for TSA coatings have been aluminum-vinyl and silicone-aluminum. Silicone-aluminum has been found to provide the best seal coating performance [16].

TSA and Thermally Sprayed Zinc (TSZ) are two anodic coatings that have been used a lot in marine atmosphere throughout history. The corrosion protection mechanisms for TSA in marine environment is that it forms a thin compact film of aluminum oxide on the surface. The oxide film is stable in a wide pH-range and cause low uniform corrosion rates. The oxide film will however limit the ability of the coating to provide protection (galvanic) current. This limits TSA from protecting large damages in the coating. Zinc coatings are on the other hand electrochemically more

active, and will provide effective cathodic protection to steel. The active behaviour of Zinc coatings will however increase the reaction rates, causing higher depletion rates and reduced lifetime of the coating. [14]

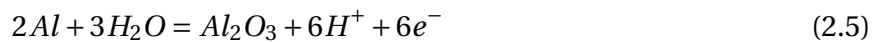
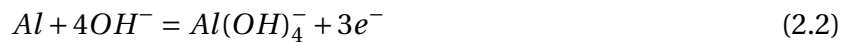
Long lasting protective properties of TSA have in general been favored compared with the anodic abilities to TSZ, when selecting a coating for long lifetime in marine environments. Zn-Al alloys have been created to combine the protective properties of Zinc and Aluminum. The optimum alloy composition seem to depend on the application. 85% Zinc - 15% Aluminum is widely used. [14]

## 2.2 Corrosion of Aluminum

Corrosion can be explained as the degradation of a material's properties or mass over time due to environmental effects [18]. This occurs because the elements wants to reach their most thermodynamically stable state.

Aluminum is generally an un-noble metal in the galvanic series. This should make aluminum a very reactive material. What makes aluminum corrosion resistant, is that it quickly develops a passive oxide layer which prevents further corrosion of the material. Re-oxidation of the layer will occur if the oxide layer is removed due to e.g. mechanical impacts.

The electrochemical reactions which take place when aluminum is exposed to SW can be seen from Equation 2.1 to Equation 2.5. Equation 2.6 is a chemical reaction. For corrosion to occur there must be an anodic reaction and a cathodic reaction. The anodic reaction for aluminum can be seen from Equation 2.1. The anodic reaction in alkaline solutions (i.e.  $\text{pH} > 7$ ) can be seen from Equation 2.2. The cathodic reaction in SW can occur from hydrogen evolution (Equation 2.3) or oxygen reduction (Equation 2.4), or a combination between these. The aluminum does further easily react with the environment, and an oxide layer is formed in accordance with Equation 2.5. Chemical dissolution of the oxidation layer is happening according to Equation 2.6. The dissolution rate is depending on pH and concentration of  $\text{AlO}_2^-$ .



A Pourbaix diagram shows a pH - potential plot where different corrosion products of aluminum are thermodynamically stable. It represents where a metal is immune (i.e. no corrosion occurring), is suffering from corrosion (i.e. anodic dissolution) and where the metal is passive (i.e. an oxidation layer is created and inhibits further dissolution of the metal). The left diagram on Figure 2.5 shows a theoretical Pourbaix diagram for Aluminum in SW. The oxidation layer (passive region) is stable between a pH of approximately 2.5 and 4.2. This is not ideal for application in sea water where the average  $\text{pH} \approx 8.2$ .

Aluminum alloys in the 5000-series such as the AlMg5 represents a different Pourbaix-diagram, where the passive region is active in a broader pH-range. This is because it contains small amounts of alloyed elements such as Mg and Mn, which makes the oxide layer more robust.[4]

An experimental Pourbaix diagram for an alloy in the 5000 series is represented in the right part of figure 2.5. This shows that aluminum may be used in SW ( $\text{pH} \approx 8.2$ ) and remain passive in the range from approximately -860 mV SCE to -1200 mV SCE.

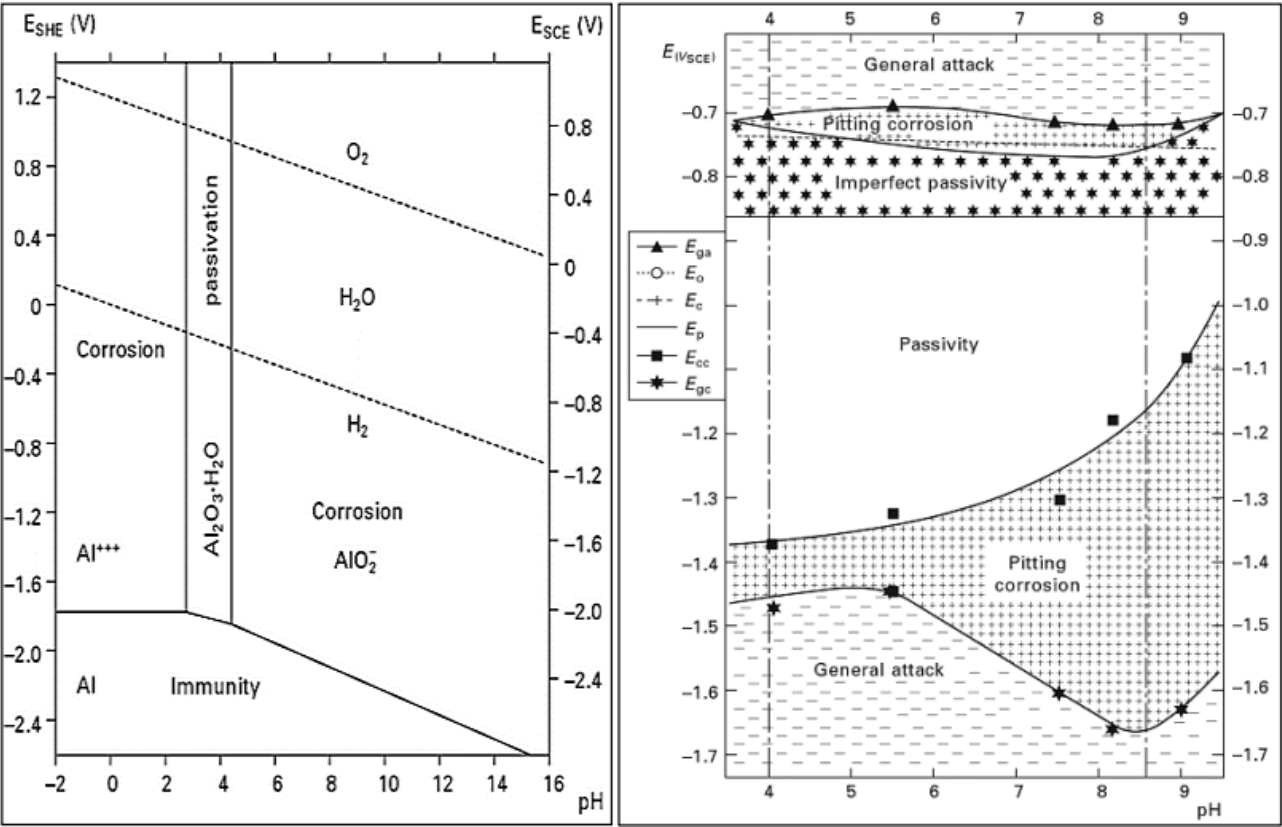


Figure 2.5: The left illustration is a Pourbaix diagram for pure aluminum in SW, while the right illustration is an experimental Pourbaix diagram for aluminum alloy 5086 in a chloride solution [4].

The corrosion rate is thus dependant on the pH of the SW. Figure 2.6 shows the corrosion rate as a function of pH.

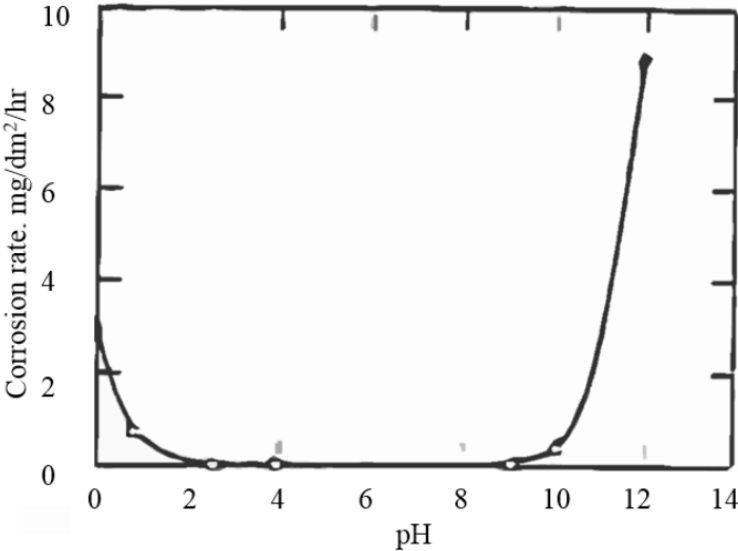


Figure 2.6: The corrosion rate as a function of pH [5].

### 2.2.1 Effect of temperature

At conditions of reversibility Nernst Equation (2.7) shows that increased temperature should give a decrease in reversible potential, where  $R$  is the universal gas constant,  $T$  is the absolute temperature in Kelvin,  $n$  is the number of electrons in the reaction,  $F$  is the Faradays constant and  $[Red]$  and  $[Ox]$  is the concentration of the products and reactants, respectively.

$$E_{cell} = E^0 - \frac{RT}{nF} \ln \frac{[Red]}{[Ox]} \quad (2.7)$$

The temperature affects the stability of the oxide layer. The general trend at high temperatures is that the oxide is stable within a narrower pH-range and that it shifts to left towards a more acidic solution. This means that the danger of corrosion increases in alkaline and neutral environments with increasing temperature [6]. Figure 2.7 shows Pourbaix diagrams for aluminum and the effect of increased temperature for the stability of the oxide layer.

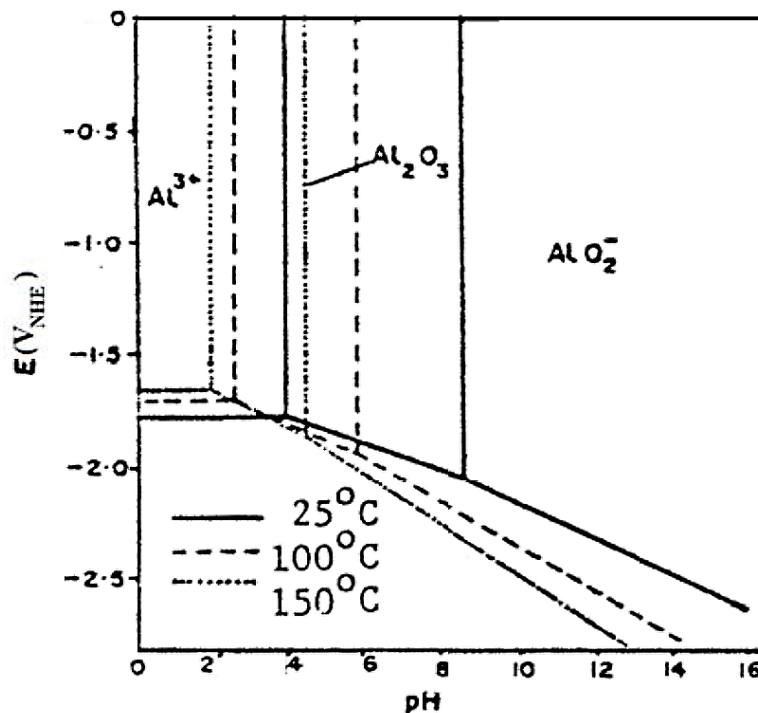


Figure 2.7: Effect of temperature on the passivity of aluminum in water, illustrated in a Pourbaix diagram [6].

The effect of SW temperature on aluminum alloys was studied by Ezuber et al. in 2008 [7]. The aluminum alloys AA5083 (Al-Mg) and AA1100 (pure aluminum) were tested in stagnant seawater at 23 and 60°C. Recorded Polarization Curves revealed that increased temperature caused a negative shift in OCP by approximately 200 mV and a decrease in pitting potential values by 40 mV. Increased temperature also seemed to increase the passive current densities. Figure 2.8 shows the recorded polarization curves on pure Aluminum and Al-Mg at 23 and 60 °C.

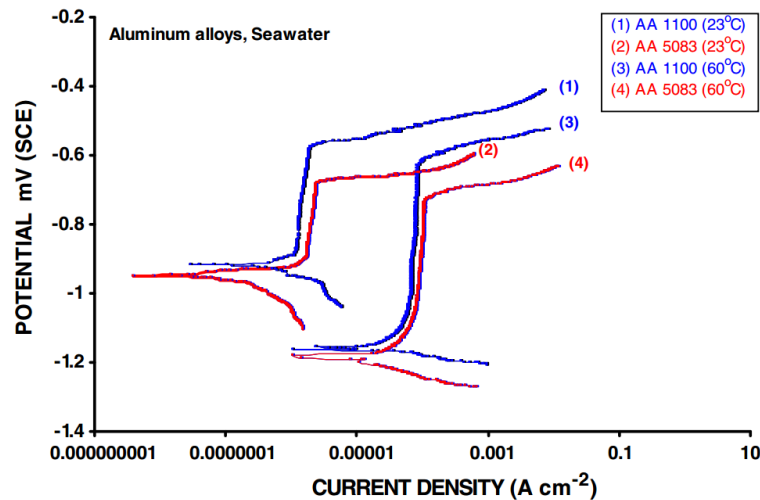


Figure 2.8: Polarization Curves for Aluminum alloys in SW at 23 and 60°C [7].

It has also been found that the susceptibility to pitting and crevice corrosion may increase at elevated temperatures and pressure together with chloride content. [4]

## 2.2.2 Pitting Corrosion

Pitting corrosion can occur when aluminum is exposed to environments containing chloride ions and when the potential of the metal has exceeded a critical value  $E_C$ , which is called the critical pitting potential. When the oxide film on aluminum gets into contact with chloride ions, it becomes unstable and breaks down at specific points, which causes localized corrosion. This results in pits forming on the aluminum surface [7]. The mechanism behind pitting corrosion is not fully understood, and several theories have been published. However, there is consensus that  $(Cl^-)$  ions play an important role as it is somehow attracted to the surface of aluminum [19]. The attacks concentrate around intermetallic particles which will act cathodic while the pit will act anodic. The galvanic contact is the driving force for pit propagation, and the pit sizes can grow deep and be difficult to detect.

## 2.2.3 Crevice Corrosion

Crevice Corrosion is a local corrosion form which occurs in narrow cavities. Narrow cavities formed between Aluminum and rubber gaskets can e.g. cause crevice corrosion. The crevice opening is sufficiently wide so that fluid initially can enter, but is at the same time so tight that the fluid is stagnant within the crevice. At first, there is limited difference in the chemistry of fluid inside and outside the crevice. Cathodic and anodic reactions occur at the same speed within and outside the crevice. After some time, dissolved oxygen will become depleted in the crevice and the crevice itself will restrict access of dissolved oxygen from outside the crevice. This prevents formation of  $OH^-$  inside the crevice, which results in a potential difference between the inside and outside. The crevice is transformed to an anode, while the outside is turned into a cathode in this cell. Aluminum corrodes and migration of  $Cl^-$  ions into the crevice initiates to preserve electroneutrality.  $Cl^-$  ions react with water and form hydrochloric acid. The pH will decrease and the oxide layer is subsequently attacked, which activates the Aluminum surface and increases the corrosion rate significantly. [20, 21]

## 2.3 Corrosion of TSA

Corrosion of TSA is not similar to corrosion of solid aluminum alloys. The main difference between them is related to the surface structure, topography and the oxidized particles that are present within the coating due to the high temperature during the thermally spraying process. The overall effect is an increased oxide layer which is more stable, compared with a thin oxide layer that is created on a smooth surface of rolled aluminum sheets. The difference in oxide layer thickness will provide a smaller dissolution rate for TSA, and hence a smaller reduction in coating thickness. [22]

Intermetallic particles that are present in TSA due to spraying process or impurities will initially cause high corrosion rates. This is because the particles are causing weakened spots for formation of the oxide, if they are electrochemically more noble than aluminum. The resulting corrosion mechanism is pitting, which was described in Section 2.2.2. The mechanism is mainly localized and will have greatest impact in the start of exposure. The micropits which are initiated around the particles increase the exposed area of the cathodic particles. The effect from this can be seen from Figure 2.9, where the open circuit potential (OCP) significantly drops from above -900 mV SCE to below -1050 mV SCE. During exposure, repassivation of the oxide will occur, due to removal or undermining of the intermetallic particles. This represents the slow increase in potential throughout the exposure period. [5, 4]

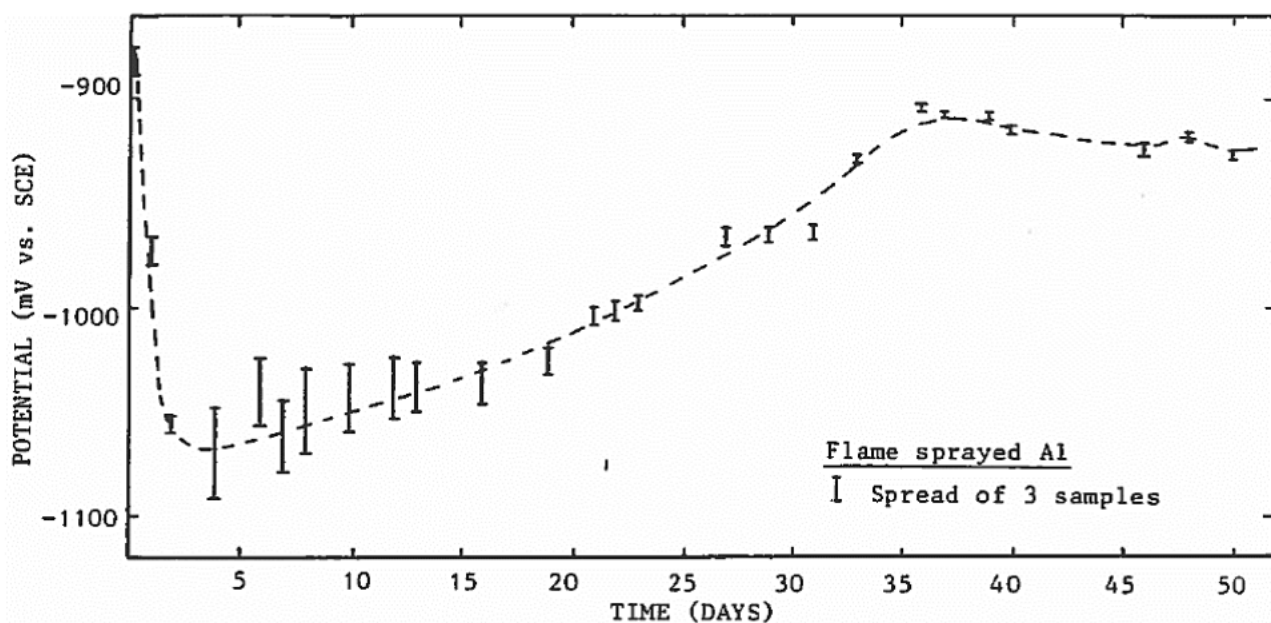


Figure 2.9: The open circuit potential of flame sprayed aluminum during exposure in SW [5].

It has been reported that the OCP of flamesprayed or electric arc sprayed Al 99.5% have stabilized within a range of approximately -910 to -950 mV SCE, after 11 months of exposure. Other similar aluminum coatings have stabilized within a potential range of approximately -900 to -1000 mV SCE, depending on spraying method and use of sealer. [5]

The effect of elevated seawater temperature is that the OCP decreases. The effect is connected to the concentration of oxygen [5]. Table 2.1 shows OCPs during exposure of TSA at three different temperatures. Increased temperature seems to give more negative potential in the beginning of exposure, however it increases during exposure and is in fact more positive after one month of exposure.

Table 2.1: OCP of TSA at elevated temperatures. Adapted from Fischer et al. [10].

Temperature [°C]	Potential [mV Ag/AgCl]		
	Initial (Day 1-2)	1 Month	3 Months
8 (ambient)	-800	-1000	-
70	-1040	-970	-945
100	-1115	-950	-950

Another study of flame sprayed aluminum and arc sprayed aluminum showed that OCP of samples at 60 °C stabilized at a potential approximately 50 mV more negative compared with samples exposed at 8 °C, after 2 months of exposure. [23]

## 2.4 Measurement methods for corrosion testing

It is possible to conduct approximates for corrosion rates by performing electrochemical measurements. Two methods amongst others can be used in order to do this: Polarization Curves and Linear Polarization Resistance (LPR).

Polarization curves are obtained by polarizing the sample in both cathodic and anodic direction, while measuring the net current flow. This is done by measuring the voltage drop over a known resistance. Polarizing means shifting the potential from the present open circuit potential(OCP) in a step-wise approach, and simultaneously measuring the current that is required in order to hold the potential. The results can be plotted in a Potential - log current diagram. Overvoltage curves are obtained by taking the asymptotes of the linear part of the polarization curves. The elongation of the overvoltage curves will result in an intersection between the overvoltage curves for cathodic and anodic direction and also the OCP. From this intersection, the corrosion current density can be solved.

From the overvoltage curves, the cathodic and anodic tafel constants (slope of the curve),  $b_c$  and  $b_a$  can be solved. The tafel constants can further be used to make an approximation of corrosion rates by using the LPR method.

The LPR method is a much quicker corrosion measurement compared with the polarization curves method. However it is required that the tafel constants are found before the corrosion rate can be obtained. The method involves shifting the potential in a small range ( $\pm 20$  mV) from the OCP. This is performed for both the cathodic and anodic direction. The current demand to hold the applied potential is measured after some time. The linear relationship between the potential and net current in a small range close the OCP, makes it possible to calculate the corrosion rate by using the Stern-Geary's Equation 2.8 [24]:

$$R_P = \frac{\Delta E}{\Delta I} = \frac{b_a \cdot |b_c|}{2.3 \cdot I_{corr} \cdot (b_a + |b_c|)} \quad (2.8)$$

Where:

$\Delta E$  -  $|E_{applied} - OCP|$

$\Delta I$  - Net current measured vs. OCP current

$I_{corr}$  - Corrosion current

Solving for  $I_{corr}$  and converting to current density  $i_{corr}$ , by dividing by exposed sample area gives Equation 2.9:

$$i_{corr} = \frac{b_a \cdot |b_c|}{2.3 \cdot R_P \cdot (b_a + |b_c|) \cdot A} \quad (2.9)$$

Where:

$i_{corr}$  - Corrosion current density [A/m<sup>2</sup>]

$b_a$  - Anodic tafel constant [V/decade]

$b_c$  - Cathodic tafel constant [V/decade]

$R_p$  - The Polarization Resistance [ $\Omega$ ]

$A$  - Exposed surface area of sample [m<sup>2</sup>]

The corrosion rate can be calculated using Faraday's law. It is converted to mm/year or  $\mu\text{m}/\text{year}$  for practical reasons. The corrosion rate can be calculated in accordance with Equation 2.10

$$CR = K \cdot \frac{i_{corr} \cdot M}{n \cdot \rho} \quad (2.10)$$

Where:

$CR$  - Corrosion rate [mm/year]

$K$  - 3268

$i_{corr}$  - Corrosion current [A/cm<sup>2</sup>]

$n$  - Electrons exchanged

$\rho$  - Density [g/cm<sup>3</sup>]

## 2.5 Cathodic Protection

Cathodic Protection (CP) is a well-established form of corrosion protection, which have been known for over 150 years [20]. The general principle of cathodic protection is that the material to be protected is applied to an external current so that the electrode potential of the material is depressed towards the immune area. The material is converted into a cathode in an electrochemical cell, hence the name of CP. For protection of local corrosion forms, the potential is depressed under a protective potential. The external current can be produced in two ways: With help of an un-noble material in form of Sacrificial Anodes which is coupled to the construction to be protected, or with help of Impressed Current Cathodic Protection.

CP in conjunction with coatings, or alone, is in general recognized as the best technical and economical solution for effective corrosion control of submerged components in marine environments [25, 20, 26]. The coating will limit the current drainage from CP system, which will reduce the number of e.g. required anodes. A CP system with organic coatings will provide numerous advantages compared with a system with no coating (bare steel). Cost savings with regards to reduced anode weight, reduced installation costs and providing long term protection are some examples which are beneficial for a CP system with coatings.

The driving force for external current produced from Sacrificial Anodes is the difference in electrode potential between the anode and the cathode [27]. The sacrificial anodes will corrode and "sacrifice" themselves on behalf on the cathode (material to be protected), which will be cathodically protected by the current which is released from the anode. The potential drop in the electrolyte is of high importance when it comes to how well the CP system works. Seawater has in general low resistivity and low potential drop, while mud can have high resistivity and high potential drop making cathodic protection of steel in mud more difficult compared with seawater.



Figure 2.10 shows a general galvanic series of metal and alloys in seawater. It shows that Aluminum, Zinc and Magnesium are materials which have negative potentials compared with steel, and hence will have a driving force in providing protection currents to steel under exposure in seawater. Magnesium has a potential of approximately  $-1.6$  V Ag/AgCl in seawater, which will cause a strong driving force in providing protection currents. This can cause hydrogen embrittlement in some steel due to hydrogen evolution on the cathode. Aluminum and Zinc based alloys has a potential of approximately  $-1.05$  to  $-1.1$  V Ag/AgCl and are normally used as anode material in seawater with low resistivity. They will cause sufficient protection currents to steel and limit the chance of hydrogen evolution and problems from hydrogen embrittlement. Anodes from Magnesium alloys are often used in environments where the resistivity of the medium is high, where a strong driving force to overcome the potential drop is required [20].

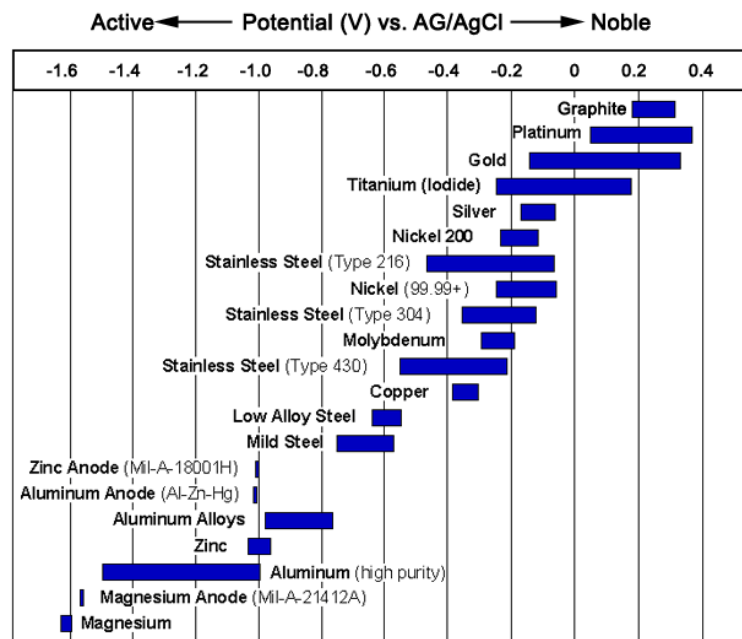


Figure 2.10: A general galvanic series of metal and alloys in seawater [8].

Cathodic currents in seawater will induce oxygen reduction (Equation 2.4), which produce hydroxol ions at the surface of the protected material. This will increase the interfacial pH and cause increased carbonate ions concentration. They will precipitate, creating an inorganic layer on the surface. Depending on the potential, some magnesium hydroxide can also precipitate. This mix in deposits are generally called "calcareous deposits". [28, 29]

Various forms for calcareous deposits will form on CS in seawater during CP. They consist mainly of  $\text{CaCO}_3$ ,  $\text{MgCO}_3$  and  $\text{Mg}(\text{OH})_2$ , which will precipitate when the solubility of calcium and magnesium ions is exceeded. They form at pH levels between 8 and 10 and since natural seawater normally are supersaturated in calcium carbonates, precipitation of these are most likely to form. [25]

Calcareous deposits will precipitate over time and lower the current demand from anodes during exposure because they will build up and act as a barrier/insulation between the CS surface and seawater. [28, 29, 25]

Disadvantages of CP are mainly related to formation of hydroxol ions and hydrogen at the surface of the protected material. This can cause disbonding ("cathodic disbonding") of organic coatings at the coating/metal interface. Hydrogen evolution may cause hydrogen atoms to become absorbed in the metal matrix, which makes the material more brittle. Components which are subjected to high stresses can suffer from Hydrogen Induced Stress Cracking. [11]

### 2.5.1 CP by Sacrificial Anodes

Sacrificial anodes made from Aluminum are most used for steel in seawater, due to their high capacity in ampere hours per kilogram. Table 2.2 shows design data for Aluminum and Zinc based sacrificial anodes. Aluminum has generally higher capacity compared with Zinc and a lower OCP. Since Zinc based alloys have higher electrochemical performance, they have been considered more reliable in marine sediments with high bacterial activity. [11]

Table 2.2: Recommended design data for Aluminum and Zinc based sacrificial anodes [11].

Anode Mat. Type	Environment	Closed Circuit Pot. [mV Ag/AgCl]	Electrochemical Capacity [Ah/kg]
Al-based	Seawater	-1050	2000
	Sediments	-950	1500
Zn-based	Seawater	-1000	780
	Sediments	-950	700

Since aluminum have passivating abilities in the form of the oxide layer which is created, some alloying elements are added which increases the aluminums ability to activate. Alloying elements of particular interest which change the electrochemical properties of Aluminum to more active abilities are Zinc and Indium. Zinc and Mercury (Hg) can also be used to activate the aluminum matrix, but are however less used due to toxic abilities of the Mercury.

Zinc and Indium effects electrochemical properties of a traditional aluminum anode by shifting the pitting potential to more negative values, i.e. in the cathodic direction. Zinc has a synergistic effect with small contents of In, which causes the oxide layer on Aluminum to destabilize and crack, hence activating the alloy at lower potentials. [30, 31]

The Al-Zn-In alloy shows good performance in seawater. It has an average potential of -1.1 V Ag/AgCl and an efficiency over 90% have been reported in some cases, related to uniform attack [30]. An optimum concentration of Zn and In have been found to be 5 wt.% and 0.02wt.%, respectively. This mix seems to provide a more uniform corrosion of the sacrificial anode, which will utilize the whole capacity of the anode, causing increased performance and lifetime of the Al-Zn-In alloy [32].

The sacrificial anode which is used in this project is a CORAL A High Grade Al-In-Zn alloy, from Skarpenord Corrosion [9]. According to the manufacturer it has a capacity of 2585 Ah/kg and an OCP of -1.09 V Ag/AgCl in ambient sea water. Its performance data in mud are slightly less, 2400 Ah/kg and a OCP of -1.05 at temperatures from 0 to 20°C. The Zinc and Indium contents are 3.5 - 5.0 wt.% and 0.015 - 0.025 wt.%, respectively. Technical data of the Al-In-Zn alloy from Skarpenord Corrosion is included in Figure A.1 in the Appendix section.

### 2.5.2 Cathodic Protection of steel

Protection criteria ( $E_p$ ) for steel in natural seawater is generally below -800 mV Ag/AgCl [11]. This potential does not stop corrosion of CS completely, but practice has shown that the rate of corrosion at this potential is so small that it has limited significance. For steel embedded in mud at the sea bottom, the corrosion environment can be affected by  $H_2S$  formed due to sulfate-reducing bacteria [20]. Under such conditions, steel can corrode faster compared with exposure to seawater.  $E_p$  for exposure in mud is therefore as a general rule set below -900 mV Ag/AgCl [20]. The design protective potential in anaerobic environments, including typical seawater sediments are also discussed in DNV-RP-B401, Recommended practice, Cathodic Protection Design [11]. However, it states that the protection potential is not a variable.

According to DNV-RP-B401 [11],  $E_p$  should be in the range -0.9 to -1.05 V Ag/AgCl for a correctly designed anode CP system. Over-protection can occur for values less negative than -1.15 V Ag/AgCl, but will not apply for CP from sacrificial anodes based on Al or Zn.

Table 2.3 from DNV-RP-B401 [11] shows recommended initial and final design current densities for steel exposed in seawater as a function of depth and climatic region based on surface water temperature. The data in the table reflect expected influence of depth, calcareous deposits formed by CP and temperature.

It is expected that the dissolved oxygen content is decreased at large depths, due to reduced amount of dissolution from air, photo synthesis and decreased temperature. This results in slow formation rate of calcareous deposits which is expected to contain more  $Mg(OH)_2$  compared with calcareous deposits formed in shallow water. [33]

Table 2.3: Recommended initial and final design current densities ( $A/m^2$ ) for seawater exposed bare metal surfaces, as a function of depth and "climatic region" based on surface water temperature [11].

Depth (m)	'Tropical' ( $>20^\circ C$ )		'Sub-Tropical' ( $12-20^\circ C$ )		'Temperate' ( $7-11^\circ C$ )		'Arctic' ( $<7^\circ C$ )	
	<i>initial</i>	<i>final</i>	<i>initial</i>	<i>final</i>	<i>initial</i>	<i>final</i>	<i>initial</i>	<i>final</i>
0-30	0.150	0.100	0.170	0.110	0.200	0.130	0.250	0.170
>30-100	0.120	0.080	0.140	0.090	0.170	0.110	0.200	0.130
>100-300	0.140	0.090	0.160	0.110	0.190	0.140	0.220	0.170
>300	0.180	0.130	0.200	0.150	0.220	0.170	0.220	0.170

It should also be noted that the design current densities shall be increased by  $0.001 A/m^2$  for each  $^\circ C$  the metal/environment interface is assumed to exceed  $25^\circ C$ . This is to account for increased convective and diffusive mass transfer of oxygen, induced by heat transfer. [11]

DNV [11] recommends that bare steel surfaces which are buried in sediments, should have a design current density (initial/final and average) of  $0.020 A/m^2$ , regardless of geographical location and depth.

### 2.5.3 Cathodic Protection of Aluminum

CP of Aluminum can occur because aluminum is part of the total structure (mostly steel) which is cathodically protected. CP of aluminum can be used under immersed conditions where it is desirable to keep aluminum in the passive region (Figure 2.5), preventing pitting corrosion [20, 4]. This can be beneficial for especially long exposure conditions [34].

Protection of Aluminum is achieved by maintaining the protective oxide (passivity) of the surface, since Aluminum in practice don't have an immune region under normal exposure conditions. This means that the protection is anodic rather than cathodic [4]. CP is however used here, since it is the most common term for protection of materials.

CP of Aluminum is cost effective, since limited current is needed to hold aluminum within the passive region. It requires approximately 10 times less current, compared with what is required for steel in seawater [34].

The low current demand on Al compared with steel can be described from cathodic reactions occurring on cathodic intermetallic sites, which represents a very small fraction of the total surface area. For steel, the entire surface will be accessible for cathodic reactions. [4]

The cathodic reactions on the intermetallic particles will cause weakened spots for formation of the oxide at the beginning of exposure (similar with corrosion of TSA, explained in Section 2.3), due to increased pH close to the surface. This causes micropitting/etching of the aluminum matrix

around the particle, and will increase the exposed area of intermetallic particles, before they are undermined or removed. [4]

Current requirement for aluminum during CP in SW, can further be reduced by an order of magnitude with time compared with freely exposed surfaces, due to removal, instead of undermining of particles [4]. This is related to a process called "cathodic etching", which apply during CP. Figure 2.11 [5] shows a schematic description of the mechanism. The rate of removal of these particles depends on the cathodic polarized potential.

Potentials between -1.1 and -1.3 V SCE show good results with regards to particles removal. A more positive potential than -1.1 V can cause repassivation before the particle is removed, while a more negative potential than -1.3 V can cause too deep pits which exposes new intermetallic particles. [35]

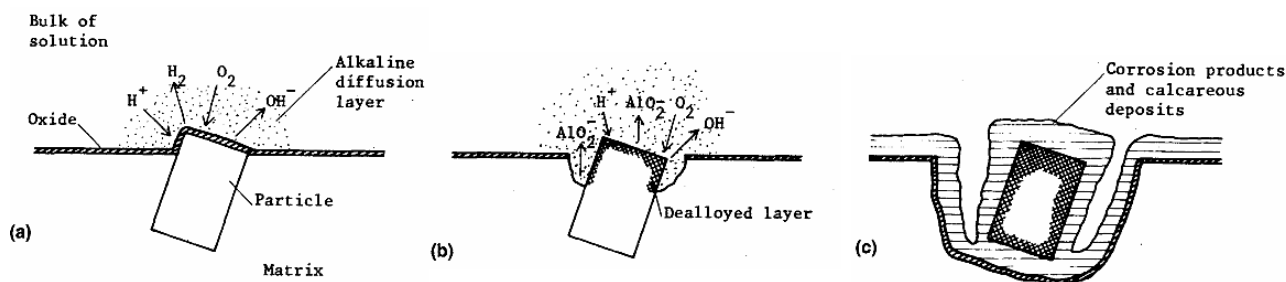


Figure 2.11: Schematic description of mechanism from CP of aluminum alloys in SW : (a) development of alkaline diffusion layer; (b) crevicing of matrix compound around the particle and selective dissolution of the particle; (c) repassivation of the surface after detachment or undermining of particle. Adapted from [5].

CP of aluminum works well if pitting at low flow rates is the dominant corrosion mode. If uniform corrosion from chemical dissolution becomes the dominant corrosion mode, CP of aluminum may increase the corrosion rate instead of reducing it. This is because the dissolved oxygen is continuously replaced by formation of new oxide at the metal-oxide interface. [4]

#### 2.5.4 Cathodic Protection of TSA

The protection potential for TSA and solid aluminum is quite similar. The protection potential for TSA is generally within the range -900 to -1100 mV Ag/AgCl exposed in SW at ambient temperatures. The potential where the oxide film is stable is dependant on pH, type of alloy and temperature.

Similar with what was explained in previous section (2.5.3), the presence of intermetallic particles will cause increased current demand during CP of TSA at the beginning of exposure. As these particles are undermined or detached, the surface will cause decreased current demand from the CP system.

The current density demand for TSA during CP (-1030 mV Ag/AgCl) have been reported to be  $5 \text{ mA/m}^2$  for unsealed coatings, and less than  $1 \text{ mA/m}^2$  for sealed coatings after 18 months of exposure. [36, 5]

CP of TSA at high temperatures in SW can cause TSA coatings to provide protection currents to anodes and bare steel in the beginning of exposure. This was experienced in the project work [37], where the TSA samples were polarized to -1070 mV SCE at 47 and 80°C. This can be linked to the OCP measurements, where the potentials were lower with increased temperature, in the beginning of exposure, making it more negative compared to the polarized potential at the times where anodic currents from the TSA coatings were observed. This can be unfortunate as this can

cause rapid consumption of the coating and decrease the lifetime of the coating. Similar behaviour was experienced in Wilsons Master Thesis [38], Department of Engineering Design and Materials report [39] to Statoil on Subsea Coating for Cooling TSA test, and was also detected where TSA in combination with CP was used for a high temperature subsea pipeline [40].

CP of TSA in Mud can have detrimental effects on the oxide layer in mud compared with SW. Knudsen et al. [41, 42] found that transportation of  $\text{OH}^-$  (which is produced by cathodic reactions), by diffusion and water flow probably is limited in mud, due to reduced/no flow of SW. This will cause increased pH at the TSA/mud interface which destabilizes the oxide layer and activates the aluminum. The aluminum corrodes and consumes  $\text{OH}^-$  according to Equation 2.2 in alkaline conditions. It was found that the pH seemed to adjust itself within the upper pH limit for passivity of aluminum due to this. Knudsen et al. [41] also found that excessive cathodic polarization of TSA in mud, i.e. -1200 mV Ag/AgCl is detrimental to TSA, since high current densities was measured indicating failure of the oxide layer. It was also found that the corrosion rate of TSA polarized to -1100 Ag/AgCl increased with temperature. From  $10\mu\text{m}/\text{y}$  at ambient temperature to approximately  $20\mu\text{m}/\text{year}$  at  $95^\circ\text{C}$  after 170 days of exposure. The corrosion rate decreased however with time and seemed to correlate with cathodic current density.

DNV [11] recommends a design current density of  $10\text{ mA}/\text{m}^2$  for components coated with aluminum or zinc in SW for initial/final and mean values. For internally heated components, the design current density shall be increased by  $0.0002\text{ A}/\text{m}^2$  for each  $^\circ\text{C}$  that the metal/SW interface is assumed to exceed  $25^\circ\text{C}$ . The increment is based on increased diffusion coefficient of oxygen [5].

This means that the design protection current densities should be 10, 15 and  $21\text{ mA}/\text{m}^2$  for temperatures at 22, 50 and  $80^\circ\text{C}$ , respectively.



---

# Chapter 3

## Literature Review

Limited results exist when it comes to experience with DSA. However, there are some instances where this concept has been applied.

Daily and Burns published articles in 2003 and 2004 [43, 44] where a thermally sprayed anode alloy (Al-Zn-In) was applied by electric arc spray to the substructure and superstructure elements of the San Luis Pass Bridge in Galveston. The bridge was located in a harsh marine environment. This was performed in order to ensure that rebar was cathodically protected. Problems for reinforced concrete structures occur when salt penetrates the concrete and reaches the surface of the reinforced steel. The steel loses passivity and begins to corrode when a threshold level of chloride ion concentration is exceeded. The corrosion products can cause a build up of tensile forces which eventually causes concrete cracking. The initial data from this concept indicate that CP is well established and that the coating adheres well to steel.

Results from field and research do not exist, when it comes to experiences with DSA used as a coating at elevated temperatures in seawater and for exposure in mud. Some, but limited experience with TSA used at elevated temperatures and for exposure in mud exists. A summary of the most relevant studies from literature and in-house experiences in NTNU and Sintef are presented below.

W.H. Thomasson published an article in 1985 about Offshore Corrosion Protection with TSA [23]. Field studies about electrochemical properties of flame sprayed TSA were conducted in SW. The effect of corrosion fatigue was also evaluated. He found that holidays (bare steel) as large as 50% could be cathodically protected by TSA for a few years. He estimated that a 200 $\mu$ m TSA coating could protect a 6% holiday for 30 years. The corrosion fatigue test showed that the TSA coated steel experienced no disbanding after 2 million cycles. The overall conclusion was that TSA would provide effective long-term corrosion protection in severe environments associated with offshore facilities.

In 1995, the Heidrun Tension Leg Platform was installed off the coast of Norway, with a 50 years design life [45]. TSA was applied on the tethers, risers, and deck undersides. Supplementation by CP from sacrificial anodes was applied onto the TSA coatings. The anodes were mounted on the TLP hull and sea floor templates. After four years of exposure, serious coating damage was revealed on two oil export risers and one gas export riser in the splash zone. These risers operated at temperatures well above ambient SW temperatures (50°C). The locations of the coating damage indicated that the removal was related to SW impact, since the coatings experienced maximum removal at the sides facing the sea currents and waves. The primary cause for the TSA deterioration was believed to be from a "thermal-cycling" effect, due to limited heat transfer from the hot production tube via the annulus space which was filled with a packer fluid. These were concerns leading to further research. It was found that TSA coatings with a thickness of  $\approx$  400 to 450  $\mu$ m and above would rapidly develop blister, while a thickness of  $\approx$  200  $\mu$ m or less would perform adequately [45].

Gartland and Eggen [5, 22] at Sintef produced several reports from 1991 to 1993 on the behaviour of TSA in SW. The available reports tell that TSA during experimental research showed good protective properties when exposed in SW. They found that the effect of increased temperature was more negative OCPs. The results also showed that the narrowing in the pH-interval (see Figure 2.7) for where the oxide layer is stable as a function of increased temperature, may not be so narrow as predicted in theoretical calculations [5]. However, the results were based on limited data. The effect of time on cathodic current densities on several coatings was measured, and it was found that the current densities decreased during exposure. The samples were polarized to -1030 mV Ag/AgCl and the current densities after 18 months of exposure were 5 and 1 mA/m<sup>2</sup>, for unsealed and sealed coatings, respectively [5]. They found that the steady state corrosion potentials of TSA coatings will be in the range -900 to -1000 mV SCE after a few weeks. They also found initial corrosion rates of 10 µm/year, decreasing to ≈ 2 µm/year after 11 months of exposure.

Wolfson [16] published an article in 1996, based on corrosion control of subsea piping systems using TSA in saline mud. He performed four and twelve months exposure tests with mud extracted from the natural Gulf of Mexico. He coupled bare steel with TSA coated steel, in order to simulate coating damages. OCPs for the TSA coating and current density requirement for the bare steel were measured. The results showed that the TSA coating could provide CP to ≈ 5 % coating holiday factor. He found that a 254 µm thick sealed TSA coating can ensure CP of a subsea pipeline with 5 % holidays and have a lifetime longer than 25 years. He found that the effect of silicone-aluminum sealers did not limit the CP abilities from TSA coatings in saline mud environments.

CP of TSA in Mud can have detrimental effects on the oxide layer in mud compared with SW. Knudsen et al.[41, 42] found that transportation of OH<sup>-</sup> (produced by cathodic reactions) by diffusion and water flow probably is limited in mud. This will cause increased pH at the TSA/mud interface which destabilizes the oxide layer and activates the aluminum. It was found that the pH seemed to adjust itself within the upper pH limit for passivity of aluminum due to this. Knudsen et al.[41] found that excessive cathodic polarization of TSA in mud, i.e. -1200 mV Ag/AgCl is detrimental to TSA, since high current densities were measured indicating failure of the oxide layer. It was also found that the corrosion rate of TSA polarized to -1100 Ag/AgCl increased with temperature, from 10µm/y at ambient temperature to approximately 20µm/year at 95°C after 170 days of exposure. The corrosion rate decreased however with time and seemed to correlate with cathodic current density.

Wilson [38] published his Master Thesis in 2014, where the effect of temperature on protection current requirement and calcareous deposit development on TSA for subsea heat exchangers was examined. The experimental design included internal heating of test spools exposed to SW at 10°C. Internal heating temperatures of e.g. 50°C, 70°C and 90°C (amongst others), caused exposed TSA surface temperatures of 25°C, 45°C and 60°C, respectively. The results were based on exposure periods up to 60 days. He found that the corrosion rates increased at elevated temperatures. The corrosion rate decreased during exposure from 50 µm/year initially to 8 µm/year after 65 days of exposure. The corrosion rate with no internal heating was initially 27 µm/year, but decreased to 2 µm/year after 150 days. He also found that the current density requirement for TSA was very low compared with steel, with a current demand of ≈ 2-5 mA/m<sup>2</sup>, which increased slightly at elevated temperatures. He found that elevated temperatures will decrease the initial OCPs of TSA, which will cause a temporary shift in current flow from TSA to anodes. It was found that calcareous deposits will form on TSA at all temperatures, both freely exposed and cathodically polarized samples.

The Department of Engineering Design and Materials was engaged by Statoil to execute a research project [39] regarding the properties of TSA under CP in SW at elevated temperatures. The experimental design was similar with Wilsons design in his Master thesis [38]. It was found that the cathodic current density stabilized below 10 mA/m<sup>2</sup> after 100 days at all temperatures. The surfaces were polarized within a range -1050 to -1070 mV Ag/AgCl. Similar with what Wilson found



---

[38], the electrochemical potential was initially more negative than the polarized potential which caused the TSA coating to act as an anode at this polarized potential. Cross section thickness measurements of not exposed samples vs. exposed samples indicated thickness degradation after 9 months of exposure. Higher temperature seemed to cause increased thickness reduction. A probable explanation was a combined effect between electrochemical corrosion and chemical dissolution.

CP of TSA at high temperatures in SW can cause TSA coatings to provide protection currents to anodes and bare steel in the beginning of exposure. This was experienced in the specialization project work [37], where the TSA samples were polarized to -1070 mV SCE at 47 and 80°C. This was linked to the OCP measurements, where the potentials were lower with increased temperature, in the beginning of exposure, making it more negative compared to the polarized potential at the times where anodic currents from the TSA coatings were observed. This can be unfortunate as this can cause rapid consumption of the coating and decrease the lifetime of the coating. Similar behaviour was experienced in Wilsons Master Thesis [38], Department of Engineering Design and Materials report to Statoil on Subsea Coating for Cooling TSA test [39], and was also detected where TSA in combination with CP was used for a high temperature subsea pipeline [40].

Recent studies and results achieved in previous projects show that TSA works well for corrosion protection at ambient SW temperatures and can provide CP to small damages in a coating for a long period of time both in SW and mud. CP of TSA in SW can be a problem at elevated temperatures. Excessive cathodic polarization of TSA in mud is detrimental on TSA at elevated temperatures.

DSA can be an alternative solution to TSA, since the coatings chemical composition will be close to those of Sacrificial Anodes (Al-Zn-In). This should decrease the current demand during CP, and since no thickness limitations of the DSA coating has been found yet, it can provide increased lifetime compared to TSA coatings. The DSA coating will in addition provide adequate protection to steel, compared with TSA, since the DSA surface should activate easier in terms of providing protection currents both at ambient temperatures as well as at elevated temperatures. The high resistivity present in mud should favor use of DSA coating compared with TSA, due to more active abilities compared with TSA.



---

# Chapter 4

## Experimental Work

This chapter presents the experimental part of the thesis. In order to keep a simple structure of the experimental work the different tests are separated in different sections. The experimental work for the Exposure at elevated temperatures is presented in Section 4.1, while the experimental work for the Exposure in mud is presented in Section 4.2.

### 4.1 Exposure at elevated temperatures

The Exposure at elevated temperatures experiment has been conducted in the corrosion laboratory at Perleporten, NTNU.

Electrochemical measurements on TSA, DSA and Anode (Al-Zn-In) samples were performed in three separate rebuilt glass beakers (containers) containing natural seawater (SW), at three different temperatures:

$T_1 \approx 22^\circ\text{C}$  (ambient room temperature),  $T_2 \approx 50^\circ\text{C}$  and  $T_3 \approx 80^\circ\text{C}$ .

Important experience with the equipment were made in the earlier specialization project [37], where a quite similar setup was used. The experimental design was however continuously evaluated throughout the experimental period in order to ensure that proper results were obtained.

#### 4.1.1 Materials included in the experiment

The materials included in the experiment involved DSA-samples, TSA-samples, Anode-samples, Carbon Steel (CS) cubes and M3-rods. Information about the test-samples and materials used are presented below:

##### **DSA-Samples:**

The DSA coating consists of one thermally sprayed layer applied by electric arc spray to one side of a carbon steel plate. The coating is made by recasting Al-Zn-In anodes to DSA. The recasting process is described in Quales Master thesis [12]. The anode-coating was applied onto carbon steel plates ( $T \approx 6$  mm) by Total Coating AS in Drammen.

A chemical composition analysis of the DSA coating was performed by SINTEF MOLAB in September 2016 [46]. The results showed that the content of zinc was approximately 2.5 wt% in the DSA coating, which was a reduction from 4.7 wt% in the 2 mm wire used in the electric arc process. A small reduction of In was revealed i.e. from 0.022 wt% to 0.018 wt%.

The thickness is  $\approx 1000 - 1100$   $\mu\text{m}$  based on SEM measurement of one unexposed sample. This is consistent with data from the coating distributor. The samples were cut circular by water jetting into appropriate size ( $\varnothing \approx 28$  mm) in order to fit with the outlets of the rebuilt beaker and screw cap. The front surface of a DSA-sample is presented to the left in Figure 4.1.

**TSA-Samples:**

The TSA test-samples are based on chemically pure aluminum (i.e. 99.5% Al). The thickness is  $\approx 200 - 400 \mu\text{m}$  on the exposed side of the sample. The measurements are based on one cross section analysis in SEM of one unexposed sample. The coating was applied onto carbon steel plates ( $T \approx 10 \text{ mm}$ ) by Total Coating AS in Drammen. Further, the samples were cut circular by water jetting into appropriate size ( $\text{Ø} \approx 28 \text{ mm}$ ) in order to fit with the outlets of the rebuilt beaker and screw cap. The front surface of a TSA-sample is presented to the 2nd left in Figure 4.1.

The application process of the DSA and TSA coatings is in accordance with the process that is described in Quaales Master thesis[12]: *"The carbon steel surfaces were grit blasted to Sa ½ according to ISO 8501-1 before electric arc spraying. In addition, sharp edges and corners were rounded by grinding or disc sanding to a min of 2 mm radius. Both coatings were applied using electric arc thermal spray technique, Osu Hessler 300A with a modified pistol for smooth surfaces. A 9.5 mm die and a pressure of 7 bar was used under the cleaning process with an oil/water separator to secure that the air was free from oil and water. Surface dust was controlled with the use of pressure sensitive tape method according to ISO 5202-3 and salts and chlorides were controlled using Bresle Test according to ISO 8502-6. The roughness was determined by using comparator according to ISO 8503. No sealer was applied on the coating."*

**Anode-Samples:**

The Anode test-samples are made from commercial Al-Zn-In anode material. The anode samples are made from CORAL A Highs Graded alloys delivered from Skarpenord Corrosion [9]. Information about the alloy is presented in Figure A.1 in the Appendix Section. The samples were cut circular by water jetting into suitable size ( $\text{Ø} \approx 27 \text{ mm}$ ), so that they matched the outlets and screw caps. The front surface of an Anode-sample is presented to the 2nd right in Figure 4.1.

**CS-cubes:**

The CS-cubes are plain carbon steel. They were cut to size 10x10x10 mm, so that the exposed area was about as big as the exposed area of the test-samples. One regular sized CS-cube is presented to the right in Figure 4.1.

**M3-rods:**

The M3-rods are stainless steel and were included to ensure electrical contact with the CS-cubes in the bulk electrolyte of the containers, while shorter M3-rods were included to facilitate electrical contact on the unexposed side of the samples.



Figure 4.1: Front side of test samples -Left: DSA sample, 2nd Left: TSA sample, 2nd Right: Anode sample, Right: CS-cube.

Holes were drilled into the intended unexposed sides of the TSA-, DSA- and Anode test-sample. A hole was also drilled into one side of the CS-cube. The holes were female threaded to size M3.

The test samples were thoroughly cleaned with acetone after the drilling and threading process, to ensure that no oil or dirt was present on the surface of test samples prior to exposure.

#### 4.1.2 Experiment setup

The experiments were conducted in three rebuilt glass beakers (containers) made by NTNU/SINTEF. The containers had eight connection points, where it was possible to connect the samples using rubber gaskets and plastic screw caps. The screw cap had holes to ensure metallic contact on the back side of the sample.

Seven test samples were connected to each container. An outlet connection with a rubber tube was connected to one out of the four bottom connections. The outlet was used for controlling the pH-level of the bulk SW throughout the exposure period, and to regularly exchange the natural seawater.

Experiences from the project work [37] revealed leakage problems at the connections points, especially where the thermally sprayed samples were connected. In order to prevent leakage problems it was decided to apply blue silicon gel onto the surface of all samples. This created an additional barrier against leakage. The application of blue silicon gel onto a sample is presented in Figure 4.2.



Figure 4.2: Application of blue silicon gel onto a thermally sprayed sample, creating an extra barrier against leakage.

Leakage testing of the containers were performed with fresh tap water before the experiment was started. Replacement of rubber gaskets and screw caps were performed at locations where leakage occurred.

The CS-cubes were securely tightened with the M3-rods using a shift key. This prevented looseness between the CS-cubes and the rods, which ensured proper electrical contact between the two. Heat shrinkable tubing was put on the part of the rods that would stand in the seawater. A heat dryer was used to shrink the tubing onto the rods. This ensured that only the CS-cube pulled current from the test samples. A picture of the CS-cubes attached to M3-rods with shrinkable tubing is presented in Figure 4.3.

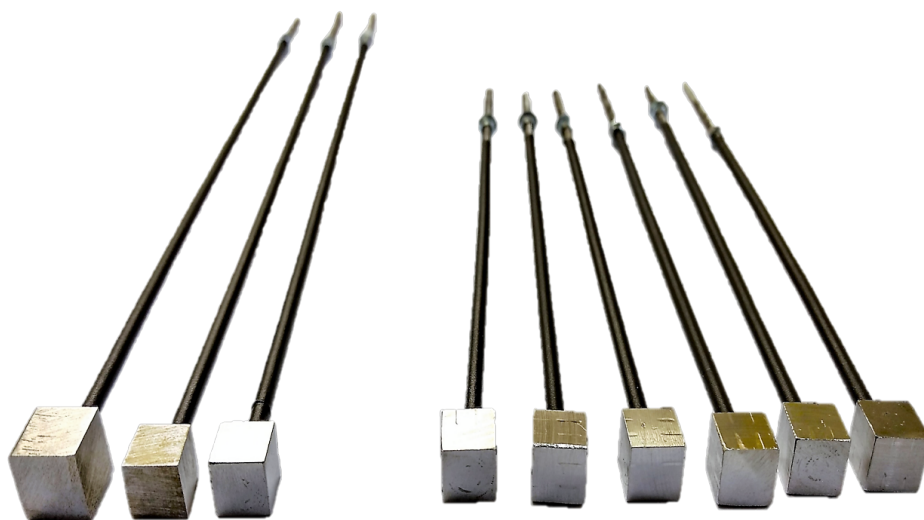


Figure 4.3: CS-cubes attached to M3-rods with shrinkable tubing.

Holes were drilled through the transparent plastic lid, so that the CS-cubes could align in a fixed distance with the to-be-connected samples inside the glass container. M3-nuts with washer were used above and below the plastic lid to securely fasten the M3-rods with the plastic lid. The position of the plastic lid on the container was further fixed, so that the position of the lid remained in the same location.

The three longest rods which are presented to the left on Figure 4.3 were coupled with the anode samples connected to one of the four bottom outlets. Due to lack of one regular sized CS-cube, a slightly bigger CS-cube was used for connection with the Anode-sample at the 22°C experiment. This caused an area ratio which was different compared with the other connections between the samples and the CS-cubes.

Holes were drilled in the transparent plastic lid, so that the Platinum counter electrode easily could be placed into the seawater when conducting Linear Polarization Resistance (LPR), and for obtaining Polarization Curves on selected samples.

A sealing strip was used between the container and plastic lid to avoid rapid water evaporation on the 80°C experiment. Blue silicon gel was used to seal old drilled holes in the plastic lid.

Similar with the design in the project work, it was decided to attach insulation and aluminum foil on the protruding parts of the 80°C container. This reduced the heat loss to the environment. The required temperature of the bulk seawater was  $\approx 82\text{-}83^\circ\text{C}$ , in order to achieve a surface temperature of approximately 80°C on the test samples.

The reference electrodes used for the roomtemperature experiment and 50° experiment were Saturated Calomel Electrodes (SCE), while a saturated Silver/Silver-Chloride (Ag/AgCl) electrode was used for the 80°C experiment. All reference electrodes were calibrated against a zinc electrode exposed to artificial seawater in the lab in order to verify that they were showing correct results prior experiment start and after end of exposure.

The general parts in the experimental design of the 80°C experiment is presented in Figure 4.4. A simple picture of the 22°C experiment with additional description of parts is presented in Figure 4.5.



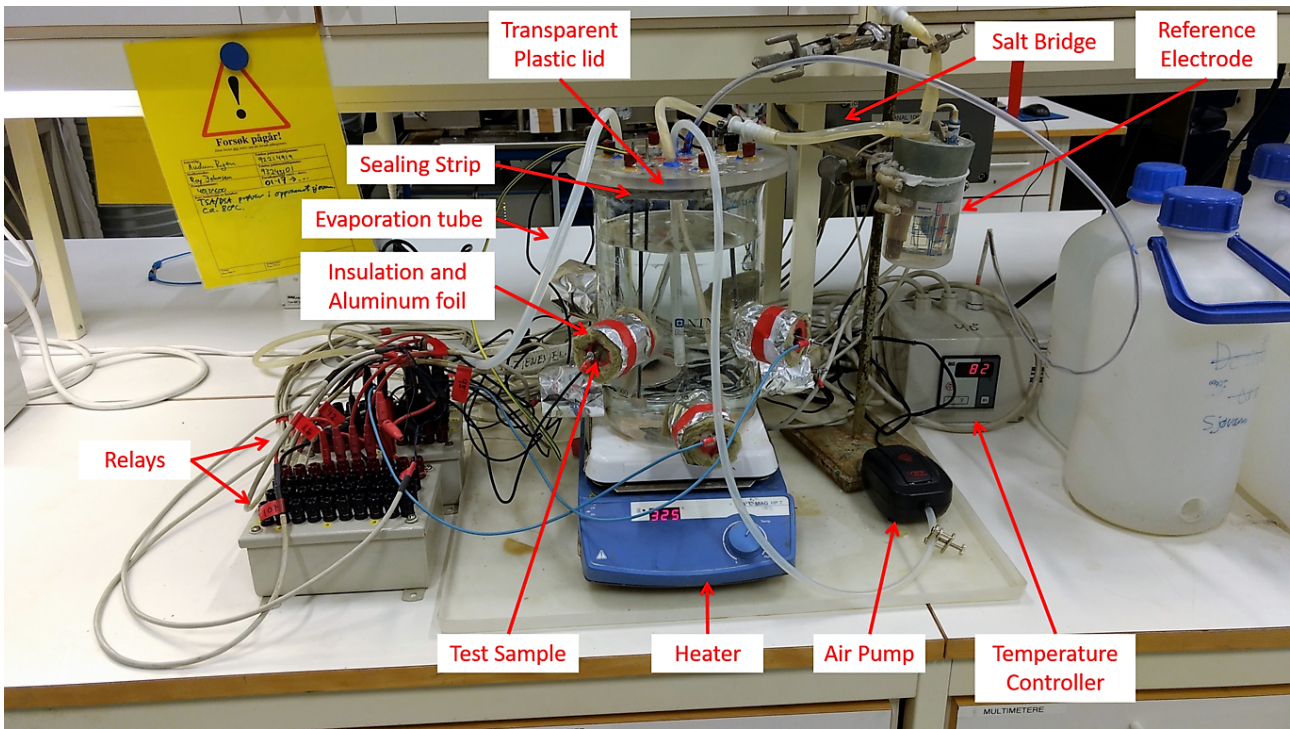


Figure 4.4: The 80°C experiment with general description of parts.

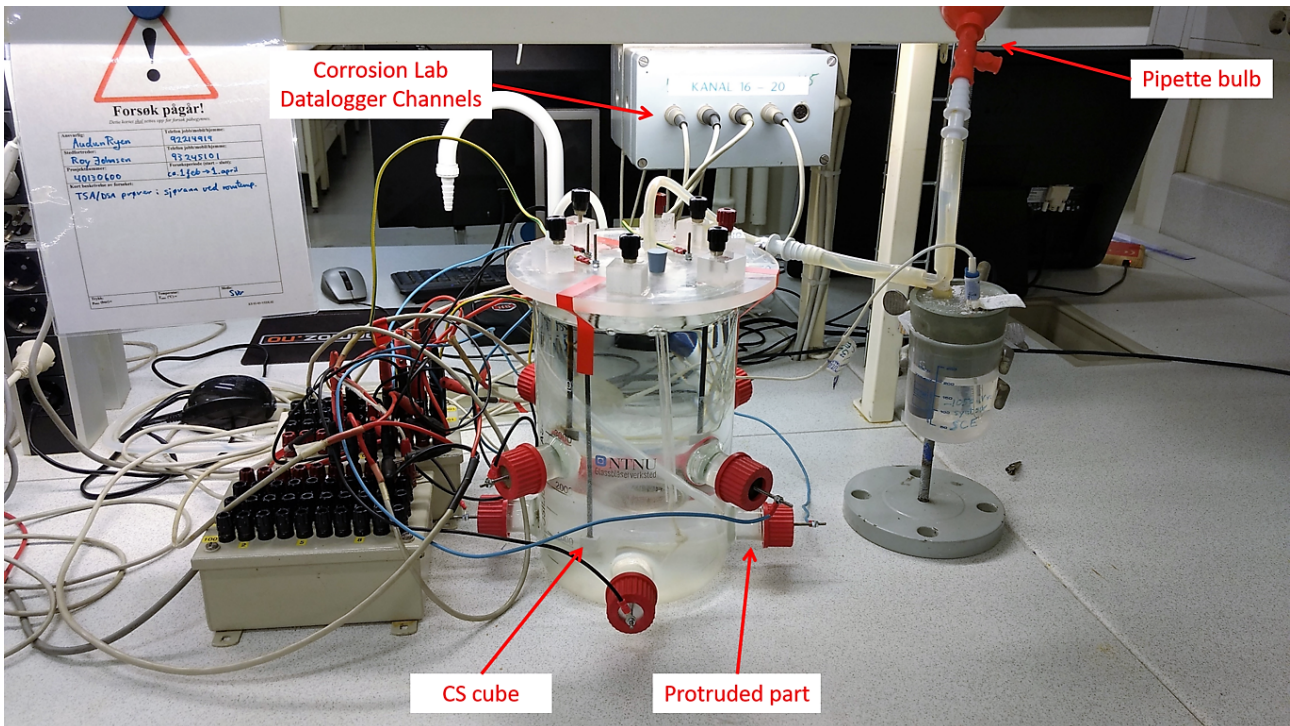


Figure 4.5: The 22°C experiment and additional description of parts.

### 4.1.3 Test sample setup

Ten test-samples were connected to each container: Three DSA samples, two TSA samples, two Anode samples and three CS-cubes. The sample setup was arranged in the following identical manner for all three temperatures:

- One DSA, TSA and Anode sample were galvanically coupled with three separate CS-cubes. Galvanic current was measured by voltage drop over a known resistance throughout the exposure period. Galvanic couple potentials were measured on DSA and TSA connections after approximately 1 month of exposure.
- One DSA, TSA and Anode sample were freely exposed to natural seawater. The Open Circuit Potential (OCP) was measured throughout the exposure period.
- One DSA sample was freely exposed and used for obtaining Polarization Curves in the beginning of exposure and towards the end of exposure. This DSA sample was also used for LPR measurements once a week.

The sample setup was identical for all temperatures in order to facilitate simple comparison between the test results in order to determine the effect of temperature.

Corrosion Lab Datalogger was used to continuously measure the electrochemical properties during the test period. The interval for collecting measurement values on all long-term tests was three minutes. OCP was measured on the freely exposed samples vs. the corresponding reference electrode present at the container. The current demand for the galvanic connections was measured by a voltage drop (volt. drop  $< 2\text{mV}$ ) over an applied resistance which was known. A simple schematic description of the arrangement of samples and CS-cubes is presented in Figure 4.6.

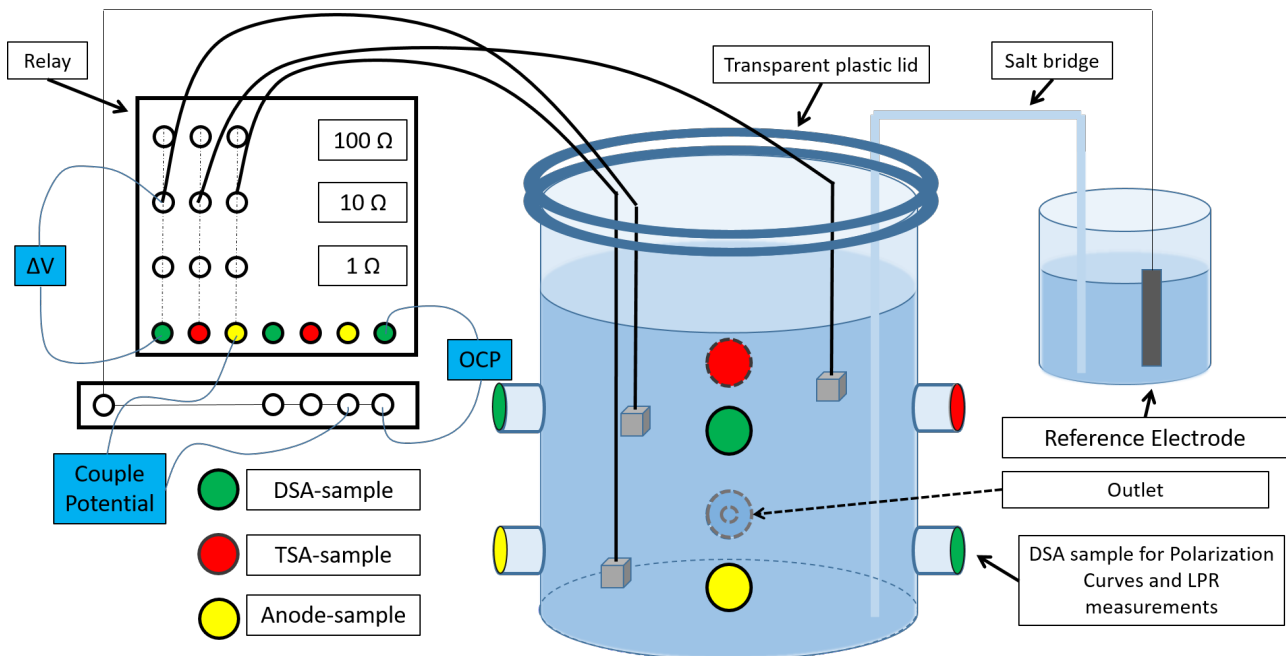


Figure 4.6: A simple schematic description of the setup of samples on each container.

The measured voltage drop was converted to current densities by applying Ohms law and dividing the current by the test samples exposed area, not the exposed area of the CS-cubes. A complete list of the test sample arrangement and results obtained for all temperatures is presented in Table A.1 in the Appendix section.



#### 4.1.4 Experimental Conditions

The conditions of which the DSA, TSA and Anode samples were exposed to, are described in this section.

##### Seawater and seawater movement

All test-samples were exposed to fresh natural SW retrieved from SINTEF Sea Lab. The SW was pumped from 80 meters depth in Trondheimsfjorden. Air pumps were included in the experiment design in order to avoid stagnant conditions for the SW. It pumped air at ambient room temperature, through rubber tubes, via the plastic lid and into the SW.

This ensured some movement of the SW, and that the SW had high oxygen saturation. The amount of movement this caused in the protruding parts of the container, is uncertain. The amount of air that was pumped varied with respect to the different pumps that were installed. Tube clamps were attached to the tubing so that the amount of air flow was a little less on the 50 and 80°C container in order to avoid rapid water evaporation.

##### Replacement of seawater

The seawater was replaced with fresh SW at certain intervals in order to prevent the samples from being exposed to the same electrolyte throughout the exposure period. This made the experiments to some extent more realistic. The natural SW was preheated so that the temperature in the containers remained as stable as possible after the replacement. The SW was substituted by discharging SW through the outlet, and replenishing SW through a funnel in the lid, so that the level remained above the top exposed samples and CS-cubes. The seawater was preheated to approximately 53°C and 70°C for the respectively 53°C and 83°C containers. The seawater was preheated to only 70°C, due to health, safety and environment considerations. Approximately five liters were used for each container when the seawater was replaced.

##### Temperature

The temperature of the 50°C and 80°C experiments were controlled by a temperature sensor attached to a temperature controller. The power cord to the heater was attached to the temperature controller. Experiences learned from experimental design in the project work [37] showed that some adjustments had to be made to ensure that the samples were exposed to the desired temperature. Heat loss through the container, protruding parts and back sides of samples caused some difference between the temperature of the seawater in the middle of the container and the temperature of exposed surfaces of the samples. The temperature of the exposed surface were measured by a Fluke 80TK Thermocouple Module temperature sensor within the container. The accuracy of the sensor was affirmed by the temperature controller and by body temperature measurement beneath the tongue. It was also decided to attach insulation and aluminum foil to the protruding parts of the 80°C experiment, since the heat loss was higher at this container. This reduced the amount of heat required in order to expose the samples surfaces to 80°C. Insulation and aluminum foil can be seen in Figure 4.4. Table 4.1 presents the temperature in the container and the temperature of the exposed surfaces of the samples.

Temp. in container [°C]	Temp. of the exposed surfaces of the samples [°C]
22	22
53	≈ 50
83	≈ 80

Table 4.1: Temperatures in the containers vs. the temperature of the exposed surfaces of the samples.

The difference in temperature may be a sign that the movement of seawater in the protrusions is limited.

### pH of the seawater

The pH of seawater in the containers was measured frequently in order to determine possible changes in chemistry. pH-measurements of the SW was performed from the outlet by releasing a tube clamp on the rubber tubes. A small volume of stagnant SW in the tubes was first removed, before seawater in the containers was collected in small sample cups. pH-measurements were performed by a PHM210 - Standard pH meter - MeterLab. The pH meter was calibrated prior to each measurement using two IUPAC buffer solvents that were expected to be within the range of the pH of SW ( $\text{pH}_{\text{SW}} \approx 8.0\text{-}8.2$ ; Green = pH 7.0 and Blue = pH 10.012).

### 4.1.5 Linear Polarization Resistance Measurements

LPR measurements were performed on DSA-samples at each temperature in order to get an estimate of the development of the polarization resistance ( $R_p$ ) throughout the exposure period. LPR was performed in average one time per week on the same (prior-polarized) sample. The measurements were performed by using a three electrode system and by following this procedure: The OCP was measured and noted for the samples. The freely exposed was polarized 20 mV in cathodic direction. It was held at this potential for approximately five minutes, in order for the potential drop to stabilize. The measured value was noted. The potentiostat was set on "standby" for approximately five minutes, in order for the test sample to return as close as possible to the initial OCP. The sample was finally polarized 20 mV in anodic direction for approximately five minutes. The  $R_p$  was calculated by taking the average value from the results in cathodic and anodic direction. A simple schematic description of the setup is presented in Figure 4.7.

### 4.1.6 Polarization Curves

Anodic polarization curves were obtained on DSA samples at each temperature after one day of exposure, using the same setup as for performing LPR measurements which is presented in Figure 4.7. This was performed to document the anodic properties of the coatings at the beginning of exposure. The following procedure was followed to record anodic polarization curves:

1. The OCP was measured.
2. The sample was polarized in anodic direction from OCP in a stepwise approach. The speed of the polarization was 600 mV/hour.
3. The steps selected were 25 mV every 2.5 minutes. The potential was adjusted and held in order for the voltage drop to stabilize. The measured potential drop over the resistance was noted, and the next step was started.
4. The procedure was repeated until the applied potential reached approximately -600 mV SCE.

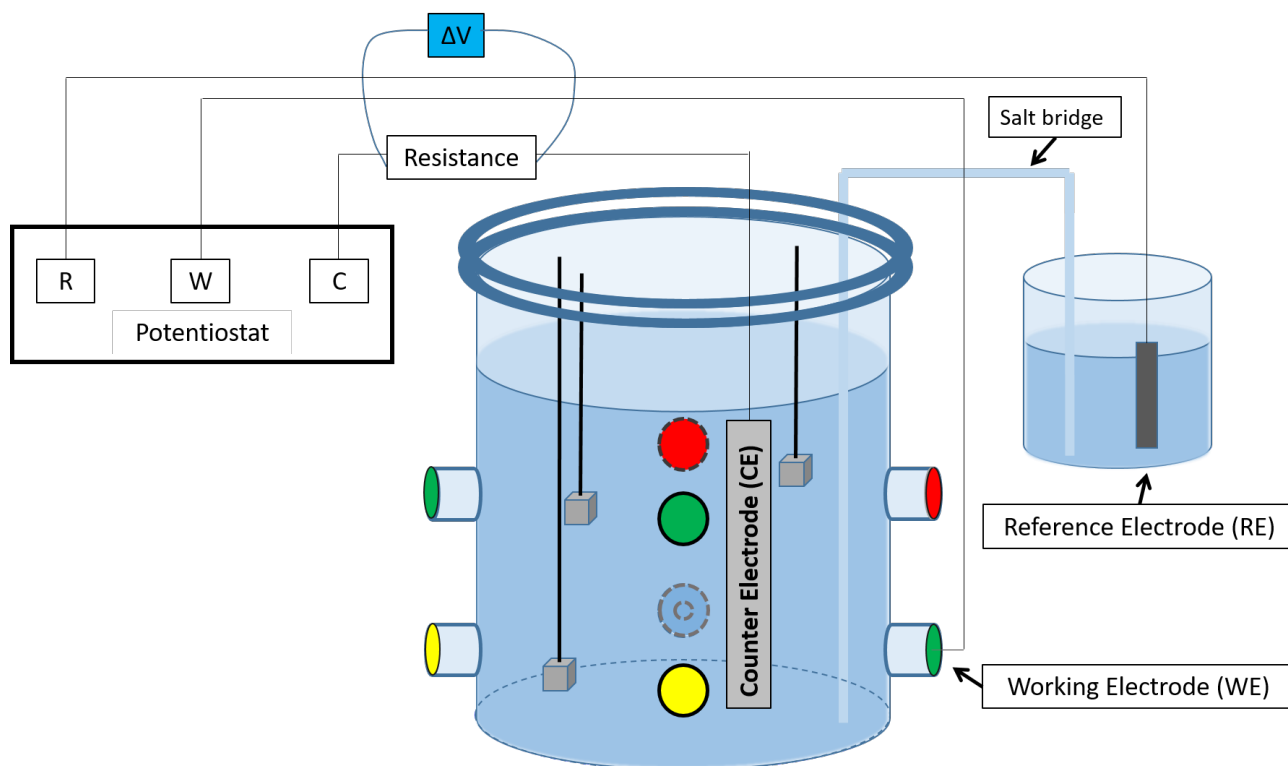


Figure 4.7: A simple schematic description of the setup when performing LPR measurements.

Polarization Curves were finally recorded on the prior polarized DSA samples after 63 days of exposure using a portable GAMRY Potentiostat. This was performed by polarizing the samples from -200 mV vs. OCP to approximately -500 mV SCE in an attempt to reach the pitting potentials of the coatings. Due to poor performance on the prior polarized DSA samples exposed at 50°C and 80°C, it was decided to record polarization curves on all freely exposed DSA samples. Polarization Curves on freely exposed TSA and Anode samples at all temperatures were also included, in order to compare the electrochemical properties of the coatings. The potential drop were converted to absolute current densities by applying Ohms law and dividing the current on the exposed surface area of the samples. The X-axis was scaled logarithmic and applied potential was converted to mV SCE. This means that it was subtracted 45 mV on potentials measured with a Ag/AgCl reference electrode, since this was the measured difference between the reference electrodes prior and post exposure. Absolute current density was plotted vs. applied potential.

#### 4.1.7 Visual Observations and cleaning with Nitric Acid

Visual observations of the samples were performed immediately after the samples were disconnected from the containers, to get an overall impression of the samples after the end of exposure. The CS-cubes were rinsed in tap water and observed to detect approximate amount of calcareous deposits. They were also visually examined to detect possible corrosion products, indicating that the CS cubes had received too little protection current from the coatings or had little amount of calcareous deposits.

The samples were further rinsed in distilled water and dried. Then they were washed in 65 % nitric acid ( $\text{HNO}_3$ ) for three minutes in order to try to get rid of corrosion products on the surface of the samples. They were further rinsed thoroughly in distilled water before they were placed to dry. Since many of the samples still had a lot of corrosion products after the washing in the acid, they were tried brushed off with a stiff dish brush. Later they were washed in 65 % nitric acid ( $\text{HNO}_3$ ) for three minutes one more time, and rinsed thoroughly in distilled water.

Visual observations of all samples were performed after the cleaning process, in order to detect possible signs of significant degradation or faults.

#### **4.1.8 Optical Microscopy**

Optical Microscopy (OM) of the samples were performed on new DSA and TSA sample. A line scan was performed in order to achieve a surface topography of the samples.

#### **4.1.9 Surface and Cross Section Analysis**

Surface examination and cross section analysis were performed using Scanning Electron Microscopy (SEM) on TSA and DSA samples in order to determine the chemical composition of the coatings and coating thickness prior and post exposure. The chemical composition of the surface of the coatings and cross sections was determined by Energy-Dispersive X-ray Spectroscopy (EDS). The samples were cut in half using a diamond cut-off wheel. One half was used for cross section analysis and embedded in a phenolic, hot mounting resin with carbon filler, Poly-fast. This was done in order to avoid damaging the edges during the grinding and polishing process. The embedded samples were mechanically fine grinded using SiC paper in a step-wise approach from P-120 to P-4000. Subsequently they were polished using plates with diamond spray with grain sizes from 3 $\mu$ m to 1 $\mu$ m. The samples were cleaned in ethanol, before they were analyzed in SEM. The machine used for SEM and EDS analysis was a Quanta FEG 650 machine, in the nanomechanical lab at MTP. The following samples were included in the cross section analysis:

- Unexposed DSA and TSA samples.
- Freely exposed DSA and TSA samples at all temperatures.
- Galvanic coupled DSA and TSA samples at all temperatures.

## 4.2 Exposure in Mud

The Exposure in Mud experiment was conducted at SINTEF SeaLab located at Brattøra, Trondheim. Electrochemical measurements on TSA, DSA and CS were performed on samples embedded in mud exposed in natural seawater at approximately 10°C.

Visual, OM and SEM examination were performed at the end. The initial surface conditions were also documented before exposure.

### 4.2.1 Materials included in the experiment

The materials included in the experiment were almost similar with the materials used in the exposure at elevated temperatures experiment. The thickness of DSA coating is  $\approx 1000 - 1150 \mu\text{m}$  based on cross section measurement of one unexposed sample in SEM. The coating thickness of TSA coating is  $\approx 150 - 300 \mu\text{m}$  on one side of the sample, and  $\approx 100 - 250 \mu\text{m}$  on the opposite side. The measurements are based on cross section measurement of one unexposed sample in SEM. Anode samples were not included in this experiment. Other differences were that the DSA and TSA samples were cut rectangular into size 50 x 50 mm from different plates. The CS samples were collected from the Realization Lab at MTP and cut rectangular to 50 x 50 mm.

Holes were drilled in one short side of the samples and female threaded to size M3. The CS, TSA and DSA samples are presented in Figure 4.8, respectively to the top, middle and bottom. The test samples edges were grinded using SiC paper P-120 in order to facilitate proper adhesion with painting. The test samples were thoroughly cleaned in acetone after the cutting, drilling and grinding process.

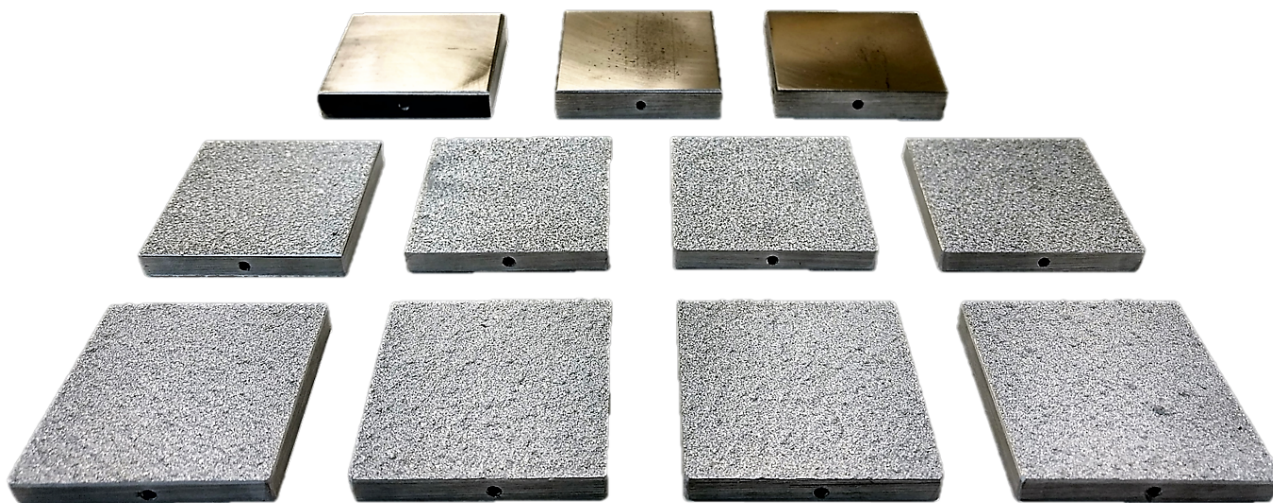


Figure 4.8: Test samples to be embedded in mud -Top: CS samples, Middle: TSA samples, Bottom: DSA samples.

### 4.2.2 Experiment setup

Each test sample was securely tightened with an approximately 300 mm long M3 rod in order to ensure proper electrical contact between the two. Heat shrinkable tubing was put on the part of the rods that would stand in the seawater and mud. A heat dryer was used to shrink the tubing onto the rods. The samples were coated with Jotamastic 87 STD038 Grey mixed with Jotamastic 87 STD COMP B in a ratio 6 to 1 so that only one of the 50x50 mm side of the samples were exposed. They were left to dry for approximately 24 hours. The samples were coated two times in order to ensure that the barrier between the seawater and the sample beneath the coating was proper. The



exposed surfaces of the painted samples and back sides are presented in respectively Figure 4.9 and Figure 4.10.

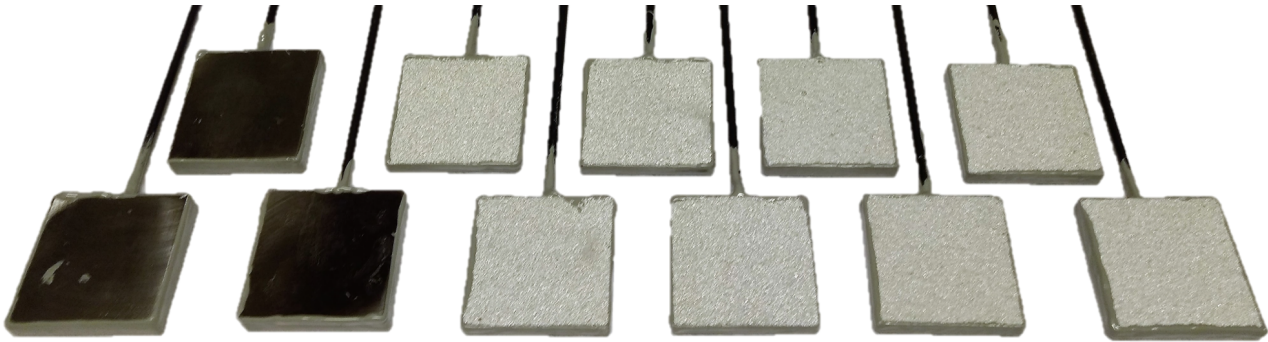


Figure 4.9: Exposed side of coated test samples to be embedded in mud -Left: CS samples, Middle: TSA samples, Right: DSA samples.

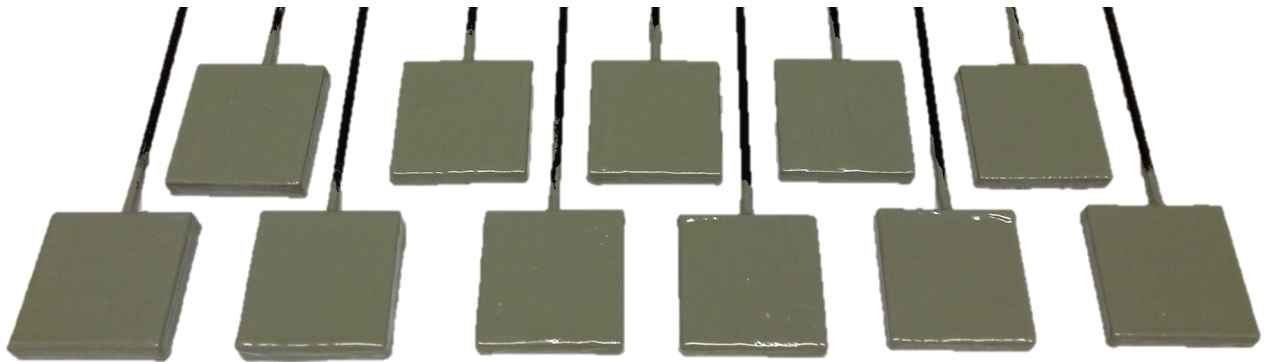


Figure 4.10: Coated side of test samples to be embedded in mud -Left: CS samples, Middle: TSA samples, Right: DSA samples.

The mud was taken from the shoreline outside Statoil Rotvoll, Trondheim. The location in the shoreline was picked randomly, and appropriate amount of mud was collected in a robust plastic container. The location where mud was collected and amount are presented in Figure 4.11.



Figure 4.11: Left: Mud collected at the shoreline outside Statoil Rotvoll, Right: Amount of mud collected in container.

The experiment was performed in a robust plastic container. A hole was drilled, for installation of a drain connection. The container was thoroughly washed using standard detergent and rinsed in tap water. The samples were fastened in two plastic planks with suitable size for the M3 rods. The planks went crosswise over the container and were securely fastened in the plastic container.

An aluminum plank with a hole was placed crosswise over the container, for placement of inlet tubing with natural seawater. The mud was softened with SW, and was dug to the side so that the samples could be placed below the mud line. The samples were placed parallel with each other. The exposed surface of CS was placed against the exposed surface of the DSA and TSA sample. The distance between the CS sample and DSA sample in the galvanic coupling was measured to approximately 45 mm. The samples were then buried in mud, approximately 20-30 mm below the mud/water line. The embedding of samples in mud are presented in Figure 4.12.

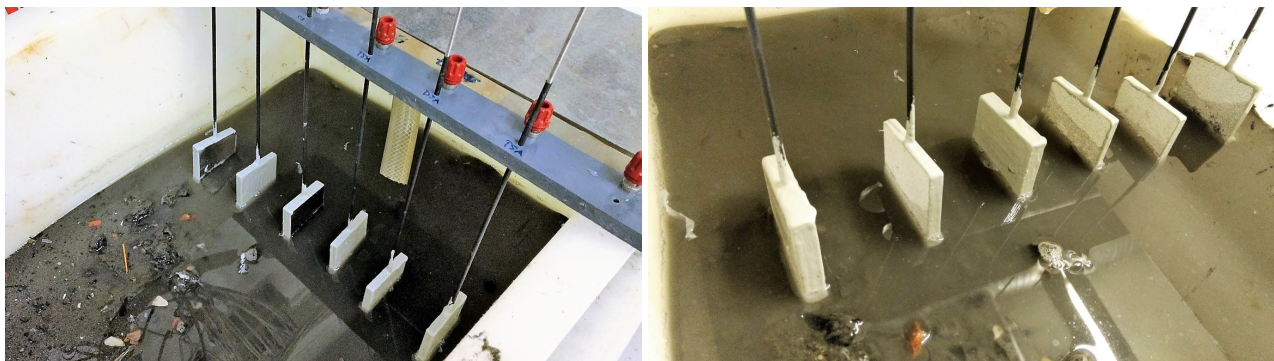


Figure 4.12: Left: Picture of samples to-be-embedded in mud, Right: Picture of samples from the opposite direction.

### 4.2.3 Test sample setup

In total 11 samples were embedded in mud: Four DSA samples, four TSA samples and three CS samples. The sample setup was arranged in the following manner:

- One DSA and TSA sample were galvanic coupled with two separate CS samples. Galvanic current was measured by voltage drop over a known resistance throughout the exposure period. The galvanic couple potential was measured on both connections.
- One DSA and TSA sample were polarized potentiostatically to  $-1100$  mV Ag/AgCl. The galvanic current was measured by voltage drop over a known resistance throughout the exposure period. The polarized/applied potential was also measured throughout the exposure period.
- One DSA, TSA and CS sample were freely exposed in mud. The Open Circuit Potential (OCP) was measured throughout the exposure period. The CS sample was used for obtaining cathodic polarization curve towards the end of exposure.
- One DSA and TSA sample were freely exposed in mud and used for LPR measurements every week. These samples were also used for obtaining polarization curves towards the end of exposure.

Corrosion Lab Datalogger was used to continuously measure the electrochemical properties during the test period. The interval for collecting measurement values on all long-term tests were three minutes. OCP was measured on the freely exposed samples vs. a Ag/AgCl saturated KCl reference electrode. The current demand for the galvanic connections and polarized samples were measured by a voltage drop (volt. drop  $< 2$  mV) over an applied resistance which was known. A general picture of the experiment is presented in Figure 4.13.



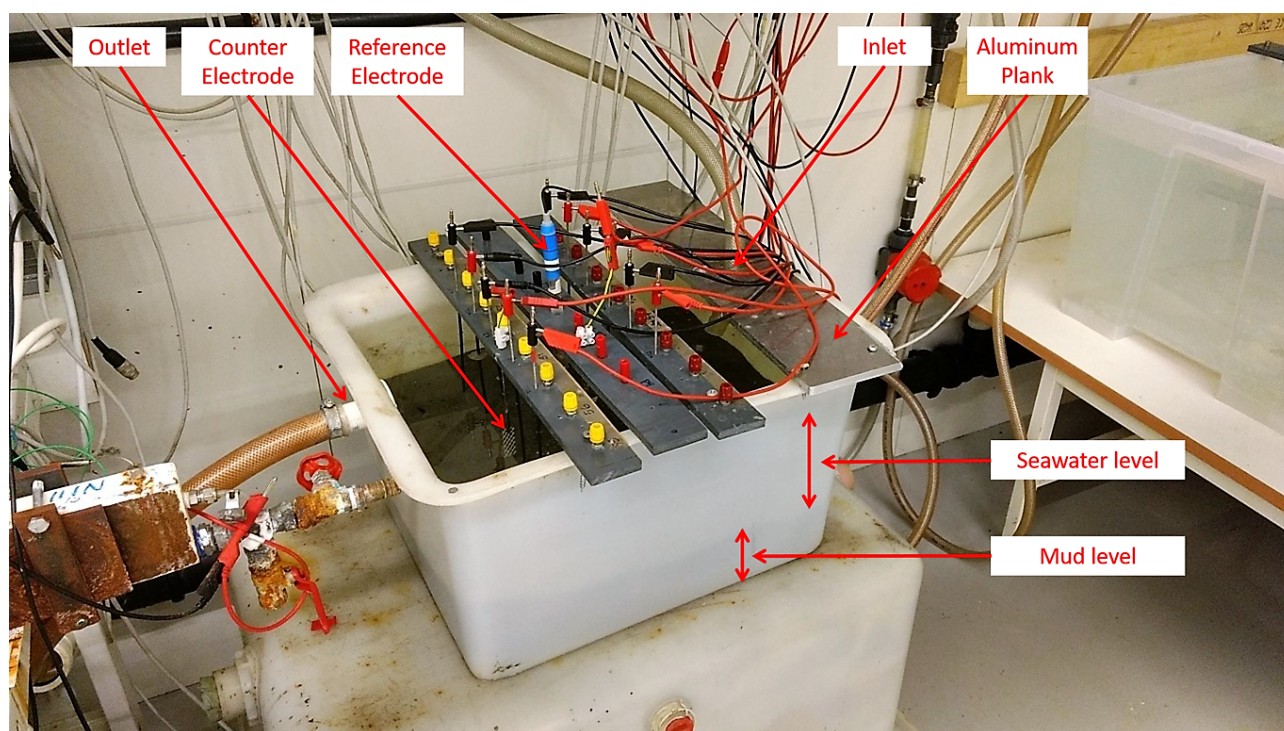


Figure 4.13: A general overview of the experiment in mud and description of parts.

#### 4.2.4 Experimental Conditions

The conditions of which the DSA, TSA and CS samples were exposed to, are described in this section.

##### Embedded samples

The top side of the samples were embedded approximately 20-30 mm below the mud/seawater interface. A deeper embedding was not possible due to limited amount of mud in the container. The samples were placed parallel with each other, and the distance between the galvanic coupled samples were approximately 45 mm.

##### Mud

The contents of the mud has not been documented yet. The visual perception of the mud is that it includes a lot of fine-grained sand. Most likely it also contains some soil in addition to various forms of microorganisms. The location where mud was collected has although been documented in Figure 4.11.

##### Seawater

The seawater used in the experiment was natural, pumped from 80 meters depth in Trondheimsfjord. The refill rate was approximately 0.1 liters/min, contributing to nearly stagnant conditions.

##### Temperature

The temperature of the seawater has been measured to be approximately 10°C throughout the exposure period. Temperature measurements of the mud approximately 5 mm below the mud/seawater interface were approximately 11°C. It is assumed that the temperature is increasing at increased depth and also depending on the location in the container.



### **pH of seawater**

The pH of seawater is assumed to be approximately 8.1, although no measurement has been performed.

### **4.2.5 Linear Polarization Resistance Measurements**

LPR measurements were performed on freely exposed DSA and TSA samples on a weekly basis. The measurements were performed in the same manner as described in Section 4.1.5.

### **4.2.6 Polarization Curves**

Polarization curves were obtained on DSA and TSA samples after 61 days of exposure. Cathodic polarization curve was obtained on freely exposed CS sample towards the end of exposure period. A portable GAMRY machine was used to obtain the curves. The polarization curves of the DSA and TSA samples were performed by polarizing the samples from -200 mV vs. OCP to approximately -450 mV Ag/AgCl. This was approximately the same range as for the samples for the exposure at elevated temperatures (-500 mV SCE). The cathodic polarization curve of the CS sample was performed by polarizing from OCP to approximately -1100 mV Ag/AgCl.

### **4.2.7 Visual Observations and cleaning with Nitric Acid**

Visual observations of the samples were performed immediately after the samples were dug out from the mud, to get an overall impression of the samples after the end of exposure. The samples were further transported in separate plastic bags to NTNU, Perleporten. The samples were rinsed in tap water in order to wash off mud which was attached to surfaces. They were further brushed with a dishwasher brush and rinsed in distilled water and dried. Visual observations were performed and pictures of the samples were taken with the cellphone. They were then washed in 65 % nitric acid (HNO<sub>3</sub>) for three minutes in order to try to get rid of possible corrosion products on the surfaces. They were further rinsed thoroughly in distilled water before they were placed to dry.

Visual observations of samples were performed after the cleaning process, in order to detect possible signs of significant degradation, coating failure, various forms for microorganisms or faults.

### **4.2.8 Surface and Cross Section Analysis**

The preparation and cross section analysis were performed in the same manner as described in Section 4.1.9.

The following samples were included in the cross section analysis:

- Unexposed DSA and TSA samples.
- Galvanic coupled DSA and TSA samples.
- Polarized DSA and TSA samples.
- Freely exposed DSA and TSA samples.



---

## Chapter 5

# Electrochemical Results - Exposure at Elevated Temperatures

The electrochemical results from exposure at elevated temperatures are presented in this chapter. The results have been divided into sections in order to keep a simple overview over them. The OCPs are presented in Section 5.2. The Galvanic Coupled Potentials are presented in Section 5.3. Galvanic Currents are presented in Section 5.4. Linear Polarization Resistance measurements and Polarization Curves are presented in respectively Section 5.5 and Section 5.6.

All potentials have been converted to mV SCE. This involves subtracting 45 mV from potentials in the 80°C container which was performed with a Ag/AgCl reference electrode. A small difference between the SCE reference electrodes meant that it was added 2 mV to the potentials of the 22°C container. The reference electrode potentials were checked and compared with each other using the setup at Corrosion Lab, prior and post exposure. Negligible differences (<2mV) were observed post exposure.

The excel function "Moving Average" has been used on data in order reduce the amount of fluctuating behavior in the graphs. The selected interval for moving average was 30. This straightens the curves and it becomes easier to see the difference, especially on Galvanic Current Measurements and Polarization Curves. It has been checked thoroughly that this function has not manipulated the results, by plotting both graphs with and without Moving Average and comparing them. All graphs that are presented, have been designed using "Moving Average".

In order to document the effect of pH on the electrochemical results, the pH measurements are included in Section 5.1. The times where sea water was substituted in the containers are also included in the Section 5.1, since the pH of the containers are directly related to the replacement of seawater.

Data loss occurred because of faults with the program Corrosion Lab Datalogger. Data loss happened for all experiments at day 14.84 to 15.54 (17 hours), day 31.5 to 31.83 (8 hours), day 36.82 to 37.98 (28 hours) and day 38.69 to 38.82 (3 hours). This is represented by as straight lines in the graphs.

The times when SW was replaced with fresh SW on all containers is marked with a black arrow in the Figures, while the times when SW was replaced only in the 80°C container is marked with a red arrow in the Figures.

The Polarization Curves were recorded after 63 days, while the exposure period for all experiments was 65 days.

## 5.1 pH measurements and Replacement of Seawater

This section presents the pH measurements and when replacement of seawater was performed. Figure 5.1 shows the pH measurements of the seawater in the containers.

Most of the pH measurements for the 22°C container are stable at approximately 7.9 to 8.1 throughout the exposure period. The pH measurements for 53°C container show a slightly decrease from day 1 to day 10. However, most of the pH measurements for 53°C container are stable within a range 8.2 to 8.4 from day 11 throughout the exposure period. pH measurements of the 83°C container show declining pH up until replacement of seawater. A small increase is observed after one day of exposure in replaced seawater (day 10 and 11, day 36 and 37 and day 59 and 60), before the pH decreases.

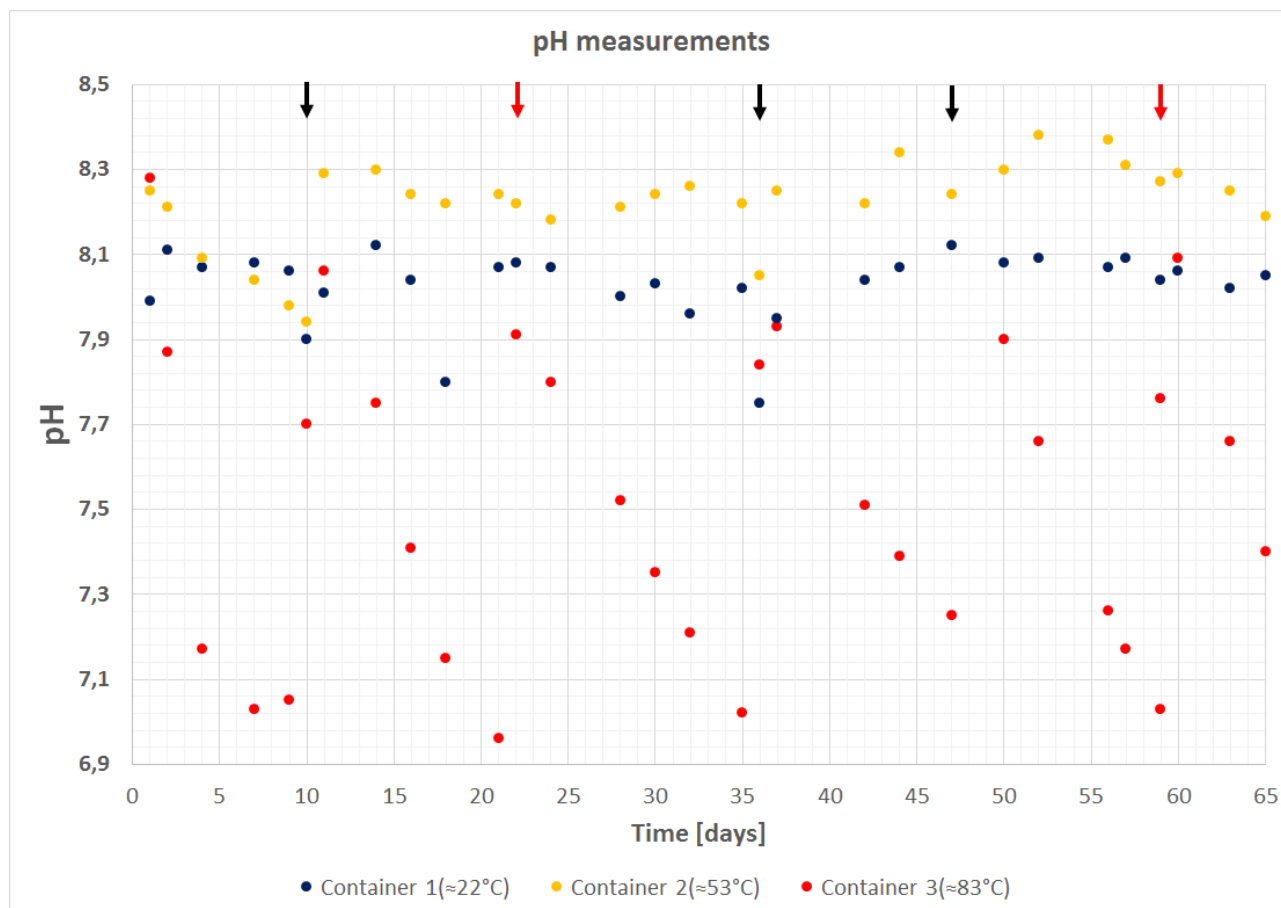


Figure 5.1: pH measurements of containers throughout exposure period. The arrows show when SW was replaced in the containers (Black = All containers, Red = 80°C container).

Table 5.1 presents the exact times when natural SW was replaced in the containers. The temperature fell to approximately 75°C for some minutes after replacement of SW in 83°C container was performed. pH of the fresh natural seawater was measured to be within a range of approximately 7.8 to 8.0.

Table 5.1: Exact times when replacement of natural seawater was performed.

Time [days]	Container		
	22°C	53°C	83°C
9.8	X	X	X
21.7			X
35.8	X	X	X
46.8	X	X	X
58.8			X

Figure 5.1 shows that the pH in 80°C container are affected by the replacement of seawater,

since pH of "new" natural SW is approximately 7.8 - 8.0. An increase in pH can also be observed on measurements performed one day after SW replacement on the 80°C container. pH was however not always measured one day after replacement.

## 5.2 Open Circuit Potentials

Figure 5.2 shows the OCP measurements of freely exposed DSA and TSA samples at all temperatures. The times when SW was replaced with fresh SW on all containers are marked with black arrows, while the times when SW was replaced only in the 80°C container are marked with red arrows. All TSA and DSA samples at all temperatures experience a rapid decrease in potential during the initial days of exposure. The samples exposed at 50 and 80°C decrease and reach their most negative potentials during the initial day of exposure, while the DSA and TSA samples exposed at 22°C reach their most negative potentials at day 2 and 3, respectively. The potentials on samples exposed at 80°C increase significantly from below -1300 mV SCE to above -1000 mV SCE during the initial 3 days of exposure. The potentials on samples exposed at 80°C decrease significantly during the first day after SW is replaced at all times due to pH change in the container (Figure 5.1), before they increase slowly up until next replacement. The samples exposed at 50°C are also affected by the replacement of SW, while the samples exposed at 22°C are not affected by SW replacement. The trend is that all potentials increase throughout exposure period, neglecting the sudden decreases from the times when SW was replaced.

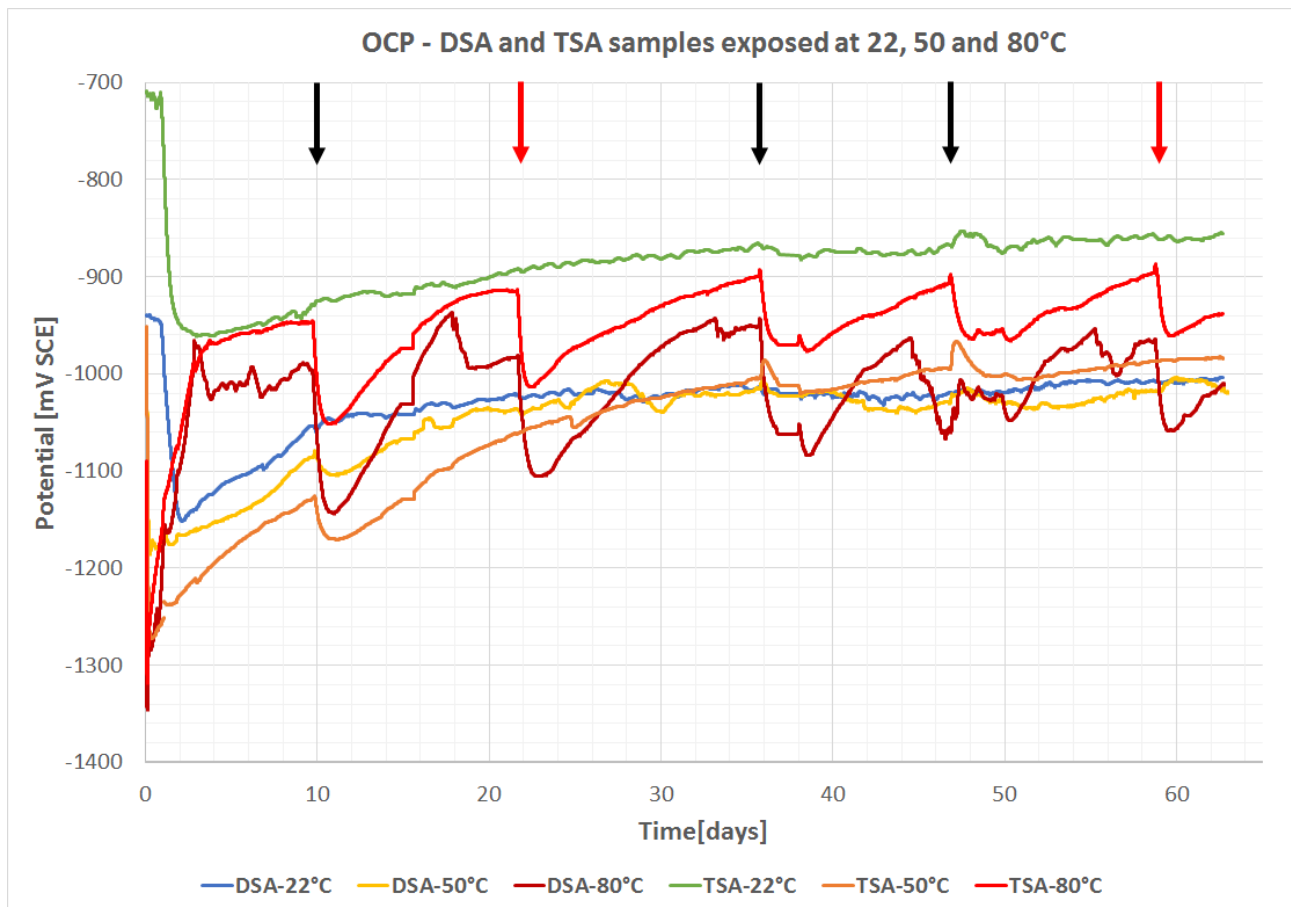


Figure 5.2: OCP of freely exposed DSA and TSA samples at all temperatures throughout exposure period. The arrows show when SW was replaced in the containers (Black = All containers, Red = 80°C container).

Figure 5.3 shows the OCP measurements of freely exposed Anode samples at all temperatures.

The anode samples at 50 and 80°C experience a rapid decrease in potential during the initial day of exposure. The OCP of anode sample at 22°C shows apparently lots of noise. In the start of exposure this was believed to be a result from bad connections or fault in the datalogger cable. The apparent noise has been attempted rectified, but it appear like the measurements are correct. It appears like the potential moves within a certain range for the anode samples.

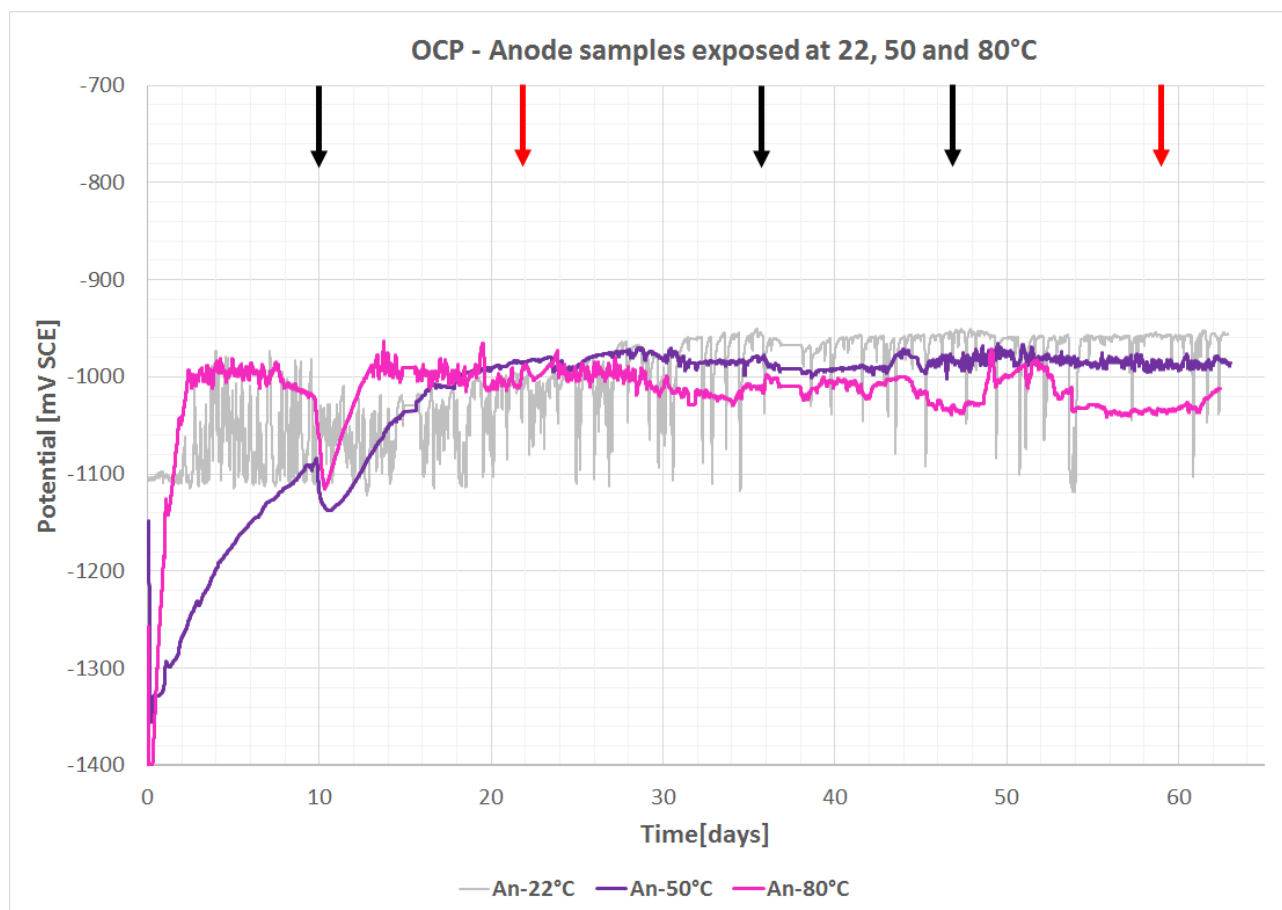


Figure 5.3: OCP of freely exposed Anode samples at all temperatures throughout exposure period. The arrows show when SW was replaced in the containers (Black = All containers, Red = 80°C container).

Table 5.2 shows the initial OCP i.e. the lowest potential during the first three days of exposure vs. the end OCP after 63 days of exposure. The values are taken from moving average values which means that the initial potentials are less/slightly less compared with the potentials listed in this table. The end potentials for the 80°C samples are taken from the pH was 7.6, and should be slightly less for a pH value at 8 compared with the results in the listed table.

The table shows that increased temperature gives more negative OCP initially, and that all OCP are increasing throughout exposure period.

Table 5.2: OCP development during the exposure period for all samples at all temperatures.

Sample	OCP [mV SCE]					
	Initial (Day 1-3)			End (Day 63)		
	22°C	50°C	80°C	22°C	50°C	80°C
DSA	-1150	-1185	-1345	-1004	-1020	-1010
Anode	-1100	-1350	-1445	-955	-985	-1010
TSA	-960	-1270	-1320	-855	-985	-940

### 5.2.1 The effect of pH

Figure 5.4 shows the effect of pH at OCP measurements of DSA and TSA samples at 80°C. Increased pH gives more negative potential and vice versa.

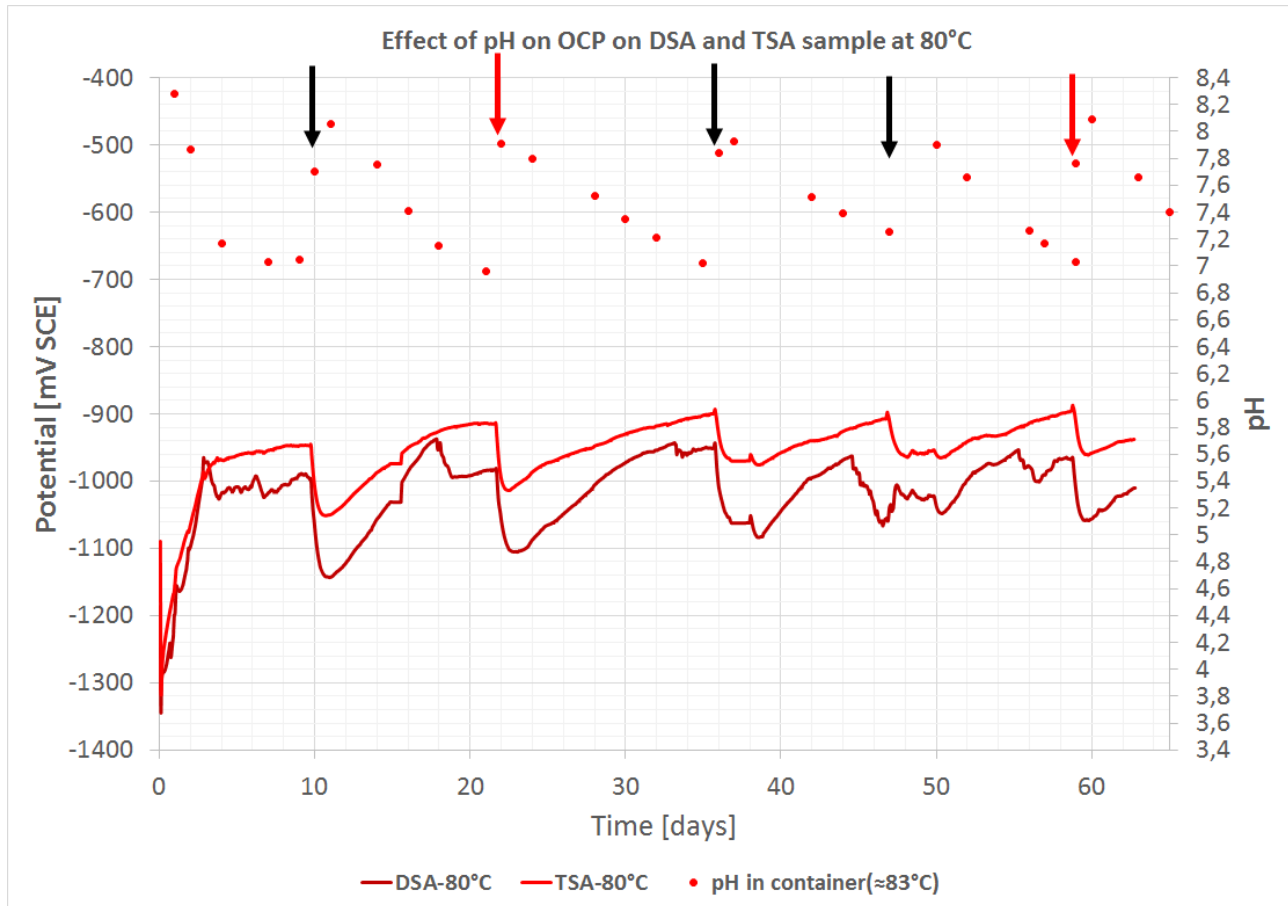


Figure 5.4: OCP of DSA and TSA samples at 80°C and pH measurements of the 80°C container throughout the exposure period. The arrows show when SW was replaced in the containers (Black = All containers, Red = 80°C container).

## 5.3 Galvanic Coupled Potentials

This section presents the Galvanic Coupled Potentials. These measurements were originally not part of the measurement setup, but were included after approximately 32 days of exposure. Due to limited amount of Corrosion Lab Datalogger channels, the galvanic coupled potential of Anode samples were not measured.

Figure 5.5 shows the galvanic coupled potentials of DSA and TSA samples at all temperatures from day 32 throughout exposure period. All coupled DSA samples show potentials more negative compared with the coupled TSA samples. Increased temperature gives more positive potentials for all couplings. The couple potentials are fairly stable throughout exposure period, but are slightly increasing. The coupled DSA sample at 50°C fluctuates between the coupled DSA samples at 22 and 80°C.

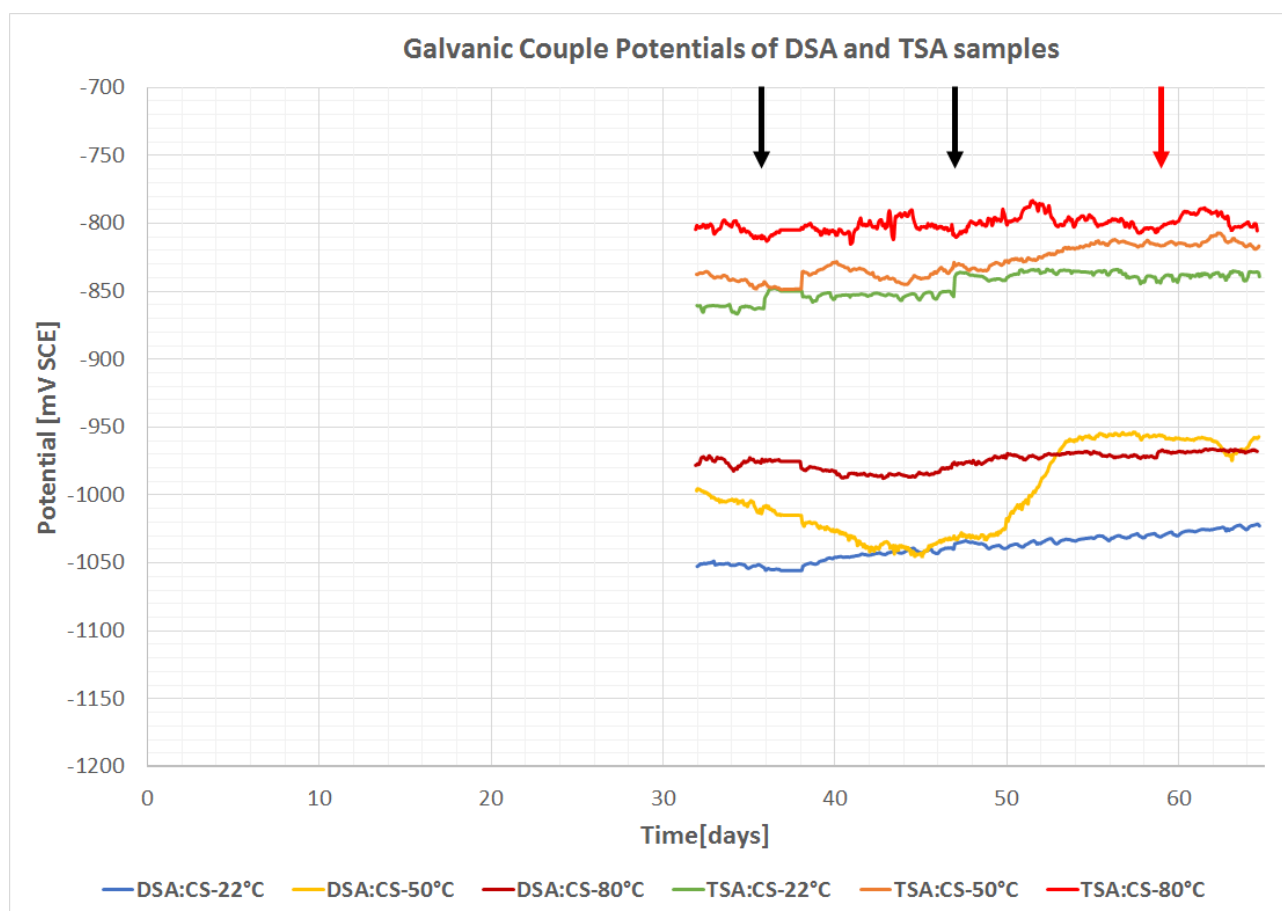


Figure 5.5: Galvanic couple potentials of DSA and TSA sample at all temperatures throughout the exposure period. The arrows show when SW was replaced in the containers (Black = All containers, Red = 80°C container).

Table 5.3 shows the development in Couple Potentials from day 32 throughout exposure period. The Couple Potentials are increasing slightly throughout exposure period. The galvanic couple potentials for the DSA samples are approximately 140 to 200 mV more negative compared with the coupled TSA samples.

Table 5.3: Galvanic Couple Potential development during the exposure period for samples at all temperatures.

Sample	Galvanic Couple Potential [mV SCE]					
	Middle (day 32)			End (Day 65)		
	22°C	50°C	80°C	22°C	50°C	80°C
DSA:CS	-1050	-995	-980	-1020	-960	-970
TSA:CS	-860	-840	-805	-840	-820	-800

### 5.3.1 The effect of pH and replacement of seawater

The effect of pH change in the 80°C container does not seem to affect the Galvanic Coupled Potentials exposed at 80°C. The effect of SW replacement in the 22°C container at day 36 and 47 is however slightly detectable on the 22°C TSA sample in Figure 5.5. A small increase in potential is slightly detectable at the time of SW replacement.



## 5.4 Galvanic Currents

This section presents the Galvanic Currents. The current densities have been calculated using the exposed surface areas of DSA, TSA and Anode samples which are approximately  $0.0038 \text{ m}^2$ , based upon an average exposed sample diameter  $\varnothing$  of approximately  $0.022 \text{ m}$ . The area ratio between the samples and CS-cubes have been calculated to be approximately  $0.63$ . Since the Anode sample at  $22^\circ\text{C}$  was coupled to a slightly bigger CS-cube, the area ratio for this connection was calculated to be approximately  $0.44$ . The y-axis on all graphs have been scaled from  $0$  to  $1000 \text{ mA/m}^2$ , so that differences between the graphs towards the end of exposure are detectable. However, current density values above  $1000 \text{ mA/m}^2$  are included to the top right position. This shows the high current densities that were measured in the beginning of exposure.

Initial current densities for the galvanic coupled TSA sample at  $80^\circ\text{C}$  are removed due to contact error and noise. Some current density values for the coupled DSA sample at  $22^\circ\text{C}$  were removed due to contact error and noise towards the end of the exposure.

Figure 5.6 shows Galvanic Currents of coupled DSA, TSA and Anode samples at all temperatures throughout the exposure period. The figure shows initially very high current densities which are decreasing throughout exposure. Increased temperature seems to give increased current densities initially, which however are decreasing rapidly. The current density is highest for the anode sample at  $80^\circ\text{C}$  at the end of exposure period, while the anode sample at  $50^\circ\text{C}$  has least current density at the end of exposure period.

Small peaks can be observed at the times when SW was replaced in the containers.

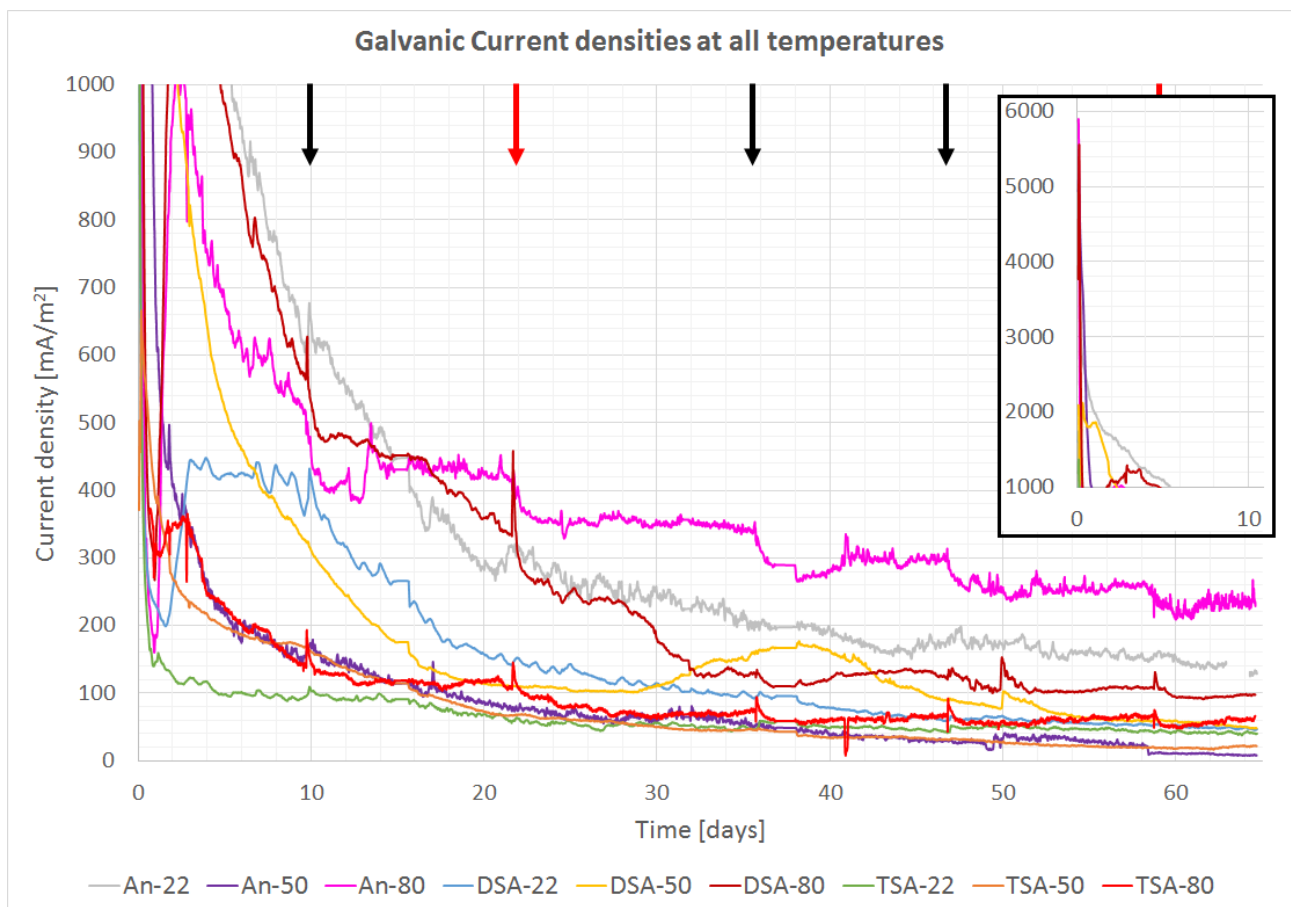


Figure 5.6: Galvanic Currents of Coupled DSA, TSA and Anode samples at all temperatures throughout the exposure period. The arrows show when SW was replaced in the containers (Black = All containers, Red =  $80^\circ\text{C}$  container).

Table 5.4 shows the development in Galvanic Currents throughout exposure period. The initial galvanic current density is the maximum current density detected on the coupled sample, while the end galvanic current density is the end current density at the end of the exposure period (day 65).

No significant difference in initial current density is spotted between the galvanic coupled samples at 22 and 50°C. It seems like the galvanic coupled samples at 80°C exhibit highest current densities in the beginning of exposure.

TSA:CS samples have lowest current densities at the end of exposure, while Anode:CS samples have overall higher current densities at the end. The DSA:CS samples have current densities in the range in between or closer to the TSA:CS samples.

The effect of temperature on the end current densities is less significant between 22 and 50°C, while the coupled samples at 80°C have higher current densities towards the end.

Table 5.4: Galvanic Current densities on coupled DSA, TSA and Anode samples during the exposure period at all temperatures.

Sample	Galvanic Currents from Samples [ $\text{mA}/\text{m}^2$ ]					
	Initial (day 1)			End (Day 65)		
	22°C	50°C	80°C	22°C	50°C	80°C
DSA:CS	1700	2100	5500	46	48	98
TSA:CS	1350	670	>372*	40	22	66
Anode:CS	5200	5100	5900	130	8	230

\* = Loss of data initially, due to contact error.

#### 5.4.1 The effect of pH and replacement of seawater

The effect of pH change in the 80°C container from approximately 7 to 8 at day 10 when SW replacement was performed seems to slightly decrease the current densities of the coupled DSA and Anode samples. This can be seen in Figure 5.6. The effect is however less detectable for the coupled TSA sample. Small disturbances in the form of immediate increases can be seen clearly on the curves on Figure 5.6, at day 10 and 22. They are still visible, but however less at day 36, 47 and 59.

The effect of pH on the 22°C and 50°C containers is not visible on the measurements, due to overall stable measurements. Small disruptions in the form of immediate increased current densities are however visible at some samples at the time of SW replacement.

## 5.5 Linear Polarization Resistance measurements

The LPR measurements of the DSA sample at 22°C has throughout the exposure period been quite easy to measure, since the potential drop have stabilized within a certain range. The potential drop when doing LPR measurements of the samples at 50°C and 80°C has not stabilized in the same manner, making it hard to select the potential drop for the calculation. One LPR measurement at day 43 of the samples showing the disruptions in potential drop is presented in Figure 5.7.

Figure 5.7 shows the disruptions in potential drop of the DSA samples exposed at 50°C and 80°C. First sample is the DSA sample exposed at 50°C, polarized in cathodic and then the anodic direction, while the second measurement is the DSA sample exposed at 80°C, polarized in cathodic and then the anodic direction. Each measured value was obtained in a frequency of 10 seconds and the resistance was 1000 Ω. The potential drop is fluctuating between negative and positive values making it demanding to select values. The selected values for the 80°C sample in this instance were -2 mV and 2 mV for respectively the cathodic and anodic direction.

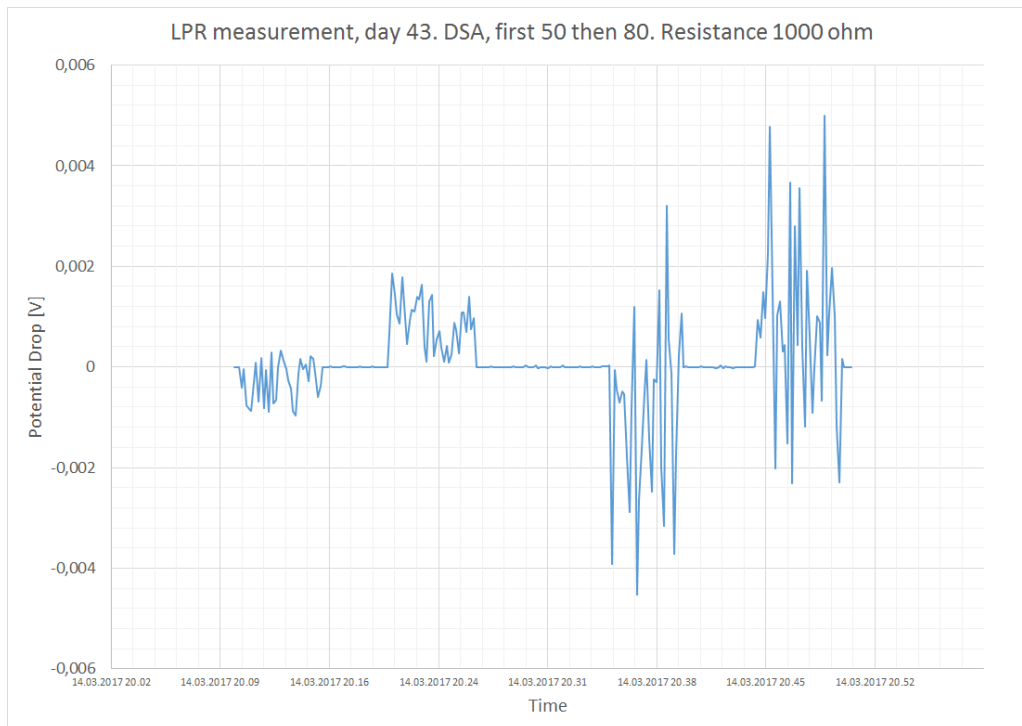


Figure 5.7: LPR measurement of the 50 and 80°C DSA samples at day 43 showing fluctuating behavior.

The fluctuating behavior is present on the LPR measurements of the DSA samples at 50°C and 80°C, from approximately day 8 throughout the exposure period. This makes the results less reliable.

A defect potentiostat made the LPR measurement of DSA sample at 22°C at day 29 incorrect and is therefore excluded from the results. The results from the measurements are plotted as  $1/R_p$ , so that the trend corresponds with the corrosion rate according to Equation 2.9.

Figure 5.8 shows decreasing inverse avg. Polarization Resistance ( $1/R_p$ ) values, meaning that the corrosion rates are decreasing for DSA samples at all temperatures throughout the exposure period.  $1/R_p$  is highest for the freely exposed DSA sample at 22°C, while  $1/R_p$  for the sample exposed at 50°C is slightly lower compared to the DSA sample at 80°C.

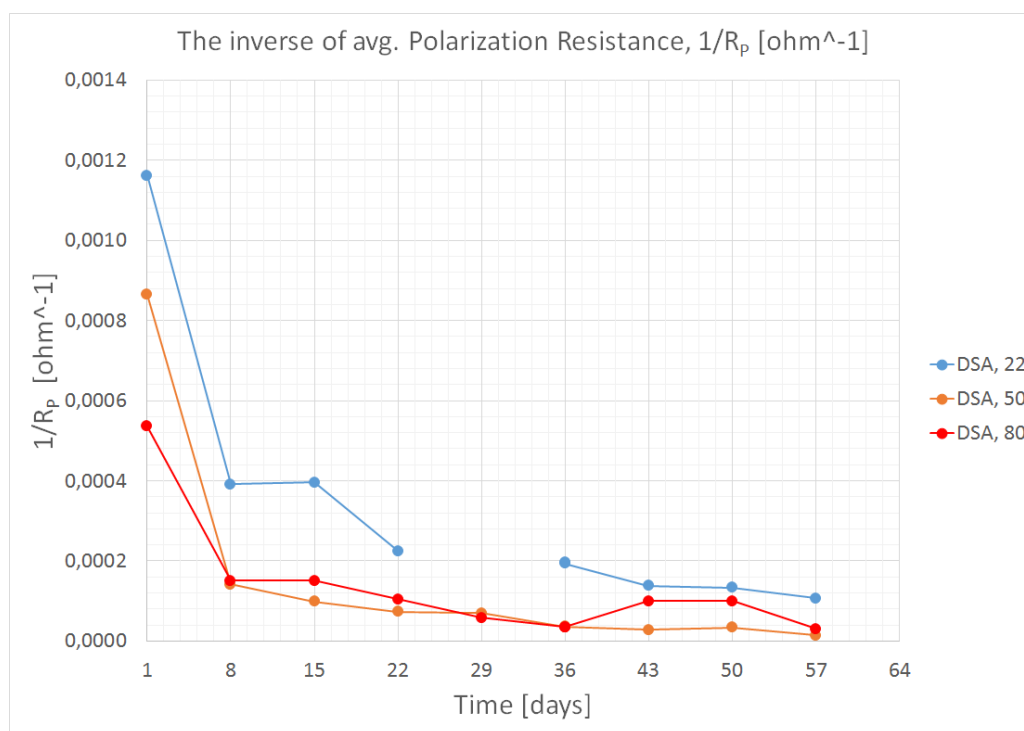


Figure 5.8: The results from LPR measurements of DSA samples at all temperatures, plotted as  $1/R_p$ .

Two LPR measurements were performed at day 36, one before SW replacement and one after SW replacement. This was done to see if SW replacement had a major influence on the measurements. Any difference was not detected.

Table 5.5 shows the  $R_p$  values in Cathodic and Anodic direction gained from the measurements. The table shows significant differences in  $R_p$ , depending on the polarized direction.

Table 5.5:  $R_p$  values for both cathodic and anodic direction and computed average value.

Day	Polarization Resistance values, $R_p$ [ohm]								
	DSA, 22°C			DSA, 50°C			DSA, 80°C		
	$R_p$ , Cath.	$R_p$ , Anod.	$R_p$ , Avg.	$R_p$ , Cath.	$R_p$ , Anod.	$R_p$ , Avg.	$R_p$ , Cath.	$R_p$ , Anod.	$R_p$ , Avg.
1	1320	402	861	1102	1213	1157	2006	1723	1864
8	2591	2519	2555	7605	6579	7092	6515	6757	6636
15	2786	2270	2528	9615	10753	10184	6250	7018	6634
22	5405	3472	4439	16529	10753	13641	10753	8299	9526
29				13072	15385	14228	14286	20000	17143
36	6667	3571	5119	36364	18182	27273	20000	36364	28182
36	6667	3636	5152	36364	20000	28182	36364	20000	28182
43	10000	4444	7222	50000	20000	35000	10000	10000	10000
50	10000	5000	7500	40000	20000	30000	10000	10000	10000
57	13333	5405	9369	100000	40000	70000	33333	33333	33333

## 5.6 Polarization Curves

This section presents the Polarization Curves that were recorded on samples at day 1 and after 63 days of exposure. Anodic polarization curves from OCP to approximately -600 mV SCE were recorded after 1 day of exposure on DSA samples at all temperatures.

Polarization Curves from -200mV vs. OCP to approximately -500 mV SCE were recorded on the following samples at all temperatures at day 63 of exposure:

- Freely exposed DSA samples
- Freely exposed TSA samples
- Freely exposed Anode samples

As previously stated in the beginning of this Chapter, the excel function "Moving Average" with a selected interval of 30, has been applied on the Polarization Curves recorded with a Gamry reference 600 at day 63. This leads to smooth curves that are desirable. This means that the first 29 measurements are missing, which removes the first 5 mV from -200 mV vs OCP in anodic direction from the plot. The function also causes the curve to drag slightly to the right in areas where many measurements differ from its original path.

OCPs measured prior to recording polarization curves show a slightly less OCP compared with what the polarization curves show. The difference is in a range of approximately 2 to 30 mV. The OCP measured prior to recording the Polarization Curves are generally more realistic and has been used if discussing OCPs, since it shows the more accurate OCP of samples at that point of exposure.

### 5.6.1 DSA, Anodic Polarization Curves at day 1

Figure 5.9 shows the anodic polarization curves recorded after one day of exposure.

Figure 5.9 shows that the samples have different OCPs. The OCPs of the samples at 22°C, 50°C and 80°C were measured to be -948, -1255 and -1205 mV SCE respectively, prior to the recording. Passive behavior is visible from approximately -1150 to -950 mV SCE on the DSA samples exposed at 50°C and 80°C. The figure shows that the transition zone between passive/active zone is reached at approximately -925 mV SCE, where all samples experience a rapid increase in anodic current density. The curves show a parabolic shape with increased applied potential. The current densities are highest and lowest for the 80°C and 22°C sample, respectively.

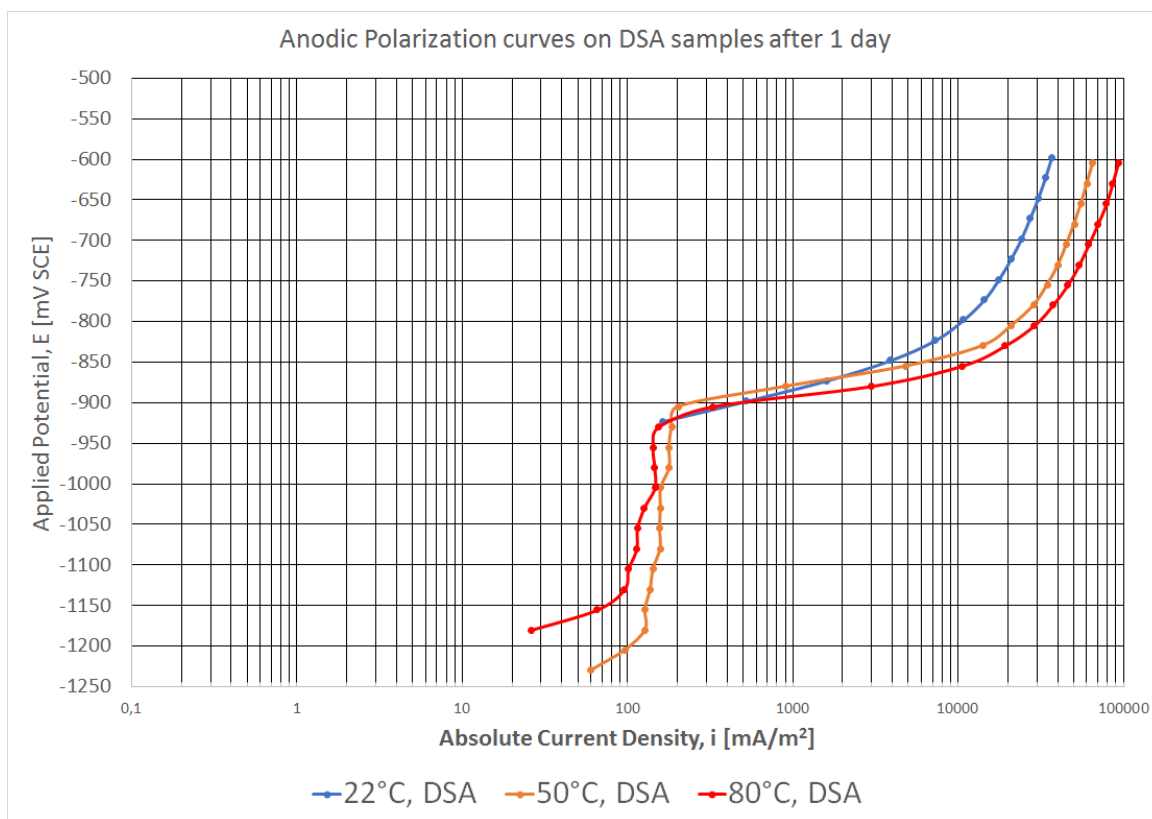


Figure 5.9: Anodic Polarization Curves recorded on DSA samples after one day of exposure.

### 5.6.2 DSA, Freely Exposed samples at day 63

Figure 5.10 shows the polarization curves recorded on freely exposed DSA samples at all temperatures after 63 days of exposure.

The OCPs of the samples at 22°C, 50°C and 80°C were measured to be -1007, -1017 and -1010 mV SCE respectively, before the recording started. The Polarization Curves show in general active anodic behavior above OCP. The freely exposed DSA sample at 22°C appears most anodically active from OCP to -800 mV SCE. It seems that some sort of passivating behavior is present at the freely exposed 80°C sample from OCP to -875 mV SCE. The cathodic curves appear quite similar at all temperatures.

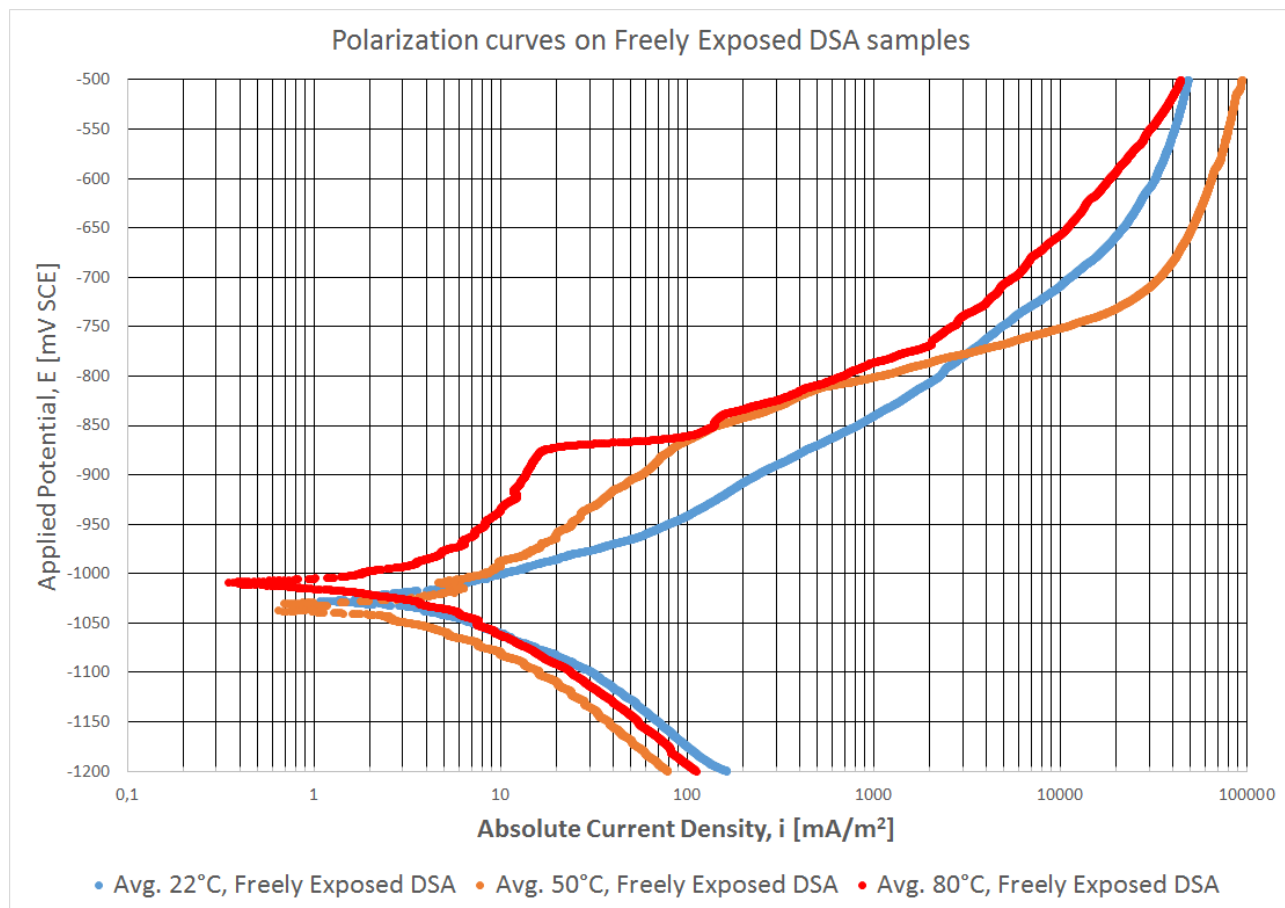


Figure 5.10: Recorded Polarization Curves on freely exposed DSA samples after 63 days.

### 5.6.3 TSA, Freely Exposed samples at day 63

Figure 5.11 shows the polarization curves recorded on freely exposed TSA samples after 63 days of exposure.

The OCPs of the samples at 22°C, 50°C and 80°C were measured to be -858, -979 and -938 mV SCE respectively, before the recording started. Figure 5.11 shows generally passive anodic behavior of the TSA samples. The 22°C sample shows active behavior from approximately -625 mV SCE. The placement of the curves show that the corrosion current density at OCP is highest for the TSA sample at 22°C, while it is lowest for the TSA sample at 50°C.

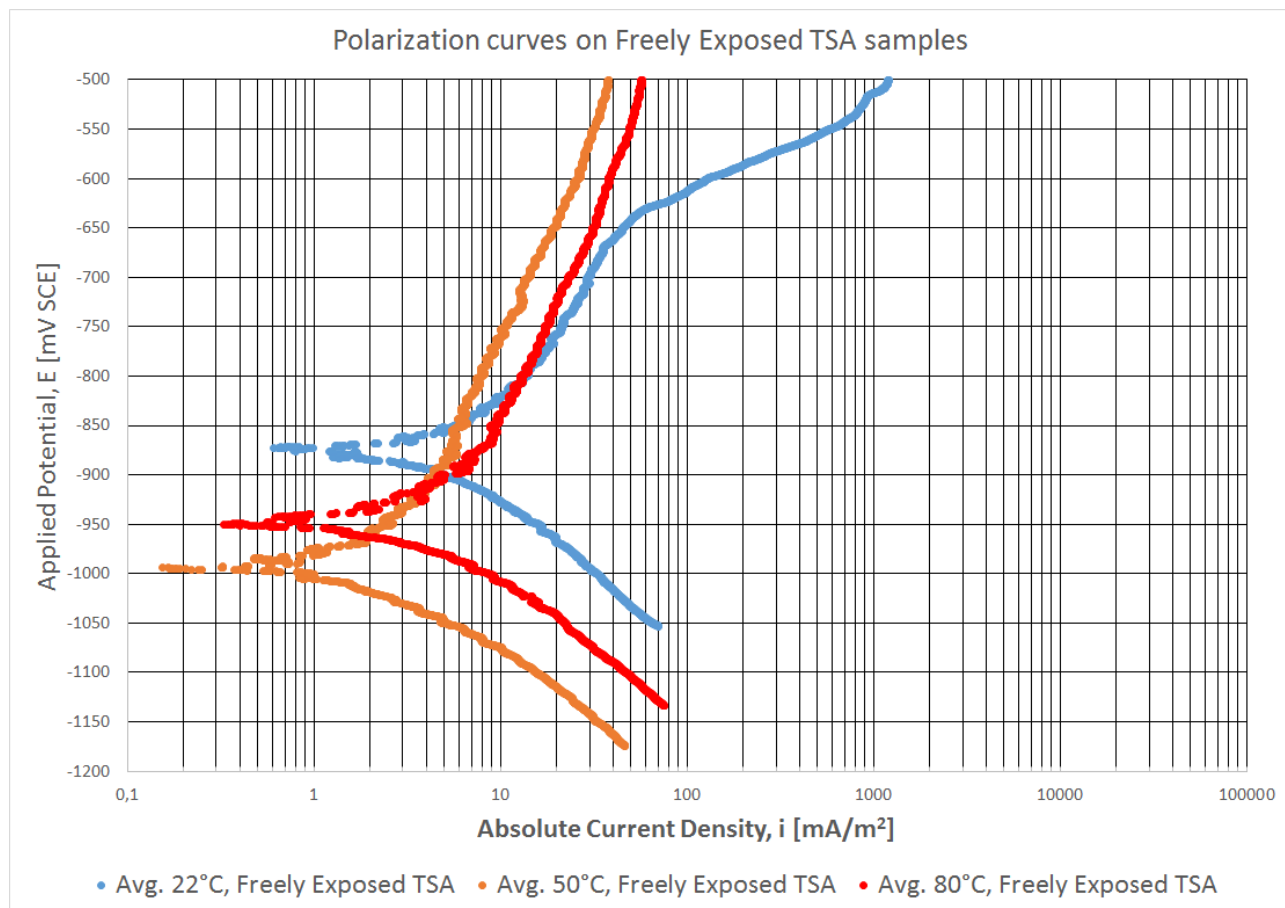


Figure 5.11: Recorded Polarization Curves on freely exposed TSA samples after 63 days.

### 5.6.4 Anode, Freely Exposed samples at day 63

Figure 5.12 shows the polarization curves recorded on freely exposed Anode samples after 63 days of exposure.

The OCPs of the samples at 22°C, 50°C and 80°C were measured to be -956, -982 and -1010 mV SCE respectively, before the recording started. Figure 5.12 shows generally active anodic behavior of the Anode samples. Signs of passive behavior are not present on the samples in the anodic direction. The cathodic curve on the 80°C sample is steeper at higher current density compared to the other two temperatures, indicating that the corrosion rate at OCP is higher for the 80°C sample. The placement of the curves and direction of the anodic and cathodic curves show that the corrosion current densities at OCP are increasing at elevated temperature.

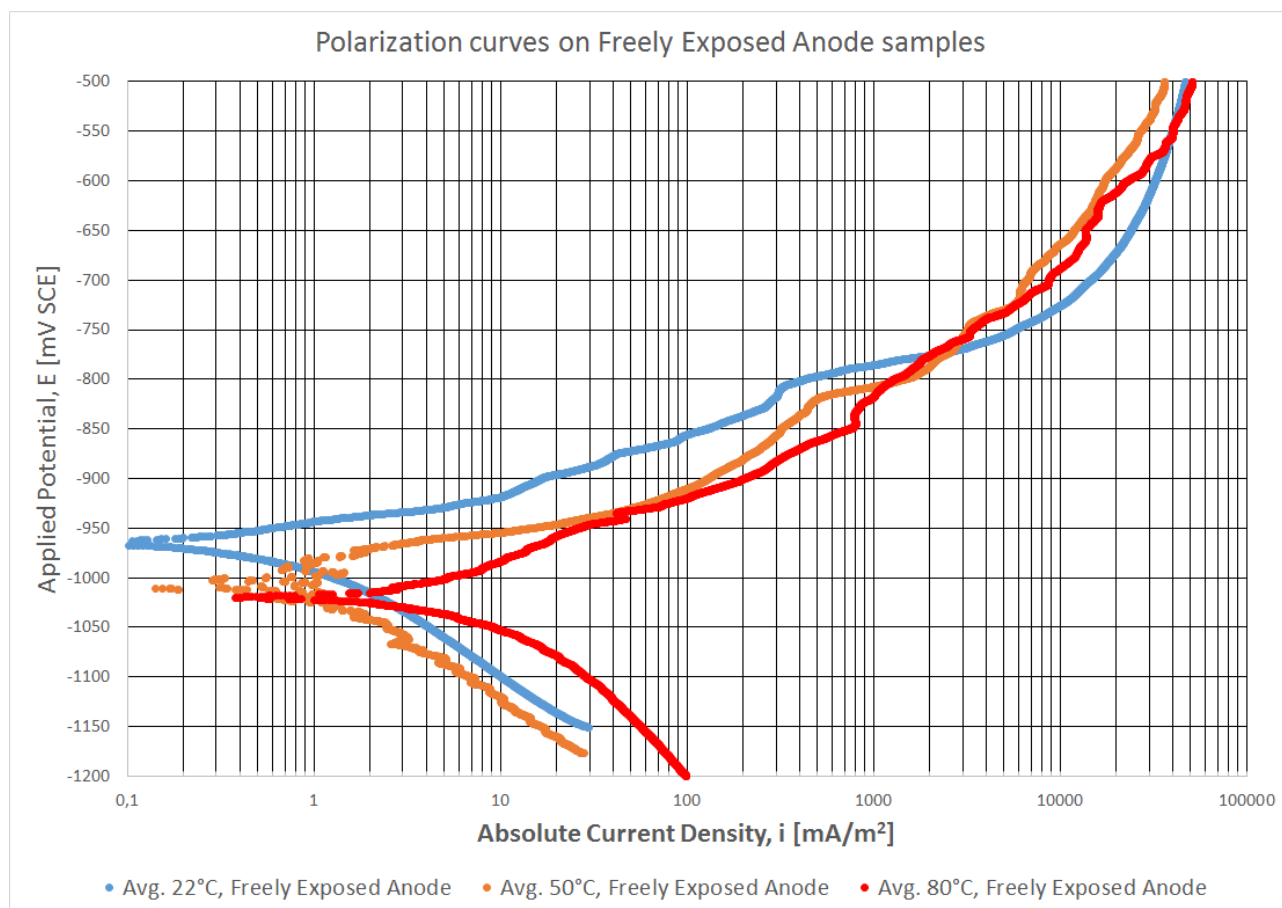


Figure 5.12: Recorded Polarization Curves on freely exposed Anode samples after 63 days.



### 5.6.5 22°C, Freely Exposed samples at day 63

Figure 5.13 shows a comparison of the polarization curves recorded on freely exposed samples at 22°C, after 63 day of exposure. It shows the different properties of the freely exposed samples, when exposed to 22°C.

Figure 5.13 shows that the DSA and Anode samples have similar active anodic behavior, while the TSA sample has passive anodic behavior. The OCP is most negative for the DSA sample, while it is most positive for the TSA sample. The placement of the curves shows that the self corrosion current densities are highest for the DSA and TSA sample, while it is less for the anode sample.

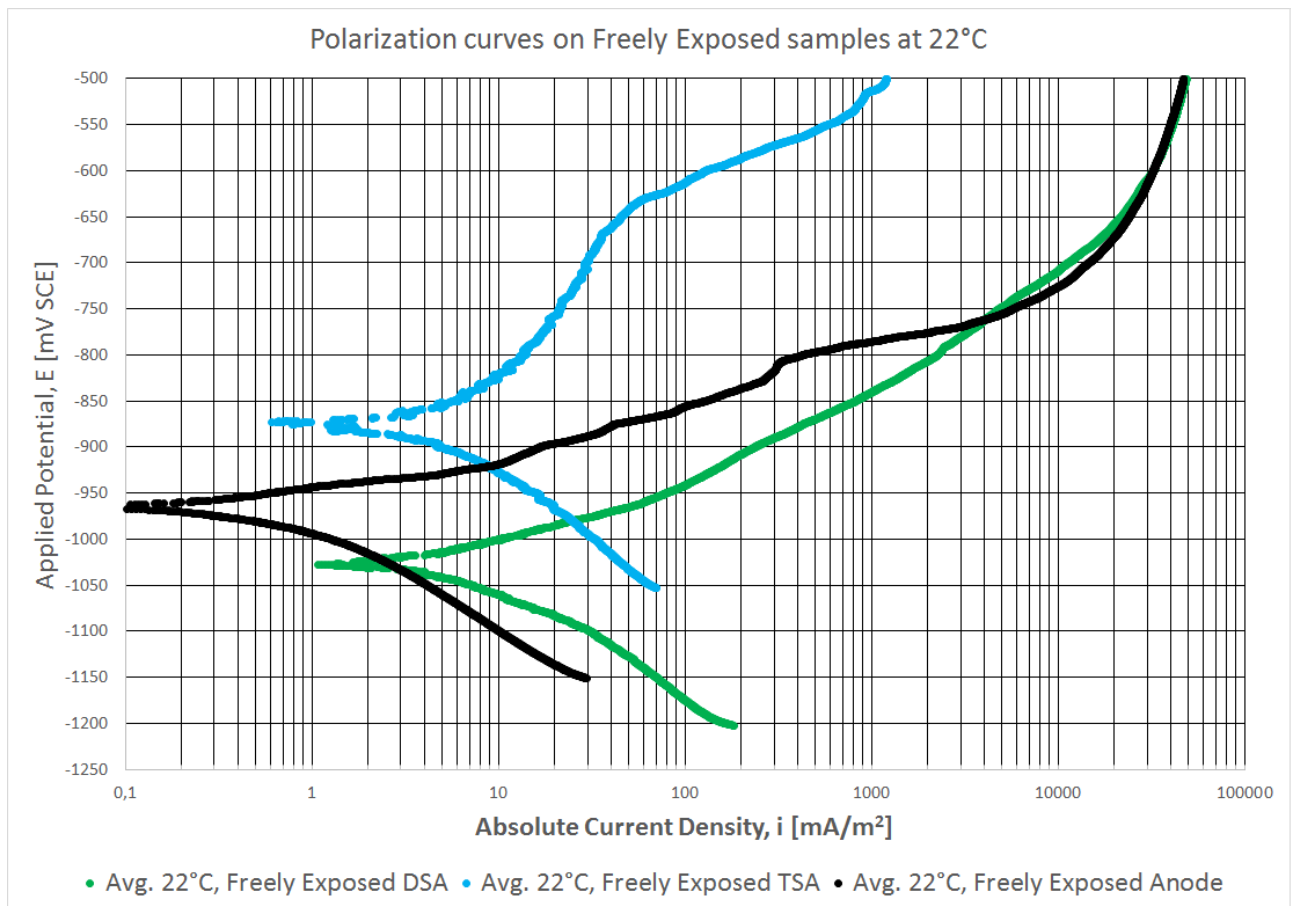


Figure 5.13: Recorded Polarization Curves on freely exposed samples at 22°C, after 63 days of exposure.

### 5.6.6 50°C, Freely Exposed samples at day 63

Figure 5.14 shows the polarization curves recorded on freely exposed samples at 50°C, after 63 day of exposure. It shows a comparison of the different properties of the freely exposed samples.

Figure 5.14 shows that the DSA and Anode samples have similar active anodic behavior, while the TSA sample has passive anodic behavior. The OCP is most negative for the DSA sample, while it is slightly more positive for the TSA sample compared with the Anode sample. The placement of the curves shows that the corrosion current densities at OCP are highest for the DSA sample, while it is less for the anode sample compared with the TSA sample.

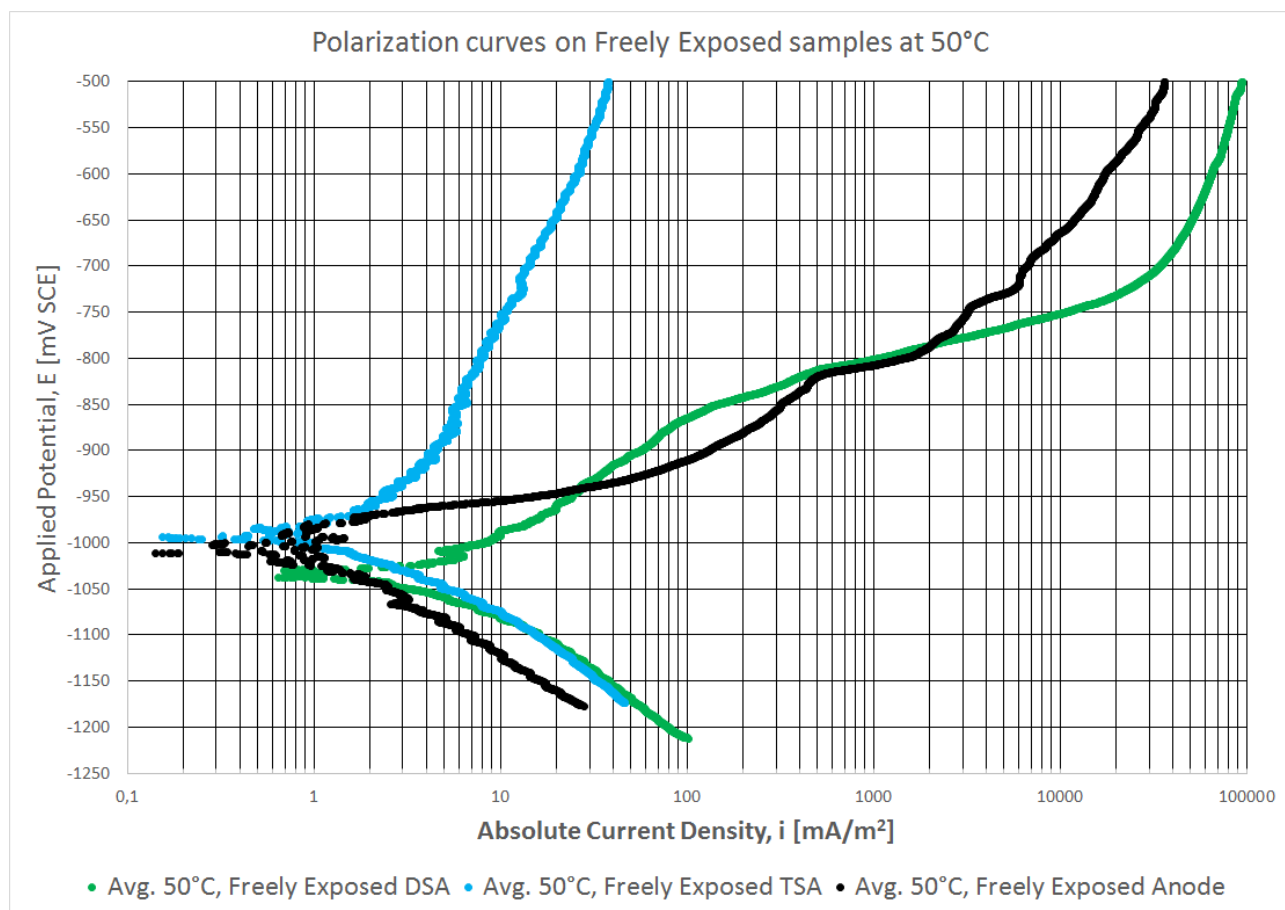


Figure 5.14: Recorded Polarization Curves on freely exposed samples at 50°C, after 63 days of exposure.

### 5.6.7 80°C, Freely Exposed samples at day 63

Figure 5.15 shows the polarization curves recorded on freely exposed samples at 80°C, after 63 day of exposure. It shows the different properties of the freely exposed samples, when exposed to 80°C.

Figure 5.15 shows that the Anode sample has active anodic behavior. The DSA sample shows passive anodic behavior up until approximately -825 SCE, and active anodic behavior from this point and up, while the TSA sample shows in general passive anodic behavior. The OCP is slightly more negative for the Anode sample compared with the DSA sample, while it is more positive for the TSA sample. The placement of the curves shows that the corrosion current densities at OCP are quite similar for all samples.

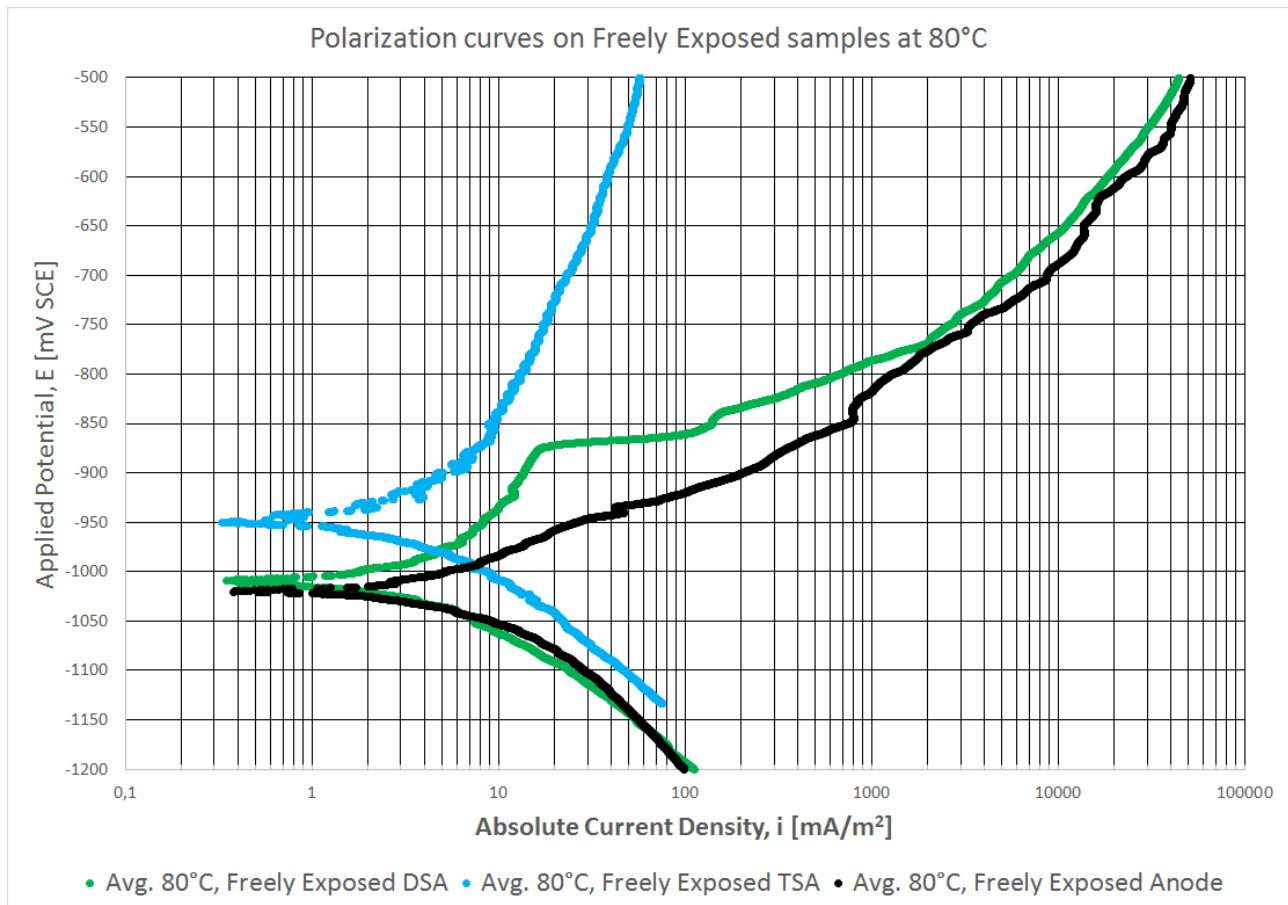


Figure 5.15: Recorded Polarization Curves on freely exposed samples at 80°C, after 63 days of exposure.

### 5.6.8 Summary - Polarization Curves

The graphical solutions as well as other properties are summarized in Table 5.6. The graphical solutions for the Polarization Curves, which includes OCP, corrosion current density and anodic and cathodic tafel constants are included in the Appendix Section. The graphical solutions for freely exposed samples at 22°C, 50°C and 80°C are included in Figure B.1, B.2 and B.3, in the Appendix section, respectively.

## 5.7 Corrosion Rates

The corrosion rates of freely exposed DSA samples are calculated from the LPR measurements of prior polarized DSA samples. They are calculated from avg. Polarization Resistance in both

cathodic and anodic direction which are listed in Table 5.5. The tafel slopes used in the calculation are however from the Polarization Curves from day 63 for freely exposed DSA samples, which are listed in Table 5.6. Stern Gearys Equation (2.9) and Corrosion Rate Equation (2.10) were used in the calculation. The physical data which were used for the calculation are listed in Table A.2 in the Appendix section. The calculation is based upon an average exposed surface of  $0.0038 \text{ m}^2$ . It is assumed that the DSA and TSA coatings have a porosity of  $\approx 10\%$ .

Figure 5.16 shows the calculated corrosion rates at OCP from LPR measurements throughout exposure. The results from day 63 are calculated from graphically solving the corrosion current density, since no LPR measurement was performed prior recording the polarization curves. The difference in corrosion rate from LPR and from graphically solving polarization curves appear to be small.

Figure 5.16 shows high corrosion rates at day 1, which are decreasing rapidly up until day 8. The corrosion rates are further decreasing slightly throughout exposure. The Figure shows slightly different trends compared to the LPR results in Figure 5.5, due to different anodic and cathodic tafel constants.

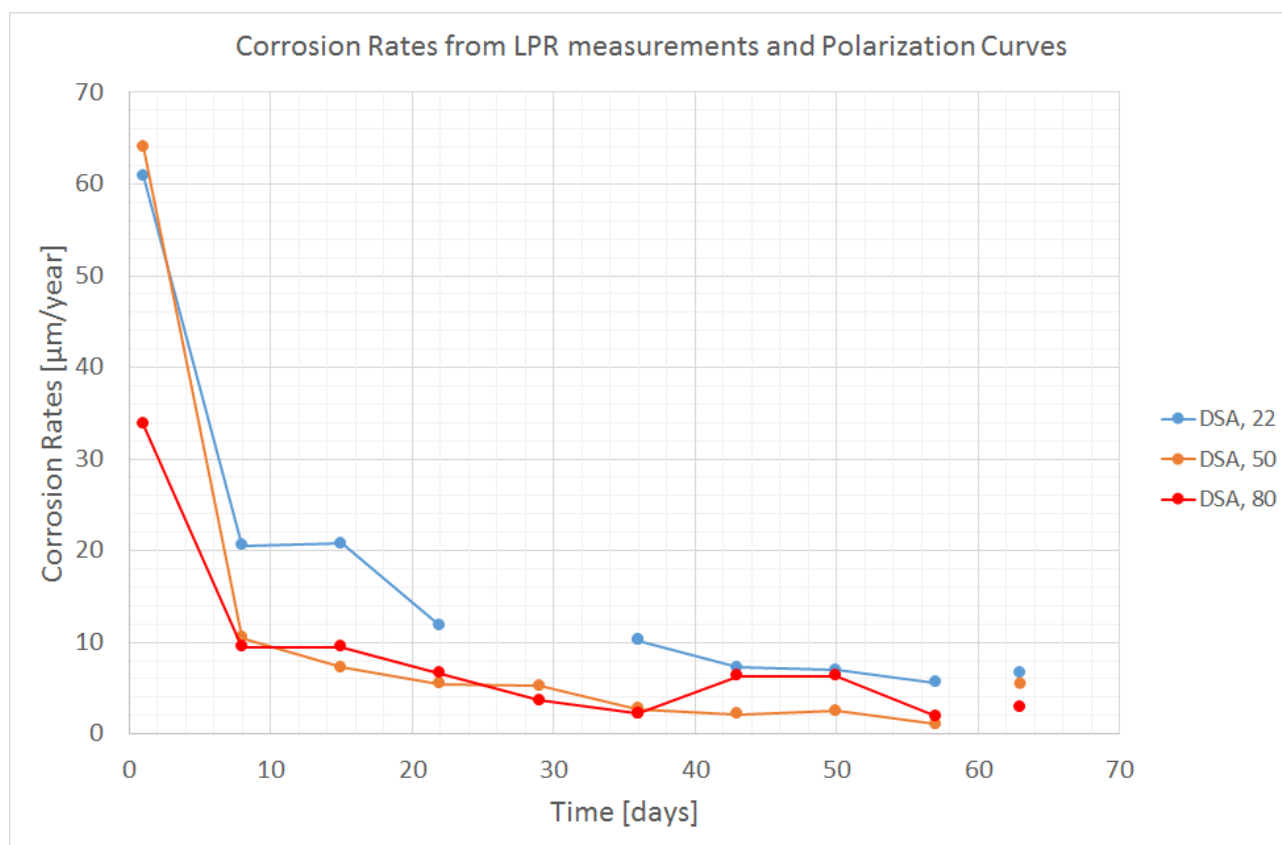


Figure 5.16: Corrosion rates from LPR on freely exposed DSA samples which were polarized at day 1. The three single points (day 63) are calculated from graphical solution of Polarization Curves.

## 5.8 Summary - Electrochemical Results

Table 5.6 shows a summary of the electrochemical properties for the freely exposed samples and galvanic coupled samples after 63 days at all temperatures. The total corrosion rates are assumed applicable for the galvanic coupled samples. They are calculated by adding the self corrosion rates with the corrosion rates from galvanic currents.

Table 5.6: Summary of electrochemical properties of freely exposed and coupled samples after 63 days.

	TSA			DSA			Anode		
	22	50	80	22	50	80	22	50	80
<b>Temperature [°C]</b>	22	50	80	22	50	80	22	50	80
<b>OCP [mV SCE]</b>	-858	-979	-938	-1007	-1017	-1010	-956	-982	-1010
<b>OCP Pol. Curv. [mV SCE]</b>	-878	-995	-948	-1028	-1037	-1012	-960	-1014	-1023
<b>Pitting Potential [mV SCE]</b>	-625	>500	>500	-1025	-1025	-875	-950	-950	-1000
<b>Anodic Behavior [Act., Pass., Act/Pass]</b>	Pass.	Pass.	Pass.	Act.	Act.	Act./Pass.	Act.	Act.	Act.
<b>Anodic Tafel Constant, ba [mV/dec]</b>	160	160	225	60	90	85	60	40	80
<b>Cathodic Tafel Constant, bc [mV/dec]</b>	-150	-95	-125	-80	-105	-80	-110	-95	-120
<b>Corr. Curv. Dens. Pol. Curv. [mA/m<sup>2</sup>]</b>	5.5	1.5	4	6	5	2.6	0.8	1	7
<b>Corr. Rate, at OCP; POL [µm/year]</b>	6.65	1.81	4.84	6.63	5.52	2.87	0.8	1	6.97
<b>Corr. Curv. Dens. LPR. [mA/m<sup>2</sup>]</b>	-	-	-	5.06*	0.96*	1.71*	-	-	-
<b>Corr. Rate, at OCP; LPR [µm/year]</b>	-	-	-	5.59*	1.05*	1.89*	-	-	-
<b>Couple Potential [mV SCE]</b>	-840	-820	-800	-1020	-960	-970	-	-	-
<b>Galv. Curr. Dens. [mA/m<sup>2</sup>]</b>	46	48	98	40	22	66	130**	8	230
<b>Galv. Corr. Rate. [µm/y]</b>	50.83	53.03	108.28	48.38	26.61	79.83	129.52**	7.97	229.14

\*) Based on LPR measurements of Prior Polarized DSA samples at day 57. \*\*) A slightly less area ratio.



---

## Chapter 6

# Electrochemical Results - Exposure in Mud

The electrochemical results from Mud Exposure are presented in this chapter. The results have been divided into sections in order to keep a simple overview over them. The OCPs are presented in Section 6.1. The Galvanic Coupled Potentials and Galvanic Currents are presented in Section 6.2. The results from polarizing the samples to -1.1 V vs. Ag/AgCl are presented in Section 6.3. Linear Polarization Resistance measurements and Polarization Curves are presented in respectively Section 6.4 and Section 6.5.

The excel function "Moving Average" has been used on data in order to reduce the amount of fluctuating behaviour in the graphs. The selected interval for moving average was 30. This straightens the curves and it becomes easier to see the difference, especially on Galvanic Current Measurements and Polarization Curves. It has been checked thoroughly that this function has not manipulated the results, by plotting both graphs with and without Moving Average and comparing them. All graphs that are presented, have been designed using "Moving Average".

A Ag/AgCl saturated KCl reference electrode was used to measure all potentials, which is why the potentials have the denomination [mV Ag/AgCl].

Data loss occurred on some tests because of power failure in Sintef SeaLab. This prevented one of the Corrosion Lab Datalogger boxes, which handled some of the channels, to start logging when the power was back. Since this was quickly discovered, it had limited impact on the results. It resulted however in loss of data from day 43.94 to day 44.02.

The polarization curves were recorded at day 61, and the total exposure period for all samples was 62 days.

## 6.1 Open Circuit Potentials

Figure 6.1 shows the OCPs of the the freely exposed samples embedded in mud.

The OCP of the DSA sample decreases in the beginning of exposure, before it increases further to approximately -910 mV Ag/AgCl at day 4 and is stable for 2 days. The potential decreases rapidly to approximately -1090 mV Ag/AgCl at day 10. The further development is that the potential increases steadily up until -980 mV Ag/AgCl at day 24. The potential is fairly stable throughout the exposure period.

The OCP of the TSA sample increases in the beginning of exposure. It drops from -740 to 920 mV Ag/AgCl and is fairly stable throughout the exposure period.

The OCP of the CS sample increases slowly from -732 to -709 mV Ag/AgCl throughout the exposure period.

Trends and observations that can be extracted from the graphs are that while the DSA potential decreases at the beginning, the TSA potential increases. The DSA sample increases in potential slightly later. They both drop significant in potential from -740 to -910 mV Ag/AgCl and from -910 to -1080 mV Ag/AgCl, for the TSA and DSA sample respectively. While the TSA sample is fairly stable throughout exposure (increasing slightly), the DSA sample increases to -970 mV Ag/AgCl and is later on fairly stable. The difference in potential between the DSA and TSA sample is within a range of approximately 50 to 90 mV from day 25 throughout the exposure period.

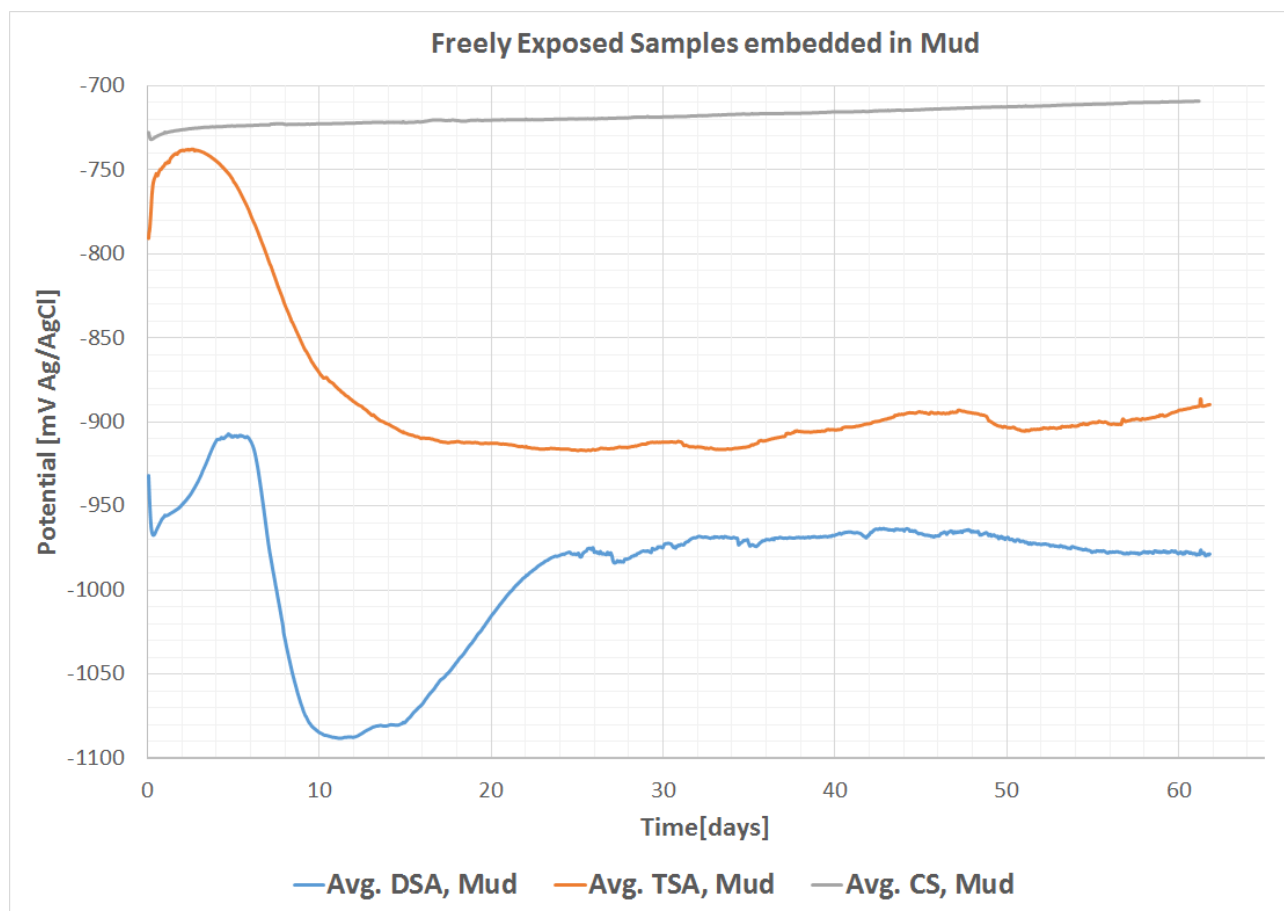


Figure 6.1: OCP of the freely exposed samples embedded in mud.



## 6.2 Galvanic Coupled Potentials and Currents

This section presents the Galvanic Coupled Potentials and Currents of the galvanic coupled samples in mud. The current density is calculated from the area of the DSA and TSA samples ( $0.0025 \text{ m}^2$ ). The area ratio between the samples are approx. 1:1 anyway, so the current density on the CS in theory should be similar with the current densities on the DSA and TSA samples. The logging of galvanic coupling potential was started one day after the tests started.

Figure 6.2 shows the galvanic couple potential and current density on the coupled DSA sample. The figure shows that the couple potential decreases rapidly from  $-906$  to  $-1076$  mV Ag/AgCl between day 1 and 6. It increases substantially from  $-1076$  to  $-950$  mV Ag/AgCl between day 6 and 18. The potential is fairly stable afterwards, but increases slowly throughout exposure. The end potential at day 62 is approximately  $-916$  mV Ag/AgCl.

The current density graph of the coupled DSA sample shows mirror like behaviour compared with the couple potential. It increases from  $6$  to  $42 \text{ mA/m}^2$  from day 2 to 5. It decreases to approximately  $10 \text{ mA/m}^2$  and is slowly decreasing throughout the rest of exposure. The end current density is approximately  $5.5 \text{ mA/m}^2$ .

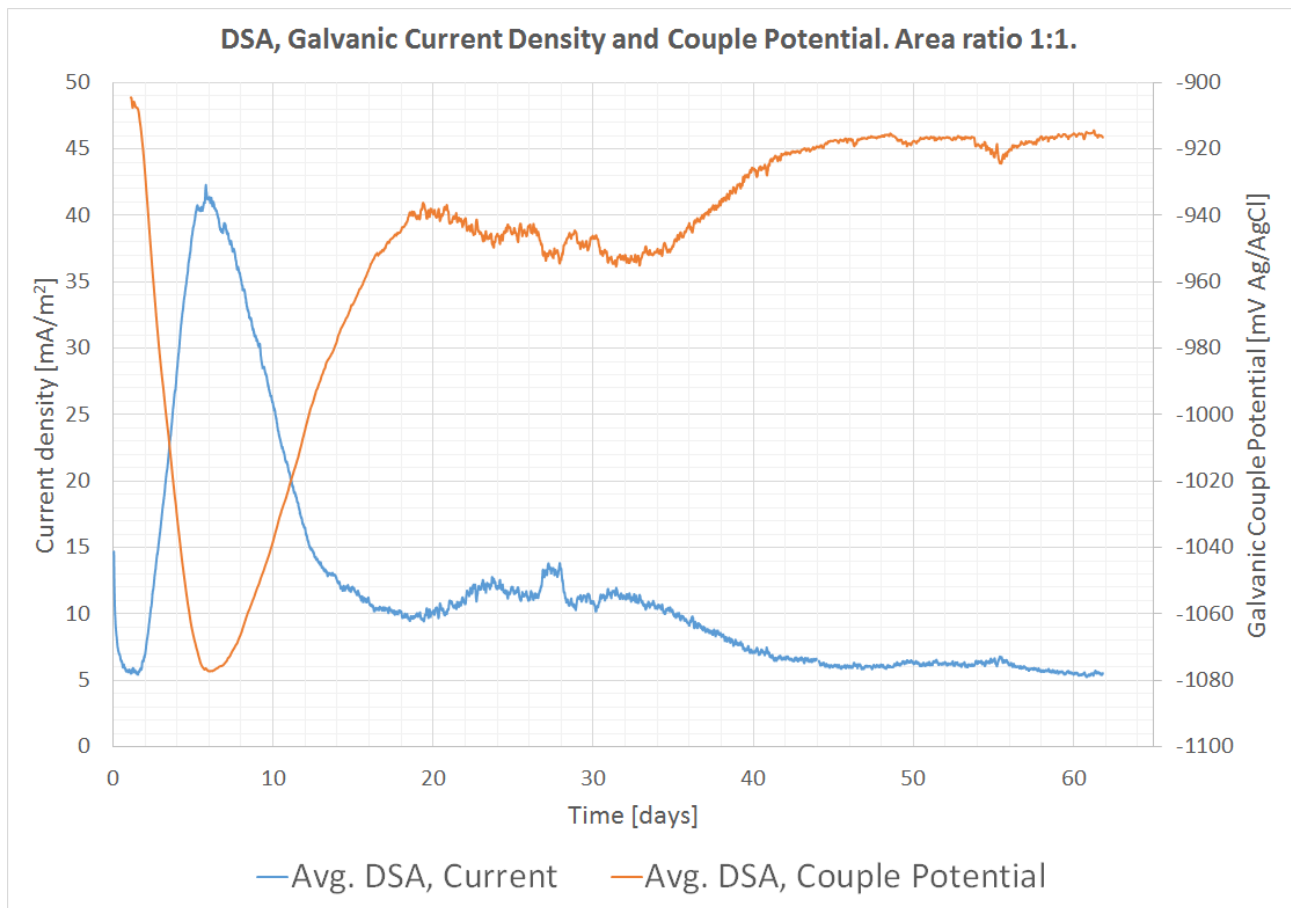


Figure 6.2: Galvanic current density and couple potential of a DSA:CS coupling embedded in mud.

Figure 6.3 shows the galvanic couple potential and current density on the coupled TSA sample. The vertical axes have been scaled so that both the potential and current density have sufficient resolution. The figure shows that the couple potential decreases steadily from -729 to -870 mV Ag/AgCl between day 4 and 36. The potential is fairly stable and increases slightly throughout exposure. The end potential at day 62 is approximately -850 mV Ag/AgCl.

The current density graph of the coupled TSA sample also shows mirror like behaviour compared to the couple potential. It decreases from 1 to 0.2 mA/m<sup>2</sup> from day 0 to 2, and increases fairly stable to almost 7 mA/m<sup>2</sup> at day 40. It is fairly stable throughout the exposure period. The end current density is approximately 6.5 mA/m<sup>2</sup>.

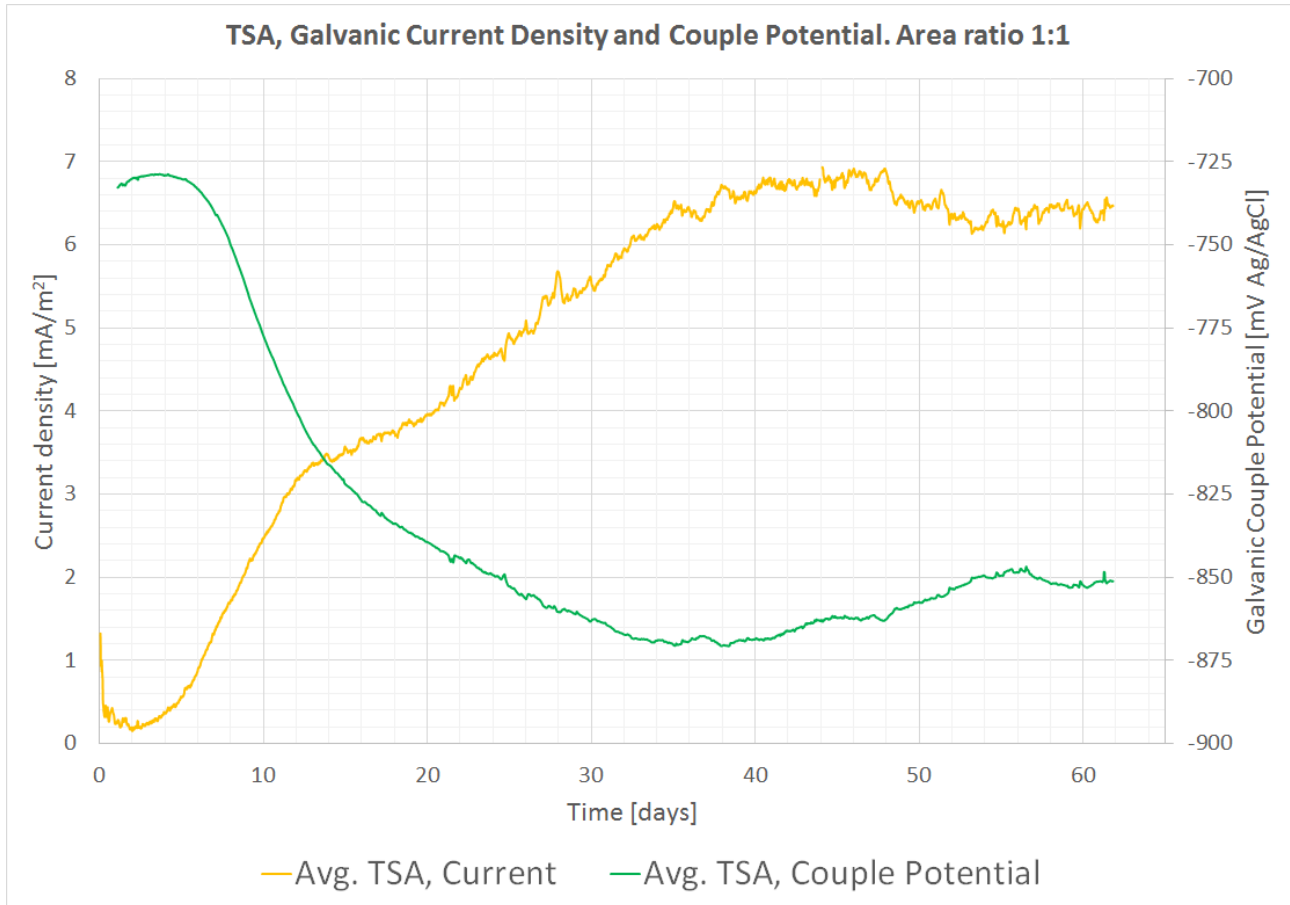


Figure 6.3: Galvanic current density and couple potential of a TSA:CS coupling embedded in mud.

Figure 6.4 shows a comparison between the galvanic current densities of the coupled DSA and TSA samples. It shows that the coupled DSA sample provides increased level of protection current density, especially from day 2 to day 16. The galvanic current density is approximately 5 mA higher from day 18 to 32, from where the galvanic current density of the DSA coating decreases and intersects with the current density curve for the TSA coating at day 41. The current densities are quite similar from this point throughout exposure (DSA slightly less).

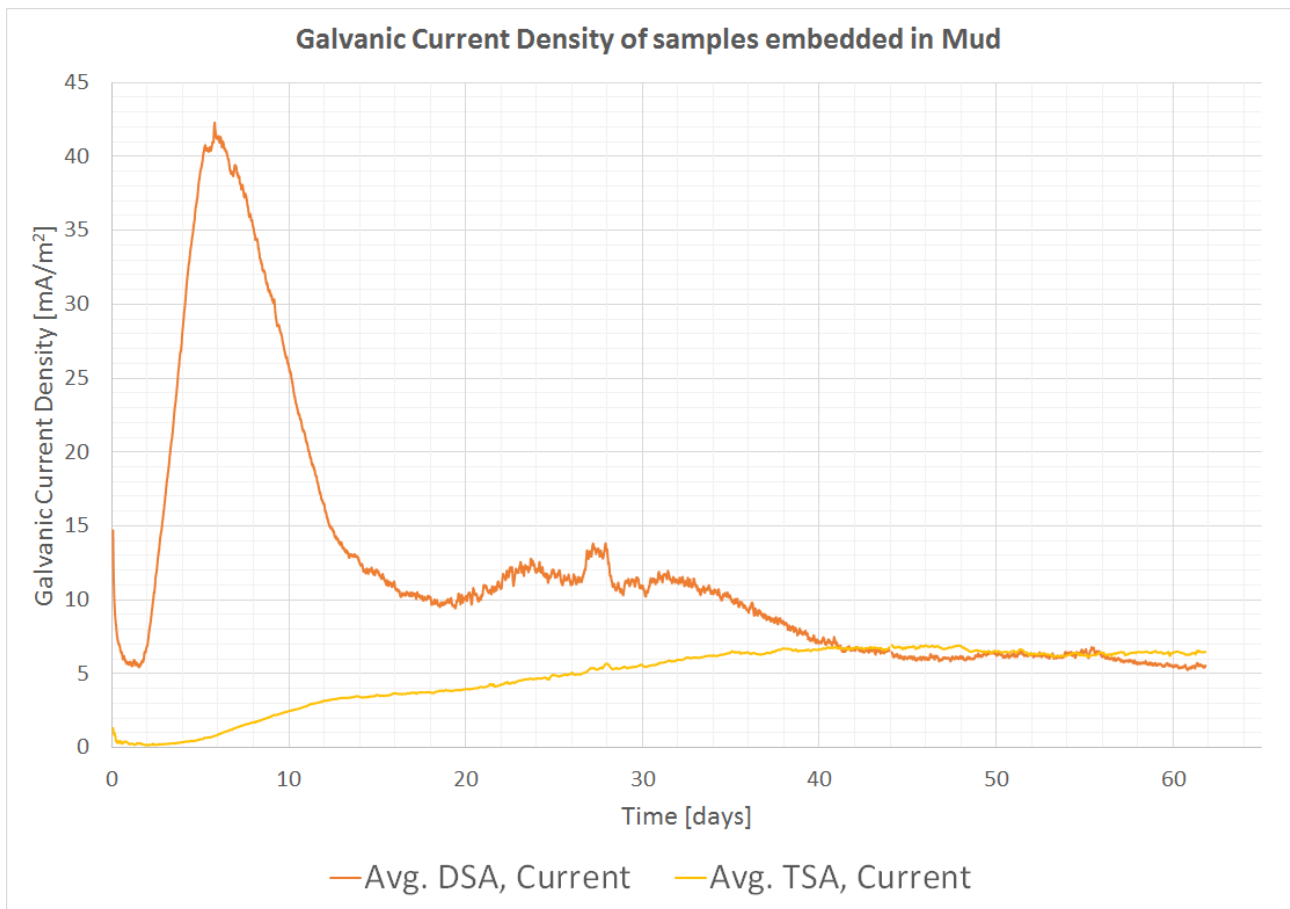


Figure 6.4: Galvanic current densities for the coupled DSA and TSA coating embedded in mud.

Figure 6.5 shows a comparison between the galvanic couple potentials of the DSA and TSA samples. The DSA:CS couplings are significantly more negative in the range from day 2 to 18. The difference in potential between the DSA:CS and TSA:CS couplings is approximately within the range 60 to 100 mV from day 20 throughout exposure.

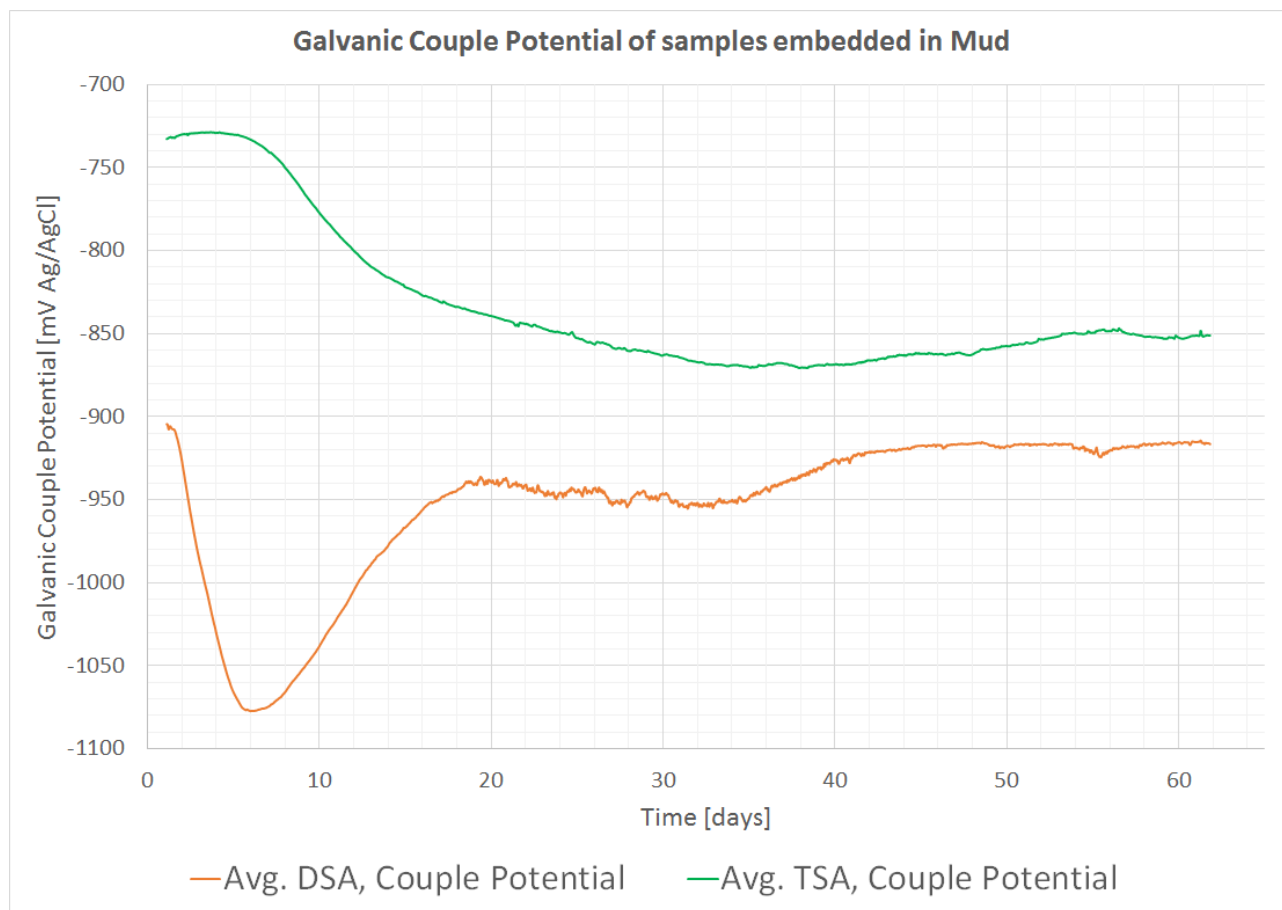


Figure 6.5: Galvanic couple potentials for the DSA and TSA coating embedded in mud.

Trends and observations that can be extracted from the graphs are that the DSA coating provides more protection current, and hence provides a lowering in potential for the galvanic coupling, which overall means increased level in protection for the cathodically protected CS. Even though the DSA:CS couple potential is 50-60 mV more negative compared with the TSA:CS couple potential from day 40 throughout exposure, the CS drains similar or slightly less current from the DSA compared with the TSA within this period. Little or no cathodic protection of the CS is present in the beginning of exposure for TSA:CS coupling. The TSA:CS potential decreases below -800 mV Ag/AgCl at day 12 which is the recommended protection potential for steel in seawater. It does not decrease below -900 mV Ag/AgCl which is the recommended protection potential for steel embedded in the seabed [20]. The DSA:CS potential is below -900 mV Ag/AgCl throughout the exposure.

### 6.3 Current Densities of Polarized Samples

This section presents the current densities of the potentiostatically polarized samples. The applied potential was set at -1.05 V Ag/AgCl in the beginning, and was later corrected to -1.1 V Ag/AgCl at day 1. The current densities have been calculated using the exposed surface areas which are approximately  $0.0025 \text{ m}^2$ . These results show in general how much current the coatings drains or provide, during a Cathodic Protection (CP) scenario beneath the seabed.

Figure 6.6 shows the current densities of the potentiostatically polarized samples. The current densities are positive and approximately at  $10 \text{ mA/m}^2$  in the beginning of exposure for both the polarized DSA and TSA samples. It shifts to negative during the first day of exposure. The current densities increase from -2 and -6  $\text{mA/m}^2$  to approximately -13  $\text{mA/m}^2$  for respectively the DSA and

TSA sample when the applied potential was adjusted from -1.05 to -1.1 V Ag/AgCl. It decreases and increases slightly for the DSA sample from day 2 to 11. Further it decreases slightly to  $-10 \text{ mA/m}^2$  and is fairly stable throughout the exposure period. The current density for the polarized TSA sample increases steadily from  $-12$  to  $-25 \text{ mA/m}^2$  between day 2 and 13. A steady decrease from  $-25$  to  $-14 \text{ mA/m}^2$  between day 25 to 62 is visible.

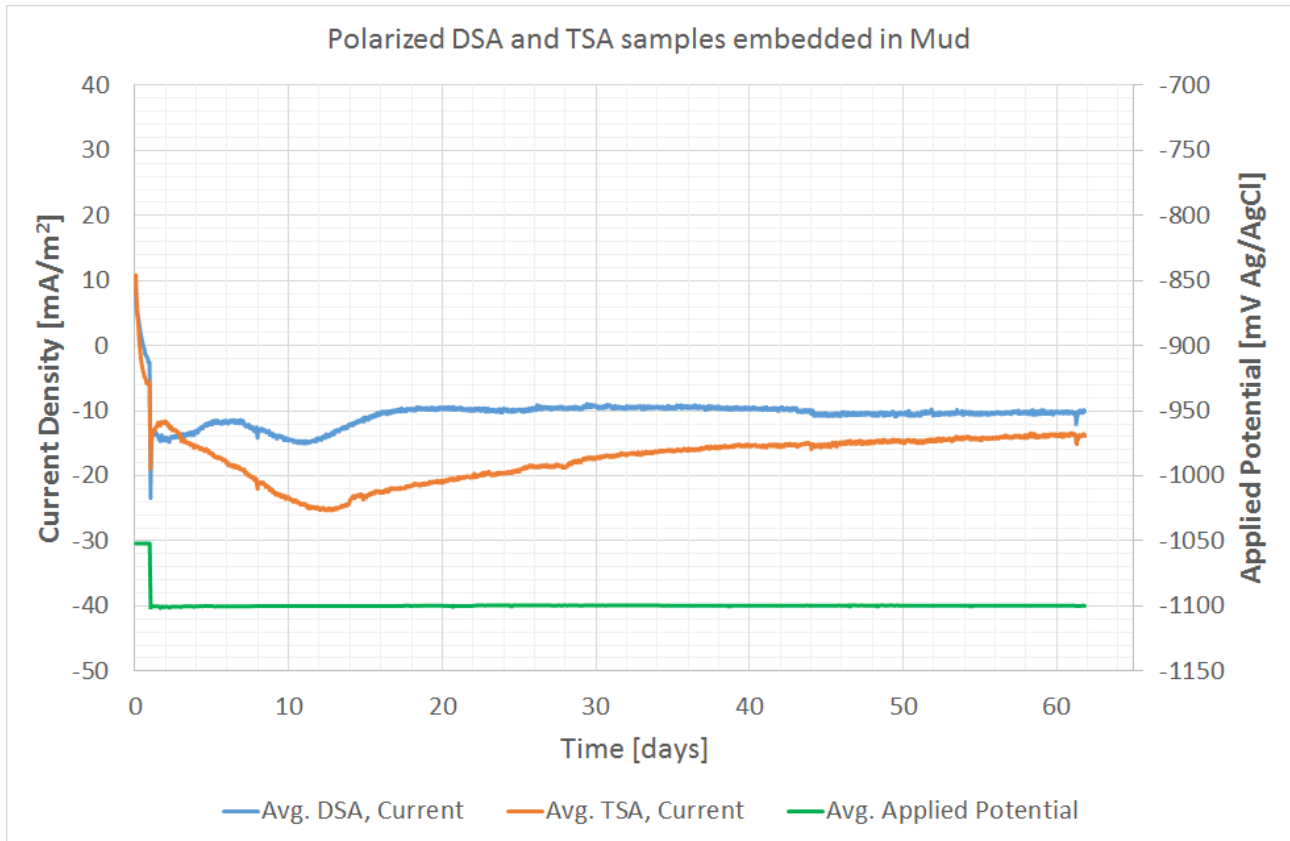


Figure 6.6: Current densities and applied potential of the potentiostatically polarized samples embedded in mud.

Trends and observations that can be extracted from the graphs are that the DSA coating require less current density compared with the TSA coating. The difference at the end of exposure is small, but overall the DSA coating requires less current density. The current density for DSA coating seems to be stable at approximately  $-10 \text{ mA/m}^2$  from day 16 throughout exposure, while the current density for the TSA coating decreases slowly but steady. The positive current densities which are present in the beginning of exposure mean that the coatings provide protection currents to the anode at the very beginning.

## 6.4 Linear Polarization Resistance measurements

The way LPR measurements were performed is described in Section 4.2.5. The measurements were performed after one day of exposure, and further on a weekly basis. The result from each LPR measurement is an average Polarization Resistance ( $R_p$ ). The  $R_p$  is calculated using Equation 2.8. The average  $R_p$  is calculated based on an average for the cathodic and anodic direction. A high  $R_p$  means that the samples have high resistance against polarization i.e. the corrosion rate is low. A low  $R_p$  means that the samples have less resistance against polarization i.e. the corrosion rate is high. The relation in corrosion rate is also visible from Stern Gearys Equation 2.9.

The LPR measurements of the samples have throughout the exposure period been quite easy to measure, since the potential drop have stabilized within a certain range for both the anodic and cathodic direction. The results are plotted as inverse avg. Polarization Resistance ( $1/R_p$ ), so that the results show the trend in corrosion rates.

Figure 6.7 shows the results from LPR measurements on freely exposed DSA and TSA samples. The avg. ( $1/R_p$ ) for the DSA sample increases from day 1 to 15, and decreases to day 22. It is fairly stable from this point throughout the exposure period. The avg. ( $1/R_p$ ) for the TSA sample decreases from day 1 to 8. It increases slightly at day 15, before it decreases throughout the exposure period.

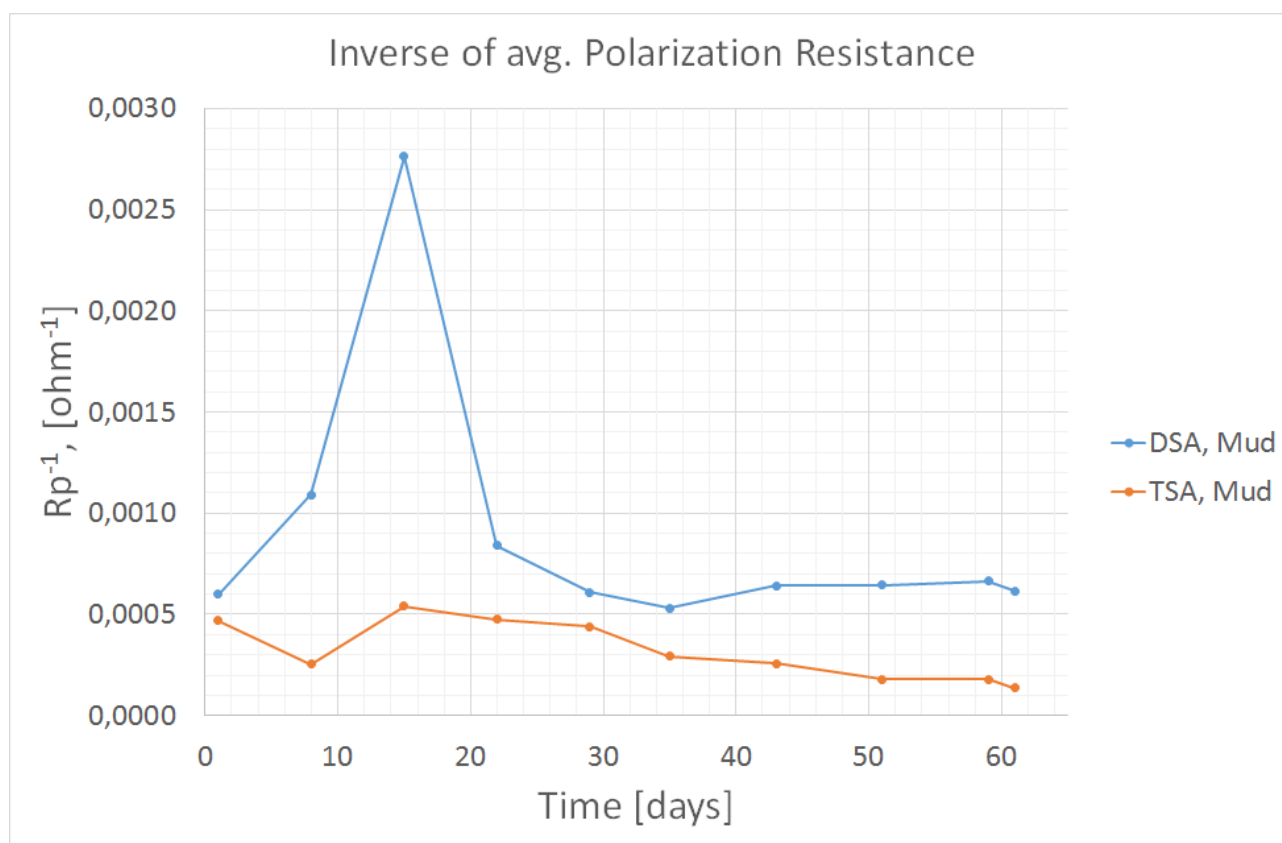


Figure 6.7: The results from LPR measurements in mud, plotted as  $1/R_p$ .

Table 6.1 shows the  $R_p$  values in Cathodic and Anodic direction gained from the measurements. The table shows great differences in  $R_p$ , depending on the polarized direction.

Table 6.1:  $R_p$  values for both cathodic and anodic direction on freely exposed samples in mud, and avg. value.

Day	Average Polarization Resistance, $R_p$ [ohm]					
	DSA, Mud			TSA, Mud		
	$R_p$ . Cath.	$R_p$ . Anod.	$R_p$ . Avg.	$R_p$ . Cath.	$R_p$ . Anod.	$R_p$ . Avg.
1	2000	1333	1667	2857	1399	2128
8	1333	500	917	7143	741	3942
15	385	339	362	2857	847	1852
22	1429	952	1190	3333	870	2101
29	2222	1053	1637	3636	909	2273
35	2667	1111	1889	5714	1111	3413
43	2222	889	1556	6667	1127	3897
51	2353	741	1547	10000	1111	5556
59	2222	784	1503	10000	1111	5556
61	2500	741	1620	13333	1176	7255

Trends and observations that can be extracted from the graph and table are that the DSA sample in general have lower polarization resistance in both anodic and cathodic direction, meaning that it should corrode more than a TSA coating. The low polarization resistance in anodic direction for the DSA sample is due to the ability it has to provide protection currents, when galvanically coupled to a nobler material. The DSA coating corrodes most at day 15. The OCP of DSA sample in Figure 6.1 shows that the OCP at this period of time (day 15) is approximately -1080 mV Ag/AgCl. The results from LPR measurements can further be compared to the OCPs in Figure 6.1.

## 6.5 Polarization Curves

This section presents the Polarization Curves recorded on freely exposed (however used for LPR measurements) DSA and TSA samples at day 61 of exposure. Cathodic polarization curve was also recorded on the freely exposed CS sample at day 61. The DSA and TSA samples were polarized from -200mV vs OCP to approximately -450 mV Ag/AgCl, while the CS sample was polarized from OCP to -1100 mV Ag/AgCl.

As previously stated in the beginning of this Chapter, the excel function "Moving Average" with a selected interval of 30, has been applied on the Polarization Curves recorded with the Gamry Machine. This leads to smooth curves that are desirable. This means that the first 29 measurements are missing, which removes the first 5 mV from -200 mV vs OCP in anodic direction from the plot. The function also causes the curve to drag slightly to the right in areas where many measurements differ from its original path. The overall result from using this function is satisfying. The general trend of the curves does not seem to be manipulated.

OCPs measured prior to recording polarization curves show similar or slightly less OCP compared with what the polarization curves show. The difference is within a range of 5 to 23 mV.

Figure 6.8 shows the polarization curves recorded on DSA and TSA samples. The cathodic polarization curve on CS is also included. The figure shows that the freely exposed DSA and TSA samples have similar slopes on the cathodic curves. The anodic curves show that while TSA sample shows passive anodic behavior above -900 mV Ag/AgCl, the DSA sample shows active anodic behavior above the same potential. Active behavior/pitting potential is reached at approximately -625 mV Ag/AgCl for the TSA sample. The cathodic curve for the CS shows linear behaviour on the log plot. The placement of curves show that the OCP for the TSA sample is approximately 50 mV higher compared with the DSA sample.

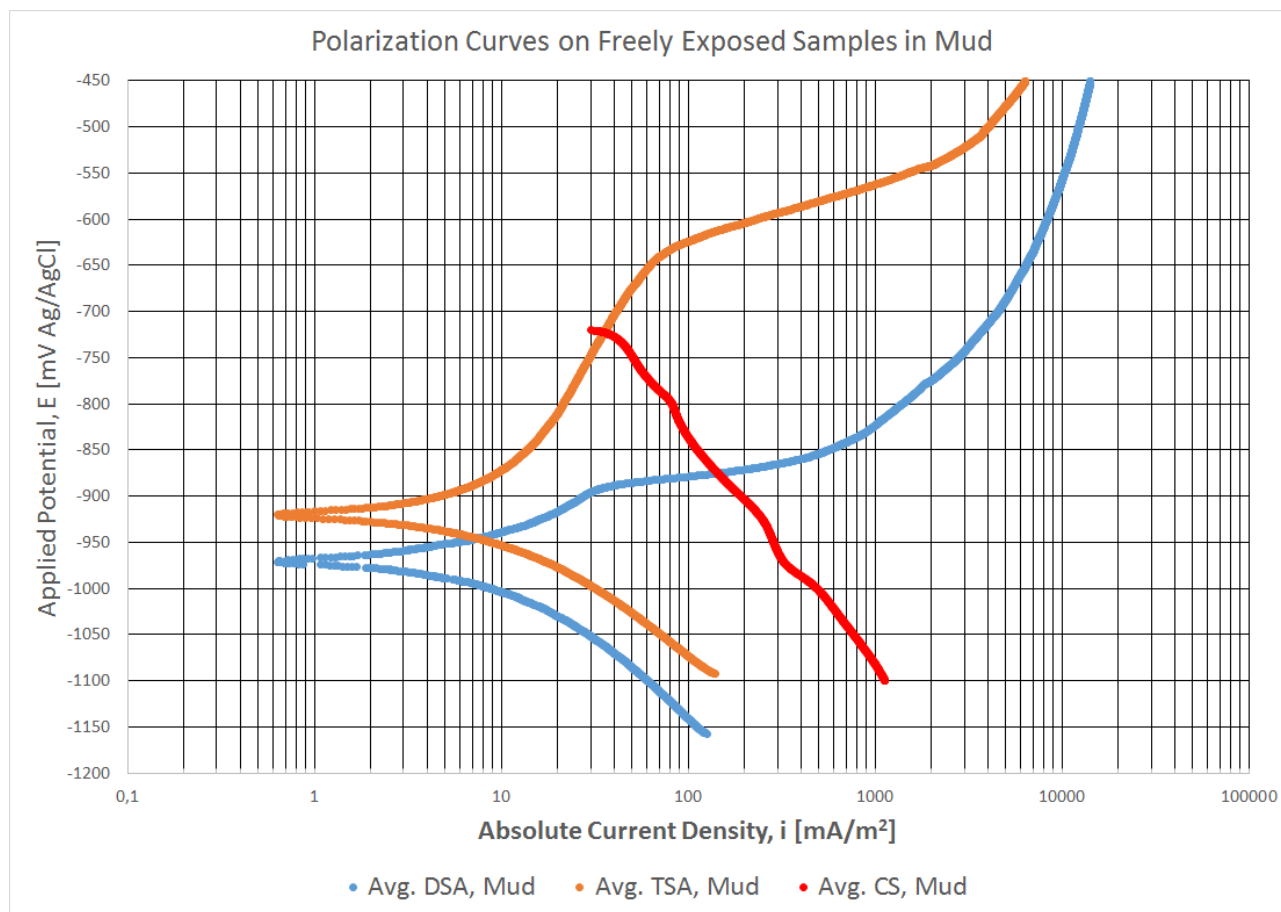


Figure 6.8: Recorded Polarization Curves on freely exposed samples in mud at day 61.

### 6.5.1 Summary - Polarization Curves

Table 6.2 shows a summary of the most important data obtained from the Polarization Curves. It includes OCP measured prior exposure and OCP according to Polarization Curves. It also includes graphically solved corrosion current densities, anodic and cathodic tafel Constants. The visible pitting potentials are listed and the general anodic behavior from the coatings is included.

The graphical solution for the Polarization Curves, which includes OCP, corrosion current density and anodic and cathodic tafel constants is included in Figure B.4 in the Appendix Section.

Table 6.2: Data and abilities obtained from the Polarization Curves at day 61.

	DSA, Mud	TSA, Mud	CS, Mud
Temperature in SW [°C]	11	11	11
OCP [mV Ag/AgCl]	-966	-902	-709
OCP Pol. Curv. [mV Ag/AgCl]	-971	-925	-
Corr. Curr. Den., $i$ [mA/m <sup>2</sup> ]	9	6.5	-
An. Taf. Con., $b_a$ [mV/dec]	70	180	-
Cat. Taf. Con., $b_c$ [mV/dec]	-140	-110	-250
Anodic behavior [Act, Pass, Act/Pass]	Act.	Pass.	-
Pitting Pot. [mV Ag/AgCl]	-900	-625	-



## 6.6 Corrosion Rates

The corrosion rates are calculated from avg. Polarization Resistance in both cathodic and anodic direction which are listed in Table 6.1. The tafel slopes used in the calculation are from the Polarization Curves from day 61 for freely exposed samples in mud, which are listed in Table 6.2. Stern Gearys Equation 2.9 and Corrosion Rate Equation 2.10 were used in the calculation. The physical data which were used for the calculation are listed in Table A.2 in the Appendix section.

Figure 6.9 shows the calculated corrosion rates from LPR measurements throughout exposure. The single points (with no lines) at day 61 are calculated from graphically solving the corrosion current densities from the polarization curves. The graphical solution shows corrosion rates which are 4-5  $\mu\text{m}$  bigger compared with the solution from LPR measurements at this point.

Figure 6.9 shows that the corrosion rate for the DSA sample is increasing from 5 to 25  $\mu\text{m}/\text{year}$  up until day 15, from where it decreases and is fairly stable between 5 - 8  $\mu\text{m}/\text{year}$  from day 21 throughout the exposure period. The corrosion rate for the TSA sample decreases from 7 to 4  $\mu\text{m}/\text{year}$  between day 1 and 8. It increases to 8 at day 15 before it decreases steadily to approximately 2-3  $\mu\text{m}/\text{year}$  at day 61. The Figure shows slightly different trends compared with the LPR results in Figure 6.7, due to different anodic and cathodic tafel constants as well as slightly different densities of the coatings.

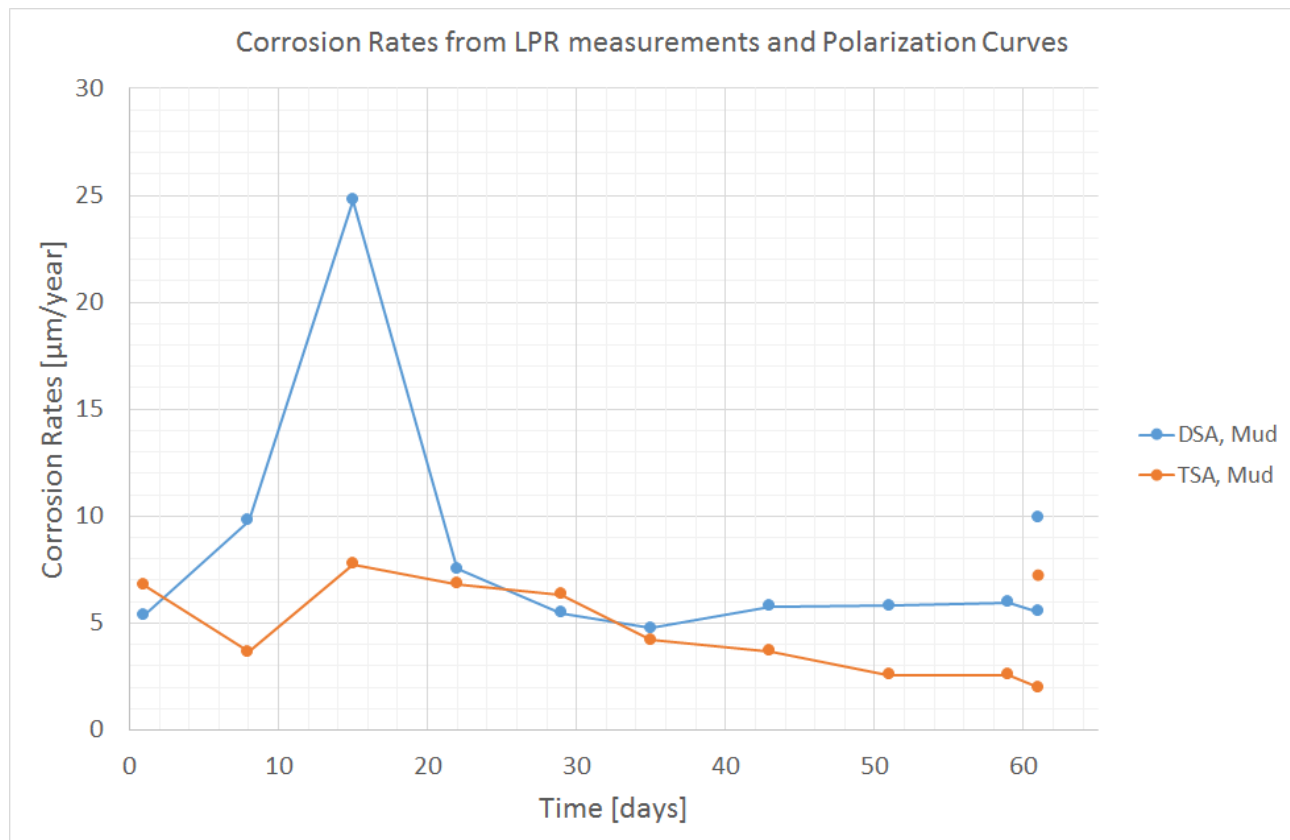


Figure 6.9: Corrosion rates from LPR on freely exposed DSA and TSA samples in mud. The two single points (day 61) are calculated from graphical solution of Polarization Curves.

## 6.7 Summary - Electrochemical Results

Table 6.3 shows a summary of the electrochemical properties after 62 days of exposure. The data from the Polarization Curves were obtained after 61 days. The OCP of the CS steel sample was obtained before cathodic polarization curve was obtained. The OCP values for the TSA and DSA sample were obtained from the freely exposed samples (no LPR), while the OCP values from the Polarization Curves were obtained one day earlier on another set of samples (LPR). This explains the difference in OCP for the TSA sample embedded in mud.

The OCP for the DSA sample is more negative compared with the TSA sample. The pitting potential is significantly more negative for the DSA sample, which explains the active anodic behaviour. The galvanic corrosion rate is calculated from the galvanic current density at the respective couple potential. The current density requirement at  $-1.1$  V Ag/AgCl is slightly less for the DSA sample compared to the TSA sample.

Table 6.3: Summary of electrochemical properties of samples embedded in Mud after 62 days.

	TSA, Mud	DSA, Mud	CS, Mud
<b>Temperature, SW [°C]</b>	10	10	10
<b>OCP [mV Ag/AgCl]</b>	-890	-978	-709
<b>OCP Pol. Curv. [mV Ag/AgCl]</b>	-925	-971	-
<b>Pitting Potential [mV Ag/AgCl]</b>	-625	-900	-
<b>Anodic Behavior [Act., Pass., Act/Pass]</b>	Pass.	Act.	-
<b>Anodic Tafel Constant, ba [mV/dec]</b>	180	70	-
<b>Cathodic Tafel Constant, bc [mV/dec]</b>	-110	-140	-225
<b>Corr. Curr. Dens. Pol. Curv. [mA/m<sup>2</sup>]</b>	6.5	9	-
<b>Corrosion Rate, Pol. Curv. [µm/year]</b>	7.2	9.95	-
<b>Corr. Curr. Dens. LPR. [mA/m<sup>2</sup>]</b>	1.6	5	-
<b>Corrosion. Rate, LPR [µm/year]</b>	1.98	5.53	-
<b>Couple Potential [mV Ag/AgCl]</b>	-851	-916	-
<b>Galvanic Curr. Dens. [mA/m<sup>2</sup>]</b>	6.5	5.5	-
<b>Galvanic Corr. Rate. [µm/y]</b>	7.2	6.1	-
<b>Polarized Potential [mV Ag/AgCl]</b>	-1100	-1100	-
<b>Curr. Dens. Req., -1.1 V Ag/AgCl, [mA/m<sup>2</sup>]</b>	-14	-10	-

---

# Chapter 7

## Coating Examination - Exposure at elevated temperatures

This chapter presents the results from cross section analysis of samples, prior and post exposure. The initial surface conditions has been documented visually by means of pictures, OM and SEM. The chemical composition have been been documented by use of EDS. The cross sections have been examined by using SEM and EDS of cutted samples embedded in a phenolic, hot mounting resin with carbon filler, Poly-fast.

### 7.1 Visual Examination

#### 7.1.1 Prior Exposure

Figure 7.1 shows the general initial surface conditions of the samples used in the experiments. It shows that both the DSA and TSA samples look similar. A slight difference in color can be seen. The TSA sample appears slightly more yellow compared with the DSA sample. The roughness appear visually similar on both coatings. The Anode sample and CS cube are smooth and shiny.



Figure 7.1: Initial surface conditions of test samples -Left: DSA sample, 2nd Left: TSA sample, 2nd Right: Anode sample, Right: CS-cube.

Figure 7.2 shows the cross section of a new DSA and TSA sample. This is the appearance after the cutting, embedding, grinding and polishing process. These samples were used to document the initial coating thicknesses and chemical composition of the coatings in SEM. These samples were also used for the optical microscopy which is presented in Section 7.2. The cross sections show that the DSA sample has a thicker coating compared to the TSA sample. The cross section of the TSA sample appears more rough and is significantly thinner compared with the DSA sample.

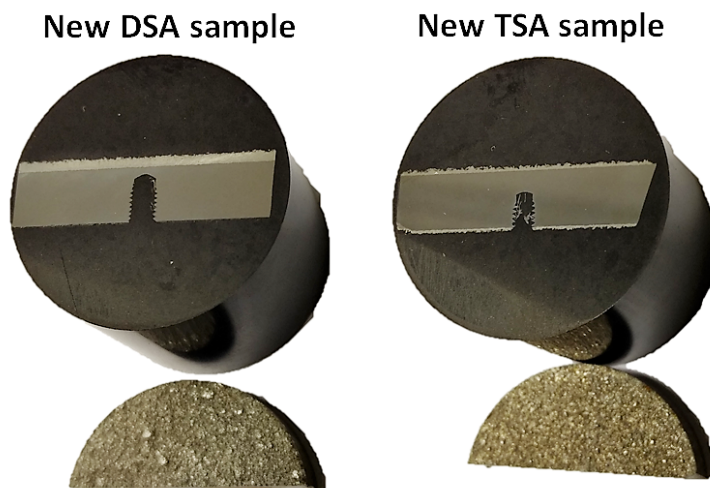


Figure 7.2: Cross section of new DSA and TSA sample.

### 7.1.2 Post Exposure

The samples were detached from the containers and visual observations were performed on the samples, immediately after the end of exposure. Afterwards the samples were cleaned twice in Nitric acid, and a new visual observation was performed. It was observed that there were large amounts of corrosion products in the outlets of the containers where the galvanic coupled samples were attached. The amount was less in the protrusions of the 22°C container while largest amount was observed in the 80°C container. Figure 7.3 shows the protruding part of 80°C container where the coupled DSA sample was attached. Large amounts of corrosion products are visible on the picture.



Figure 7.3: Corrosion products in the protruding part of 80°C container, where the coupled DSA sample was attached.

Figure 7.4 (Left) shows the samples exposed at 22°C, immediately after exposure. The coupled DSA, TSA and Anode samples have higher degree of white corrosion products compared to the freely exposed samples. It seems like the blue silicone gel and rubber gasket have ensured that only the area in the middle have been exposed, which was the intention.

Figure 7.4 (Right) shows the samples exposed at 22°C, after cleaning twice with Nitric Acid. The coupled Anode sample shows significant amount of metal loss. The coupled DSA sample shows areas where there is high altitude difference (less visible on the figure). The height is significantly higher compared with unexposed area, indicating possible adhesion/cohesive failure. No visible degradation/deformation of the coupled TSA sample is visible. The freely exposed samples show no visible signs of degradation or deformation.

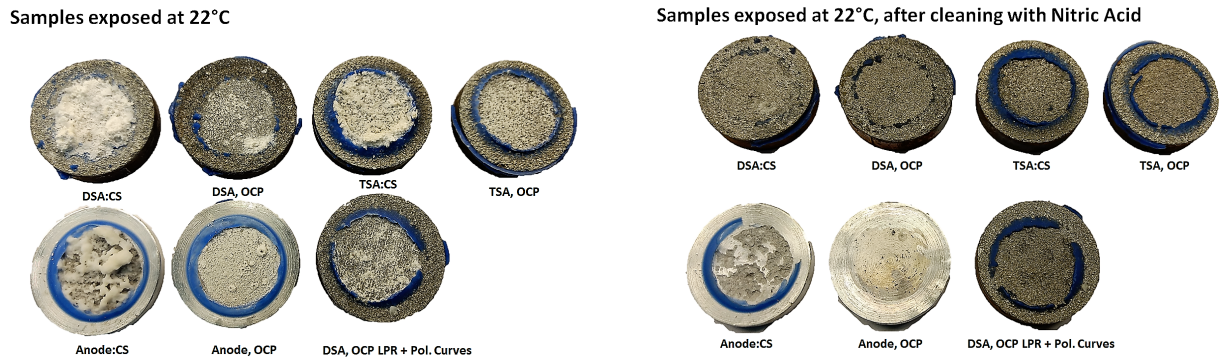


Figure 7.4: Left: Samples at 22°C, immediately after exposure. Right: After cleaning with Nitric Acid.

Figure 7.5 (Left) shows the samples exposed at 50°C, immediately after exposure. Increased amounts of corrosion products on the coupled samples compared with the freely exposed samples is visible. Small signs of possible crevice corrosion on the coupled DSA and TSA sample are visible, due to presence of corrosion products beneath the gasket and blue silicone gel.

Figure 7.5 (Right) shows the samples exposed at 50°C, after cleaning twice with Nitric Acid. The coupled Anode sample shows significant degradation represented by deep pits. Altitude difference visible on the coupled DSA sample, similar with the coupled DSA sample at 22°C, indicating possible adhesive/cohesive failure. The coupled TSA sample shows degradation due to possible crevice corrosion beneath the location of the blue silicon gel and rubber gasket. No degradation or deformation on the freely exposed samples is visible. It appears that some corrosion products still are left on the exposed surfaces.

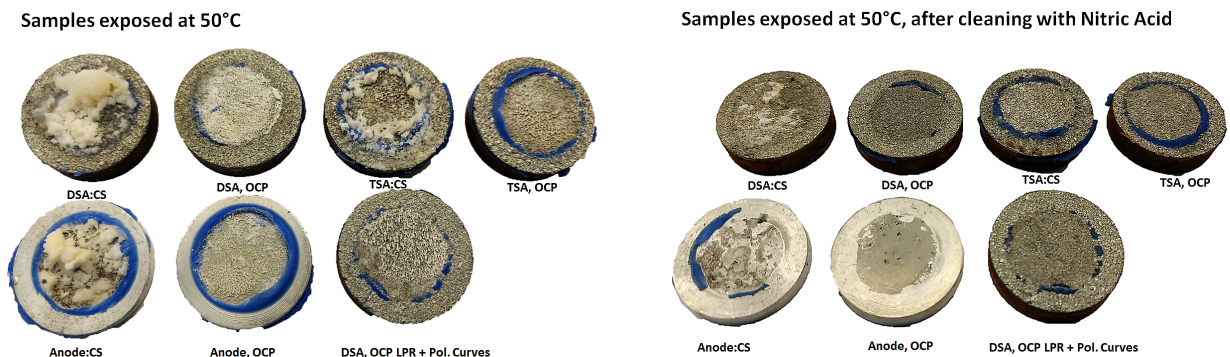


Figure 7.5: Left: Samples at 50°C, immediately after exposure. Right: After cleaning with Nitric Acid.

Figure 7.6 (Left) shows the samples exposed at 80°C, immediately after exposure. Significant amounts of corrosion products on the galvanically coupled samples compared with the freely exposed samples is visible. It seems like the coupled DSA and TSA samples have suffered from significant crevice corrosion, beneath the rubber gasket and blue silicon gel due to presence of corrosion products on the whole surface. The corrosion products on some samples have some amount of a brownish color, indicating corrosion products from iron. The coating may have failed, due to significant degradation or micropits. The rubber gasket and blue silicon gel may have failed on the coupled DSA and TSA samples exposing CS around the edge of the coating as well.

Figure 7.6 (Right) shows the samples exposed at 80°C, after cleaning twice with Nitric Acid. Significant amounts of corrosion products are still left on the surfaces of the coupled DSA, TSA and Anode sample. Significant degradation of coating on coupled DSA and TSA samples is visible, on areas beneath the rubber gasket and blue silicon gel. This indicates significant crevice corrosion.



The coupled DSA sample shows altitude difference on areas in the middle, where the coating to some extent is still intact, indicating possible adhesive/cohesive failure similar with the coupled DSA samples at 22 and 50°C. Coating is completely removed on some locations on the coupled TSA sample close to the edge. Degradation on the freely exposed samples is not visible.

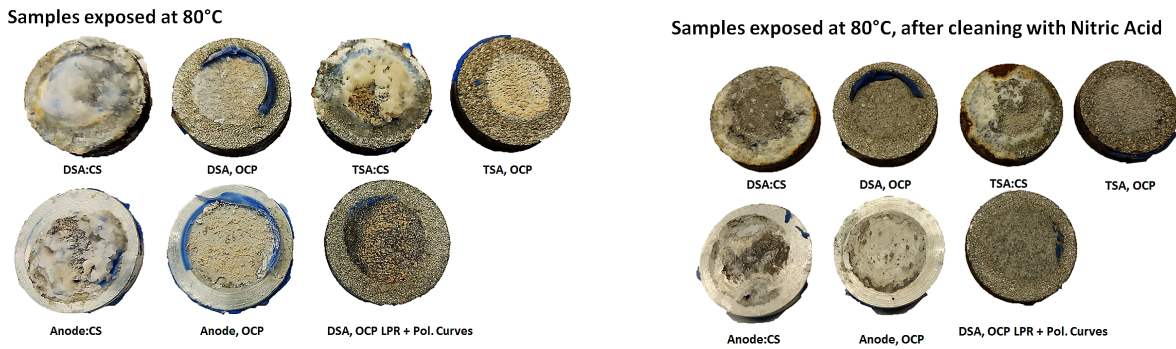


Figure 7.6: Left: Samples at 80°C, immediately after exposure. Right: After cleaning with Nitric Acid.

Figure 7.7 shows cross sections of coupled DSA samples at all temperatures. A cross section of coupled TSA sample at 80°C is included. All coupled DSA samples show areas of cohesive failure within the coating. The coupled DSA and TSA sample at 80°C shows significant coating degradation in areas beneath the rubber gasket and blue silicone. These are indications of significant crevice corrosion.

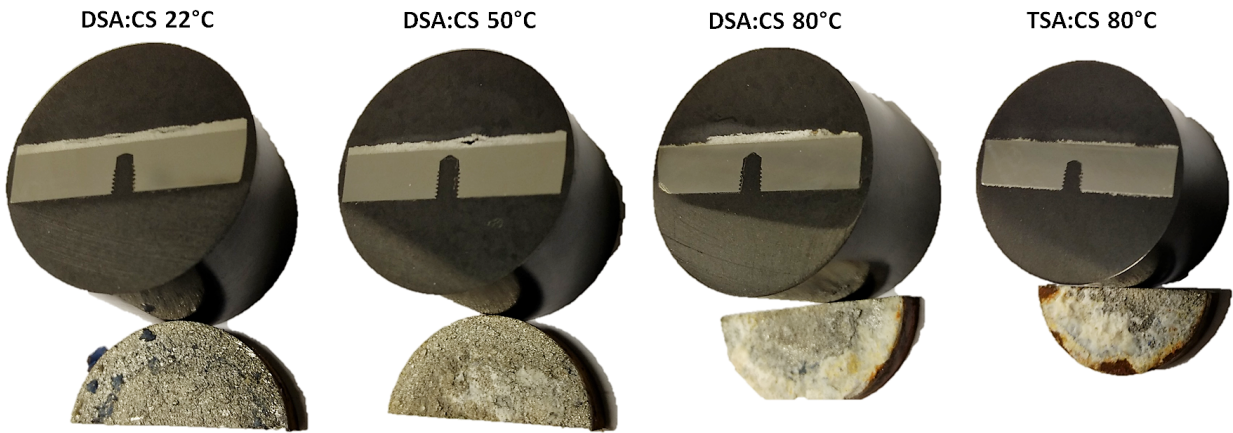


Figure 7.7: Cross sections of selected coupled samples at 22°C, 50°C and 80°C showing cohesive failure and crevice corrosion.

Figure 7.8 shows the galvanic coupled CS cubes at all temperatures. The picture was taken when the calcareous deposits were completely dry.

All CS cubes show presence of calcareous deposits on the surfaces. The CS cube coupled with TSA at 50°C shows less amount of calcareous deposits and the color is brown, indicating corrosion products from CS. This indicates that the CS sample have received limited amount of protection current from the TSA sample. The calcareous deposits on all CS cubes at 50°C appear thinner and more dense compared with the deposits on the 22 and 80°C samples. The calcareous deposit layer on the CS cube coupled with TSA at 80°C, seems less attached to CS, since the deposits on this cube were more easily separated from the rod, when the rod was unscrewed from the cube using a shift key.

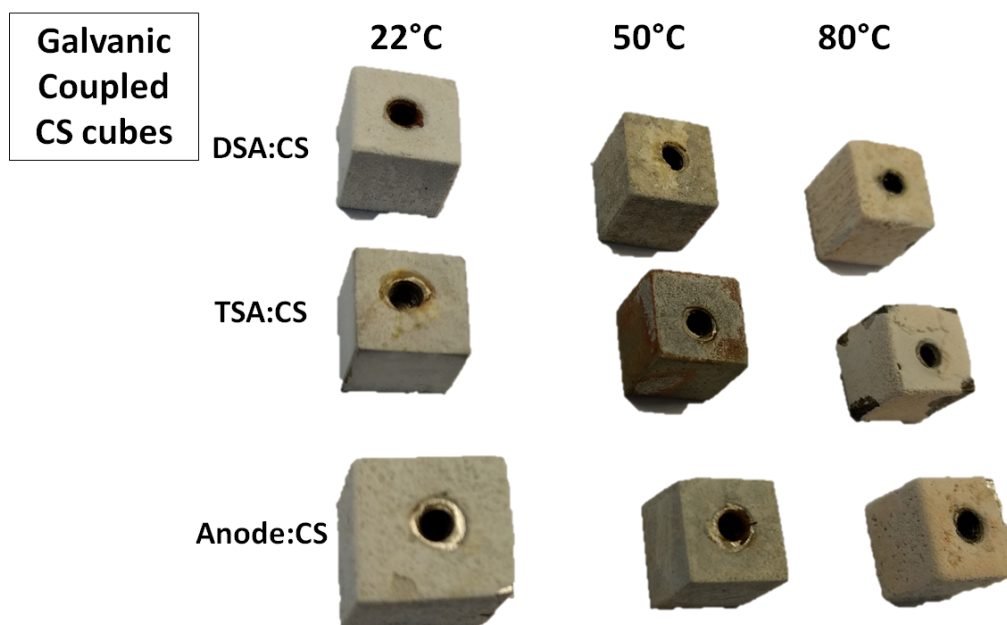


Figure 7.8: Galvanic Coupled CS cubes at all temperatures.

## 7.2 Optical Microscopy

OM was performed on a new (not exposed) DSA and TSA sample to document the surface topography of the coatings. OM of exposed samples were not performed due to presence of corrosion products on several surfaces. The Microscope used was a Alicona Confocal Microscope - Infinite Focus, located in the Tribology Lab, at Perleporten. The optic used was IFM G4 2\_5x.

Figure 7.9 (Left) shows a 3D figure, from a complete surface scan of a new DSA sample. The 3D image is created by mapping several individual scans together. The coloring gives an indication of the height of the surface, which can be compared with the height range located to the bottom left of the figure.

Figure 7.9 (Right) shows a 2D image, from a complete surface scan of a new DSA sample. The image shows a black line, indicating the position for a line scan which creates a surface topography of the coating. The line scan is performed from left to right.

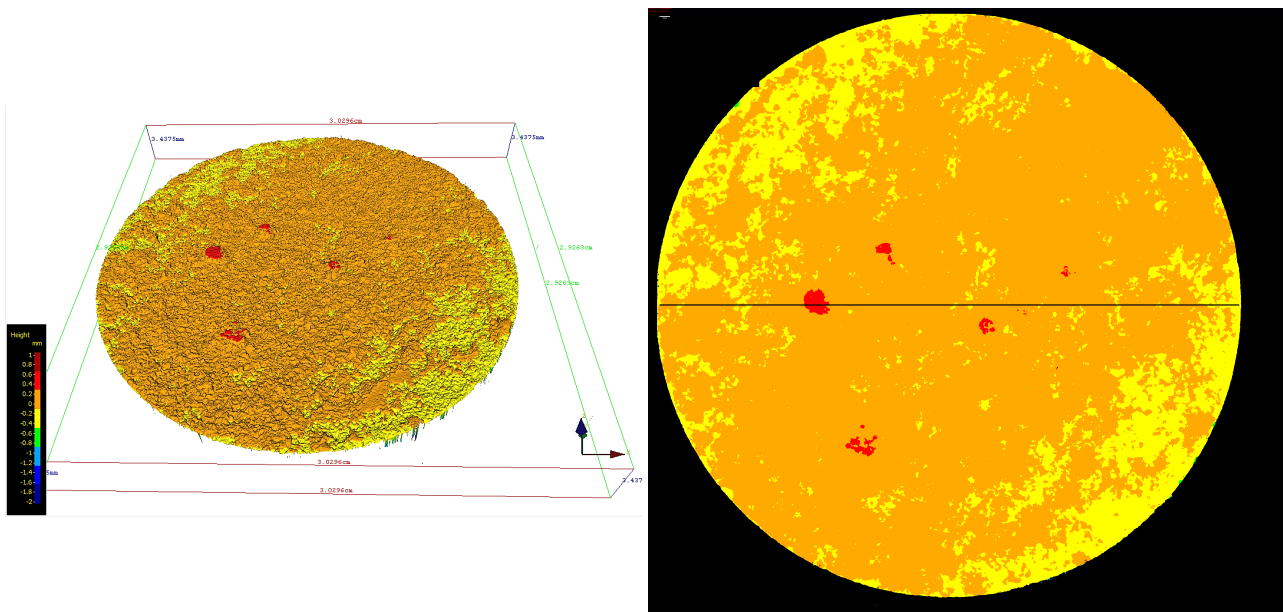


Figure 7.9: Left: 3D figure of a new DSA sample, showing the contour of the surface of coating. Right: 2D figure of a new DSA sample, showing the location for the line scan.

Figure 7.10 shows the surface topography from the linescan which is marked with a black line in Figure 7.9 (Right). A reference plane in z-direction ( $z=0$ ) was created from several selected points in the surface of the coating, which creates an average plane. The surface topography shows a rough surface of the coating with several peaks and deep areas.

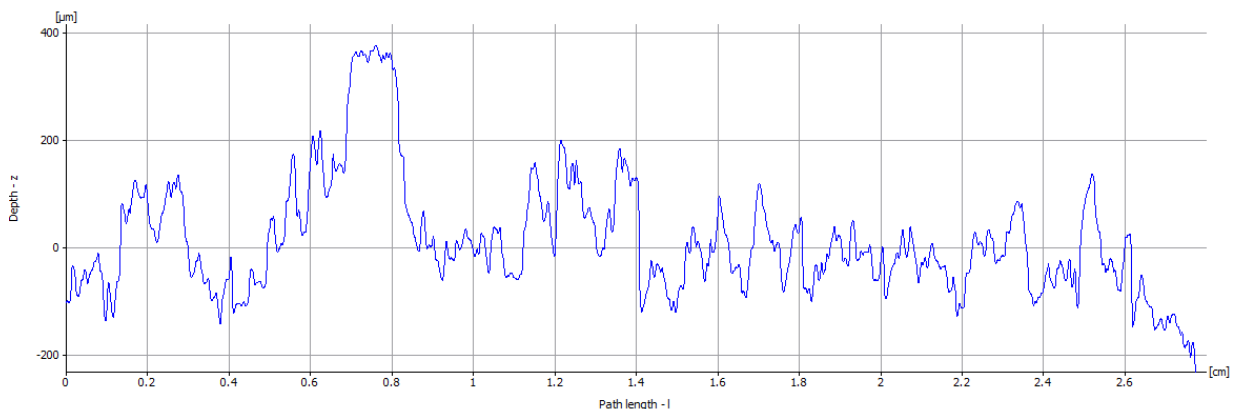


Figure 7.10: Surface topography of a new DSA from a line scan.

Figure 7.11 shows a 3D figure and 2D image, from a smaller surface scan of a new TSA sample. The image shows black lines, indicating the position for a line scan which creates a surface topography of the coating.



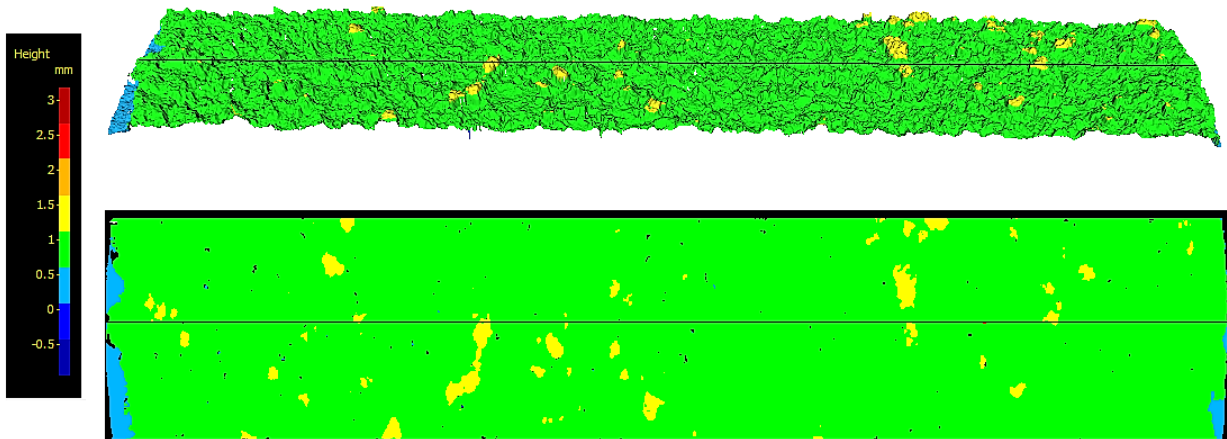


Figure 7.11: 3D figure and 2D image of a new TSA sample. The black lines are showing the locations for a line scan.

Figure 7.12 shows the surface topography from the linescan which is marked with black lines in Figure 7.11. A reference plane in z-direction ( $z=0$ ) was created from several selected points in the surface of the coating, which creates an average plane. The surface topography shows a rough surface of the coating with several peaks and deep areas. Some deep areas can be seen at approximately 0.82 and 1.5 cm in path length.

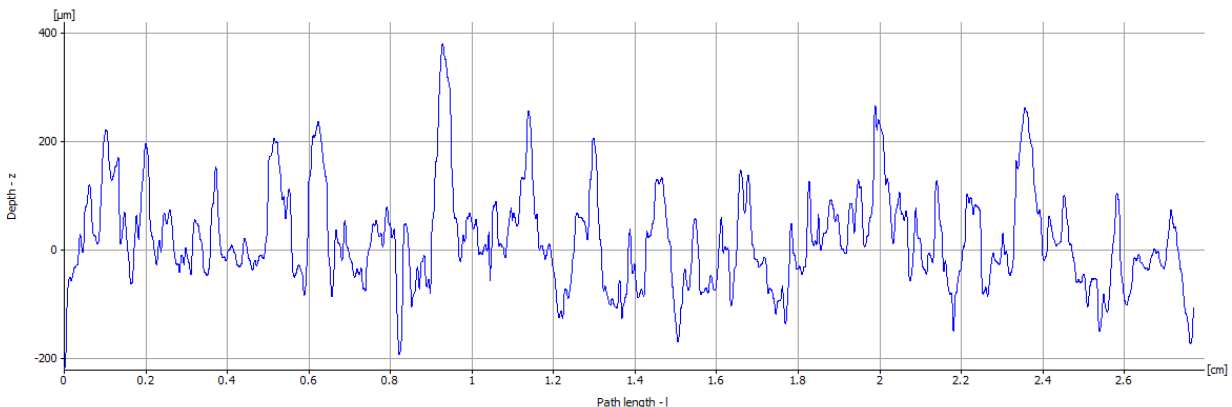


Figure 7.12: Surface topography of a new TSA from a line scan.

## 7.3 EDS of Cross Sections

### 7.3.1 Sources for Inaccuracy

The EDS results, i.e. the chemical composition of selected points and areas, are to some extent unreliable. This is especially true for elements which it is expected to be limited amount of within a coating (e.g. Zn or In).

Elements of interest (e.g. Zn and In) can be selected manually when conducting EDS, even though no significant signals of these are detected from the spectrum. This is most likely due to the significant amount of aluminum, which "hides" the presence these.

Figure 7.13 shows a specter from EDS of Spot 1 of unexposed DSA sample. It shows that no/limited signals from Zn and Indium are present from this point (red circle). Strong signals of Aluminum are detected as expected.

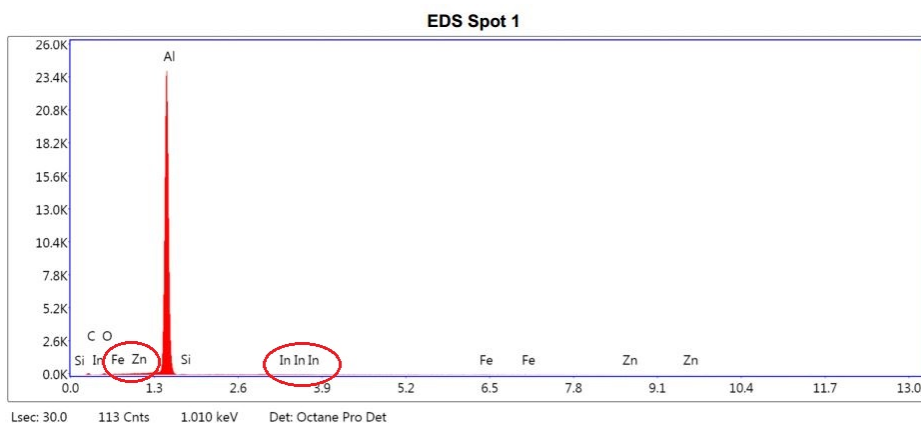


Figure 7.13: Specter from EDS of Spot 1 of unexposed DSA sample.

The chemical composition from this spectre is presented in Figure 7.14. It shows that the Error % for the contents of Zn and Indium are significant, i.e. 66.7% and 56.5%, respectively. This means that these amounts of Zn and In are inaccurate. Presence of these are however most likely.

Element	Weight %	Atomic %	Net Int.	Error %	Kratio	Z	R	A	F
C K	10.44	20.64	17.56	16.12	0.0106	1.1469	0.9415	0.0888	1.0000
O K	1.34	1.99	12.59	18.64	0.0033	1.0993	0.9637	0.2213	1.0000
ZnL	0.09	0.03	2.14	66.68	0.0010	0.8364	1.1455	1.2996	1.0272
AlK	87.21	76.78	5755.29	1.53	0.8264	0.9800	1.0057	0.9655	1.0015
SiK	0.42	0.35	10.52	24.30	0.0015	1.0017	1.0126	0.3695	1.0021
InL	0.06	0.01	1.04	56.46	0.0005	0.7312	1.2370	0.9794	1.0283
FeK	0.43	0.18	7.06	40.92	0.0040	0.8442	1.0683	0.9945	1.0981

Figure 7.14: Chemical composition from EDS of Spot 1 of unexposed DSA sample.

Small signals can manually be selected from a typical specter, i.e. (e.g. Figure 7.13), when zooming in on the lower section of the spectrum. These signals have been chosen conservatively when EDS was performed, and the most fitting proposal from the program has been selected.

### 7.3.2 Prior Exposure

Figure 7.15 shows cross section measurements for a representative area and selected areas/spots for EDS examination on an unexposed DSA sample.

Table 7.1 shows the results from selected points and areas (Figure 7.15) from the EDS examination. It shows overall expected results. Area 2 gives a chemical composition which is close to expected results for the DSA coating. Presence of carbon can be from ethanol or from particles from the embedding material.

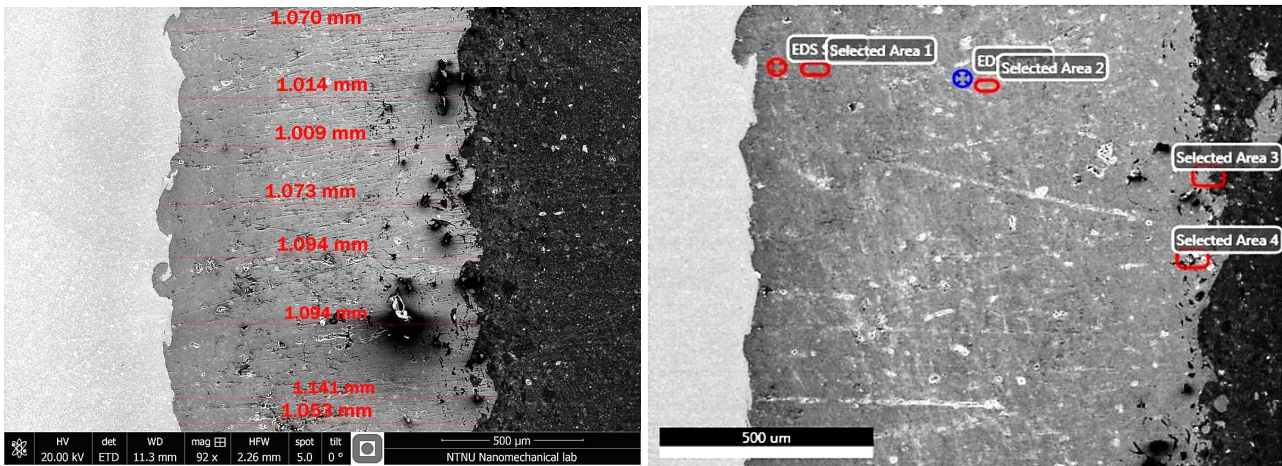


Figure 7.15: Left: Cross section measurements of unexposed DSA sample, Right: Areas/Spots for EDS.

Table 7.1: Results from EDS of selected points and areas on unexposed DSA sample.

Element [wt%]	Spot 1	Area 1	Spot 2	Area 2	Area 3	Area 4
C	10.44	6.90	10.06	-	70.48	18.89
O	1.34	3.13	2.89	1.37	3.74	2.80
Zn	0.09	-	0.96	3.00	1.03	2.35
Al	87.21	88.99	86.09	95.53	24.42	75.80
Si	0.42	0.37	-	-	0.26	-
In	0.06	-	-	0.10	0.08	0.16
Fe	0.43	0.61	-	-	-	-
Total	99.99	100.00	100.00	100.00	100.01	100.00

Figure 7.16 shows cross section measurements for a representative area and selected areas/spots for EDS examination on an unexposed TSA sample. The cross section shows thickness measurements from approximately 220 to 475  $\mu\text{m}$ . The lowest thickness measurement was approximately 140  $\mu\text{m}$ , while the thickest measurement was approximately 745  $\mu\text{m}$ .

Table 7.2 shows the results from selected points and areas (Figure 7.16) from the EDS examination. It shows overall expected results. Significant content of Aluminum was detected, and content of Fe on points close to the Al/CS interface was also detected.

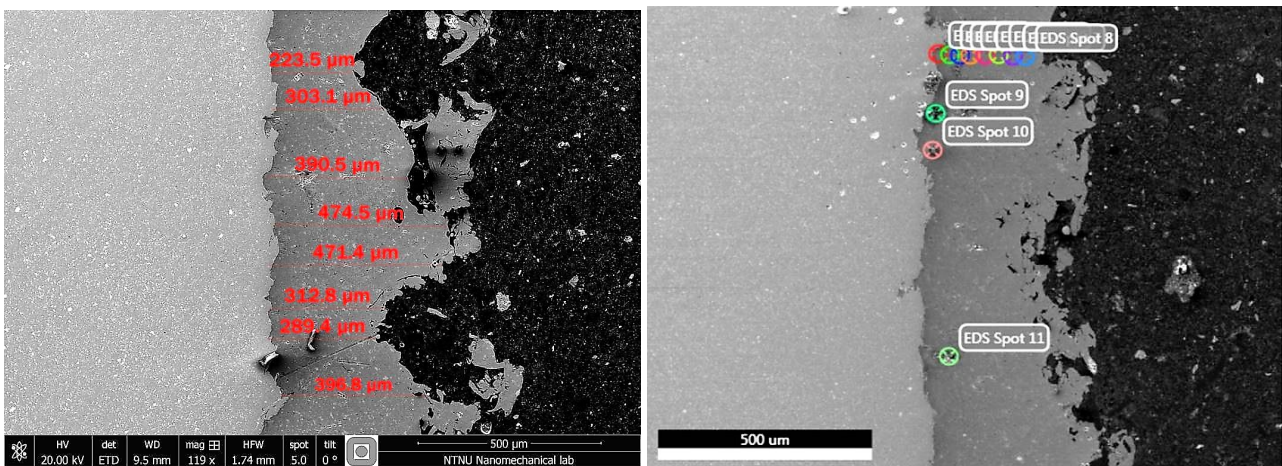


Figure 7.16: Left: Cross section measurements of unexposed TSA sample, Right: Areas/Spots for EDS.



Table 7.2: Results from EDS of selected points on unexposed TSA sample.

Element [wt%]	Spot 1	Spot 2	Spot 4	Spot 5	Spot 6	Spot 8	Spot 11
O	6.19	-	0.46	0.7	-	-	1.37
Al	91.4	95.86	99.54	99.3	100	100	89.73
Fe	2.41	-	-	-	-	-	4.12
Si	-	4.14	-	-	-	-	4.78
Total	100	100	100	100	100	100	100

## 7.4 Post Exposure

### 7.4.1 Samples exposed at 22°C

Figure 7.17 shows cross sections and measurements of representative areas and selected areas/spots for EDS examination on galvanic coupled DSA sample.

Table 7.3 shows the results from selected points and areas on Figure 7.17 (Right) from the EDS examination. It shows increased content of Fe close to the DSA/CS interface and surprisingly contents of Ar at some locations.

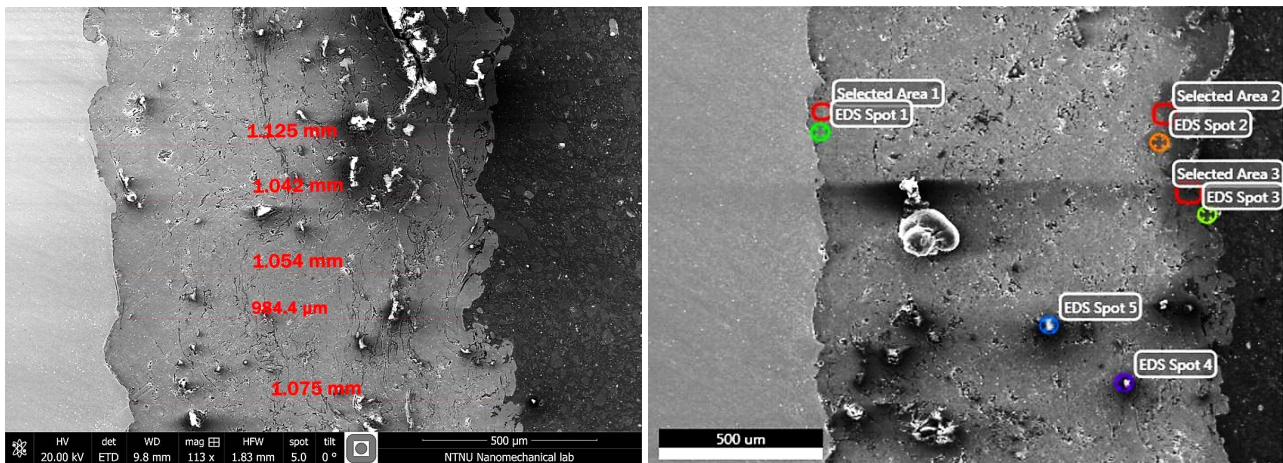


Figure 7.17: Left: Cross section measurements of galvanic coupled DSA sample. Right: Areas/Spots for EDS.

Table 7.3: Results from EDS of selected points and areas on galvanic coupled DSA sample.

Element [wt%]	Area 1	Spot 1	Area 2	Spot 2	Area 3	Spot 3	Spot 4	Spot 5
O	4.21	1.81	9.25	4.39	10.61	4.31	55.57	48.37
Zn	0.27	-	3.84	1.9	2.62	1.95	0.5	0.49
Al	91.4	94.49	80.04	77.61	75.72	92.14	39.12	48.14
Si	1.83	0.98	6.08	15.47	10.19	0.56	0.28	1.1
Ar	1.04	1.25	0.73	0.63	0.85	1.05	-	-
Fe	1.25	1.46	-	-	-	-	-	-
In	-	-	0.07	-	-	-	-	-
S	-	-	-	-	-	-	4.53	1.67
Cl	-	-	-	-	-	-	-	0.24
Total	100	99.99	100.01	100	99.99	100.01	100	100.01

Figure 7.18 shows cross section measurements and possible crevice corrosion (Left) and selected areas/spots for EDS examination (Right) on galvanic coupled TSA sample at 22°C.

Table 7.4 shows the results from selected points and areas (Figure 7.18) from the EDS examination. It shows increased content of Fe close to the TSA/CS interface and contents of Ca and Mg at some locations, indicating precipitation of calcareous deposits.

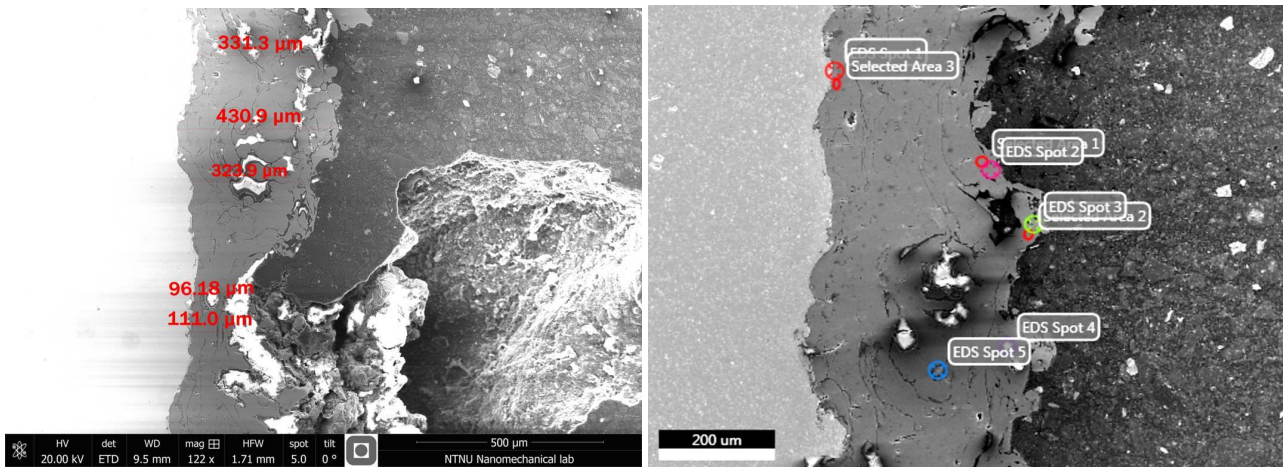


Figure 7.18: Left: Cross section measurements of galvanic coupled TSA sample at 22°C with significant degradation beneath rubber gasket. Right: Areas/Spots for EDS.

Table 7.4: Results from EDS of selected points and areas on galvanic coupled TSA sample at 22°C.

Element [wt%]	Spot 1	Area 1	Area 2	Area 3	Spot 2	Spot 3	Spot 4	Spot 5
O	0.81	0.91	1.71	1.81	3.37	1.55	32.32	51.53
Al	97.15	97.42	96.65	96.18	95.05	97.28	60.85	39.26
Ar	1.27	1.33	1.26	1.29	1.23	1.17	-	-
Fe	0.76	0.34	-	0.72	0.35	-	-	-
Si	-	-	0.38	-	-	-	1.58	0.32
S	-	-	-	-	-	-	4.76	5.93
Ca	-	-	-	-	-	-	0.49	-
Mg	-	-	-	-	-	-	-	0.77
Cl	-	-	-	-	-	-	-	1.99
Total	99.99	100	100	100	100	100	100	99.8

The chemical composition of the freely exposed samples at 22°C shows similar content compared with the coupled samples. Contents of Fe is detected close to the DSA/CS and TSA/CS interface, while the contents close to/at the edges mainly are C, Si and S. Carbon can be from ethanol or from the embedding material. It is not very well understood why the the composition shows Si and S. It can be from impurities in the coating or from the embedding material. Mg and Ca are located at a few spots, which indicates precipitation of calcareous deposits on the TSA and DSA coatings.

Cross section measurements and EDS of the freely exposed samples at 22°C are included in Appendix C.

## 7.5 Samples exposed at 50 and 80°C

The chemical composition of the samples at 50 and 80°C shows overall similar content compared with the samples at 22°C. Contents of Fe is detected close to the DSA/CS and TSA/CS interface, while the contents close to/at the edges mainly are C, Si and S. Presence of carbon can be from ethanol or from particles from the embedding material. It is not very well understood why the the composition shows Si and S. It can be from impurities in the coating or from the embedding material. Mg and Ca are located at a few spots and areas, which indicates precipitation of calcareous deposits on the TSA and DSA coatings.

Cross section measurements and EDS of the samples at 50 and 80°C are included in Appendix C.

## 7.6 Thickness evaluation in SEM

The cross section thicknesses of TSA and DSA coating of samples are presented in this section. The prior exposure results are based on cross section analysis in SEM of one unexposed sample of TSA and DSA. The overall impression for the unexposed samples is that DSA sample coating shows a uniform thickness, while the TSA sample coating shows erratic thickness appearance.

The post exposure results are also based on one cross section analysis in a representative area of the exposed part of the coating. Cross section measurements at areas where cohesive failure was present were not performed. Due to the roughness of the coating and substrate, the average values have been given in a range which represents the whole coating area. Minimum values are also given, which show the lowest thickness measured at local areas of the coating. Local areas of degradation were found at some locations beneath the rubber gaskets and blue silicone gel. These results have been included in the table below. Table 7.5 and Table 7.6 show the results for the respective DSA and TSA samples included in the cross section analysis.

Table 7.5: Cross section thickness results for exposed DSA samples at 22, 50 and 80°C.

Temp. [°C]	Sample	Prior Exposure		Post Exposure	
		Min. [µm]	Av. [µm]	Min. [µm]	Av. [µm]
22	OCP	900	1000 - 1100	795	950 - 1100
	Coupled			980	1000 - 1100
50	OCP			905	950 - 1100
	Coupled			904	950 - 1100
80	OCP			975	1000 - 1100
	Coupled			960 <sup>1)</sup>	975 - 1100

1) 175 - 250 µm in crevice.

Significant deviations are present within the results in Table 7.5. The freely exposed DSA sample at 22°C shows highest thickness reduction when looking at the minimum thickness at a local area, while the minimum thickness values on the other exposed samples show increased thicknesses compared with the prior exposure result. The average thickness values post exposure show no decreased thicknesses, particularly for the higher range of the average results. The coupled DSA sample at 80°C shows significant thickness reduction at large areas in the crevice.

Significant deviations are also present within the results in Table 7.6. The average thickness appears to be very similar prior and post exposure. When looking at the minimum thickness prior exposure, it gets difficult to predict coating degradation. Significant thickness reduction in crevice is detected on coupled TSA samples at all temperatures. Increased temperature seems to give more severe degradation within the crevice.

Table 7.6: Cross section thickness results for exposed TSA samples at 22, 50 and 80°C.

Temp. [°C]	Sample	Prior Exposure		Post Exposure	
		Min. [µm]	Av. [µm]	Min. [µm]	Av. [µm]
22	OCP	135	200 - 400	215	250 - 400
	Coupled			170 <sup>1)</sup>	200 - 400
50	OCP			106	250 - 400
	Coupled			124 <sup>2)</sup>	180 - 400
80	OCP			143	200 - 400
	Coupled			180 <sup>3)</sup>	200 - 400

1) 95 µm in crevice, 2) 0-40 µm in crevice, 3) 0 µm in crevice,





---

# Chapter 8

## Surface Examination - Mud Exposure

### 8.1 Visual Examination

This Section presents the visual examination of the samples embedded in mud, prior and post exposure.

#### 8.1.1 Prior Exposure

Figure 8.1 shows the initial surface conditions of the samples. The DSA and TSA surface appear rough and compact. The DSA surface appear slightly brighter compared with the TSA samples, while the CS surfaces are smooth and shiny.

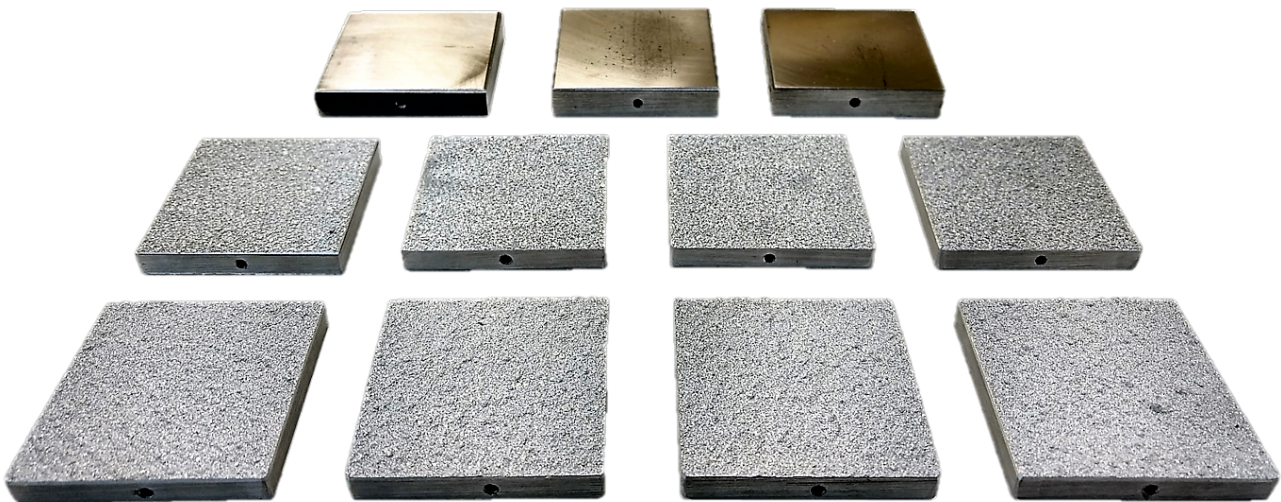


Figure 8.1: Test samples prior exposure in mud -Top: CS samples, Middle: TSA samples, Bottom: DSA samples.

Since the samples used for the Mud Exposure test were cut from a different DSA and TSA plate, "new" (unexposed) samples were cut, embedded and grinded in order to document the initial thickness and chemical composition of the coatings. Figure 8.2 shows the cross section of a new DSA and TSA sample. They appear similar with the new samples for the exposure at elevated temperatures.

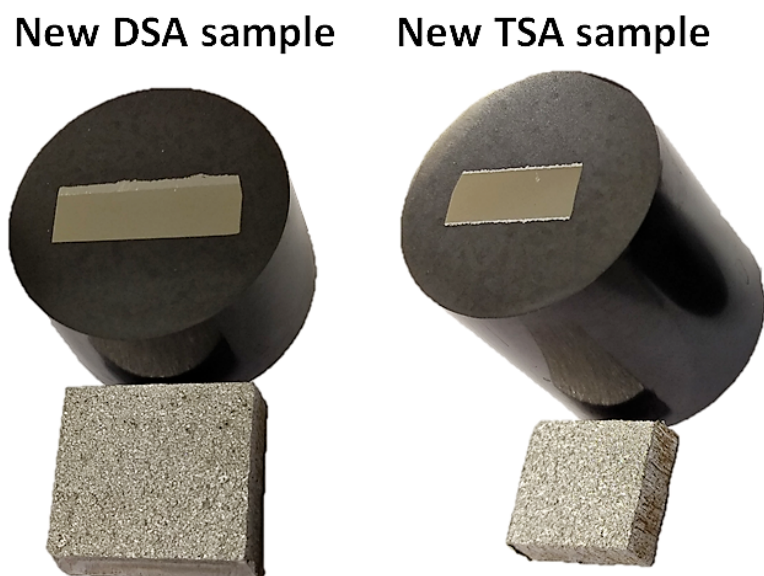


Figure 8.2: Cross sections of new DSA and TSA sample -Left: DSA sample, Right: TSA sample.

### 8.1.2 Post Exposure

When the samples were dug up from the mud, there were significant amount of mud attached to the rough surfaces of the DSA and TSA samples. It appeared that the mud was better attached to the polarized samples compared with the other samples. A strong smell of sulfur was generally noticed when the samples were collected from the mud and seawater. It appeared that the smell was strongest from the mud that was attached to the polarized DSA and TSA samples.

The coating on all samples appeared to be in overall good condition. The coupled CS surfaces and freely exposed CS surface also appeared to be in good condition i.e. no brown corrosion products observed. However, due to transportation of samples in plastic bags from SeaLab to Perleporten, the CS surfaces experienced some light corrosion. Since the CS surfaces overall appeared well at first, no pictures are presented of them.

It was observed that the bottom part of shrinking tube (above the coating), which was embedded in mud had some brown color. It appeared to have similar color with light corrosion products from iron.

Figure 8.3 shows the surfaces of the exposed samples in mud after the cleaning process which is described in Section 4.2.7, however prior to the cleaning with Nitric Acid. The coupled DSA sample appear to be in overall good condition. Some altitude difference is however observed on the surface, possible due to corrosion providing protection current, or due to cohesive failure within the coating. The color is slightly darker compared with an unexposed sample, and some cracks are visible at the edges of the coating.

The coupled TSA sample shows some dark spots on the surface, which did not fell off during the cleaning and brushing process. One of the dark spots was scraped off and poured into dilute hydrochloric acid. It bubbled vigorously in the start and the content smelled sulfur, indicating possible microorganisms.

The polarized DSA and TSA samples appear significantly darker compared with the unexposed samples, however no significant degradation was observed. The freely exposed samples appear to be in good condition, with no discoloration.

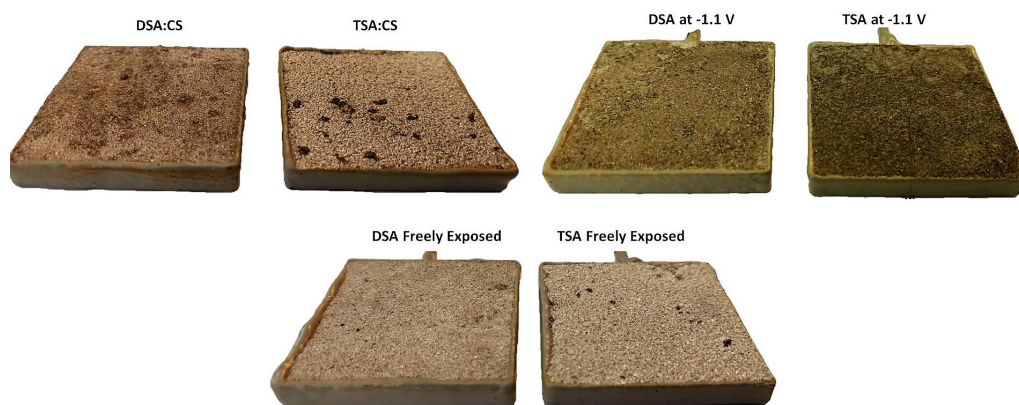


Figure 8.3: Samples embedded in mud after rinsing and brushing.

The samples were further cleaned once in Nitric Acid. The polarized DSA and TSA samples experienced heavy activity when immersed in Nitric Acid, while the other samples experienced limited activity.

Figure 8.4 shows the samples after cleaning with Nitric Acid. It shows limited difference compared with the samples before the cleaning. However, it seems like the black points and areas on the coupled samples have been removed. The polarized samples appear to some extent similar, however slightly brighter. The black spots on the freely exposed samples have been removed.



Figure 8.4: Samples embedded in mud after cleaning in Nitric Acid.

## 8.2 EDS of Cross Sections

### 8.2.1 Prior Exposure

EDS of cross sections on new DSA and TSA samples show similar contents with unexposed samples for the exposure at elevated temperatures. Some contents of zinc is found in the DSA coating, while indium is generally not found. Contents of Iron is found close to the TSA/CS and DSA/CS interface.

Cross section measurements and EDS of the new samples to be embedded in mud are included in Appendix D.

## 8.2.2 Post Exposure

EDS of exposed TSA and DSA samples shows some contents of Mg and Ca close to / at the exposed surface of the coating. It seems that there is no significant difference depending on if the samples were coupled with CS, polarized to -1.1 V Ag/AgCl or freely exposed in the mud.

Cross section measurements and EDS of exposed DSA and TSA samples embedded in mud are included in Appendix D.

## 8.3 Thickness evaluation in SEM

The cross section thicknesses of TSA and DSA coating of samples are presented in this section. The prior exposure results are based on cross section measurement in SEM of one unexposed sample of TSA and DSA. Since the TSA sample had coating on both sides, they were measured on each side.

The post exposure results are based on one cross section measurement in a representative area of the exposed part of the coating. The average values have been given in a range which represents the whole coating area. Minimum values are given, which show the lowest thickness measured at local areas of the coating. Table 8.1 shows the results for both DSA and TSA samples included in the cross section analysis.

The table does not show any significant deviation in average thickness. Some degradation in average thickness for the polarized DSA sample is plausible, but uncertain. It is difficult to detect degradation of TSA samples in mud since it appears that the coatings have slightly different thicknesses on opposite sides of the samples. Which side of the coating that has been exposed is uncertain. It is visible that both sides have very low thickness at local areas on both new and exposed TSA coatings.

Table 8.1: Cross section thickness results for DSA and TSA samples embedded in mud.

Sample	Prior Exposure		Post Exposure	
	Min. [ $\mu\text{m}$ ]	Av. [ $\mu\text{m}$ ]	Min. [ $\mu\text{m}$ ]	Av. [ $\mu\text{m}$ ]
DSA:CS	900	1000 - 1150	850	1000 - 1150
DSA OCP			800	950 - 1150
DSA POL			860	900 - 1100
TSA:CS	50 <sup>1</sup>	150 - 300 <sup>1</sup>	35	100 - 250
TSA OCP	40 <sup>2</sup>	100 - 250 <sup>2</sup>	120	200 - 300
TSA POL			85	150 - 250

1) At one side of sample. 2) At the opposite side of the sample.

---

# Chapter 9

## Discussion - Elevated Temperatures in SW

### 9.1 Effect of pH

The effect of pH (from replacement of SW) in the 80°C container affects the OCP measurements on especially the TSA and DSA samples. Initially, it seems to cause an even faster increase in potential. This is highlighted in Figure 5.4, where OCPs of TSA and DSA are plotted vs. measured pH. The reason why pH decreases most significantly in the 80°C container and not the 22°C or 50°C container is uncertain. However, concerns over utilizing aluminum alloy anodes in sealed environments were addressed in 2017 [47], where it was found that use of Aluminum anodes for CP in stagnant water environments within offshore monopiles can result in a reduction in water pH over time. One of the possible reasons, amongst others, was believed to be [47];

*a) Hydrolysis of Aluminium anode corrosion products to produce acidic conditions in the immersed environment. The pH of the environment will decrease as the Aluminium ion concentration increases.*

This thesis does not further address this problem, but the effect of decreased pH is however highlighted. The reason why the pH drops more significantly in the 80°C container, can be increased corrosion products observed in the protrusions of this container where the coupled samples were attached (Figure 7.3).

Figure 9.1 shows a suggestion for development of OCP on 80°C samples based on a pH level of approximately 8, which is assumed applicable for natural seawater. It should be noted that this is purely based on the pH-measurements and measured potential response, from which is highlighted in Figure 5.4. This prediction is highly uncertain, but is however included. The response on the anode sample is only observed at day 10. The anode sample responds probably different since it is an alloy and not a thermally sprayed coating.



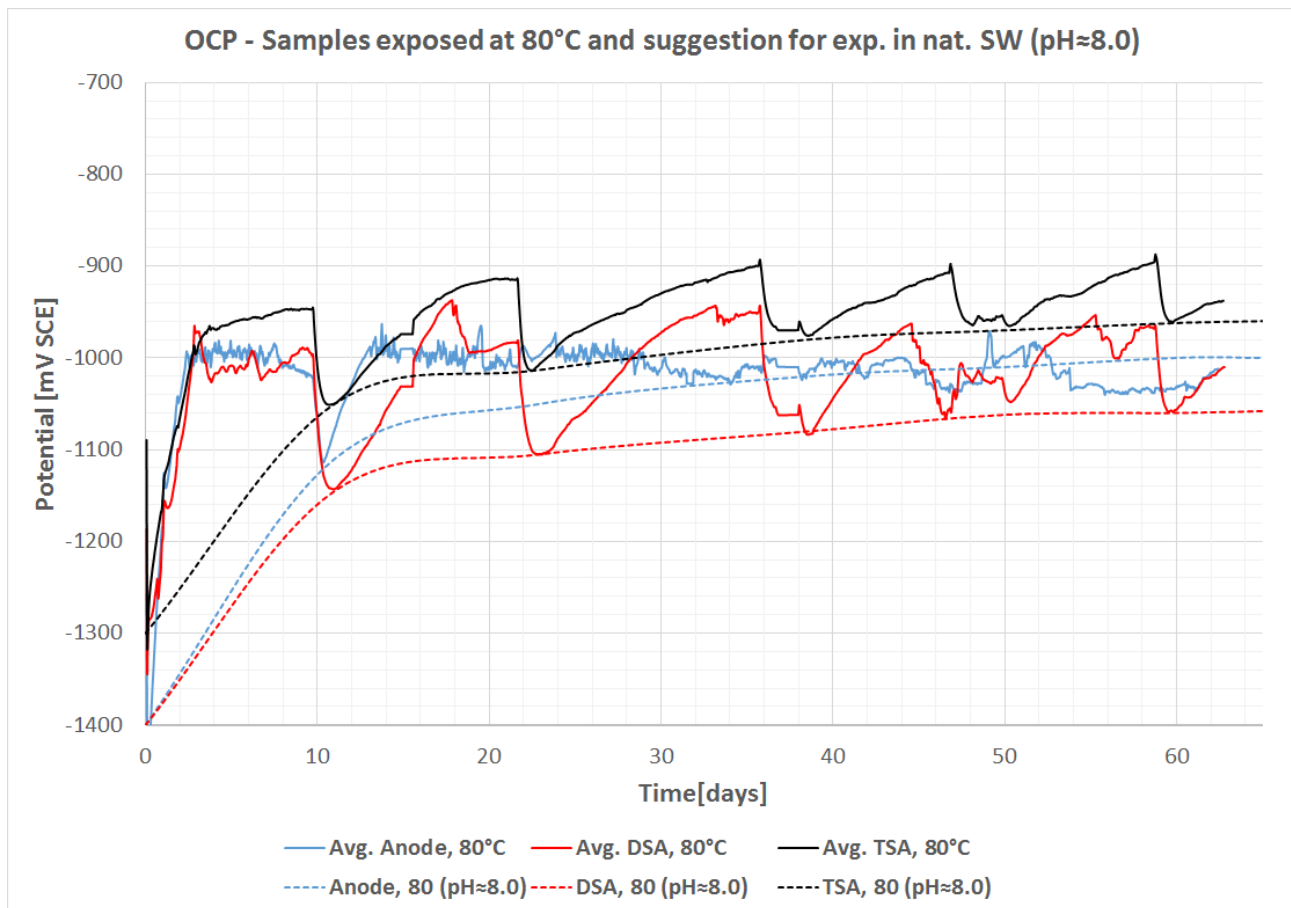


Figure 9.1: Suggestion for OCP development of samples at 80°C assumed applicable for real exposure conditions in natural SW.

Some response in OCP from pH change is also visible for the 50°C samples at day 10 (Figure 5.2). This reflected a pH increase from 7.9 to 8.3 (Figure 5.1). From this point, limited response is detected in the graphs, probably due to overall stable pH measurements throughout the exposure.

The combined effect of the pH decrease and high temperature in the 80°C container is that this probably have caused the samples to create a passivating oxide layer more quickly. The following was written in Section 2.2, about the effect of temperature on pH range, where the oxide layer is stable:

*"The temperature affects the stability of the oxide layer. The general trend at high temperatures is that the oxide is stable within a narrower pH-range and that it shifts to left towards a more acidic solution. This means that the danger of corrosion increases in alkaline and neutral environments with increasing temperature [6]."*

This effect seems to fit well with what is observed in the measurements, but the pH drop will however not reflect real exposure conditions at elevated temperatures in SW.

The effect of temperature, pH and potential on corrosion properties of AA5083 and AA6082 was investigated by Nese in his Msc Thesis [48]. He measured the OCP development of AA5030 and AA6082 in synthetic SW with a pH level of 3 at room temperature and compared them to OCP development in a similar setup but with different pH-values (pH = 8.2, and pH = 10). The results showed that the OCP increased by approximately 140 to 180 mV, when the pH was decreased from 8.2 to 3. Similar trends with regards to pH drop are found in this thesis, but with a shorter pH drop. The combined effect with high temperature seems to cause a significant potential drop at all times when pH is rising. This probably indicates that the range where the oxide layer on DSA and TSA are stable are dependant on the temperature which can be seen in Figure 2.7 in Section 2.2.1.

Table 9.1: A summary of electrochemical properties of freely exposed and coupled samples after 63 days with a suggestion for OCPs for pH $\approx$ 8.0 for the 80°C container.

	TSA			DSA			Anode		
	22	50	80	22	50	80	22	50	80
Temperature [°C]									
OCP [mV SCE]	-858	-979	-938	-1007	-1017	-1010	-956	-982	-1010
OCP at pH $\approx$ 8.0 [mV SCE]	-	-	-960	-	-	-1060	-	-	-1000
OCP Pol. Curv. [mV SCE]	-878	-995	-948	-1028	-1037	-1012	-960	-1014	-1023
Pitting Potential [mV SCE]	-625	>500	>500	-1025	-1025	-875	-950	-950	-1000
Anodic Behavior [Act., Pass., Act/Pass]	Pass.	Pass.	Pass.	Act.	Act.	Act./Pass.	Act.	Act.	Act.
Anodic Tafel Constant, ba [mV/dec]	160	160	225	60	90	85	60	40	80
Cathodic Tafel Constant, bc [mV/dec]	-150	-95	-125	-80	-105	-80	-110	-95	-120
Corr. Curr. Dens. Pol. Curv. [mA/m <sup>2</sup> ]	5,5	1,5	4	6	5	2,6	0,8	1	7
Corr. Rate, Pol. Curv. [µm/year]	6,65	1,81	4,84	6,63	5,52	2,87	0,8	1	6,97
Corr. Curr. Dens. LPR. [mA/m <sup>2</sup> ]	-	-	-	5,06*	0,96*	1,71*	-	-	-
Corr. Rate, LPR [µm/year]	-	-	-	5,59*	1,05*	1,89*	-	-	-
Couple Potential [mV SCE]	-1020	-960	-970	-840	-820	-800	-	-	-
Galv. Curr. Dens. [mA/m <sup>2</sup> ]	46	48	98	40	22	66	130	8	230
Galv. Corr. Rate. [µm/y]	50,83	53,03	108,28	48,38	26,61	79,83	129,52	7,97	229,14

## 9.2 Electrochemical Properties after 63 days

If we assume that the suggestion in Figure 9.1 is applicable and consider a pH level of 8.0 in the 80°C container, we will get adjusted OCP values compared to Table 5.6 in the results section. Table 9.1 shows the electrochemical properties after 63 days and an additional row for the adjustment of OCP values for the samples in the 80°C container. It is difficult to adjust other electrochemical properties to the pH change, but since it is likely that the decrease in pH has caused more passivating behaviour compared with a stable pH value of  $\approx 8.0$ , we should probably expect increased corrosion current densities at OCPs and increased corrosion rates since the potential much more likely will be more negative throughout exposure (Figure 9.1).

## 9.3 Open Circuit Potential

### Unexpected OCPs

Some unexpected results have occurred. They are listed in the beginning of this section so that they are highlighted.

The OCP measurement on freely exposed TSA sample at 50°C do not show expected results (Figure 5.2). It shows similar behaviour compared to the DSA sample, or a potential which is slightly less compared with the DSA sample at 50°C from start of exposure until approximately 30 days. From this point, the potential is slightly more positive compared to the DSA sample throughout exposure. The reason for the more negative potential can not be explained well. A mix-up between the TSA and DSA sample was at first believed to be the explanation, but was quickly neglected. The TSA samples have coating on the unexposed side, while the unexposed side of the DSA sample is bare. The polarization curve on the TSA sample at 50°C (Figure 5.14) shows expected behaviour with respect to passive anodic behaviour. No significant difference in chemical composition was found in EDS of cross section of this sample compared to the other TSA samples. (See Appendix C)

The OCPs on Anode samples at 22°C and 80 °C show fluctuating behaviour. It starts at -1100 mV SCE, and evidently starts to fluctuate after a short time. This was believed to be a result from bad connection or faults in the datalogger cable in the beginning of exposure. It was attempted to rectify the apparent failure, but the measurements are correct. It appears that the potential moves within a certain range for the anode samples. According to supervisor, this has occurred on some OCP measurements of anode samples at in house experiments at NTNU. The polarization curves of Anode samples show OCPs which match. The end potential for the Anode sample at 22°C is -956 mV SCE. This deviates from what Quale measured in his M.Sc. thesis [12]. He measured stable OCP at  $\approx -1100$  mV Ag/AgCl for anode samples at 10°C for an exposure period of 2 months. This should correspond measurements at  $\approx -1145$  mV SCE. A possible explanation for the unexpected high potential on 22°C Anode sample is that the surface gets passivated due to stagnant conditions in the protrusion.

### Effect of Time

The development of the OCPs for freely exposed DSA and TSA samples (Figure 5.2) with regards to exposure period (time) follow the same trend as for the OCP development seen in Figure 2.9, for flame sprayed aluminum during exposure in SW [5].

All samples experience a decrease in potential in the beginning of exposure (first 1-2 days), before an increase in OCP is observed on all DSA and TSA samples during exposure period. The reason for this is explained in Section 2.3:

*Intermetallic particles that are present in TSA due to spraying process or impurities will initially cause high corrosion rates. This is because the particles are causing weakened spots for formation of*



*the oxide, if they are electrochemically more noble than aluminum. The resulting corrosion mechanism is pitting, which was described in Section 2.2.2. The mechanism is mainly localized and will have greatest impact in the start of exposure. The micropits which are initiated around the particles increase the exposed area of the cathodic particles. The effect from this can be seen from Figure 2.9, where the potential significantly drops from above -900 mV SCE to below -1050 mV SCE. During exposure, repassivation of the oxide will occur, due to removal or undermining of the intermetallic particles. This represents the slow increase in potential throughout the exposure period. [5, 4]*

The slow increase in potential can also be seen in correlation with corrosion products which probably fill the pores in the coating (since no sealer was applied), and work as a barrier between the SW and surface, causing passivating behaviour.

### **Effect of Temperature**

The general effect of increased temperature is that the OCPs are more negative. This is in agreement with what Gartland states in "Protective properties of Al-based Coatings in seawater" about TSA [5]:

*The general effect of increasing seawater temperature on the TSA-coating will be to decrease the free corrosion potential.*

It is observed from Figure 5.2 that increased temperature gives lower initial potentials (i.e. more negative) for the freely exposed DSA and TSA samples in the beginning of exposure. This is believed to be due to increased kinetic reactions from anodic dissolution and increased cathodic current densities related to oxygen reduction. More negative potentials initially (day 1 - 3) as a function of increased temperature fits well with what Fischer et. al.[10] found which is listed in Table 2.1. The increased level of kinetic reactions as a function of temperature is probably best explained from Nernst Equation 2.7.

The difference in OCP as a function of increased temperature is however decreasing throughout exposure period. This is probably due to reduced level of kinetic reactions as the surfaces become passivated throughout exposure, due to removal or undermining of intermetallic particles and filling of corrosion products in the pores of the coatings, which was explained in previous Section (Effect of Time).

If assuming that the adjustment of OCP from the pH measurements made in Figure 9.1 from Figure 5.4 is applicable, the end potentials after 63 days show that increased temperature give overall more negative potentials on all samples.

Wilson, in his M.Sc. thesis [38] found that high temperatures initially will cause TSA to have very negative OCPs. TSA samples with a surface temperature of 60 and 45°C dropped down to -1200 and -1100 mV Ag/AgCl ( $\approx$  -1245 and -1145 mV SCE) respectively, before they increased to  $\approx$  -940 and -910 mV vs Ag/AgCl ( $\approx$  -985 and -955 mV SCE) after approximately 40 days. He found some instances where the OCPs in the end (40 days) were more positive with increased temperature. More negative potentials initially as a function of increased temperature is similar to the results in this thesis. The end OCPs in this thesis are overall more negative as a function of increased temperature. The results in this thesis fits more with Thomason [23] results. He found that OCPs of TSA samples at 60°C stabilized at a more negative value compared to samples exposed at 8°C.

### **Effect of type of coating**

The effect of type of coating is significant, if the unexpected OCP measurement of the TSA sample at 50°C is neglected. The OCPs of DSA samples are generally more negative compared to the TSA samples. The potential is approximately 120 to 200 mV more negative for the DSA sample vs. the TSA sample at 22°C throughout exposure, while the OCP is approximately 80 to 100 mV more negative for the DSA sample vs. the TSA sample at 80°C, if assuming that the adjustment with

regards to pH is applicable. The more negative potential for the DSA coating is caused by the alloying contents of Zn and In which shifts the OCP in the negative direction.

The OCPs of anode samples are overall more positive compared to the DSA samples at 22 and 50 °C after 63 days. This was overall not expected since the chemical composition of the DSA coating shows reduced amount of Zn and In compared to the conventional anode. It was expected that this would cause a more positive potential for the DSA coating compared with the bulk material (anode).

More positive OCPs for the Anode samples compared to the DSA samples was not what Quale found in his M.Sc. thesis [12]. He found that both anode (Al-Zn-In) and wire from anode showed OCPs approximately 80 to 90 mV more negative compared with the DSA sample at exposure in natural SW at 10°C.

## 9.4 Galvanic Coupled Samples

There are several causes which brings uncertainties and affects the galvanic coupling potentials and galvanic currents presented in Figure 5.5 and Figure 5.6, respectively.

### Crevice Corrosion

Significant crevice corrosion was found on coupled DSA and TSA samples at 80°C. This has probably caused the current to flow from the crevice to the exposed surface of the coatings in addition to bare steel, due to a expected potential difference in the crevice compared to the outside of the crevice. This makes the crevice an anode and the outside surface a cathode as explained in Section 2.2.3. This makes it hard to predict coating degradation at the exposed area. As a result, the galvanic current density measurements are practically useless for these coupled samples. The following was written in the theory section about the effect of Temperature:

*It has been found that the susceptibility to pitting and crevice corrosion may increase at elevated temperatures and pressure together with chloride content. [4]*

With regards to elevated temperatures and chloride content, this is exactly what has happened in this thesis. Crevice corrosion seems to be a significant issue at elevated temperatures. This may be a limitation in the experiment design, due to the rubber gasket and blue silicon gel. The reason why this seems to be a higher concern for the coupled samples, and not the freely exposed samples has not been found.

### Cohesive Failure

All coupled DSA samples at all temperatures showed signs of cohesive failure. One possible reason may be that the coating has cracked due to a build up of corrosion products in the pores. Sealer application may prevent this problem. However, this was overall not expected and the reason why has not found in this thesis.

### Corrosion Products in Protrusion

Large amounts of corrosion products in the protrusions of the container are visible post exposure. Increased temperature seems to cause increased amount of corrosion products in the protrusions. This is believed to cause more stagnant conditions in the protrusions, as well as increased resistance through the protrusions which should limit the coatings ability to provide protection currents. As discussed in Section 9.1, it probably also affects the pH of the SW.

### Effect of Area Ratios

The effect of area ratios between the exposed surface of coating surface and exposed surface of CS cubes are of significant importance with regards to galvanic coupled potentials as well as galvanic currents.

The area ratios used means that the holidays (damage) of the coatings actually are bigger (almost twice as big,  $\approx 200\%$ ) compared to the rest of the intact coating. This is in general an unlikely scenario at real exposure conditions. However, the effect of area ratios will highlight the ability of the coatings to provide protection currents to holidays, which will show the ability of the coatings to provide CP.

#### 9.4.1 Galvanic Currents and Potentials

The galvanic coupled samples in the beginning of exposure (Figure 5.6), exhibit very large current densities in the beginning of exposure. Increased temperature does seem to cause elevated current densities. This effect is believed to be from bare steel which drains current on the whole surface as well as increased temperature affects the kinetics on both CS and the coupled samples.

#### Effect of time

The high current densities present in the beginning of exposure on all couplings at all temperatures, are probably due to the following reasons:

- Corrosion around intermetallic particles present at the surface of the coatings.
- Bare steel surfaces with no calcareous deposits, which drains current on the whole surface

Cathodic current densities on CS will induce oxygen reduction, which increases the interfacial pH. The following was written in Section 2.5 about CP of CS:

*Various forms for calcareous deposits will form on CS in seawater during CP. They consist mainly of  $\text{CaCO}_3$ ,  $\text{MgCO}_3$  and  $\text{Mg(OH)}_2$ , which will precipitate when the solubility of calcium and magnesium ions is exceeded. They form at pH levels between 8 and 10 and since natural seawater normally are supersaturated in calcium carbonates, precipitation of these are most likely to form. [25]*

*Calcareous deposits will precipitate over time and lower the current demand from anodes during exposure because they will build up and act as a barrier/insulation between the CS surface and seawater.[28, 29, 25]*

This fits well with what is observed in this thesis.

#### Effect of Temperature

The galvanic coupled potentials (Figure 5.5) increases (i.e. turn more positive) with increased temperature for both coupled DSA and TSA samples, and they are increasing slightly throughout exposure period. The effect is visible on the coupled DSA sample at  $22^\circ\text{C}$  vs. the  $80^\circ\text{C}$  sample, where the potential is  $\approx 50$  to  $75$  mV more negative for the lower temperature.

This is probably best explained from the recorded polarization curves obtained on freely exposed DSA and TSA samples after 63 days (Figure 5.10 and Figure 5.11). Table 9.2 shows the galvanic couple potential and galvanic current densities after 65 days of exposure, compared to similar applied potential from the polarization curves and galvanic current densities. These values should in theory be approximately similar, but the results differ. The galvanic current density values are generally almost a magnitude larger compared to the current density values from the Polarization Curves at the same potential. The only sample that shows approximate similar values is the DSA sample at  $50^\circ\text{C}$ .

Table 9.2: Galvanic Couple Potentials and Galvanic Current Densities after 65 days of exposure, vs results from Polarization Curves obtained after 63 days of exposure.

Temperature [°C]	DSA			TSA		
	22	50	80	22	50	80
<b>Galv. Cou. Pot. [mV SCE]</b>	-1020	-960	-970	-840	-820	-800
<b>Galv. Curr. Dens. [mA/m<sup>2</sup>]</b>	40	22	66	46	48	98
<b>Galv. Corr. Rate. [µm/y]</b>	48.38	26.61	79.83	50.83	53.03	108.28
<b>Appl. Pot. Pol.Curv [mV SCE]</b>	-1020	-960	-970	-840	-820	-800
<b>Curr. Dens. Pol.Curv [mA/m<sup>2</sup>]</b>	4	20	7	7	7	15
<b>Corr. Rate. Pol.Curv. [µm/y]</b>	4.42	22.1	7.73	8.47	8.47	18.14

Crevice corrosion and cohesive failure on galvanic samples activates probably more surface which cause increased current density. Another reason can be that the galvanic coupled samples in general have a more active surface compared to the samples at OCP. Even though the freely exposed samples are anodically polarized, some parts of the surface are probably still passive. This causes probably lower current densities.

Increased temperature does seem to give slightly increased passivating behavior with a more positive pitting potential for the DSA samples. This is evident from the Polarization Curves of freely exposed DSA samples in Figure 5.10.

According to Ezuber et al. [7] should an increase in SW temperature cause a negative shift in OCP and a decrease in pitting potential as well as increased passive current densities (Figure 2.8). This was what Ezuber et al. found in a study on the corrosion behavior of aluminum alloys (AA5083 and AA1100) in SW [7]. These trends do not fit with the polarization curves recorded on DSA and TSA in this thesis. The Polarization curves of Anode samples after 63 days (Figure 5.12) show similar trends on the other hand.

### Effect of type of coating

The effect of galvanically coupled DSA vs. galvanically coupled TSA is significant. The couple potential is approximately 140 to 200 mV more negative for the coupled DSA samples vs. the coupled TSA samples at all temperatures. This means that the coupled DSA samples provide more protection currents compared to the coupled TSA samples.

It is evident from Figure 5.6 that the coupled DSA samples provide generally higher current densities compared with the coupled TSA samples throughout exposure. This is a result from the contents of Zinc and Indium which has a synergistic effect as explained in the theory section:

*Zinc and Indium effects electrochemical properties of a traditional aluminum anode by shifting the pitting potential to more negative values, i.e. in the cathodic direction. Zinc has a synergistic effect with small contents of In, which causes the oxide layer on Aluminum to destabilize and crack, hence activating the alloy at lower potentials. [30, 31]*

The effect of Zinc and Indium in the DSA coatings is significant from the Polarization Curves recorded on freely exposed DSA samples in Figure 5.10 compared to the Polarization Curves recorded on freely exposed TSA samples (Figure 5.11) after 63 days of exposure.

This is similar with what Quale found in his M.Sc. thesis [12]. He found that the anodic behavior was more active for a DSA coating compared to a TSA coating.

The difference in anodic behavior is not so evident when comparing polarization curves of freely exposed DSA and Anode samples. According to polarization curves recorded for freely exposed samples at 22°C (Figure 5.13), the DSA sample provides most protection current from -1025 to -750 mV SCE. It is visible that the DSA sample has a potential which is more negative compared to the Anode sample.

This is not similar with what Quale found in his M.Sc. thesis [12]. He found that the anodic behavior for a DSA coating was slightly less compared to an Anode coating. This was because he found the potential to be 80-90 mV nobler for the DSA coating compared to the Anode potential, caused by either reduced content of alloying elements (Zn and In) due to the thermal spraying process and due to increased oxidation properties of a DSA coating compared to an anode coating.

The difference in anodic behavior when comparing the freely exposed DSA and Anode sample is the opposite at 80°C. According to the polarization curves recorded for freely exposed samples at 80°C (Figure 5.15), the Anode sample provides more current density from approximately  $\approx -1020$  mV and up compared to the DSA sample.

## 9.5 LPR measurements

The LPR measurements are generally not very reliable due to the following reasons:

- The potential drop shows fluctuating behaviour for the DSA samples at 50 and 80°C from day 8 throughout exposure.
- The selected potential drop value is selected based on an average value from the fluctuating data.
- The  $R_p$  in cathodic and anodic directions, deviates significantly at some measurements, affecting the average  $R_p$  values, and hence the corrosion rate calculations.
- The LPR measurements for the 80°C DSA sample is probably taken at different pH levels, which causes limited consistency in the LPR measurements.
- Each measured value was obtained in a frequency of 10 seconds, which may have caused randomly selected values depending on whether the potential drop was on a positive or negative peak.

The difference in polarization resistance in the cathodic and anodic direction is probably best explained by the chemical composition of the DSA coatings. The surface is much easier activated in anodic direction due to the synergistic effect of zinc and indium in the coating as explained in Section 2.5.1. This is the reason why the polarization resistance is generally lower in the anodic direction.

The potential drops are in general quite low so the fluctuating behavior does probably not affect the corrosion rates significantly.

## 9.6 Corrosion Rates

### Effect of Time

The corrosion rates for all DSA samples were highest after 1 day of exposure, before they dropped significantly at day 8, and overall decreased slowly throughout exposure period. This is what is expected with respect to time development for TSC. The reason is similar to what is described in Section 2.3 (Corrosion of TSA). Intermetallic particles will contribute to high corrosion rates in the beginning, because they are causing weakened spots for formation of the oxide. The process is related to the significant drop in OCP, in the beginning of exposure, because the particles get more exposed as corrosion around these intermetallic particles occur. The corrosion rates are decreasing during time as these particles are removed or undermined from the surface and the surface is passivated more easily.

### Effect of Temperature

When comparing the corrosion rates to the OCP development in Figure 5.2, it is evident that increased temperature causes a more significant drop in potential and that it occurs faster at elevated temperature. It is generally realized that a more negative potential for TSC is associated with increased corrosion rates [39]. The reason is due to destabilized oxide layer due to pitting corrosion which occurs at low potentials according to the experimental Pourbaix diagram in Figure 2.5 (Right).

After  $\approx 1$  day of exposure, repassivation of the DSA sample at  $80^{\circ}\text{C}$  is in full progress and the potential is increasing rapidly and is actually more positive compared to the DSA sample at  $50^{\circ}\text{C}$ . Depassivation is in progress for the DSA sample at  $22^{\circ}\text{C}$  after 1 day, as reduced temperature evidently delays the corrosion mechanism around intermetallic particles. The corrosion rates in the beginning of exposure for the freely exposed DSA samples were initially  $\approx 61$ ,  $64$  and  $33 \mu\text{m}/\text{year}$  after 1 day for the  $22$ ,  $50$  and  $80^{\circ}\text{C}$  samples, respectively, based on LPR measurements and tafel constants from polarization curves after 63 days.

The behavior mentioned above is probably the reason why the corrosion rates from Figure 5.16 show lower corrosion rate for the DSA sample at  $80^{\circ}\text{C}$  compared to the samples at  $50$  and  $22^{\circ}\text{C}$ . It is therefore expected that elevated temperature initially should cause increased corrosion rates at the very beginning.

The effect of temperature on corrosion rates towards the end of exposure is less significant. According to the corrosion current densities from the graphical solution of recorded polarization curves of DSA samples, it is evident that increased temperature gives lower corrosion rates. The calculated corrosion rates after 63 days of exposure were  $\approx 6.5$ ,  $5.5$  and  $3 \mu\text{m}/\text{year}$  for the  $22$ ,  $50$  and  $80^{\circ}\text{C}$  sample, respectively. The corrosion rates after 63 days for the freely exposed TSA samples were  $\approx 6.6$ ,  $2$  and  $5 \mu\text{m}/\text{year}$  for the  $22$ ,  $50$  and  $80^{\circ}\text{C}$  samples after 63 days, respectively. Only small differences are spotted between the TSA and DSA samples after 63 days of exposure.

Wilson, in his M.Sc. thesis[38] found corrosion rates for TSA which initially were  $50 \mu\text{m}/\text{year}$  decreasing to  $8 \mu\text{m}/\text{year}$  with a surface temperature of  $60^{\circ}\text{C}$ . These are similar trends compared to the results in this thesis.

Quale, in his M. Sc. thesis[12] found corrosion rates for DSA and TSA exposed at  $10^{\circ}\text{C}$ , which initially were  $70$  and  $39 \mu\text{m}/\text{year}$  (after 8 days). They decreased to  $31$  and  $17 \mu\text{m}/\text{year}$ , respectively after 30 days. These are also similar trends compared to the results in this. The corrosion rates in this thesis are generally lower compared to these results.

## 9.7 Thickness Evaluation

The results from thickness evaluation deal with great uncertainties when it comes to evaluating the coating degradation during exposure. The main reason is the uneven average coating distribution of the TSA samples shown in Table 7.5. The main reasons to this are that the prior exposure thickness is based on measurements on one cross section of one sample. This represents a very small area of the coating. The effect of crevice corrosion on samples as well as cohesive failure, makes the results unreliable. The effect of chemical dissolution does not seem to be significant. This makes it difficult to evaluate coating degradation as a function of temperature. The corrosion rates appear to be small as well, which probably are the reason why no significant coating degradation is visible. The effect of chemical dissolution does not seem to be a problem based on these results.

---

# Chapter 10

## Discussion - Exposure in Mud

Table 10.1 shows a summary of the electrochemical properties after 62 days of exposure.

Table 10.1: Summary of electrochemical properties of samples embedded in Mud after 62 days.

	TSA, Mud	DSA, Mud	CS, Mud
<b>Temperature, SW [°C]</b>	10	10	10
<b>OCP [mV Ag/AgCl]</b>	-890	-978	-709
<b>OCP Pol. Curv. [mV Ag/AgCl]</b>	-925	-971	-
<b>Pitting Potential [mV Ag/AgCl]</b>	-625	-900	-
<b>Anodic Behavior [Act., Pass., Act/Pass]</b>	Pass.	Act.	-
<b>Anodic Tafel Constant, ba [mV/dec]</b>	180	70	-
<b>Cathodic Tafel Constant, bc [mV/dec]</b>	-110	-140	-225
<b>Corr. Curr. Dens. Pol. Curv. [mA/m<sup>2</sup>]</b>	6.5	9	-
<b>Corrosion Rate, Pol. Curv. [µm/year]</b>	7.2	9.95	-
<b>Corr. Curr. Dens. LPR. [mA/m<sup>2</sup>]</b>	1.6	5	-
<b>Corrosion. Rate, LPR [µm/year]</b>	1.98	5.53	-
<b>Couple Potential [mV Ag/AgCl]</b>	-851	-916	-
<b>Galvanic Curr. Dens. [mA/m<sup>2</sup>]</b>	6.5	5.5	-
<b>Galvanic Corr. Rate. [µm/y]</b>	7.2	6.1	-
<b>Polarized Potential [mV Ag/AgCl]</b>	-1100	-1100	-
<b>Curr. Dens. Req., -1.1 V Ag/AgCl, [mA/m<sup>2</sup>]</b>	-14	-10	-

### 10.1 Open Circuit Potentials

The OCPs of DSA and TSA samples in Figure 6.1 show different development compared to exposure in SW at elevated temperatures. The main reason for this is different environment and reduced exposure temperature ( $\approx 10^\circ\text{C}$ ). It is evident that DSA has a more negative OCP compared to the TSA. This is similar with exposure at elevated temperatures in SW. OCPs of both TSA and DSA increase shortly after exposure, before they decrease significantly after 3 and 6 days of exposure, respectively. The small potential rise on both TSA and DSA samples is probably best explained from exposed CS at the samples. The reason for this can be bare CS in the pores of the coating, or that the coating did not cover all edges of the samples efficiently. However, the potentials stabilize in a fairly range after approximately 25 days of exposure.

Data about OCP development for DSA in mud have not been found, but some data for TSA do however exist. Wolfson [16] performed four and twelve month exposure tests in mud extracted from the natural Gulf of Mexico sea mud. He coupled bare steel together with TSA coated steel,

in order to simulate coating damages/voids/holidays in the coating. He measured OCPs for the TSA coatings with holidays of 0, 3, 5 and 10%. The coatings had a thickness of  $\approx 254 \mu\text{m}$  and were sealed with silicone-aluminum sealer.

The OCP development in this thesis fits Wolfson OCP curves for TSA with holidays from four months and twelve months of exposure for the TSA coatings. This suggests that some CS was exposed on the samples, probably due to insufficient coating on the edges or exposed areas in the pores of the coatings. The TSA and DSA samples in this thesis were not sealed, while Wolfsons TSA samples were sealed.

However, the end OCPs obtained in this thesis for the TSA and DSA samples after 62 days of exposure show values of  $-890$  and  $-978 \text{ mV Ag/AgCl}$  respectively, while Wolfson obtained values at approximately  $-940$  to  $-980 \text{ mV SCE}$  ( $-895$  to  $-935 \text{ mV Ag/AgCl}$ ) for TSA after approximately 60 days of exposure. These are similar results compared to the results in this thesis. Type of alloy is unfortunately not given in Wolfsons report [16]. It is evident from Wolfsons results that increased holiday % gives more positive potentials. The TSA coating with 0% holiday was approximately 50 to 100 mV more negative compared to the TSA coatings with holidays according to Wolfson.

We should expect a slow increase in potential by prolonged exposure according to Wolfsons results. Increased level of holiday factor should increase the potential development for TSA samples. It is expected that the DSA coating will perform better in providing protection currents to large coating defects, compared to TSA coating due to a more negative potential (larger driving force) and a more negative pitting potential (Zn and In content). This is evident from the polarization curves obtained after 61 days of exposure in Figure 6.8 and data in Table 10.1.

## 10.2 Galvanically Coupled Samples

It is evident from Figure 6.4 (Galvanic Currents to/from CS) that the DSA sample provides increased level of protection current compared to the TSA sample during exposure. According to Figure 6.5 (Galvanic Couple Potentials) does this cause a significant decrease in potential for the galvanically coupled DSA sample especially in the beginning of exposure. This is another result proving that DSA is anodically more active compared to TSA. Effective cathodic polarization of the CS occurs in the beginning of exposure, while it seems to occur somewhat later and to a smaller degree for the coupled TSA sample. The reason for this is very likely due to the contents of zinc and indium which activates the surface more quick compared to the TSA sample. This is very evident from the polarization curves in Figure 6.8 which shows that the DSA sample is significantly anodically more active compared to the TSA sample.

It is visible that the CS require slightly less current density from DSA compared to TSA towards the end of exposure (Figure 6.4). The potential is however more negative for the galvanically coupled DSA sample at this point (Figure 6.5). This is probably due to increased amount of current delivered from DSA to CS vs. TSA to CS up until this point. This has probably shifted the cathodic polarization curve of CS to the left during exposure (Figure 6.8), and maybe due to precipitation of some amounts of calcareous deposits on CS surface. This is however only a hypothesis.

The area ratios for the connections are in this instance 1:1, which represents a holiday factor of  $\approx 100 \%$ . This is a very large area ratio, which puts the coatings anodically on test. The TSA couple potential development in this thesis is significantly more positive ( $-850 \text{ mV Ag/AgCl}$ ) compared to Wolfsons potential development for the TSA coating with a holiday factor of 10% ( $-940 \text{ mV SCE} \approx 895 \text{ mV Ag/AgCl}$ ) after  $\approx 60$  days of exposure. This fits well with the assumption that increased holiday factor causes a more positive potential.

Increased level of resistivity in the mud compared to SW must be assumed. The distance between the DSA/TSA sample and CS were measured to be  $\approx 45 \text{ mm}$  in this thesis. Increased distance will probably cause higher potential drop, and hence decreased level of protection current through the mud. It is also probable that less mud will be wetted with SW at increased depth in mud. This



will probably cause increased level of protection at the upper part of CS compared to the lower part of CS, since all samples were embedded in a standing position in the mud.

It is evident that the contents of the mud will have a major influence on the wettability (the ability of SW to wet the mud). In this thesis the contents were only visually observed. The visual perception was that the mud included a lot of fine-grained sand. Fine-grained sand will probably limit wettability of SW compared to coarse-grained sand. This is only highlighted and not further addressed.

DNV [11] recommends that bare steel surfaces which are buried in sediments should have a design current density (initial/final and average) of  $20 \text{ mA/m}^2$ , irrespective of geographical location and depth. It is also a general rule that the protection criteria,  $E_p$  should be below  $-900 \text{ mV Ag/AgCl}$  [20], while DNV [11] states that that  $E_p$  is not a variable depending on the exposure conditions. The results obtained in this thesis show that DSA serve adequate protection of CS with a couple potential below  $-900 \text{ mV Ag/AgCl}$  throughout exposure, even though with a an area ratio of 1:1. According to DNV-RP-B401, should  $E_p$  be in the range  $-0.9$  to  $-1.05 \text{ V Ag/AgCl}$  for a correctly designed anode CP system. The TSA:CS coupling does not reach below  $-800 \text{ mV Ag/AgCl}$  until approximately 12 days of exposure, and does not reach below  $-900 \text{ mV Ag/AgCl}$  during exposure. The current densities after 62 days of exposure are  $6.5$  and  $5.5 \text{ mA/m}^2$  for respectively the TSA and DSA coupling. This is below the recommended current density of  $20 \text{ mA/m}^2$ , which probably is a conservative value. The DSA coupling towards the end of exposure is  $\approx -920 \text{ mV Ag/AgCl}$  with a current density to/from CS at  $\approx 5.5 \text{ mA/m}^2$ . This supports an assumption that CS probably require less current density due to the stagnant conditions in mud.

Quale, in his M.Sc. thesis [12] also found that DSA in general were more effective in cathodically polarizing CS samples compared to TSA. This was however in SW.

### 10.3 Polarized Samples

Positive current densities were present at the very beginning of exposure in Figure 6.6. According to the OCPs in Figure 6.1 does neither DSA or TSA reach below  $-1050 \text{ mV Ag/AgCl}$  (initial applied potential) in the beginning of exposure. The positive current densities are probably an effect from the cathodic polarization of samples which induce cathodic reactions on intermetallic particles which destabilizes the oxide layer in the beginning of exposure, and hence will decrease the "OCPs" of the samples during this period of time. This probably explains the initial positive currents present at the very beginning.

The further development is that TSA requires overall more current density compared to the DSA sample. This is best explained from the OCP development (Figure 6.1), which shows that the potential is more positive for the TSA sample compared to the DSA sample throughout exposure. This increases the potential difference, and hence the driving force for providing current as explained in Section 2.5 (Cathodic Protection).

The end current density requirement is respectively  $-10$  and  $-14 \text{ mA/m}^2$  for the DSA and TSA sample respectively after 62 days of exposure. This is similar with what Knudsen et al. [41] found when polarizing TSA at  $10^\circ\text{C}$  to the same potential, after approximately 60 days of exposure. Knudsen also measured LPR of polarized samples throughout exposure, which probably affected the results to some extent. We should further expect a slow decrease in current density by prolonged exposure according to Knudsens results.

### 10.4 Polarization Curves

The Polarization Curves obtained after 61 days of exposure show significant difference in anodic behavior between the freely exposed DSA and TSA sample embedded in mud. Figure 10.1 shows

the ability of the DSA coating to provide protection current compared to the TSA sample. The vertical and horizontal lines show how the coupling potential and current density should appear in a galvanic coupling with CS. The DSA:CS coupling should cause a couple potential of  $\approx -875$  mV Ag/AgCl with a current density of  $150 \text{ mA/m}^2$ , while the TSA:CS coupling will cause a couple potential of  $\approx -720$  mV Ag/AgCl with a current density of  $35 \text{ mA/m}^2$ .

The results fairly reflect the galvanic couple potentials and galvanic currents in Figure 6.2 (DSA:CS) and Figure 6.3 (TSA:CS). The difference is probably caused by increased distance (in mud) between the couplings, causing increased potential drop and reduced current. The polarization curves were, on the other hand, obtained where the current probably flowed a less distance ( $\approx 20$  mm) through the mud/SW interface from/to the counter electrode. The potential drop in SW is assumed less compared to the potential drop in mud. However, when neglecting the difference, it is evident that the DSA coating is more suited for CP in mud compared to TSA.

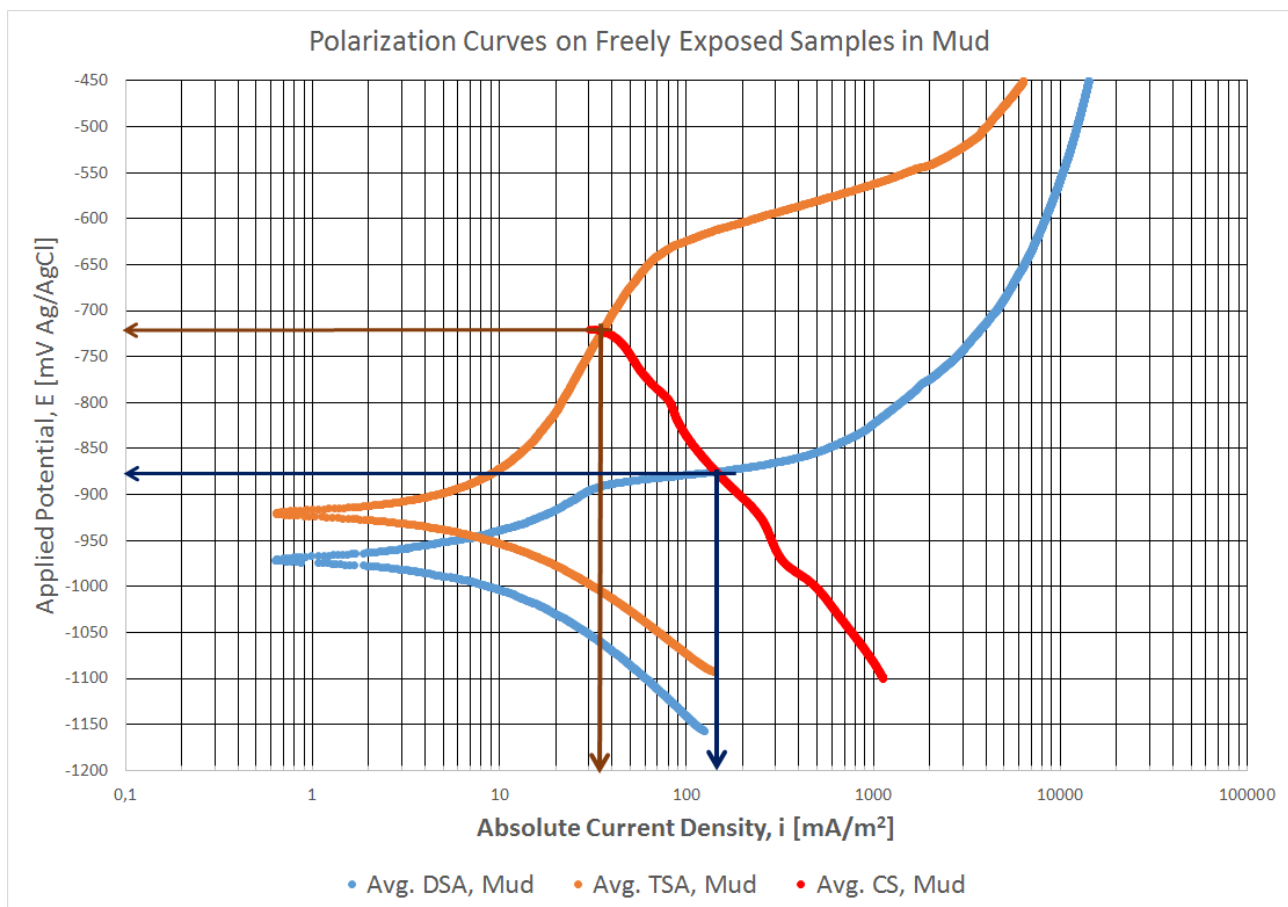


Figure 10.1: Coupling scenario of samples embedded in mud from Polarization Curves obtained after 61 days.

## 10.5 Corrosion Rates

According to the LPR measurements, the DSA coating corrodes most (Figure 6.9) after approximately 15 days of exposure ( $25 \mu\text{m/y}$ ). According to the OCP measurements (Figure 6.1), the potential at this point is at its lowest at approximately  $-1070$  mV Ag/AgCl. The reason for this is probably similar with what occurs in SW with corrosion around intermetallic particles destabilizing the oxide layer similar for DSA as for TSA. This process probably occurs slower in mud compared to SW due to limited flow of SW in mud.

The corrosion rates found in this thesis are generally low throughout exposure and are  $\approx 5.5$

and 2  $\mu\text{m}/\text{year}$  after 62 days, for the DSA and TSA samples, respectively. Wolfson [16] also found low corrosion rates on TSA samples with holidays in mud. He found corrosion rates from approximately 0.05 to 0.15 mils/year ( $\approx 1$  to 4  $\mu\text{m}/\text{year}$ ), for TSA coating with 0 to 5 % holidays. This is similar with what was found in this thesis.

Knudsen et al. [41] calculated corrosion rates on polarized TSA samples in mud (-1100 mV Ag/AgCl), by disconnecting the potentiostat approximately 30 minutes before LPR was performed, so that the sample stabilized at OCP before LPR. He found corrosion rates at approximately 10  $\mu\text{m}/\text{y}$  after 60 days of exposure.

This suggests that CP of TSA and possibly also DSA suffer from slightly higher corrosion rates in mud compared to when the samples are freely exposed in mud. Knudsen et al. [41] however found that excessive polarization (-1200 mV Ag/AgCl) combined with high temperature (95°C) are detrimental to TSA in mud due to activation of aluminum. This does not seem to be the case in this thesis.

## 10.6 Thickness evaluation

The results from thickness evaluation deal with great uncertainties when it comes to evaluating the coating degradation during exposure. The main reason is the unevenly average coating distribution of the TSA samples which can be seen in Table 8.1. The main reasons to this are that the prior exposure thickness is based on measurements on one cross section of one sample. The cross section thickness evaluation does not show any significant thickness degradation of samples embedded in mud.



---

# Chapter 11

## Conclusions

### Effects of Temperature on Electrochemical Properties in SW

- Increased temperature gives initially very negative OCPs for both DSA, TSA and Anode samples. They are however increasing during exposure.
- The OCPs of the TSA samples are more positive compared to the DSA samples, while the OCPs of the Anode samples are generally more positive compared to the DSA samples, at all temperatures.
- Increased temperature gives more positive potentials for coupled DSA and TSA samples.
- Coupled DSA samples have a potential which is  $\approx 140$  to  $200$  mV more negative compared to coupled TSA samples at all temperatures.
- Coupled DSA and Anode samples provides more current compared to coupled TSA samples throughout exposure.
- Galvanic current densities are initially high due to bare steel which require current on the whole surface, but are decreasing due to precipitation of calcareous deposits which develops on all CS cubes during exposure. Increased temperature gives initially higher current densities, and it seems like the current densities are higher for most samples at the end of exposure.
- DSA has active anodic abilities similar to those of sacrificial anodes, while TSA have passive anodic abilities.
- Increased temperature may cause the DSA coating to passivate slightly according to polarization curves.
- The corrosion rates of freely exposed samples are initially very high, but are decreasing quickly at first, then slowly throughout exposure. The corrosion rates for the freely exposed DSA samples are  $\approx 61$ ,  $64$  and  $34$   $\mu\text{m}/\text{year}$  after 1 day of exposure and decreases to  $\approx 7$ ,  $5$  and  $3$   $\mu\text{m}/\text{year}$  after 63 days of exposure, for the  $22$ ,  $50$  and  $80$   $^{\circ}\text{C}$  sample, respectively.
- Corrosion rates increase with increased temperature for the freely exposed anode samples according to polarization curves, obtained at the end of exposure.

### **Effects of Temperature on Total Degradation of DSA and TSA**

- Crevice corrosion is an increased threat for galvanically coupled DSA and TSA samples at elevated temperatures in SW in this experiment design.
- Cohesive failure of galvanically coupled DSA samples is a threat at all temperatures.
- Quantifying the effect of temperature on total degradation of DSA and TSA samples can not be done solely based on the findings in this report.

### **Electrochemical Properties in Mud**

- The OCP of DSA sample is approximately 50 to 90 mV more negative compared to the TSA sample from day 25 throughout exposure period.
- The DSA coating is anodically more active and provides more current density to CS compared to the TSA coating, especially in the beginning of exposure.
- The DSA coating requires slightly less current density compared to the TSA coating. The DSA coating requires  $\approx 10 \text{ mA/m}^2$ , while the TSA coating requires  $\approx 14 \text{ mA/m}^2$  after 2 months of exposure.
- The corrosion rate for the freely exposed DSA sample embedded in mud is increasing to  $\approx 25 \text{ }\mu\text{m/year}$  after 15 days of exposure but decreases and is overall stable at  $\approx 5 \text{ }\mu\text{m/year}$  after 2 months. The corrosion rate for the freely exposed TSA sample embedded in mud is decreasing throughout exposure and is  $\approx 2 \text{ }\mu\text{m/year}$  after 2 months.

---

# Chapter 12

## Suggestions for further work

- Conduct exposure at elevated temperatures in flowing SW in an environment where pH is stable.
- Find an experiment design where reliable data from exposure at elevated temperatures in SW can be obtained.
- Find ways to limit the reduction of Zinc content in DSA compared to the anode alloy.
- Reduce the thickness of DSA to see if this prevents cohesive failure of the coating.
- Crevice corrosion seems to be a potential threat at elevated temperatures in SW. This should be investigated further.
- Investigate if excessive cathodic polarization is a potential threat on DSA embedded in mud.
- Compare anodic properties of DSA to Zinc or Magnesium anodes in mud.





---

# Bibliography

- [1] J R Davis. *Handbook of Thermal Spray Technology*. A S M International, Materials Park, 2004.
- [2] R S C Paredes, S C Amico, Amp, Apos, and A S C M Oliveira. The Effect of Roughness and Pre-Heating of the Substrate on the Morphology of Aluminium Coatings Deposited by Thermal Spraying. *Surface & Coatings Technology*, 200(9):3049–3055, 2006.
- [3] Pierre L Fauchais, Joachim V R Heberlein, and Maher Boulos. *Thermal Spray Fundamentals : From Powder to Part*. Springer US, Boston, 2014.
- [4] K Nisancioglu. Corrosion and Protection of Aluminum Alloys in Seawater. *European Federation of Corrosion Publications*, 50:145 – 155, 2007.
- [5] P O Gartland. Protective Properties of Al-Based Coatings in Seawater. *Number STF34 F*, 91106, 1991.
- [6] K. Nisancioglu. Lecture Notes, Corrosion Course, TMM4170 - 25. Corrosion of Aluminum and Aluminum Alloys. NTNU.
- [7] Hosni Ezuber, A El-Houd, and F El-Shawesh. A Study on the Corrosion Behavior of Aluminum Alloys in Seawater. *Materials & Design*, 29(4):801–805, 2008.
- [8] Unknown. Galvanic Series of Metals in Seawater, 2016.
- [9] Skarpenord Corrosion. Technical Data - CORAL A High Grade Al-In-Zn alloy.
- [10] Karl P Fischer, William H Thomason, Trevor Rosbrook, and Jay Murali. Performance History of Thermal-Sprayed Aluminum Coatings in Offshore Service. *Materials performance*, 34(4), 1995.
- [11] Det Norske Veritas. Recommended Practice DNV-RP-B401. *Cathodic Protection Desing*, 2010.
- [12] Geir Quale. Distributed Sacrificial Cathodic Protection-A New Cost Effective Solution to Prevent Corrosion on Subsea Structures. Master's thesis, NTNU, 2016.
- [13] Mitchell R. Dorfman. 19 - Thermal Spray Coatings. In Myer Kutz, editor, *Handbook of Environmental Degradation of Materials (Second Edition)*, pages 569 – 596. William Andrew Publishing, Oxford, second edition edition, 2012.
- [14] S Papavinasam, M Attard, B Arseneult, and RW Revie. State-of-the-Art of Thermal Spray Coatings for Corrosion Protection. *Corrosion reviews*, 26(2-3):105–145, 2008.
- [15] V.R.S. Sá Brito, I.N. Bastos, and H.R.M. Costa. Corrosion Resistance and Characterization of Metallic Coatings Deposited by Thermal Spray on Carbon Steel. *Materials & Design*, 41:282 – 288, 2012.

- [16] Steve L Wolfson. Corrosion Control of Subsea Piping Systems Using Thermal Sprayed Aluminum Coatings. Technical report, 1996.
- [17] NORSOK. M-501: Surface Preparation and Protective Coating, 1999.
- [18] Philip A Schweitzer. *Fundamentals of Metallic Corrosion: Atmospheric and Media Corrosion of Metals*. CRC press, 2006.
- [19] P M Natishan and W E O'Grady. Chloride Ion Interactions with Oxide-Covered Aluminum leading to Pitting Corrosion: A Review. *Journal of the Electrochemical Society*, 161(9):C421–C432, 2014.
- [20] Einar Bardal. *Korrosjon og Korrosjonsvern*. Tapir Akademisk Forlag, second edition, 1997.
- [21] K. Nisancioglu. Lecture Notes, Corrosion Course, TMM4170 - 10. Crevice Corrosion. NTNU.
- [22] T G Eggen and J M Drugli. Sea Water Corrosion of Thermal Sprayed Aluminium, SINTEF report no. *STF34 F93108*, 1993.
- [23] WH Thomason et al. Offshore Corrosion Protection With Thermal-Sprayed Aluminum. In *Offshore Technology Conference*. Offshore Technology Conference, 1985.
- [24] Alexandre Pacheco, Andrea Schokker, Jeffery Volz, H Hamilton, and Alexandre Pacheco. Linear Polarization Resistance Tests on Corrosion Protection Degree of Post-Tensioning Grouts. *ACI Materials Journal*, 108(4):365–370, 2011.
- [25] David A. Shifler. Understanding Material Interactions in Marine Environments to Promote Extended Structural Life. *Corrosion Science*, 47(10):2335 – 2352, 2005.
- [26] Ramesh Singh. *Corrosion Control for Offshore Structures: Cathodic Protection and High-efficiency Coating*. Gulf Professional Publishing, 2014.
- [27] Roberge Pierre. Handbook of Corrosion Engineering, 1999.
- [28] Mariela Rendón Belmonte et al. Characterization of Steel Surface under Cathodic Protection in Seawater. *Anti-Corrosion Methods and Materials*, 60(3):160–167, 2013.
- [29] C Rousseau, F Baraud, L Leleyter, M Jeannin, and O Gil. Calcareous Deposit Formed under Cathodic Protection in the Presence of Natural Marine Sediments: A 12 Month Experiment. *corrosion science*, 52(6):2206–2218, 2010.
- [30] J.B. Bessone, D.O. Flamini, and S.B. Saidman. Comprehensive model for the activation mechanism of Al–Zn alloys produced by indium. *Corrosion Science*, 47(1):95 – 105, 2005.
- [31] C.B. Breslin and L.P. Friery. The Synergistic Interaction between Indium and Zinc in the Activation of Aluminium in Aqueous Electrolytes. *Corrosion Science*, 36(2):231 – 240, 1994.
- [32] Ahmad Keyvani, Mohsen Saremi, and Mohammad Reza Saeri. Anodic Behavior of Al–Zn–In Sacrificial Anodes at Different Concentration of Zinc and Indium. *International Journal of Materials Research*, 103(12):1533–1538, 2012.
- [33] J-F Yan, Ralph E White, and RB Griffin. Parametric Studies of the Formation of Calcareous Deposits on Cathodically Protected Steel in Seawater. *Journal of the Electrochemical Society*, 140(5):1275–1280, 1993.
- [34] R Gundersen and K Nisancioglu. Cathodic Protection of Aluminum in Seawater. *Corrosion*, 46(4):279–285, 1990.

- [35] Kemal Nisancioglu, Otto Lunder, and Hans Holtan. Improving the Corrosion Resistance of Aluminum Alloys by Cathodic Polarization in Aqueous Media. *Corrosion*, 41(5):247–257, 1985.
- [36] Per Olav Gartland and TG Eggen. Thermal Sprayed Aluminum Coatings in Seawater With and Without Cathodic Protection. *SINTEF Corrosion Center, N-7034 Trondheim, Norwa*, 1993.
- [37] A. Ryen. Thermally Sprayed Aluminum (TSA) used for Subsea Heat Exchangers - Coating Degradation at Elevated Temperatures. Unpublished Work., 2016.
- [38] Håvard Wilson. Thermal Sprayed Aluminium for Subsea Heat Exchanger Surfaces: Effect of Temperature on Protection Current Requirement and Calcareous Development. Master's thesis, Institutt for produktutvikling og materialer, 2014.
- [39] Roy Johnsen and Cristian Torres. ER-Subsea Coating For Cooling TSA test. Technical report, Department of Engineering Design and Materials, NTNU, 2016.
- [40] Leblanc S. Richards S. & LaFontaine J. P. Surkein, M. B. Corrosion Protection Program for High Temperature Subsea Pipeline. *NACE International.*, jan 2001.
- [41] Ole Øystein Knudsen, Jan Van Bokhors, George Clapp, Graeme Duncan, et al. Corrosion of Cathodically Polarized TSA in Subsea Mud at High Temperature. In *CORROSION 2014*. NACE International, 2014.
- [42] Anonymous. Corrosion of Thermal Spray Aluminum Coatings in Subsea Mud. *Materials Performance*, 54(3):57, mar 2015.
- [43] Steven F Daily. Galvanic Cathodic Protection of Reinforced and Prestressed Concrete Using a Thermally Sprayed Aluminum Coating. *Concrete repair bulletin*, 2003.
- [44] Steven F Daily, Wally R Burns, et al. Cathodic Protection of a Coastal Bridge in Texas Using a Thermally Sprayed Aluminum Alloy. In *CORROSION 2004*. NACE International, 2004.
- [45] William H Thomason, Stein Olsen, Trond Haugen, Karl Petter Fischer, et al. Deterioration of Thermal Sprayed Aluminum Coatings on Hot Risers due to Thermal Cycling. In *CORROSION 2004*. NACE International, 2004.
- [46] SINTEF MOLAB. 63898 - Chemical Analysis of DSA, Wire and Anode. Unpublished, sep 2016.
- [47] Alex Delwiche, Patrick Lydon, Isaac Tavares, et al. Concerns over Utilizing Aluminium Alloy Anodes in Sealed Environments. In *CORROSION 2017*. NACE International, 2017.
- [48] Ove Nese. Corrosion properties of AA5083 and AA6082 in seawater-effect of temperature, pH and potential. Master's thesis, NTNU, 2016.



# Appendix A

## A.1 Arrangement of Test Samples and Measurements Performed on samples at elevated temperatures in SW

Temperature °C	Type	Measurement
22	DSA	Current density, $i$ [ $\text{mA}/\text{m}^2$ ] and Galvanic Couple Potential [mV SCE]
22	TSA	Current density, $i$ [ $\text{mA}/\text{m}^2$ ] and Galvanic Couple Potential [mV SCE]
22	Anode	Current density, $i$ [ $\text{mA}/\text{m}^2$ ]
22	DSA	OCP [mV SCE], Polarization Curves(day 63)
22	TSA	OCP [mV SCE], Polarization Curves(day 63)
22	Anode	OCP [mV SCE], Polarization Curves(day 63)
22	DSA	OCP [mV SCE], Polarization Curves(day1 and 63) and LPR.
50	DSA	Current density, $i$ [ $\text{mA}/\text{m}^2$ ] and Galvanic Couple Potential [mV SCE]
50	TSA	Current density, $i$ [ $\text{mA}/\text{m}^2$ ] and Galvanic Couple Potential [mV SCE]
50	Anode	Current density, $i$ [ $\text{mA}/\text{m}^2$ ]
50	DSA	OCP [mV SCE], Polarization Curves(day 63)
50	TSA	OCP [mV SCE], Polarization Curves(day 63)
50	Anode	OCP [mV SCE], Polarization Curves(day 63)
50	DSA	OCP [mV SCE], Polarization Curves(day1 and 63) and LPR.
80	DSA	Current density, $i$ [ $\text{mA}/\text{m}^2$ ] and Galvanic Couple Potential [mV SCE]
80	TSA	Current density, $i$ [ $\text{mA}/\text{m}^2$ ] and Galvanic Couple Potential [mV SCE]
80	Anode	Current density, $i$ [ $\text{mA}/\text{m}^2$ ]
80	DSA	OCP [mV SCE], Polarization Curves(day 63)
80	TSA	OCP [mV SCE], Polarization Curves(day 63)
80	Anode	OCP [mV SCE], Polarization Curves(day 63)
80	DSA	OCP [mV SCE], Polarization Curves(day1 and 63) and LPR.

Table A.1: The test samples, sorted in accordance to testing temperature.

## A.2 Corrosion Rate Calculation

The corrosion rates were calculated as described in Section 2.4. The physical data used for the calculations are listed in Table A.2.

Table A.2: Physical data used for calculation of corrosion rates.

Property	Value	Unit
Faradays constant, $F$	96485	C/mol
Density of AlZnIn, $\rho_{AlZnIn}$	2.95	g/cm <sup>3</sup>
Density of DSA, $\rho_{DSA}$	2.66*	g/cm <sup>3</sup>
Density of TSA, $\rho_{TSA}$	2.43*	g/cm <sup>3</sup>
Molar Weight AlZnIn, $M_{AlZnIn}$	26.98	g/mol
Molar Weight DSA, $M_{DSA}$	26.98	g/mol
Molar Weight TSA, $M_{TSA}$	26.98	g/mol

\* Porosity of 10 % is added to DSA and TSA

## A.3 Technical data of Al-In-Zn alloy used for Anode sample and for the recasting to DSA.

## TECHNICAL DATA

### **CORAL<sup>®</sup> 'A'** **HIGH GRADE**

#### ***Al-In-Zn alloy***

Chemical composition according to NORSOK specification no. M-503, rev. 2 and certified according to DNV Type Approval program, IOD-90-TAI, November 1982.

The chemical composition and performance data of CORAL<sup>®</sup> 'A' High Grade alloy are as follows:

#### **Elements**

#### **Analysis (% by weight)**

Zn	3,5 – 5,0
In	0,015 – 0,025
Cu	max. 0,003
Fe	max. 0,09
Si	max. 0,10
Others (each)	max. 0,020
Al	Remainder

#### **Specific gravity**

2,78 kg/dm<sup>3</sup> (theoretically)

#### **Performance data in ambient sea water**

Capacity	2585 Ah/kg
Consumption rate	3,39 kg/A.yr
Closed circuit potential	-1,09 volt v.s. Ag/AgCl/sea water

#### **Performance data in sea bottom sediments (mud)**

	<u>0-20°C</u>	<u>40°C</u>	<u>60°C</u>	<u>80°C</u>
Capacity (Ah/kg)	2400	1750	1150	600
Consumption rate (kg/A.yr)	3,65	5,00	7,62	14,6
Closed circuit potential (volt v.s. Ag/AgCl/sea water)	-1,05	-1,03	-1,01	-1,00

VERSION 1/03 – SKARPENORD CORROSION a.s, NORWAY

Figure A.1: Technical data Al-In-Zn alloy used for Anode sample and for the recasting to DSA [9].





## Appendix B

### B.1 Polarization Curves on freely exposed samples at 22°C with graphical solution.

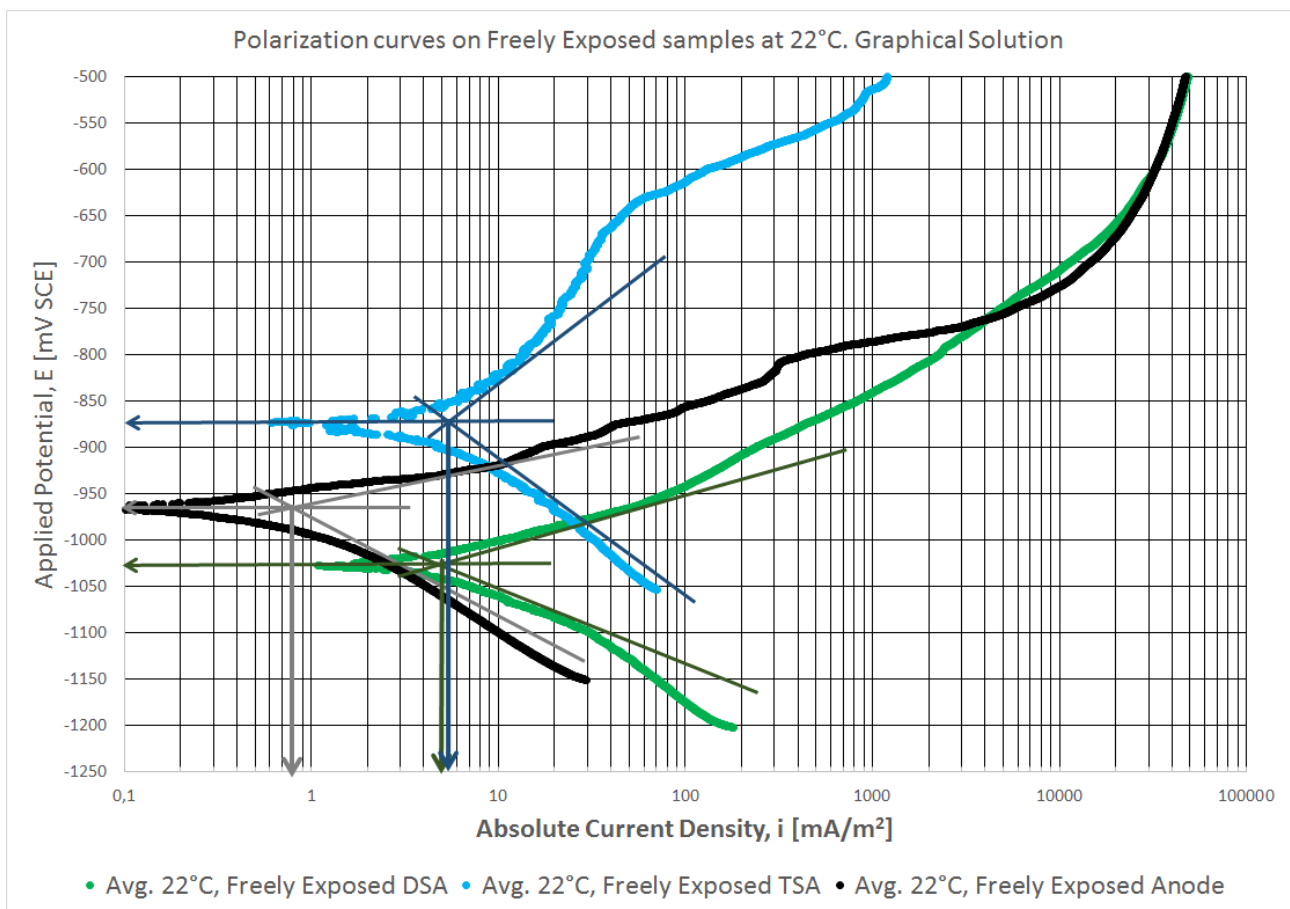


Figure B.1: Polarization Curves on freely exposed samples at 22°C with graphical solution. Day 63.

## B.2 Polarization Curves on freely exposed samples at 50°C with graphical solution.

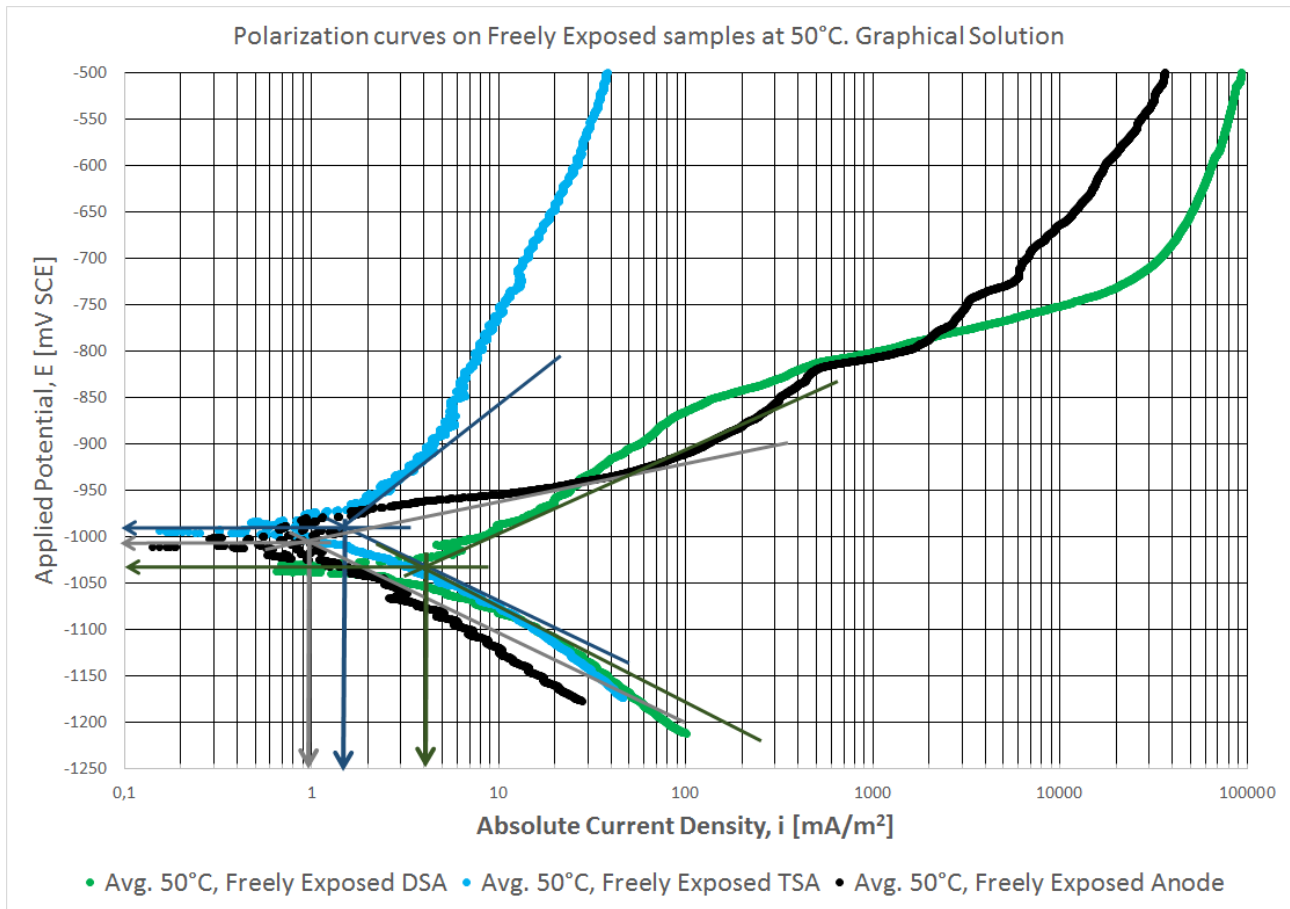


Figure B.2: Polarization Curves on freely exposed samples at 50°C with graphical solution. Day 63.

### B.3 Polarization Curves on freely exposed samples at 80°C with graphical solution.

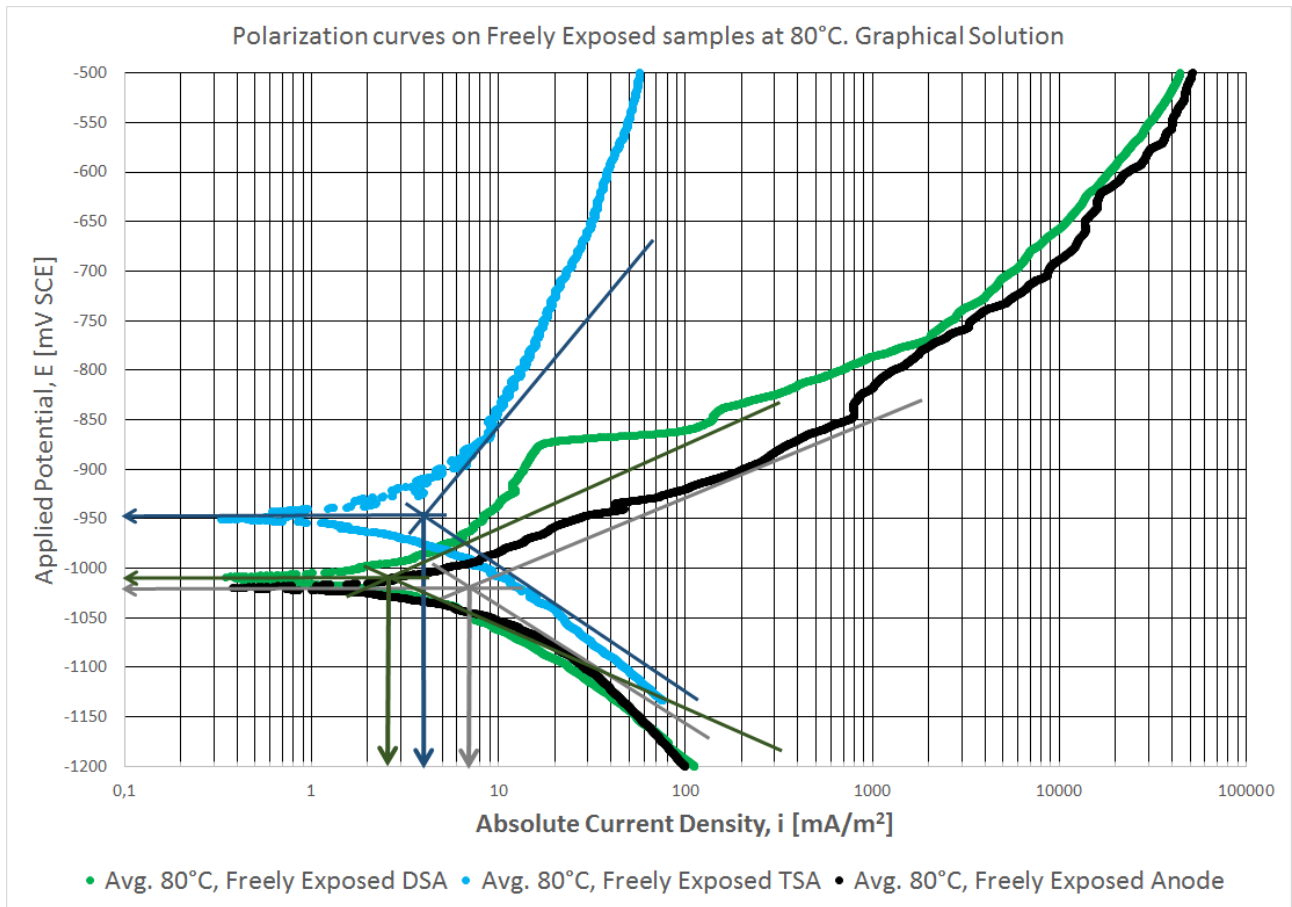


Figure B.3: Polarization Curves on freely exposed samples at 80°C with graphical solution. Day 63.

## B.4 Polarization Curves on freely exposed samples in mud with graphical solution.

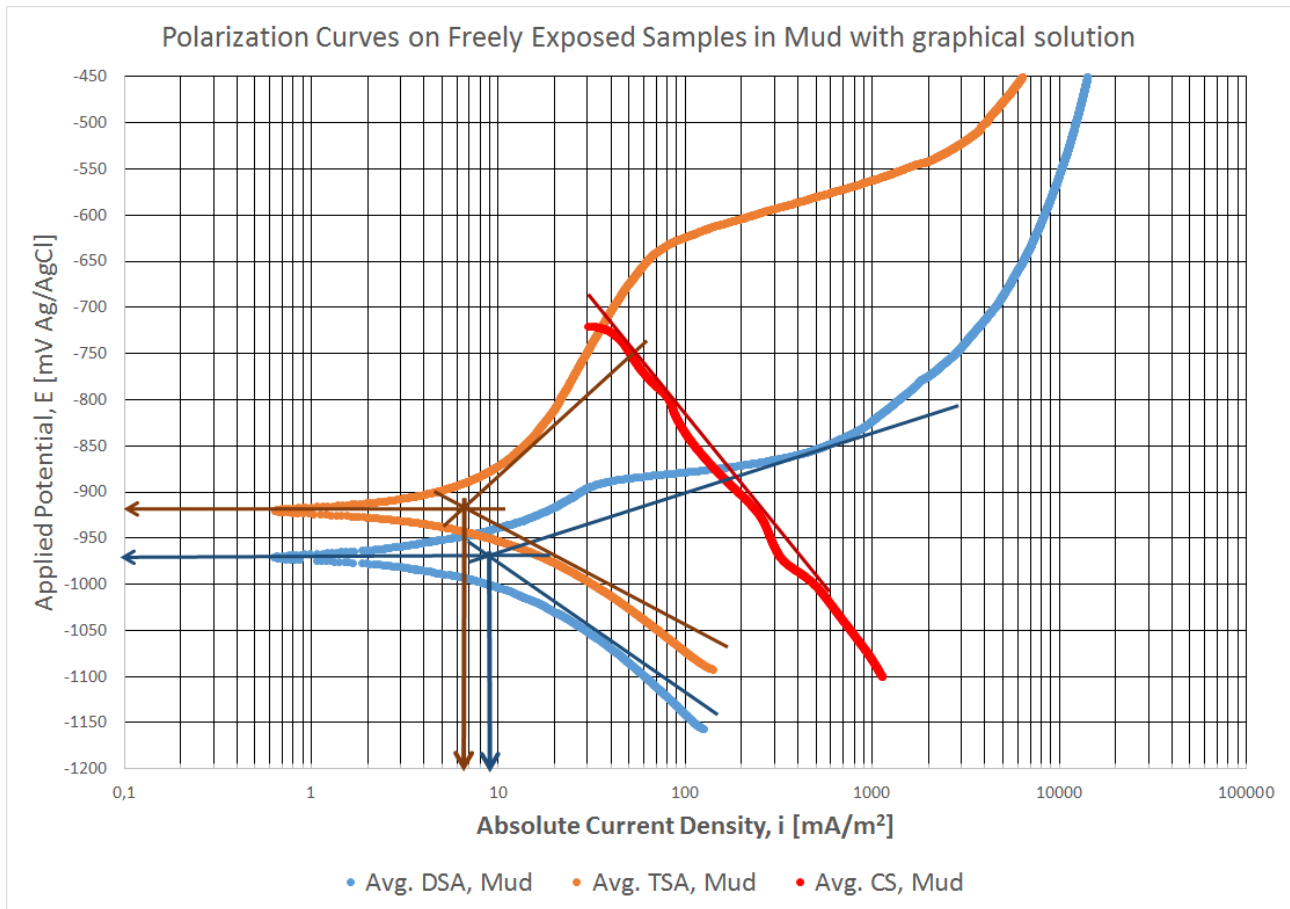


Figure B.4: Polarization Curves on freely exposed samples in mud with graphical solution. Day 61.

# Appendix C

## C.1 Cross Section Measurements and EDS of freely exposed DSA sample at 22° C

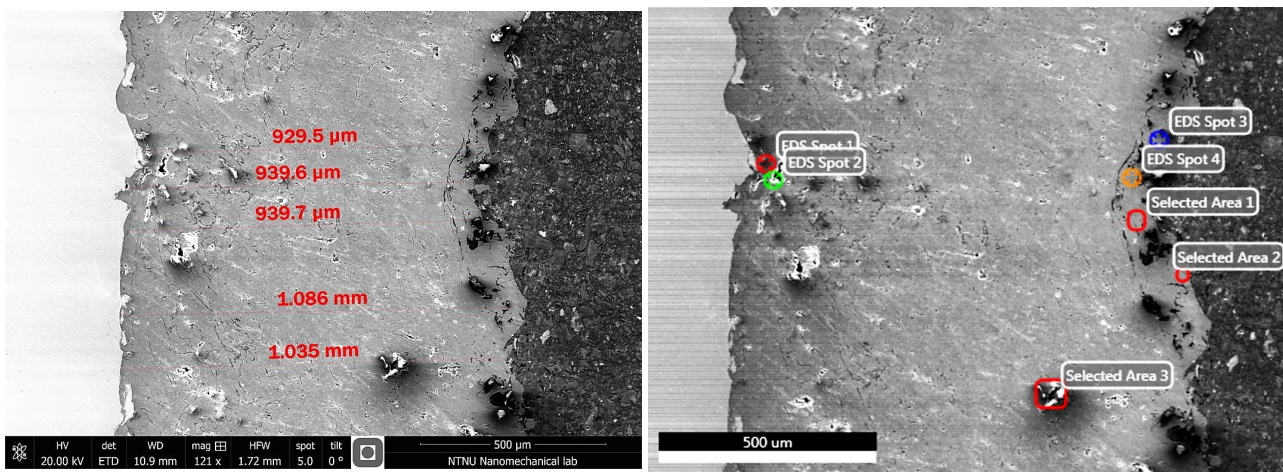


Figure C.1: Left: Cross section measurements of freely exposed DSA sample at 22°C. Right: Areas/Spots for EDS.

Table C.1: Results from EDS of selected points and areas on freely exposed DSA sample at 22°C.

Element [wt%]	Spot 1	Spot 3	Spot 4	Area 1	Area 2	Area 3
O	3.28	0.84	1.37	3.88	1.96	21.57
Al	95.65	97.28	97.13	84.97	93.52	73.8
Ar	1.07	1.1	1.08	0.84	0.86	0.48
Zn	-	0.78	0.43	2.05	3.66	1.4
C	-	-	-	7.6	-	-
Si	-	-	-	0.48	-	1.68
S	-	-	-	0.18	-	0.58
Fe	-	-	-	-	-	0.48
Total	100	100	100.01	100	100	99.99

## C.2 Cross Section Measurements and EDS of freely exposed TSA sample at 22° C

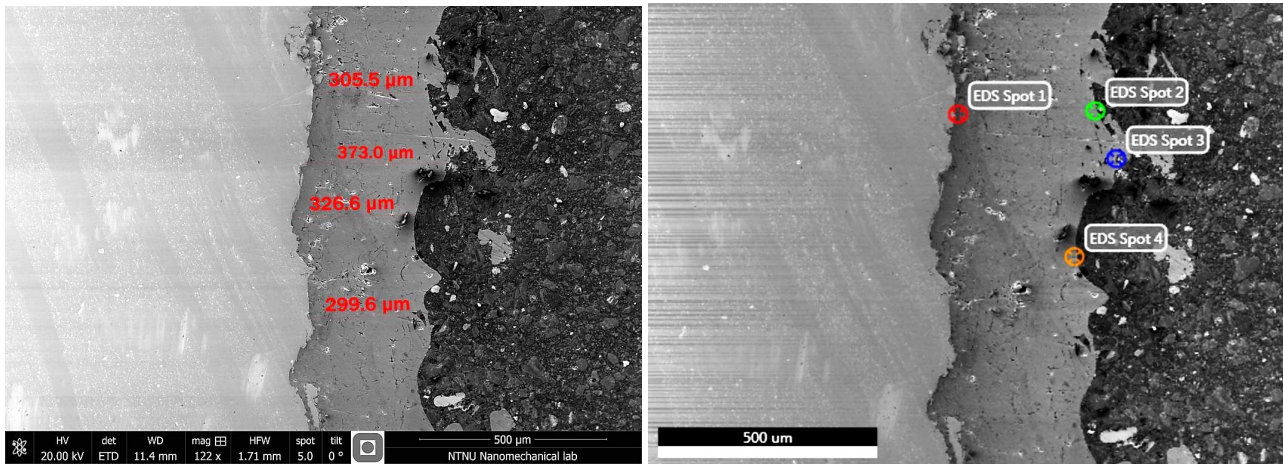


Figure C.2: Left: Cross section measurements of freely exposed TSA sample at 22°C. Right: Areas/Spots for EDS.

Table C.2: Results from EDS of selected points and areas on freely exposed TSA sample at 22°C.

Element [wt%]	Spot 1	Spot 2	Spot 3	Spot 4
O	2.59	0.93	10.48	0.33
Al	95.26	97.64	9.27	98.57
Ar	0.89	1.05	-	1.11
Fe	1.27	0.38	0.76	-
C	-	-	77.97	-
Mg	-	-	0.4	-
Si	-	-	0.83	-
S	-	-	0.12	-
Ca	-	-	0.16	-
Total	100.01	100	99.99	100.01



### C.3 Cross Section Measurements and EDS of freely exposed DSA sample at 50° C

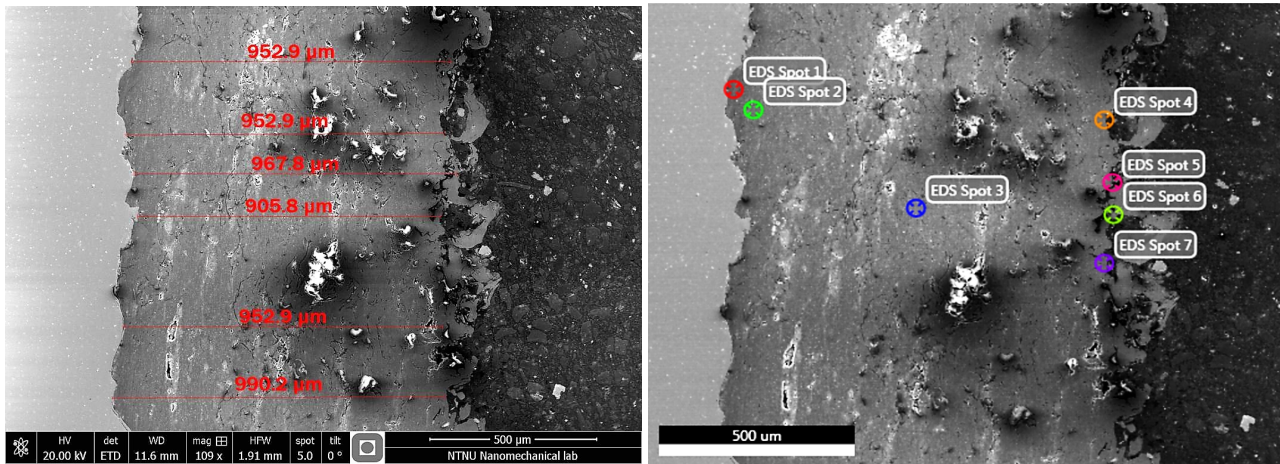


Figure C.3: Left: Cross section measurements of freely exposed DSA sample at 50°C. Right: Areas/Spots for EDS.

Table C.3: Results from EDS of selected points and areas on freely exposed DSA sample at 50°C.

Element [wt%]	Spot 1	Spot 2	Spot 3	Spot 4	Spot 5	Spot 6	Spot 7
O	2.48	1.78	2.72	4.18	12.11	1.34	1.05
Al	96.08	95.09	93.45	75.46	3.32	94.14	97.46
Fe	1.44	-	-	-	-	-	-
Si	-	3.13	0.78	2.07	0.22	-	-
Zn	-	-	2.37	2.53	-	2.43	1.49
Ar	-	-	0.68	-	-	-	-
C	-	-	-	15.75	83.74	2.08	-
Mg	-	-	-	-	0.61	-	-
Total	100	100	100	99.99	100	99.99	100

## C.4 Cross Section Measurements and EDS of freely exposed TSA sample at 50° C

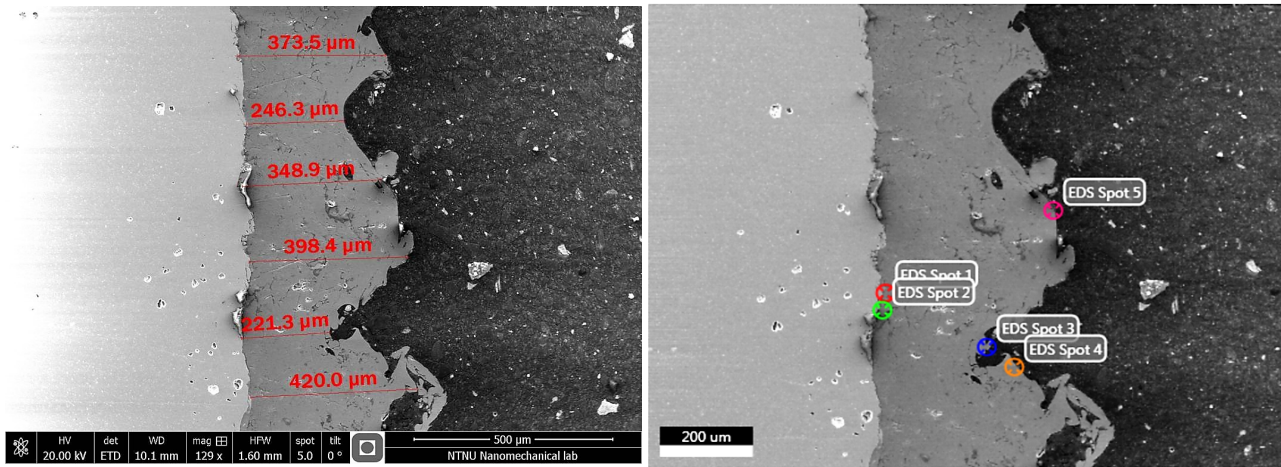


Figure C.4: Left: Cross section measurements of freely exposed TSA sample at 50°C. Right: Areas/Spots for EDS.

Table C.4: Results from EDS of selected points and areas on freely exposed TSA sample at 50°C.

Element [wt%]	Spot 1	Spot 2	Spot 3	Spot 4	Spot 5
O	0.57	1.59	1.11	-	35.5
Al	98.35	98.41	98.89	100	39.32
Fe	1.07	-	-	-	-
C	-	-	-	-	23.32
Mg	-	-	-	-	0.56
Si	-	-	-	-	0.73
S	-	-	-	-	0.57
Total	99.99	100	100	100	100



## C.5 Cross Section Measurements and EDS of coupled DSA sample at 50° C

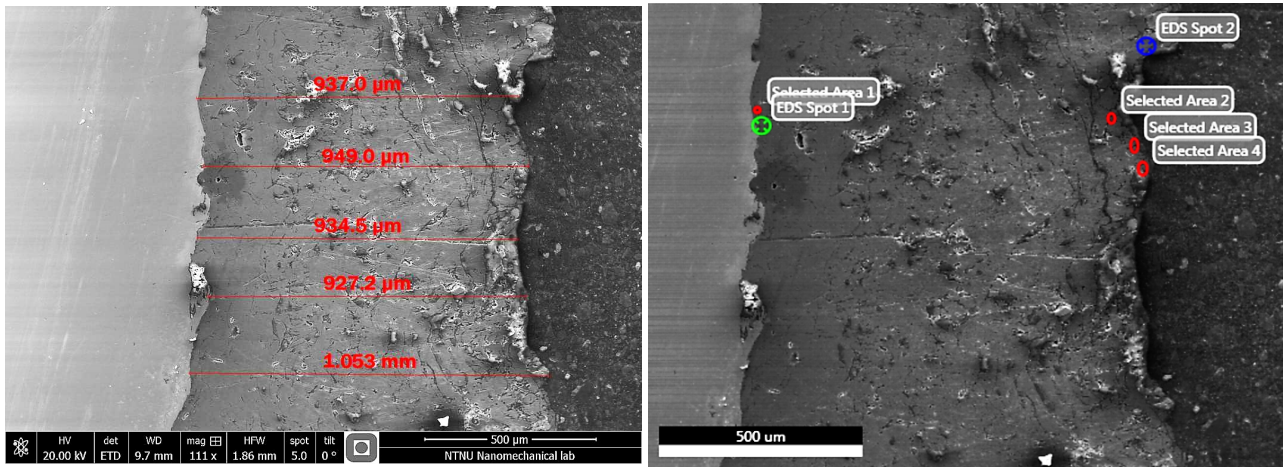


Figure C.5: Left: Cross section measurements of coupled DSA sample at 50°C. Right: Areas/Spots for EDS.

Table C.5: Results from EDS of selected points and areas on coupled DSA sample at 50°C.

Element [wt%]	Area 1	Spot 1	Spot 2	Area 2	Area 3	Area 4
O	3.54	1.15	0.64	7.28	28.16	9.93
Al	94.47	98.85	95.94	89.86	60.46	86.09
Si	1.06	-	3.42	-	1.03	0.33
Fe	0.92	-	-	-	-	-
Zn	-	-	-	1.53	1.77	3.19
S	-	-	-	0.73	0.48	-
Ar	-	-	-	0.61	0.38	0.46
C	-	-	-	-	7.29	-
Ca	-	-	-	-	0.41	-
Total	99.99	100	100	100.01	99.98	100

## C.6 Cross Section Measurements and EDS of coupled TSA sample at 50° C

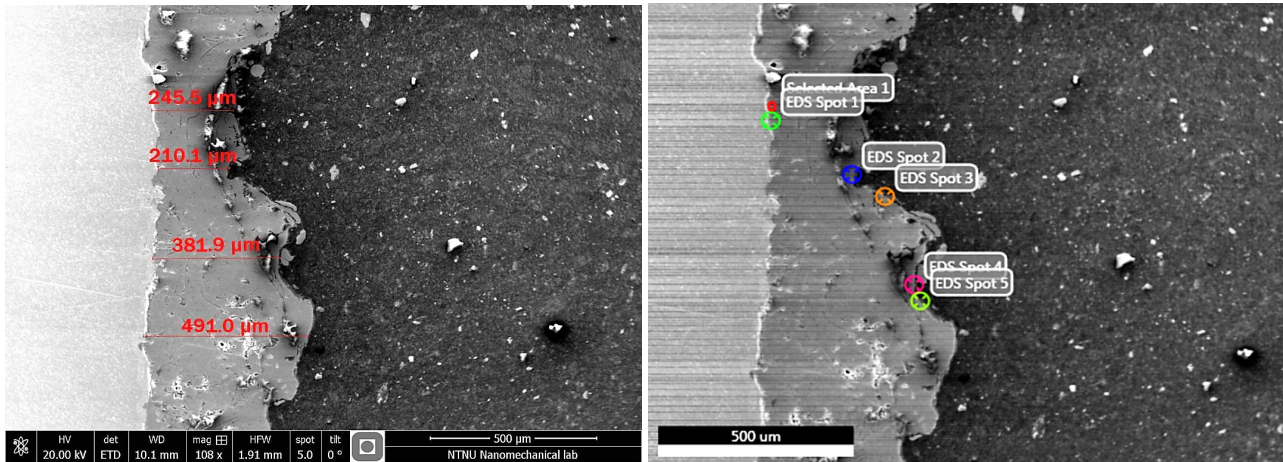


Figure C.6: Left: Cross section measurements of coupled TSA sample at 50°C. Right: Areas/Spots for EDS.

Table C.6: Results from EDS of selected points and areas on coupled TSA sample at 50°C.

Element [wt%]	Area 1	Spot 1	Spot 2	Spot 3	Spot 4	Spot 5
O	3.75	10.24	1.04	14.67	14.93	14.43
Al	84.3	88.78	97.16	51.68	22.39	2.2
Si	7.93	-	1.03	2.66	3.22	3.53
Ar	0.64	-	0.78	-	-	-
Fe	3.38	0.98	-	-	0.56	1.12
C	-	-	-	30.77	58.3	77.22
S	-	-	-	0.2	0.16	0.29
Mg	-	-	-	-	0.45	0.56
K	-	-	-	-	-	0.64
Total	100	100	100.01	99.98	100.01	99.99

## C.7 Cross Section Measurements and EDS of freely exposed DSA sample at 80° C

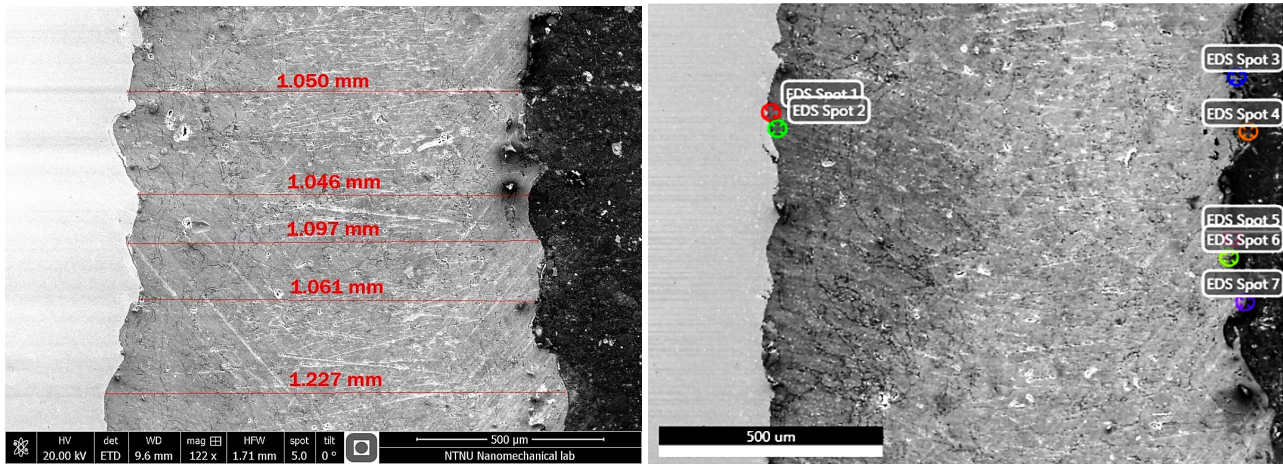


Figure C.7: Left: Cross section measurements of freely exposed DSA sample at 80°C. Right: Areas/Spots for EDS.

Table C.7: Results from EDS of selected points and areas of freely exposed DSA sample at 80°C.

Element [wt%]	Spot 1	Spot 2	Spot 3	Spot 4	Spot 5	Spot 6	Spot 7
Al	12.64	93.04	1.72	0.14	0.61	-	0.47
Mn	1.27	-	-	-	-	-	-
Fe	86.09	2.09	0.7	-	0.34	0.48	0.87
O	-	1.38	21.07	4.38	4.41	5.18	9
Si	-	3.49	4.64	-	0.54	-	0.68
C	-	-	70.06	95.49	93.54	93.96	88.3
Mg	-	-	0.63	-	-	-	0.4
S	-	-	0.42	-	0.57	0.38	-
K	-	-	0.3	-	-	-	-
Ca	-	-	0.45	-	-	-	0.27
Total	100	100	99.99	100.01	100.01	100	99.99

## C.8 Cross Section Measurements and EDS of freely exposed TSA sample at 80° C

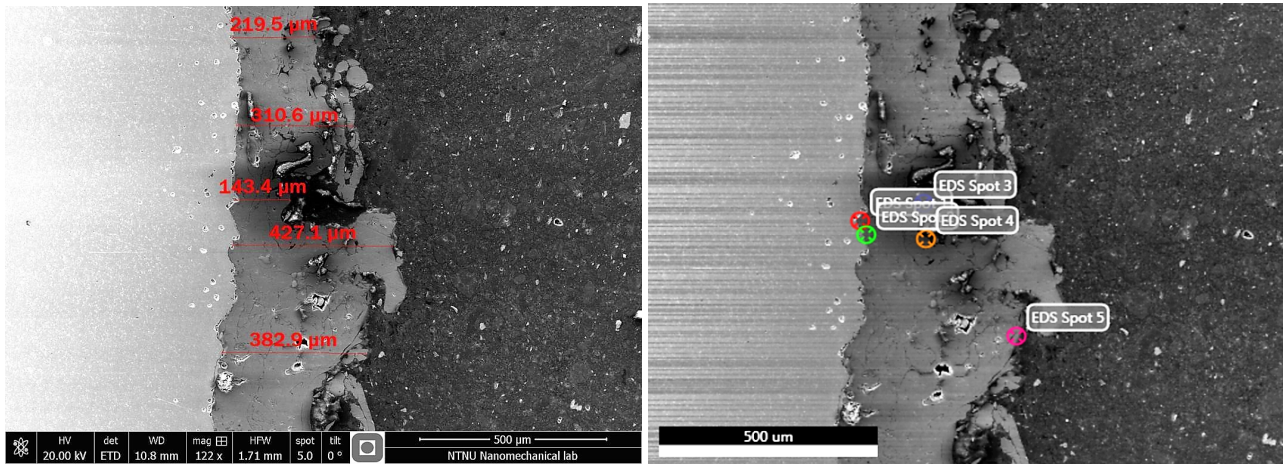


Figure C.8: Left: Cross section measurements of freely exposed TSA sample at 80°C. Right: Areas/Spots for EDS.

Table C.8: Results from EDS of selected points and areas of freely exposed TSA sample at 80°C.

Element [wt%]	Spot 1	Spot 2	Spot 3	Spot 4	Spot 5
O	10.81	2	3.75	0.63	0.68
Al	87.38	96	95.07	98.1	98.52
Ar	0.46	0.8	0.72	0.73	0.8
Fe	1.35	0.71	-	0.53	-
Si	-	0.48	0.46	-	-
Total	100	99.99	100	99.99	100



## C.9 Cross Section Measurements and EDS on coupled DSA sample at 80° C

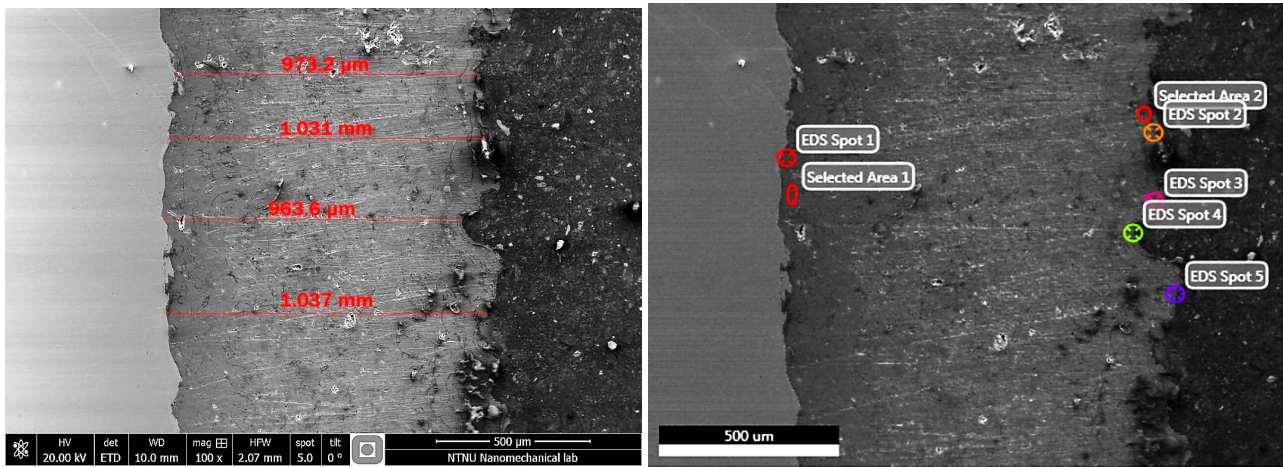


Figure C.9: Left: Cross section measurements on coupled DSA sample at 80°C. Right: Areas/Spots for EDS.

Table C.9: Results from EDS of selected points and areas on coupled DSA sample at 80°C.

Element [wt%]	Spot 1	Area 1	Spot 2	Area 2	Spot 3	Spot 4	Spot 5
O	0.84	3.35	3.46	13.4	4.19	23.02	29.23
Al	98.19	95.77	92.5	82.67	82.63	32.93	37.83
Ar	0.97	0.88	0.58	0.48	0.53	-	-
Zn	-	-	3.46	2.58	2.14	0.67	1.63
Si	-	-	-	0.52	0.6	1.89	2.19
S	-	-	-	0.35	-	0.35	0.55
C	-	-	-	-	9.9	40.29	27.92
Mg	-	-	-	-	-	0.33	0.65
Kr	-	-	-	-	-	0.53	-
Total	100	100	100	100	99.99	100.01	100

## C.10 Cross Section Measurements and EDS on coupled TSA sample at 80° C

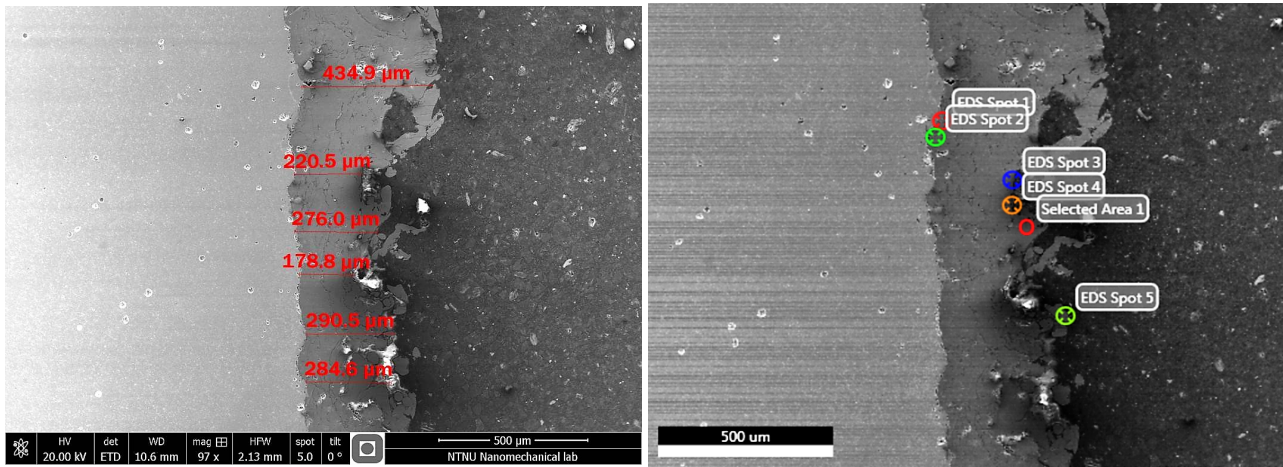


Figure C.10: Left: Cross section measurements on coupled TSA sample at 80°C. Right: Areas/Spots for EDS.

Table C.10: Results from EDS of selected points and areas on coupled TSA sample at 80°C.

Element [wt%]	Spot 1	Spot 2	Spot 3	Spot 4	Area 1	Spot 5
O	2.96	-	34.99	21.41	2.7	1.66
Al	96.36	98.43	35.29	23.84	82.41	94.06
Ar	0.67	0.89	-	-	0.58	0.74
Fe	-	0.68	0.79	1.03	-	-
C	-	-	26.4	51.92	14.31	3.55
Mg	-	-	0.26	0.24	-	-
Si	-	-	0.61	-	-	-
S	-	-	1.65	0.82	-	-
Kr	-	-	-	0.74	-	-
Total	99.99	100	99.99	100	100	100.01

# Appendix D

## D.1 Cross Section Measurements and EDS of new DSA sample for exposure in Mud

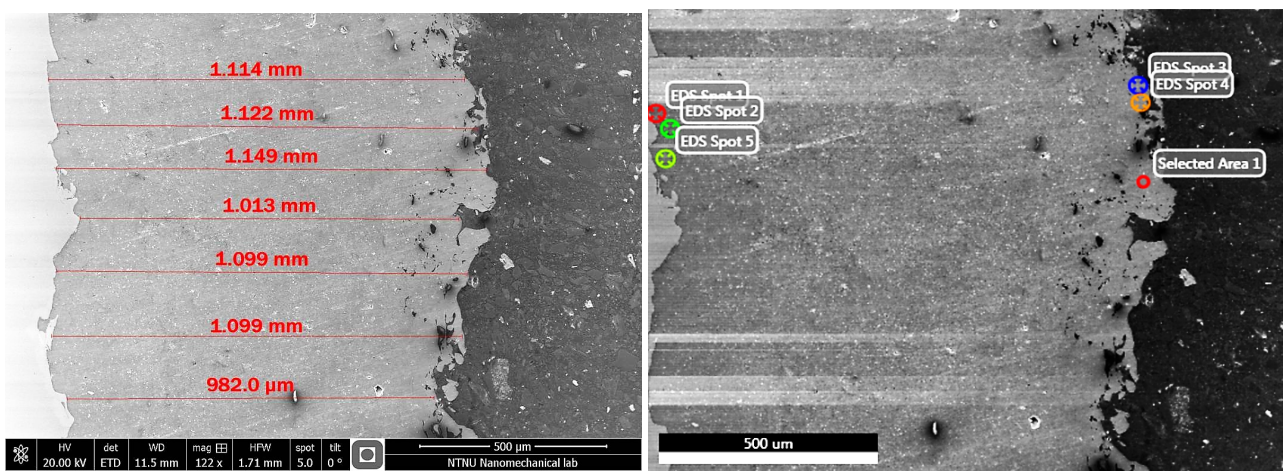


Figure D.1: Left: Cross section measurements of New DSA sample for exposure in Mud. Right: Areas/Spots for EDS.

Table D.1: Results from EDS of selected points and areas on new DSA sample for exposure in Mud.

Element [wt%]	Spot 1	Spot 2	Spot 3	Spot 4	Spot 5	Area 1
O	1.14	1.79	0.69	1.55	2.5	2.03
Al	97.24	97.45	95.2	96.63	93.58	94.22
Ar	0.71	0.76	0.58	0.79	0.65	0.61
Fe	0.92	-	-	-	2.78	-
Zn	-	-	3.54	1.03	-	2.64
Si	-	-	-	-	0.5	0.49
Total	100.01	100	100.01	100	100.01	99.99

## D.2 Cross Section Measurements and EDS of new TSA sample for exposure in Mud

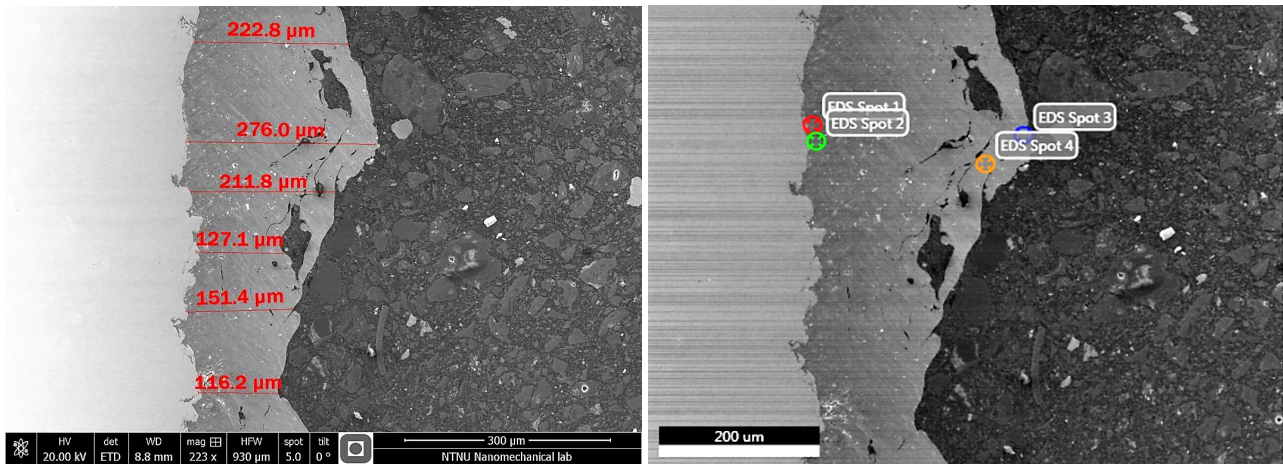


Figure D.2: Left: Cross section measurements of New TSA sample for exposure in Mud. Right: Areas/Spots for EDS.

Table D.2: Results from EDS of selected points and areas on new TSA sample for exposure in Mud.

Element [wt%]	Spot 1	Spot 2	Spot 3	Spot 4
O	11.04	7.36	2.28	1.4
Al	85.87	87.98	96.17	98.6
Si	0.73	0.43	0.65	-
Ar	0.54	-	0.9	-
Fe	1.83	1.5	-	-
C	-	2.73	-	-
Total	100.01	100	100	100



### D.3 Cross Section Measurements and EDS of coupled DSA sample embedded in Mud

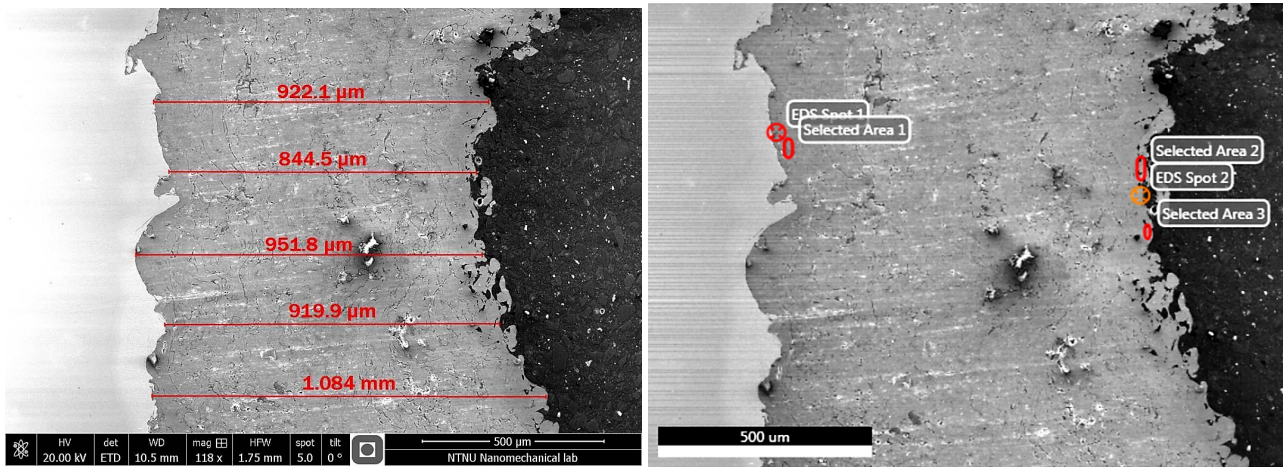


Figure D.3: Left: Cross section measurements of coupled DSA embedded in Mud. Right: Areas/Spots for EDS.

Table D.3: Results from EDS of selected points and areas of coupled DSA sample embedded in Mud.

Element [wt%]	Spot 1	Spot 2	Area 1	Area 2	Area 3
O	12.54	1.03	6.89	1.9	-
Zn	0.6	1.15	-	1.71	2.32
Al	85.08	60.95	89.95	80.62	97.68
Si	0.67	0.08	2.55	0.2	-
Fe	1.1	-	-	-	-
C	-	36.38	-	15.01	-
Ar	-	0.41	0.61	0.55	-
Total	99.99	100	100	99.99	100

## D.4 Cross Section Measurements and EDS of coupled TSA sample embedded in Mud

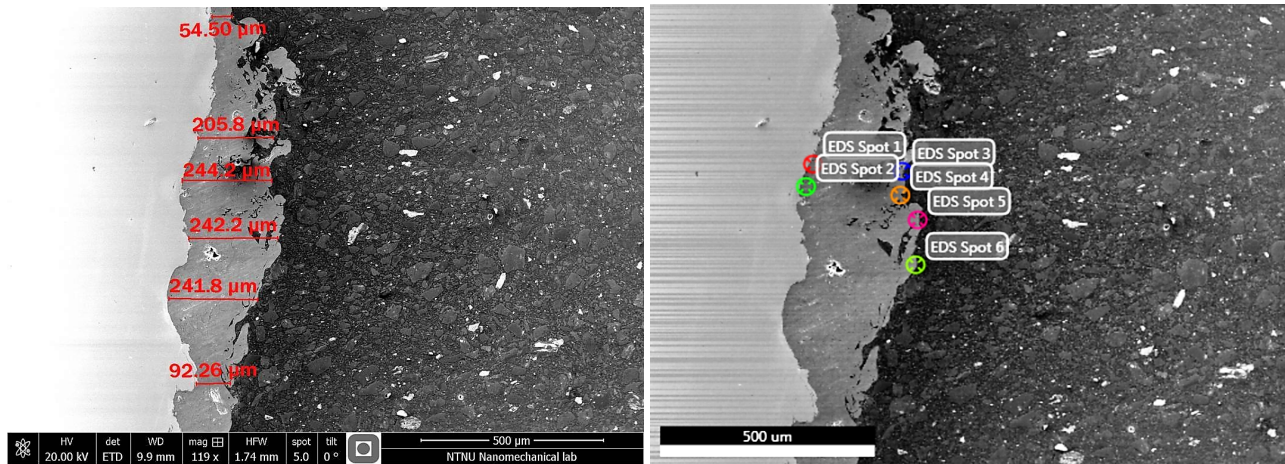


Figure D.4: Left: Cross section measurements of coupled TSA sample embedded in Mud. Right: Areas/Spots for EDS.

Table D.4: Results from EDS of selected points and areas of coupled TSA sample embedded in Mud.

Element [wt%]	Spot 1	Spot 2	Spot 3	Spot 4	Spot 5	Spot 6
O	1.84	1.49	5.3	1.84	0.59	1.57
Al	94.58	97.54	38.73	60.09	82.72	67.05
Si	1.77	-	0.49	-	-	-
Ar	0.98	0.98	0.21	0.41	0.74	0.54
Fe	0.83	-	0.37	-	-	-
Mg	-	-	0.56	-	-	-
Ca	-	-	0.31	-	-	-
C	-	-	54.03	37.65	15.96	30.84
Total	100	100.01	100	99.99	100.01	100

## D.5 Cross Section Measurements and EDS of polarized DSA sample embedded in Mud

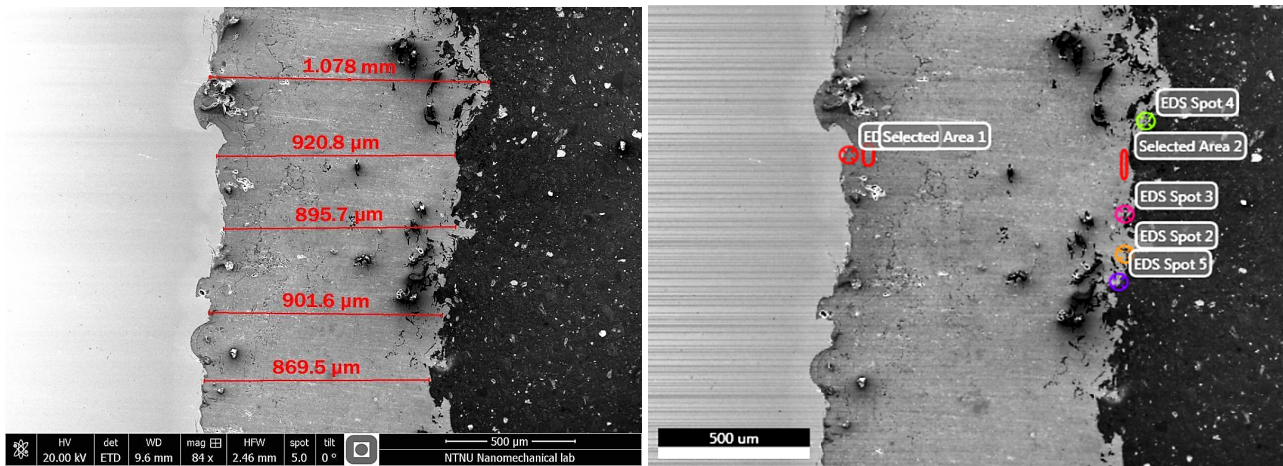


Figure D.5: Left: Cross section measurements of polarized DSA sample embedded in Mud. Right: Areas/Spots for EDS.

Table D.5: Results from EDS of selected points and areas of polarized DSA sample embedded in Mud.

Element [wt%]	Area 1	Area 2	Spot 1	Spot 3	Spot 4	Spot 5
O	3.55	7.21	3.62	5.81	2.89	1.55
Fe	1.46	-	0.3	-	-	-
Al	92.44	1.92	95.19	0.52	1.09	0.83
Ar	0.79	-	0.9	-	-	-
C	-	88.88	-	91.93	94.2	96.35
Mg	-	0.34	-	0.27	-	-
Si	1.77	1.03	-	1.01	1.17	0.69
S	-	0.35	-	0.03	0.65	0.57
Ca	-	0.27	-	0.32	-	-
Zn	-	-	-	0.11	-	-
Total	100.01	100	100.01	100	100	99.99

## D.6 Cross Section Measurements and EDS of polarized TSA sample embedded in Mud

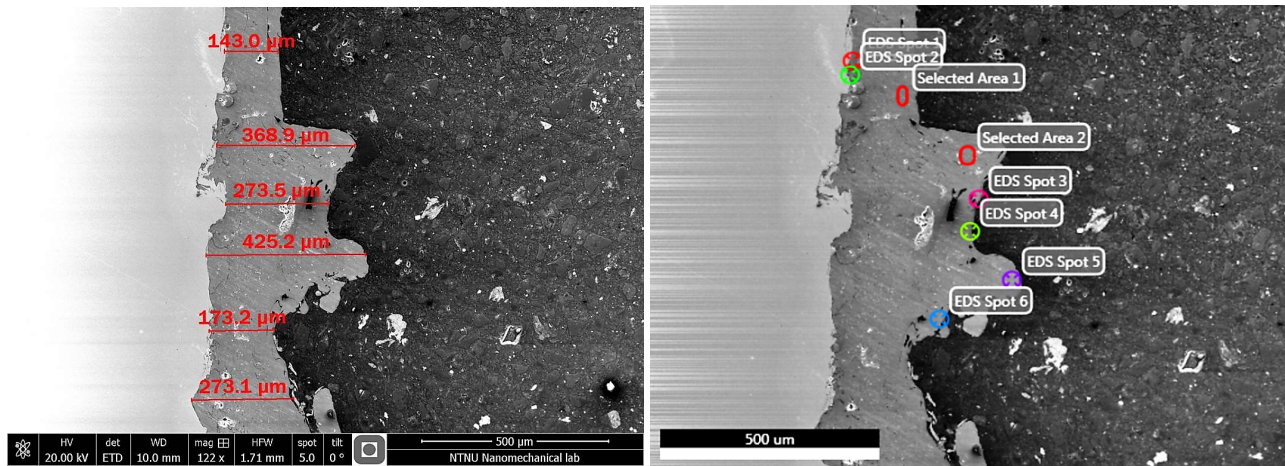


Figure D.6: Left: Cross section measurements of polarized TSA sample embedded in Mud. Right: Areas/Spots for EDS.

Table D.6: Results from EDS of selected points and areas of polarized TSA sample embedded in Mud.

Element [wt%]	Spot 1	Spot 2	Area 1	Area 2	Spot 3	Spot 4	Spot 5	Spot 6
O	1.64	30	1.96	4.7	2.26	0.94	1.2	1.44
Al	96.45	67.26	97.11	92.51	90.66	76.92	97.85	97.53
Ar	0.85	0.28	0.93	0.83	0.89	0.72	0.95	1.03
Fe	1.07	0.83	-	-	-	-	-	-
Na	-	1.1	-	-	-	-	-	-
Si	-	0.52	-	1.96	-	-	-	-
C	-	-	-	-	6.2	21.43	-	-
Total	100.01	99.99	100	100	100.01	100.01	100	100



## D.7 Cross Section Measurements and EDS of freely exposed DSA sample embedded in Mud

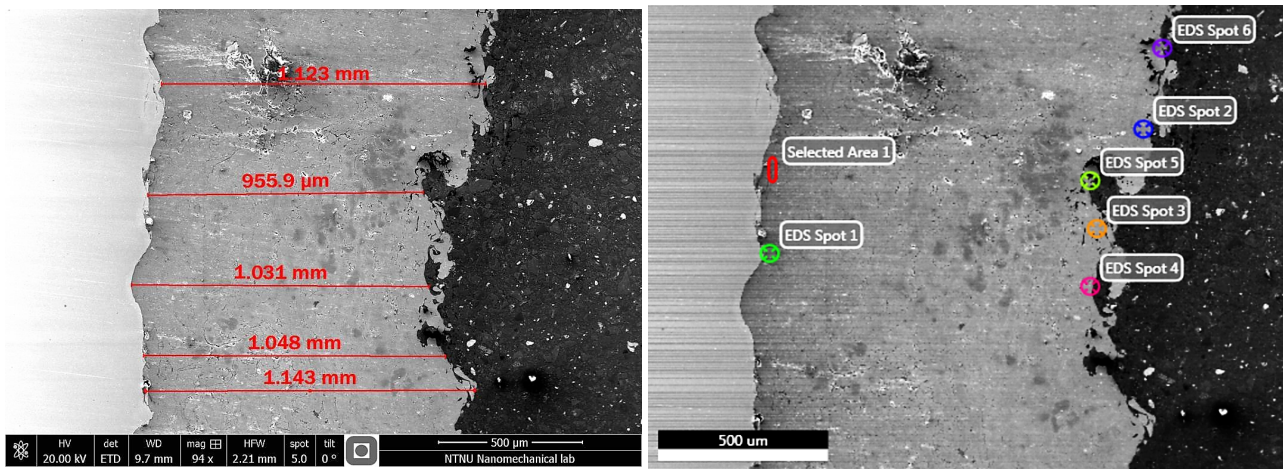


Figure D.7: Left: Cross section measurements of freely exposed DSA sample embedded in Mud. Right: Areas/Spots for EDS.

Table D.7: Results from EDS of selected points and areas of freely exposed DSA sample embedded in Mud.

Element [wt%]	Area 1	Spot 1	Spot 2	Spot 3	Spot 4	Spot 5	Spot 6
O	8.38	1.84	2.74	2.74	1.39	10.36	3.71
Zn	0.15	-	2.22	2.16	1.82	1.59	2.22
Al	87.1	93.28	94.28	93.96	71.9	38.08	93.29
Si	3.74	3.94	-	0.42	-	1.94	-
Ar	0.64	0.93	0.76	0.72	0.51	-	0.78
C	-	-	-	-	24.38	47.05	-
K	-	-	-	-	-	0.85	-
S	-	-	-	-	-	0.14	-
Total	100.01	99.99	100	100	100	100.01	100

## D.8 Cross Section Measurements and EDS of freely exposed TSA sample embedded in Mud

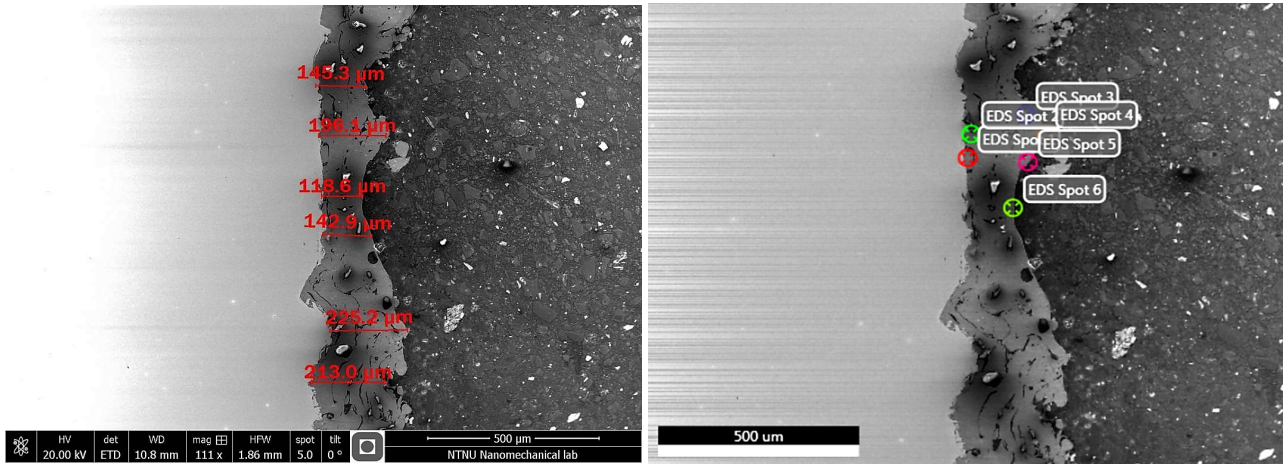


Figure D.8: Left: Cross section measurements of freely exposed TSA sample embedded in Mud. Right: Areas/Spots for EDS.

Table D.8: Results from EDS of selected points and areas of freely exposed TSA sample embedded in Mud.

Element [wt%]	Spot 1	Spot 2	Spot 3	Spot 4	Spot 5	Spot 6
O	0.84	8.7	10.01	5.02	2.18	1.65
Al	94.93	42.57	24.5	41.36	58.04	76.94
Ar	0.73	-	-	-	0.41	0.71
Fe	3.5	0.9	1.31	-	-	-
C	-	47.82	62.96	52.99	39.37	20.69
Mg	-	-	0.48	0.45	-	-
Si	-	-	0.39	0.19	-	-
Ca	-	-	0.34	-	-	-
Total	100	99.99	99.99	100.01	100	99.99

# **Appendix E**

## **E.1 Risk Assessment**

NTNU	Kartlegging av risikofylt aktivitet			Audun Ryen	Dato
 HMS				Uarbeidet av	HMS-avd.
		Godkjent av	Erstatter		
		Rektor			

Enhet: Fakultet for ingeniørvitenskap, Institutt for maskinteknikk og produksjon

Dato: 02.02.2017 Linjeleder: Torgeir Welo

Deltakere ved kartleggingen (m/ funksjon): Audun Ryen, Student

Kort beskrivelse av hovedaktivitet/hovedprosess: Masteroppgave Audun Ryen. Lab-arbeid i forbindelse med forsøk.

Er oppgaven rent teoretisk? (JA/NEI): Nei «JA» betyr at veileder innestår for at oppgaven ikke inneholder noen aktiviteter som krever risikovurdering. Dersom «JA»: Beskriv kort aktiviteten i kartleggingsskjemaet under. Risikovurdering trenger ikke å fylles ut.

Signaturer: Ansvarlig veileder:

*[Signature]*  
Student: Audun Ryen

ID nr.	Aktivitet/prosess	Ansvarlig	Eksisterende dokumentasjon	Eksisterende sikringstiltak	Lov, forskrift o.l.	Kommentar
1	Oppsett/Oppstart av forsøk	Audun	Laboratorie- og verksted – Håndbok, NTNU/SINTEF	Verneutstyr Risikovurdering Opplæring	IPMs HMS regler. Kap. 2.3, 4 og 7 i håndbok.	
2	Kjøring av forsøk	Audun	Laboratorie- og verksted – Håndbok, NTNU/SINTEF	Verneutstyr Opplæring	IPMs HMS regler. Kap. 2.4, 5 og 8 i håndbok.	
3	Avslutning av forsøk	Audun	Laboratorie- og verksted – Håndbok, NTNU/SINTEF	Verneutstyr Opplæring	IPMs HMS regler. Kap. 2.4, 5 og 8 i håndbok.	
4	Etterarbeid	Audun	Laboratorie- og verksted – Håndbok, NTNU/SINTEF	Verneutstyr Opplæring	IPMs HMS regler. Kap. 2.4, 5 og 8 i håndbok.	




NTNU	<b>Risikovurdering</b>			Utlarbeidet av	Audun Ryen	Dato
				HMS-avd.	HMSRV2601	02.02.2017
HMS				Godkjent av		Erstatter
			Rektor			

Enhet: Fakultet for ingeniørvitenskap, Institutt for maskinteknikk og produksjon

Dato: 02.02.2017 Linjeleder: Torgeir Welø

Deltakere ved kartleggingen (m/ funksjon): Audun Ryen  
(Ansv. Veileder, student, evt. medveiledere, evt. andre m. kompetanse)

Risikovurderingen gjelder hovedaktivitet: Masteroppgave Audun Ryen. Lab-arbeid i forbindelse med forsøk.

Signaturer: Ansvarlig veileder: 

Student: 

ID nr	Aktivitet fra kartleggings-skjemaet	Mulig uønsket hendelse/ belastning	Vurdering av sannsynlighet (1-5)	Vurdering av konsekvens:				Risiko-Verdi (menn-eske)	Kommentarer/status Forslag til tiltak
				Menneske (A-E)	Ytre miljø (A-E)	Øk/ materiell (A-E)	Om-dømme (A-E)		
1	Oppsett/Oppstart av forsøk	Skade på materielt utstyr Klærskader	2	A	A	B	B	B3	Varsomhet.
		Brannskader fra kokeplate eller oppvarmet vann.	1	C	A	A	B	C1	Varsomhet.
		Kuitskader ved tilfaging av eksperimentelt utstyr.	2	B	A	A	B	B2	Verneutstyr.
2	Kjøring av forsøk	Velting av kontainer med oppvarmet sjøvann. Støy fra annet arbeid i laben	1	B	A	A	A	B1	Varsomhet ved bruk av utstyr
		Lekkasje fra tanken med påfølgende oversvømmelse.	3	B	A	A	A	B3	Varsomhet mot annet arbeid i laben.
		Brenne seg på varmt vann ved påfylling av veske i beholder	2	B	A	A	A	B2	Tilsyn og lekkasjetesting for bruk av utstyr.
3	Avslutning av forsøk	Ødelegge prøver v. demontering Kuitskader ved demontering	2	A	A	B	A	B2	Varsomhet.
		Kutte fingre ved kutting av eksponerte prøver.	1	C	A	A	A	C1	
4	Etterarbeid	Skade fingre ved polering av prøver. Ødelegge SEM-maskin ved analyse.	2	B	A	A	A	B2	Vernebriller og vernehansker.
			1	A	A	C	B	C1	Opplæring i sikker bruk av SEM-utstyr.

NTNU	<h1>Risikovurdering</h1>			Utarbeidet av	Audun Ryen	Dato
				HMS-avd.	HMSRV2601	02.02.2017
HMS				Godkjent av		Erstaller
				Rektor		

## Sannsynlighet vurderes etter følgende kriterier:

	Svært liten 1	Liten 2	Middels 3	Stor 4	Svært stor 5
1 gang pr 50 år eller sjeldnere	1 gang pr 10 år eller sjeldnere	1 gang pr 10 år eller sjeldnere	1 gang pr år eller sjeldnere	1 gang pr måned eller sjeldnere	Skjer ukentlig

## Konsekvens vurderes etter følgende kriterier:



Gradering	Menneske	Ytre miljø Vann, jord og luft	Øk/materiell	Omdømme
<b>E</b> Svært Alvorlig	Død	Svært langvarig og ikke reversibel skade	Drifts- eller aktivitetsstans > 1 år.	Troverdighet og respekt betydelig og varig svekket
<b>D</b> Alvorlig	Alvorlig personskade. Mulig uførhet.	Langvarig skade. Lang restitusjonstid	Driftsstans > ½ år Aktivitetsstans i opp til 1 år	Troverdighet og respekt betydelig svekket
<b>C</b> Moderat	Alvorlig personskade.	Mindre skade og lang restitusjonstid	Drifts- eller aktivitetsstans < 1 mnd	Troverdighet og respekt svekket
<b>B</b> Liten	Skade som krever medisinsk behandling	Mindre skade og kort restitusjonstid	Drifts- eller aktivitetsstans < 1uke	Negativ påvirkning på troverdighet og respekt
<b>A</b> Svært liten	Skade som krever førstehjelp	Ubetydelig skade og kort restitusjonstid	Drifts- eller aktivitetsstans < 1dag	Liten påvirkning på troverdighet og respekt

## Risikoverdi = Sannsynlighet x Konsekvens

Beregn risikoverdi for Menneske. Enheten vurderer selv om de i tillegg vil beregne risikoverdi for Ytre miljø, Økonomi/materiell og Omdømme. I så fall beregnes disse hver for seg.

## Til kolonnen "Kommentarer/status, forslag til forebyggende og korrigerende tiltak":

Tiltak kan påvirke både sannsynlighet og konsekvens. Prioriter tiltak som kan forhindre at hendelsen inntreffer, dvs. sannsynlighetsreduserende tiltak foran skjerpet beredskap, dvs. konsekvensreduserende tiltak.

NTNU		Risikomatrikse		Audun Ryen		Dato	
				HMSRV2604		02.02.2017	
HMS/IKS				utarbeidet av HMS-avd. godkjent av Rektor		Erstatter	
							

## MATRISSE FOR RISIKOVURDERINGER ved NTNU

KONSEKVENSENS	Svært alvorlig									
	Alvorlig									
	Moderat									
	Liten									
	Svært liten									
		Svært liten	Liten	Middels	Stor	Svært stor				
<b>SANNSYNLIGHET</b>										

Prinsipp over akseptkriterium. Forklaring av fargene som er brukt i risikomatriksen.

Farge	Beskrivelse
Rød	Uakseptabel risiko. Tiltak skal gjennomføres for å redusere risikoen.
Gul	Vurderingsområde. Tiltak skal vurderes.
Grønn	Akseptabel risiko. Tiltak kan vurderes ut fra andre hensyn.